Fachbereich Mathematik und Naturwissenschaften
Fachgruppe Physik
Bergische Universität Wuppertal

Measurement of the t-Channel Single Top-Quark Production Cross-Section with the ATLAS Detector at $\sqrt{s} = 7\,\mathrm{TeV}$

Dissertation zur Erlangung des Doktorgrades
vorgelegt von
Philipp Sturm

April 19, 2012

Introduction

The aim of elementary particle physics is to explain the fundamental building blocks of matter and their interactions on a sub-nuclear scale. During the last decades the Standard Model of elementary particle physics was developed and tested by theoretical and experimental physicists. The Standard Model uses relativistic quantum field theories to describe the strong and electroweak interactions of the fundamental particles. Since the coupling strength of gravity is tens of orders of magnitudes smaller than the other interactions on sub-nuclear scales, it is is not included in the Standard Model. Although, the Standard Model is not a complete theory, its predictions have passed many stringent precision tests up to an energy scale of $\mathcal{O}(200\,\mathrm{GeV})$ in high energy physics experiments.

The interactions between the Standard Model particles are described by gauge bosons, which interact with twelve known matter particles and their corresponding anti-particles. The constituents of matter are distinguished into two classes, each consisting of six leptons and six quarks. In 1995 the heaviest of the six quarks, the top quark was discovered in proton anti-proton collisions at the Tevatron collider at a centre-of-mass energy of $\sqrt{s} = 1.8\,\mathrm{TeV}$ by the two collaborations, CDF and DØ [1, 2]. The top quark is about 40 times heavier than the second heaviest quark. Its mass of $173.2 \pm 0.9\,\mathrm{GeV}/c^2$ [3] is of the same order as the electroweak symmetry breaking scale. Thus, it plays a distinct role in precision tests of the Standard Model.

A new energy frontier is set by the Large Hadron Collider (LHC). In the data taking period of 2011, protons were brought to collision at a centre-of-mass energy of 7 TeV. This opens the opportunity to test the Standard Model up to an energy scale of $\mathcal{O}(1\,\mathrm{TeV})$.

At the energy scale available at the LHC, the top quark provides an excellent probe to test the Standard Model. At hadron colliders, the main production mechanism is the pair production due to the strong interaction. An additional production mode is predicted by the Standard Model via charged currents of the weak interaction, involving a W-t-b vertex. It is denoted as electroweak single top-quark production. Three different sub-processes are distinguished. The t- or s-channel, which are characterised by the exchange of a virtual W boson and the associated production of a top quark together with a real W boson. The predicted cross-sections at the LHC are $64.6^{+2.7}_{-2.0}\,\mathrm{pb}$ for the t-channel [4], $15.7 \pm 1.1\,\mathrm{pb}$ for the associated production [5], and $4.6 \pm 0.2\,\mathrm{pb}$ for the s-channel [6]. Compared to the Tevatron, the probability of producing a t-channel single top-quark event in a collision increases approximately by a factor of 30.

In a combined search of the s- and t-channel, the Tevatron collaborations CDF and DØ reported the observation of single top-quark production in 2009 [7, 8]. At the

LHC, the ATLAS and CMS collaborations have observed the t-channel single top-quark production process [9, 10].

Precision measurements of the single top-quark production offer several opportunities to test the predictions of the Standard Model, especially the W-t-b vertex of the weak interaction. The t-channel production cross-section is proportional to the squared absolute value of the quark-mixing matrix-element V_{tb}. In the Standard Model, this number is derived from the unitarity constraint of the matrix under the assumption of three quark generations. The measurement of the electroweak single top-quark production cross-section offers direct access to this theoretical quantity without any assumptions on the number of quark generations.

The aim of this thesis is the measurement of the single top-quark t-channel production cross-section with the first data recorded by the ATLAS detector. A dataset with an integrated luminosity of $1.04\,\text{fb}^{-1}$, recorded in the first half of 2011 at a centre-of-mass energy of 7 TeV is used.

The observable final state of the signal process is characterised by the decay products of the top-quark. The W boson originating from the top-quark decay is reconstructed in the leptonic final state in the $e\nu$ or $\mu\nu$ decay mode. Therefore, selected events have an isolated high-p_{T} electron or muon and missing transverse momentum. The hadronic final state of the W-boson decay is not a feasible channel due to the overwhelming background from multijet events. Some acceptance to $\tau\nu$ events, where the τ decays leptonically, is also contained in the dataset. Additionally, two or three jets are expected in the event. Exactly one of the jets is required to be identified as a jet containing a b quark. Compared to the background processes, a striking feature of the t-channel process is the light-quark jet which is predominantly scattered in the forward direction.

The challenge of this analysis is to extract a small fraction of signal events from a dataset which is dominated by a large number of background events. An additional difficulty is the theoretically not well predicted normalisation of some of the main background processes. Event models of the signal and background processes are constructed by using Monte Carlo simulation techniques. For the instrumental background due to the misidentification of multijet events as events featuring a charged lepton, a data-driven event model is developed. Since no single variable provides a sufficient separation power between signal and background processes, an artificial neural network (NN) is trained to classify events. For the background normalisation and signal cross-section measurement a binned maximum-likelihood fit of the continuous NN-output distribution to observed data is employed. The systematic uncertainties of the measurement are evaluated using a frequentist method. Finally, the cross-section measurement is used to determine the quark-mixing matrix element $|V_{tb}|$.

Contents

Chapter 1

The Top-Quark within the Standard Model

During the 1960s and 70s the theoretical framework of the Standard Model (SM) of elementary particle physics was developed. It is formulated by combining quantum mechanics with special relativity. The SM adheres a fundamental set of matter particles and describes the interactions amongst them on a subatomic scale, except gravity which is not included. Although it is known, that the SM is not a complete theory, it passes many high-precision tests up to an energy scale of $\mathcal{O}(200\,\mathrm{GeV})$. At the Large Hadron Collider, the predictions of the SM can be tested up to an energy regime of several TeV. This chapter provides a brief summary on the particle content of the SM and the forces that interact between the fundamental constituents of matter. The main focus is on the production mechanisms of the top quark, the heaviest elementary particle known so far. Besides top-quark pair production via the strong interaction, the three different production modes of electroweak single top-quark production are explained. At the end of the chapter a small overview on singly produced top-quarks as probe for new physics is given.

1.1 The Standard Model of Elementary Particle Physics

The SM of elementary particle physics is a quantum field theory [11], which describes the fundamental constituents of matter and the interaction amongst them. As it will be shown in this section, all matter is composed of fermions. Their interactions are mediated by gauge bosons. In nature, four fundamental forces are known: The strong, the electromagnetic, the weak, and the gravitational force. Each is described by a single theory, chromodynamics, electrodynamics, flavourdynamics, and Einstein's general theory of relativity. One of the big achievements of the SM is to explain the electromagnetic and weak interaction as manifestation of the same physical effect in one self-contained theory. The SM does not incorporate the gravitational force. First, a quantum theory of the gravitation is not formulated yet and second, it does not play a role in the sub-nuclear interaction of elementary particles because its relative strength is more than 30 magnitudes weaker than the other interactions.

Fermions

The constituents of matter in the universe are the fermions. They are point-like fundamental particles, which carry spin 1/2. One distinguishes two classes of fermions, quarks and leptons. In the SM the fermions are grouped in three generations of particles. The second and third generation are a copy of the first one with the same type of particles having a larger mass. Each generation has an electrically charged lepton with a neutral partner and two quarks having a different electric charge. Table 1.1 summarises the fermions of the SM and their properties. All visible matter of the universe is formed of the particles of the first generation. The heavier particles of the second and third generation are only produced in high energy processes and decay subsequently into the light and stable particles of the first generation. One has to note, that the mass hierarchy between the particle generations comprises five orders of magnitude. The particle masses range from a few MeV/c^2 to approximately 170 GeV/c^2. Each fermion has a corresponding anti-particle with the same mass, but opposite additive quantum numbers, e.g. the electrical charge. The fermion masses are free parameters of the SM, which have to be determined experimentally.

The electrically charged leptons of the SM are the electron (e), the muon (μ), and the tau (τ). They carry a charge of $-Q_e$. Hereby Q_e is the absolute value of the electron charge. Each is accompanied by a neutral partner called neutrino (ν). Charged leptons

Name	Symbol	El. Charge [Q_e]	Col. Charge	Mass [MeV/c^2]
up quark	u	$\frac{2}{3}$	✓	$(1.7-3.1)$
down quark	d	$-\frac{1}{3}$	✓	$(4.1-5.7)$
electron	e	-1	–	0.511
e-neutrino	ν_e	0	–	$<2\cdot10^{-6}$
charm quark	c	$\frac{2}{3}$	✓	$(1.18-1.34)\cdot10^3$
strange quark	s	$-\frac{1}{3}$	✓	$(80-130)$
muon	μ	-1	–	106
μ-neutrino	ν_μ	0	–	<0.19
top quark	t	$\frac{2}{3}$	✓	$(171.4-174.4)\cdot10^3$
bottom quark	b	$-\frac{1}{3}$	✓	$(4.13-4.37)\cdot10^3$
tau	τ	-1	–	1777
τ-neutrino	ν_τ	0	–	<18.2

Table 1.1: *The properties of the spin-$\frac{1}{2}$ particles, the fermions [12]. The electric charge is given in units of the positron charge, the mass in units of MeV/c^2. The first row presents the constituents of the stable matter in the universe. The second and third row represent the components of heavier unstable particles, which are produced in high energy processes and decay subsequently to the stable particles of the first generation.*

interact via the electromagnetic and weak force, whereas the neutrinos only take part in the weak interaction. In the SM neutrinos are assumed to be massless. However, experimental measurements have observed neutrino masses [13, 14].

The second group of fermions, the quarks, take part in the electromagnetic, weak and strong interaction. An individual flavour quantum number is assigned to each quark. For this reason, they interact with the weak force. As a consequence of carrying a colour charge, the quarks participate in the strong interaction. In nature, free colour-charged objects do not exist. Thus, no free quarks are observed [15]. They form bound states, the hadrons. The up and down quark of the first generation are the constituents of neutrons and protons. According to their electric charge, the quarks are classified as up-type $+\frac{2}{3}Q_e$ and down-type quarks $-\frac{1}{3}Q_e$. The up-type quarks are the up (u), charm (c) and top quark (t). The down (d), strange (s) and bottom quark (b) belong to the group of down-type quarks.

Bosons and Forces

Mathematically, the SM is based on a Lagrangian, which has to be invariant under certain local gauge transformations [16, 17]. This requirement is fulfilled by the symmetry group of the SM, which is $SU(3)_C \times SU(2)_L \times U(1)_Y$. These symmetries correspond to the fundamental interactions explained by the SM. Hereby, the strong force is associated with the $SU(3)_C$ symmetry and the electroweak interaction corresponds to the $SU(2)_L \times U(1)_Y$ symmetry. Those gauge symmetries are related to gauge bosons which mediate an interaction between fundamental particles. In the SM, the gauge bosons are spin-1 particles. Each symmetry corresponds to a conserved quantity which is invariant under the gauge transformation. This quantity is identified with the charge the gauge boson couples with [18], e.g. the photon couples to the electric charge. Table 1.2 gives an overview on the properties of the different gauge bosons.

The strong interaction is formulated in the framework of quantum chromodynamics (QCD) [19–21]. The underlying symmetry is the non-Abelian gauge group of a local $SU(3)_C$. As conserved quantity of the gauge transformation a three-valued charge is identified. It is denoted by the colours red, green, blue, and the corresponding anti-

Name	Force	Symbol	El. Charge [Q_e]	Col. Charge	Mass [GeV/c^2]
gluon	strong	g	0	✓	0
photon	electromagnetic	γ	0	–	0
$W^\pm$ boson	weak	$W^\pm$	± 1	–	80.403 ± 0.029
Z^0 boson	weak	Z^0	0	–	91.188 ± 0.002

Table 1.2: *Properties of the spin-1 particles, the gauge bosons [12]. The electric charge is given in units of the electron charge, the mass in units of GeV/c^2.*

colours. Massless gluons, which couple to the colour charge, are the mediators of the strong force. Since gluons carry one colour and one anti-colour charge eight different colour combinations are possible in the $SU(3)_C$. Thus, the gluons couple to each other. The only fermions that carry one colour charge are the quarks. Gluons couple with equal strength to all quarks and conserve the quark flavour in the interaction. In nature, only colour neutral objects are observed. Thus, no free quarks can exist, since quarks carry only one colour charge. They are the constituents of bound quark states, the hadrons. The bound state of a quark and antiquark is called meson, the bound state of three quarks or antiquarks is denoted as baryon. At energies of the order of the binding energy of the hadrons, the coupling strength of the strong interaction is large. So the quarks are confined into hadrons. In the case of high energetic QCD processes, the strength of the coupling gets weaker and the interaction can be described by perturbation theory.

The electromagnetic force is described by Quantum Electro Dynamics (QED). The underlying symmetry group is a $U(1)_Q$ symmetry. Massless photons, which couple to the electric charge Q mediate this force. Therefore, the range of the electromagnetic force is infinite. Since only electrically charged particles take part in this interaction no self-coupling of the photon is possible.

The weak interaction couples to all fermions, with a strength depending on the fermion type. In nature, the massive mediators of the weak force are observed as the electrically charged $W^{\pm}$ bosons and the electrically neutral Z^0 boson. Due to the large mass of the gauge bosons it is a short ranged interaction. In the case of neutrinos it is the only possibility to interact with other fundamental particles. The $W^{\pm}$ bosons interact only with left-handed particles. The Z^0 boson interacts with both chiralities, but with different strength. The weak interaction involving a $W^{\pm}$ boson does not conserve the flavour of a quark. A flavour transitions is not only possible within a generation, e.g. $c \rightarrow W^+ + s$, it also happens across the families. Without the possibility of a transition between the families, the lightest particles of a generation would be stable. In such weak interactions, the flavour eigenstate of a quark is not identical with the mass eigenstate. The transformation between the mass eigenstates (d, s, and b) and the flavour eigenstates (d', s', and b') is given by the Cabibbo-Kobayashi-Maskawa (CKM) matrix V_{CKM} [22, 23]:

$$\begin{pmatrix} d' \\ s' \\ b' \end{pmatrix} = \begin{pmatrix} V_{ud} & V_{us} & V_{ub} \\ V_{cd} & V_{cs} & V_{cb} \\ V_{td} & V_{ts} & V_{tb} \end{pmatrix} \begin{pmatrix} d \\ s \\ b \end{pmatrix}. \tag{1.1}$$

To preserve probability, the matrix has to be unitary. The strength of the charged current between two quarks i and j is proportional to the CKM-matrix element $|V_{ij}|^2$. None of the matrix parameters is predicted by theory. Thus, they have to be derived from experimental data. The current numerical values are [12]:

$$V^{\mathrm{CKM}} = \begin{pmatrix} 0.97413 \text{ to } 0.97443 & 0.2246 \text{ to } 0.2260 & 0.00330 \text{ to } 0.00358 \\ 0.2245 \text{ to } 0.2259 & 0.97330 \text{ to } 0.97329 & 0.0421 \text{ to } 0.0403 \\ 0.00836 \text{ to } 0.00822 & 0.0414 \text{ to } 0.0396 & 0.999122 \text{ to } 0.999107 \end{pmatrix}. \tag{1.2}$$

The CKM matrix is almost diagonal with small off-diagonal elements. The largest mixing across the families happens between the first and second quark generation. An overview on the different direct and indirect measurements of the individual matrix elements is given in Ref. [12]. In the SM, the matrix element V_{tb} is precisely deduced from the unitarity constraint of the 3×3 CKM matrix. A direct access to this theoretical quantity is possible by measuring electroweak single top-quark production. More details on this process are given in section 1.2.2.

Both phenomena, the electromagnetic and weak interaction can be unified to one single theory. The electroweak unification was developed by Glashow [24], Weinberg [25], and Salam [26] in the 1960s. At low energies, both interactions seem to be different entities. But it turns out, that at high energies they are the manifestation of the same effect. This is called electroweak unification. The underlying gauge symmetry of the theory is $SU(2)_L \times U(1)_Y$. The generator of the $SU(2)_L$ group is the weak isospin T. The second gauge symmetry of the theory is a $U(1)_Y$. Hereby, the generator of the symmetry group is the hypercharge Y. It is connected to the charge generator Q by $Q = T_3 + Y/2$. Now, in the unified theory, the gauge bosons are the isospin triplet $W_\mu^{1,2,3}$ and a isospin singlet B_μ. The observable gauge bosons $W^\pm$, Z^0 and γ are linear combinations of those.

In this theory, the $W_\mu^{1,2,3}$ and B_μ bosons are massless. In the SM model, the elementary particle masses are acquired by the Higgs mechanism [27–30], that introduces a scalar Higgs field. As a consequence of its non-zero vacuum expectation value, the masses of the heavy gauge bosons $W^\pm$ and Z^0 are generated, whereas the photon remains massless. Additionally, the Higgs boson appears as observable particle which has not been discovered up to now. Searches at the LEP collider exclude a mass range below $114.4\,\mathrm{GeV}/c^2$ [31] and as of the time of writing this thesis, preliminary results of the ATLAS collaboration exclude the mass ranges from $112.9\,\mathrm{GeV}/c^2$ to $115.5\,\mathrm{GeV}/c^2$, $131\,\mathrm{GeV}/c^2$ to $238\,\mathrm{GeV}/c^2$, and $251\,\mathrm{GeV}/c^2$ to $466\,\mathrm{GeV}/c^2$ [32]. By introducing gauge invariant Yukawa couplings, the masses of the fermions are acquired by coupling to the Higgs potential. The coupling strength is proportional to the fermion masses. Hence, the top quark will have a strong coupling to the Higgs boson. All particles masses and the CKM-matrix parameters are free parameters of the Higgs Lagrangian of the SM.

The interactions between elementary particles due to the fundamental forces explained before are studied in high energy collisions of hadrons or charged leptons. In case of the LHC protons are accelerated and collided. Since protons are compound objects, the actual interaction takes place between the constituents of the protons, which are denoted as partons. Thus, a description of the proton structure is necessary. The

proton consists of so-called valence quarks (uud) which are kept together by gluons. Those may split into a quark-antiquark pair, called sea quarks. Each constituent i of the proton carries a certain momentum fraction x_i of the total proton momentum p_P, hereby, the parton momentum is given by $p_i = x_i \cdot p_P$. Parton density functions (PDF) $f_{i,p}(x_i, \mu^2)$ describe the probability of finding a parton of a certain flavour and momentum fraction. The factorisation scale μ is the typical energy scale at which, the interaction takes place. Figure 1.1 shows the PDFs of the CTEQ6L [33] parametrisation for a factorisation scale $\mu^2 = (170\text{GeV})^2$, the typical scale where top-quark production processes take place.

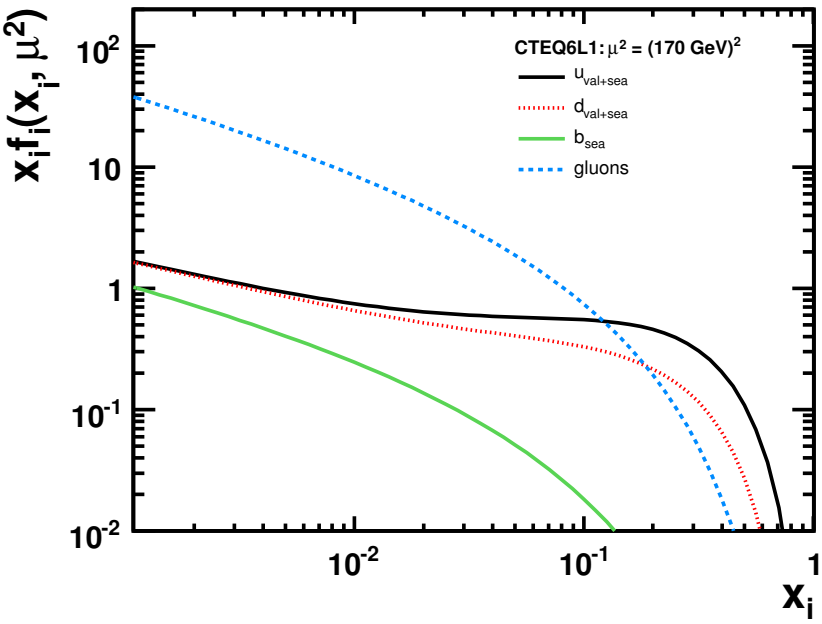

Figure 1.1: *The parton density functions of the CTEQ6L parametrisation [33] of the proton for up, down and b quarks and gluons. The contributions of the valence and the sea quarks are considered at a factorisation scale of $\mu^2 = (170\text{GeV})^2$.*

A measure of the probability to observe a certain final state X in a collision event is the cross-section σ. To compute the interaction rate the scattering process is assumed to take place between quasi-free partons. The cross-section of the incoming partons i and j to the final state X is denoted as partonic cross-section $\hat{\sigma}(ij \to X)$. In the case of hadron collisions, the partonic cross-section needs to be translated to the hadronic cross-section to obtain the interaction rate in the hadron collision. This is done by employing the factorisation ansatz. Hereby, the hadron substructure is taken into account by the convolution of the partonic cross-section $\hat{\sigma}$ with the PDF of the hadron:

$$\sigma(PP \to X) = \sum_{i,j} \int dx_i dx_j f_{i,P}(x_i, \mu^2) f_{j,P}(x_j, \mu^2) \hat{\sigma}(ij \to X; \hat{s}, \mu^2). \quad (1.3)$$

The partonic cross-section depends on the square of the centre-of-mass energy of the two colliding partons $\hat{s}$. For two hadrons having the same energy E it is defined by $\hat{s} = 4x_i x_j E^2$. The change of an initial-state ij to a final state X of a quantum system is expressed by the transition matrix element $\mathcal{M}$. It is converted to the partonic cross-section by summing all final state configurations and integrating their kinematic phase space. The convolution of $\hat{\sigma}$ with the PDF averages over the type of the initial-state partons and their kinematic phase space. Since it is impossible to compute $\hat{\sigma}$ in closed from, perturbation theory is used. Here, the interaction is expanded in a power series of the coupling constant α of the interaction. The main contribution stems from the leading-order (LO) terms of the perturbation series. Higher order corrections are important for the numerical precision and stability of the computation. But also important physical effects can appear at next-to-leading order (NLO). With increasing order, the calculation becomes extremely complex. Only for a few processes results in approximate next-to-next-to-leading-order (approx. NNLO) are available. Here, additional logarithmic terms beyond NLO are included in the calculation.

Physical processes in the parton picture can be visualised by Feynman diagrams. One example is shown in Fig. 1.2. It depicts the annihilation of an electron-positron pair to a photon, that splits into an electron-positron pair again. The perturbation series of a certain order can be visualised by a set of Feynman diagrams showing all possible graphs of the interaction. The other way round, the graphical illustration can be converted into the mathematical terms of the perturbation series by applying specific rules for the lines in the graph which denote the propagation of partons in space-time and the nodes which illustrate the coupling of the interaction.

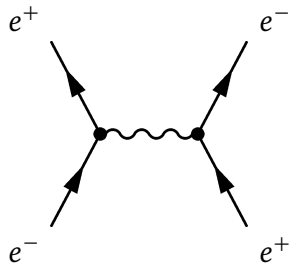

Figure 1.2: *Feynman diagram of an electron-positron annihilation into a photon, that splits to an electron-positron pair.*

1.2 The Top Quark

In 1995 the top quark was discovered at the Tevatron collider by the two collaborations CDF and DØ [1, 2] in proton-antiproton collisions at a centre-of-mass energy of 1.8 TeV. Top quarks were also observed at the LHC in the first year of operation by the ATLAS and CMS collaborations [34, 35] in 2010. Since the observation, many properties

of the top quark have been studied. The CKM-matrix parameters and the mass of the top quark have to be determined from experimental measurements because they are free parameters of the SM. At the Tevatron, the recent combination of all mass measurements yields a mass of $173.2 \pm 0.9\,\mathrm{GeV}/c^2$ [3]. It is the heaviest particle known so far with a mass 40 times larger than the mass of the b quark. The large mass leads to a very short lifetime, which is approximately $\tau_{top} \sim 10^{-25}\,\mathrm{s}$ [12]. This is shorter than the typical timescale of the strong interaction of $1/\Lambda_{QCD} \sim 10^{-23}\,\mathrm{s}$ [36]. Hence, the top quark decays before forming any bound state with other quarks. This provides the unique opportunity to study a quasi-free quark. The spin information is passed to the particles of the weak decay without any perturbation by the strong interaction. The top quark decays predominantly into a W boson and a b quark. Decays into an s quark or d quark are suppressed by the small values of the CKM-matrix elements V_{ts} and V_{td}. The final states are labelled by the subsequent decay of the W boson. Figure 1.3 depicts the two decay modes: The hadronic decay of the W boson $W \to q\bar{q}'$ (a) and the leptonic decay of the W boson $W \to \ell\nu$ (b). The branching ratios are 67.6% and 32.4% [12], respectively.

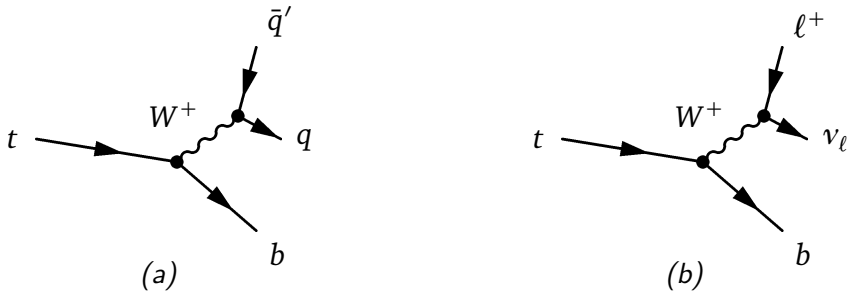

Figure 1.3: *The decay of the top quark into a b quark and a W boson. Other decay modes with an s quark or d quark in the final state are suppressed by the small CKM-matrix parameters. A hadronic decay of the W boson (a) happens with a probability of 67.6%, the branching ratio of the leptonic decay (b) is 32.4%.*

1.2.1 Top-Quark Pair Production

The primary production process of top quarks at hadron colliders is the production of a top quark antiquark pair ($t\bar{t}$) via the strong interaction. Figure 1.4 depicts the most important Feynman diagrams of $t\bar{t}$ production at leading order in α_s^2. Two relevant partonic modes can be distinguished: The quark-antiquark annihilation (a) and the gluon-gluon fusion (b)-(d). Both production modes contribute differently to the the total cross-section. At a collision energy of 7 TeV a parton momentum fraction of $x \approx \frac{2m_t}{\sqrt{s}} = 0.05$ is enough to exceed the threshold of $t\bar{t}$ production of $\hat{s} = 4m_t^2$. Hence, the gluon fusion channel contributes roughly 90% to the total cross-section, because the PDF is dominated by gluons at the low x region c.f. Fig. 1.1. Whereas at larger values of $\hat{s}$ for above the production threshold, the quark-antiquark annihilation becomes dominant.

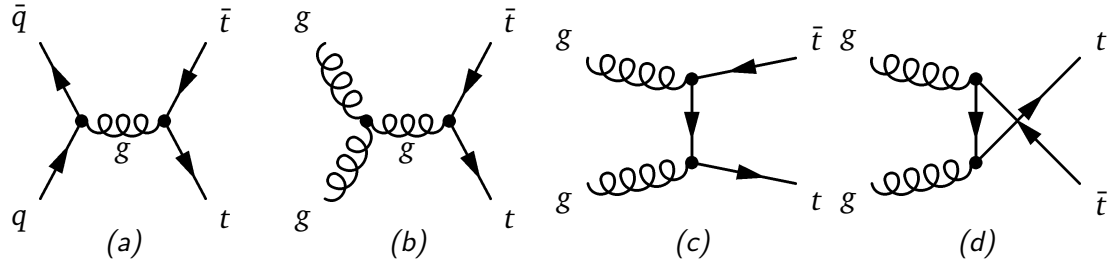

Figure 1.4: *Feynman diagrams of the $t\bar{t}$ production at leading order in α_s^2: quark-antiquark annihilation ($q\bar{q} \to t\bar{t}$) (a) and gluon fusion ($gg \to t\bar{t}$) (b)-(d).*

A perturbative QCD calculation is utilised to determine the partonic cross-sections of $ij \to t\bar{t}$. At next-to-leading order, gluon bremsstrahlung corrections and loop effects are included in the calculation. Current calculations of the $t\bar{t}$ production cross-section include higher order terms up to next-to-next-to-leading order of logarithmically enhanced terms near the threshold [37]. At a centre-of-mass energy of $\sqrt{s} = 7\,\mathrm{TeV}$ the cross-section is:

$$\sigma_{t\bar{t}}^{\text{approx. NNLO}} = 164.57\ ^{+4.30}_{-9.27}\,(\text{scale})\ ^{+7.15}_{-6.51}\,(\text{PDF})\,\text{pb}\ [38]. \tag{1.4}$$

This calculation assumes a top-quark mass of $172.5\,\mathrm{GeV}/c^2$ and uses the CTEQ6.6 [33] PDF parametrisation and its uncertainties. The scale uncertainty is evaluated at $\mu = 0.5m_t$ and $\mu = 2m_t$. At the design energy of the LHC of $\sqrt{s} = 14\,\mathrm{TeV}$ the $t\bar{t}$ production cross-section predicted to be $\sigma_{t\bar{t}}^{\text{approx. NNLO}} = 874^{+29}_{-43}\,\text{pb}$ [38].

Three final states can be distinguished by the combinations of the decay products of the top quarks, depending on the W boson decaying either hadronically or leptonically. The di-lepton channel denotes the case where both of the W bosons decay leptonically. This happens with a probability of 10.3%. If one of the W bosons decays leptonically and the other one hadronically, one speaks of the semi-leptonic channel, which contributes with 42.5%. Since a τ is difficult to identify only the e and μ final states of the W boson decay are considered in experimental measurements using the di-lepton of semi-leptonic channel. Final states including a τ account for 50% of the di-lepton and 30% of the semi-leptonic channel. Both W bosons decaying hadronically accounts for 46.2% of the cases in the full-hadronic channel. Recent, preliminary results of the ATLAS collaboration measure a $t\bar{t}$ cross-section of $\sigma_{t\bar{t}} = 179.0^{+9.8}_{-9.7}\,(\text{stat} + \text{syst}) \pm 6.6\,(\text{lumi})\,\text{pb}$ [39] in the semi-leptonic channel, using a dataset corresponding to an integrated luminosity of $\mathcal{L} = 698\,\text{pb}^{-1}$. The measurement is consistent with the theoretical approximate NNLO calculation.

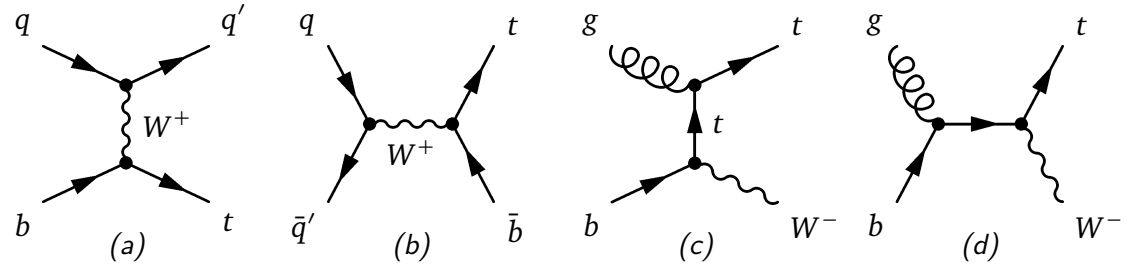

Figure 1.5: *Feynman diagrams at LO of the single top-quark production modes: t-channel (a), s-channel (b) and Wt production (c),(d).*

1.2.2 Single Top-Quark Production

An additional production mechanism of top quarks is predicted by the SM via the weak interaction. Compared to the QCD process, the weak process $qq \to Z \to t\bar{t}$ is negligible at hadron colliders. Thus, only the production of a single top-quark is of importance. Three different channels can be distinguished by the virtuallity $Q^2 = -q^2$ of the involved W boson. Here, q denotes the four-momentum of the W boson. Figure 1.5 gives an overview of the Feynman diagrams at LO of the three processes. The t-channel (a) and s-channel (b) are labelled by the virtuallity of the exchanged W boson characterising each process. Both processes involve a highly virtual W boson, which is time-like or space-like. The third process is the associated production (c) and (d). It is characterised by a real W boson in the final state together with the top quark. In 2009 the Tevatron experiments CDF and DØ reported the observation of singly produced top quarks [7, 8]. At the LHC, the ATLAS and CMS collaborations have also measured the t-channel production process [9, 10].

t-channel

The t-channel production mode is characterised by the electroweak scattering of a light quark off a b quark. A virtual, space-like W boson ($q^2 = \hat{t} < 0$) is exchanged between the two quarks. The b quark stems from a gluon splitting into a $b\bar{b}$ pair. Thus, this process is also denoted as W-gluon fusion. It is the dominant production mode of single top-quarks because it has the largest cross-section amongst the three production modes at the centre-of-mass energy of the LHC or Tevatron. Some of the Feynman diagrams at NLO are shown in Fig. 1.6. The most important contribution to the total cross-section stems from the $2 \to 3$ process (a), which includes the gluon splitting in the matrix element of the process. Hence, a second b quark is present in the final state. Cross-section calculations at NLO accuracy are based on the $qb \to tq'$ process. In those computations, the initial-state b quark is assumed to be massless. This scheme is denoted as five flavour scheme (5FS). Large logarithmic terms of the form $\log(Q^2/m_b^2)$ due to collinear initial-state $g \to b\bar{b}$ splittings are absorbed by the resummation into the PDF. In the 5FS, the properties of the second b quark are not at NLO precision since its existence appears at NLO in the matrix elements. An alternative is to consider

the $gq \to tbq'$ process at Born level. In the so called four flavour scheme (4FS) the b quark is considered to be massive. Thus, it does not enter the QCD evolution of the strong coupling and the PDF. Here, an additional particle is present in the final state of the matrix element. Therefore, the properties of the second b quark can be studied at NLO accuracy. Reference [40] compares both schemes in detail. The authors find an agreement of the NLO calculations in both schemes within 5%. However, the 4FS has a larger dependence on the scale variation than the 5FS, because the $2 \to 3$ process already contains a factor of α_s. Most of the scale dependence is due to the heavy-quark lines. The advantage of the 4FS is a reliable prediction of all relevant kinematic distributions, especially the transverse momentum and rapidity of the second b quark. The 4FS and 5FS are in general agreement but have a small residual difference, which indicates that higher-order corrections might be necessary.

Recent theoretical calculations reach an accuracy beyond the previous NLO calculations in Ref. [41]. Those include next-to-next-to-leading order logarithms to achieve an approximate NNLO accuracy. Numerical results for the LHC energies are calculated in Ref. [4]. One has to note, that in case of a proton-proton collider the production cross-section of singly produced top quarks is almost twice the one for singly produced top antiquarks. The reason can be found in the structure of the proton, which features two up valence-quarks and one down valence-quark. Two up quarks are available for top-quark production, whereas only one down quark is present leading to a top-antiquark production. The cross-section is dominated by the contribution of up and down quarks as incoming light quark. The effect of a charm or strange quark in the initial state of the light-quark line is rather small with roughly 2% . Also the production involving a W-t-d or W-t-s vertex is strongly suppressed by the small CKM-matrix elements involved [42].

At a centre-of-mass energy of $\sqrt{s} = 7\,\mathrm{TeV}$ and a top-quark mass of 172.5 GeV using the MSTW2008 NNLO PDF parametrisation [43] the numerical results are:

$$\sigma_t^{t-\mathrm{chan}} = 41.92 \pm 0.38\,(\mathrm{mass}) \pm 0.83\,(\mathrm{scale})\, ^{+0.97}_{-0.13}\,(\mathrm{PDF})\,\mathrm{pb} \tag{1.5}$$

$$\sigma_{\bar{t}}^{t-\mathrm{chan}} = 22.65 \pm 0.23\,(\mathrm{mass}) \pm 0.50\,(\mathrm{scale})\, ^{+0.41}_{-0.55}\,(\mathrm{PDF})\,\mathrm{pb}. \tag{1.6}$$

The quoted uncertainties stem from a top-quark mass variation of $\pm 1\,\mathrm{GeV}$, the dependence on the scale μ varied between $m_t/2$ and $2m_t$ and the uncertainty on the PDF parametrisation. Corrections due to the logarithmic terms at NNLO are about -1% compared to the NLO calculation. At the design centre-of-mass energy of the LHC of $\sqrt{s} = 14\,\mathrm{TeV}$ the total t-channel cross-section will be $\sigma^{t-\mathrm{chan}} = 243^{+8}_{-4}\,\mathrm{pb}$.

It is remarkably, that the t-channel production cross-section is of the same magnitude as the $t\bar{t}$ production cross-section, although it is a process of the weak interaction. The main reason for the enhancement is the scaling behaviour of the cross-sections. The cross-section of the t-channel production scales like $1/M_W^2$, whereas the $t\bar{t}$ production scales like $1/\hat{s}$. Additionally, the $t\bar{t}$ production is colour suppressed in the gluon-gluon

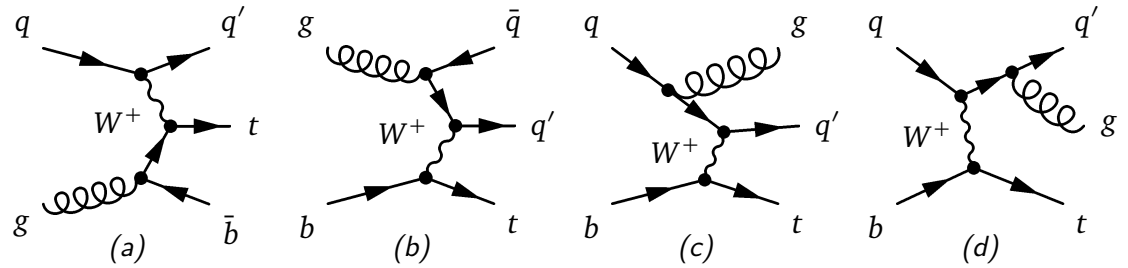

Figure 1.6: *Feynman diagrams at NLO suppressed by a factor of α_s of the t-channel single top-quark production mode: W-gluon fusion (a) and (b); initial-state (c) and final-state (d) radiation.*

fusion mode by a factor 3 because the colour combinations at the gluon vertex must match. A detailed review is given in Ref. [44].

s-channel

The production of a (t,b) quark pair by quark antiquark annihilation is denoted as single top-quark *s*-channel production. A virtual, time-like W-boson ($Q^2 = -q^2 < (m_t + m_b)^2$) is formed from the two initial-state quarks. Several Feynman diagrams at NLO are depicted in Fig. 1.7. A comparison of diagram (a) with the $2 \rightarrow 3$ t-channel diagram Fig. 1.6 (a) suggests an interference between the s- and t-channel at NLO, because both processes have the same initial and final state. But both diagrams are independently gauge invariant. The (t,b) pair produced in the s-channel process stems from a W decay. Therefore, it forms a colour singlet, whereas in the t-channel $2 \rightarrow 3$ process the (t,b) pair is colour connected with the initial-state gluon. Thus, this process forms a colour octet. The different colour structure of both diagrams prohibits an interference [45].

A theoretical prediction of the s-channel cross-section is available with a precision at approximate NNLO [6]. The s-channel production cross-section at the LHC is strongly suppressed compared to the Tevatron because of the proton structure. The antiquark has to stem from the proton sea quarks, whereas at the Tevatron the antiquark stems from the antiproton valence quarks. Hence, the s-channel will be a challenging measurement at the LHC. The cross-sections for top-quark and top-antiquark production are:

$$\sigma_t^{s-\text{chan}} = 3.19 \pm 0.07\,(\text{mass}) \pm 0.06\,(\text{scale})\, ^{+0.08}_{-0.06}\,(\text{PDF})\,\text{pb} \quad (1.7)$$

$$\sigma_{\bar{t}}^{s-\text{chan}} = 1.44 \pm 0.03\,(\text{mass}) \pm 0.01\,(\text{scale})\, ^{+0.04}_{-0.04}\,(\text{PDF})\,\text{pb}. \quad (1.8)$$

The calculation assumes a top-quark mass of 172.5 GeV and uses the MSTW2008 NNLO PDF parametrisation for a centre-of-mass energy of $\sqrt{s} = 7$ TeV. The quoted uncertainties stem from a top-quark mass variation of ± 1 GeV, the dependence on the scale μ var-

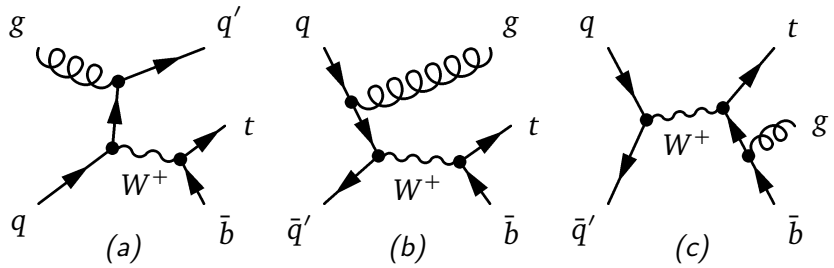

Figure 1.7: *Some Feynman diagrams at NLO, suppressed by a factor of α_s, of the s-channel single top-quark production mode: initial-state gluon splitting (a), inital-state (b) and final-state (c) radiation.*

ied between $m_t/2$ and $2m_t$ and the uncertainty of the PDF parametrisation. Compared to an NLO calculation, the cross-section is enhanced by 10% due to the approximate NNLO corrections. The cross-section at the nominal LHC centre-of-mass energy will be $\sigma^{s-\text{chan}} = 11.92^{+0.61}_{-0.68}\,\text{pb}$.

Associated Production

The third production mode of single top-quarks is the so called associated production or Wt-channel. A single top-quark is produced together with a real or close to on-shell W boson ($q^2 = M_W^2$). Feynman diagrams at LO are depicted in Fig. 1.5 (c) and (d). At the LHC Wt-production is the second most important source of single top-quarks. It makes up 19% of the total single top-quark production cross-section. The cross-section for top-quark and top-antiquark production is the same, since the initial state particles are a gluon and a b quark from the quark-sea. A theoretical approximate NNLO calculation is also available for this channel [5]. Virtual and real NLO corrections as well as corrections due to soft gluon radiation are considered. At a centre-of-mass energy of $\sqrt{s} = 7\,\text{TeV}$ with a top-quark mass of 172.5 GeV and the MSTW2008 NNLO PDF parametrisation the calculation yields:

$$\sigma^{Wt} = 15.74 \pm 0.28\,(\text{mass}) \pm 0.40\,(\text{scale})\,^{+0.66}_{-0.68}\,(\text{PDF})\,\text{pb}. \tag{1.9}$$

The quoted uncertainties to the theoretical calculation are the uncertainty to a top-quark mass variation of ± 1 GeV, the dependence on the scale μ varied between $m_t/2$ and $2m_t$ and the uncertainty of the PDF parametrisation. Compared to a NLO calculation, the NNLO soft-gluon corrections enhance the cross-section by 8%. The cross-section at the nominal LHC centre-of-mass energy is predicted to be $\sigma^{Wt} = 83^{+4}_{-5}\,\text{pb}$.

Between the Wt-channel diagrams at NLO, as presented in Fig. 1.8, and the Feynman diagrams of $t\bar{t}$ production at LO (Fig. 1.4) an interference appears. The diagrams of the associated production at NLO have the same final state as the $t\bar{t}$ diagrams. Reference [46] reviews the problem of an interference in detail. Both processes are separately well defined, if the associated production cross-section is larger than the

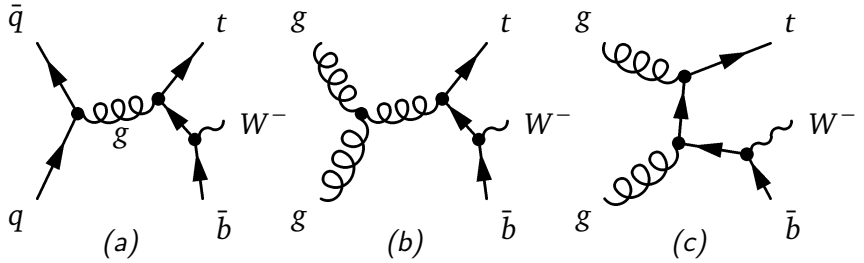

Figure 1.8: *Some Feynman diagrams at NLO, suppressed by a factor of α_s^2, of the Wt single top-quark production mode. Those graphs are equivalent to the leading-order $t\bar{t}$ graphs, with one of the top quarks already weakly decayed.*

scale uncertainty of the $t\bar{t}$ production cross-section and if the interference term is small. The former is given, the later can be assessed by removing the $t\bar{t}$ contribution to the Wt cross-section calculation. Two different schemes are available to estimate the impact of the interference term on the cross-section. In the diagram removal scheme one subtracts the $t\bar{t}$ diagrams at LO from the NLO calculation of the associated production. The second method, the diagram subtraction, implements subtractions terms in the Wt cross-section calculation that cancel the $t\bar{t}$ contribution locally [47]. Since the results of both methods agree within their scale uncertainties, if experimental cuts are considered for the cross-section calculation, the interference is small. Thus, both processes are separately well defined.

Top-Quark Polarisation

Due to the V-A structure of the weak interaction, top quarks are produced highly polarised in the s- and t-channel. In the t-channel production mode, the top quark is produced 100% polarised in direction of the light quark (c.f. Fig. 1.5). The top quark decays, before the spin information is diluted by hadronisation effects. An experimental access to the spin polarisation is possible by the decay products of the top quark. The spin information is transferred to the W boson. In its leptonic decay mode, the angle θ between the charged lepton and the light-quark jet in the top-quark rest-frame is a good observable of the polarisation. The angular distribution of the polarisation is defined by $\frac{\mathrm{d}\Gamma}{\Gamma \mathrm{d}\cos} = 0.5 \cdot (1 + \cos\theta)$ [48, 49].

Summary

Figure 1.9 shows the cross-sections of the three single top-quark production modes as a function of the centre-of-mass energy. At $\sqrt{s} = 7\,\mathrm{TeV}$ the t-channel production mode is the main source of singly produced top quarks. It accounts for 76% of the total single top-quark production cross-section. The associated production amounts for 19% of the total expected rate. Due to the gluon dominated PDF at the energies of the LHC, the s-channel production is strongly suppressed and accounts only for 5%. The reduction of the LHC collision energy from 14 TeV to 7 TeV leads to a drop in the production

cross-section by a factor of 4 for the t-channel, a factor of 3 for the s-channel, a factor of 5 for the associated production.

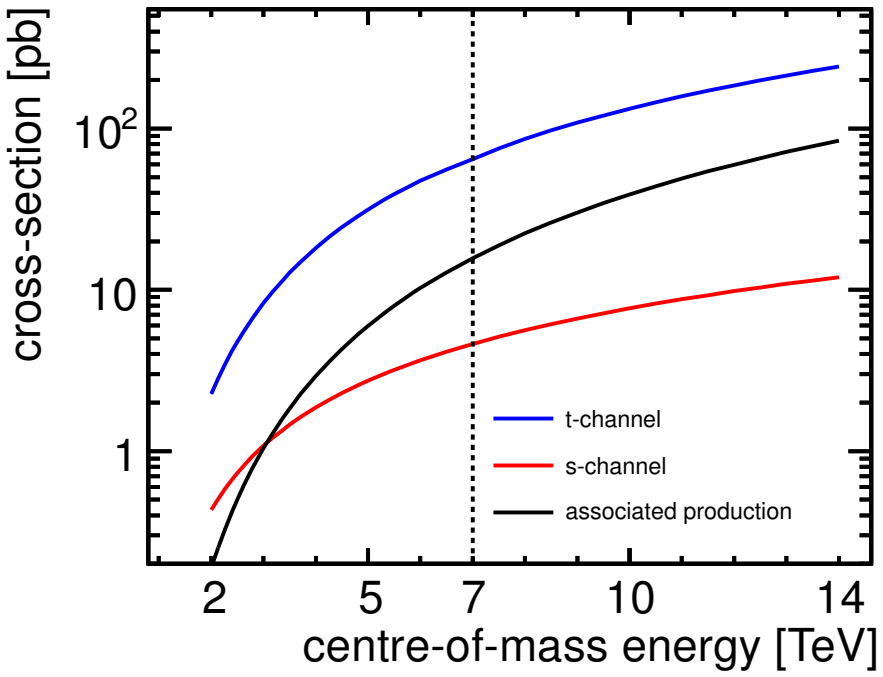

Figure 1.9: *Cross-sections of the different production modes of the single top-quark production processes as a function of the collision energy. The theoretical calculation of the t-channel [4], s-channel [6], and associated production [5] are at approximate NNLO precision.*

1.2.3 Single Top-Quark Production as a Window to New Physics

Models, that extend the SM interact with the top quark in two ways: They introduce new, heavy particles that couple to the top quark or the couplings of the top quark to the known particles of the SM are changed. New physics phenomena that appear at an energy scale Λ contribute to the production cross-section proportional to $(\sqrt{s}/\Lambda)^n$, whereas the contribution in top-quark decays scales as $(m_t/\Lambda)^n$. Hereby, n is a positive integer number or zero [50]. Thus, the production of single top-quarks at high energy colliders is sensitive to new physics phenomena. Any modification of the SM will affect the cross-sections of the three production modes in a different way.

Modified Vertex Couplings

The production of single top-quarks involves the W-t-b vertex. Thus, the cross-sections are proportional to the quark-mixing matrix element $|V_{tb}|^2$. Measuring the t-channel

cross-section makes this quantity accessible. Assuming a modification of a W-t-b coupling due to an effective operator O_{eff}, the cross-section is proportional to $|V_L|^2$:

$$V_L = V_{tb} + O_{\text{eff}} \frac{v^2}{\Lambda^2}. \tag{1.10}$$

Where Λ is the energy scale at which the new phenomena appear and $v = 246\,\text{GeV}$ is the scale of electroweak symmetry breaking. In the SM $V_L = V_{tb}$, but new physics contributions allow values larger than V_{tb} [51–53].

One possibility of a new effective coupling is the introduction of a flavour-changing neutral current (FCNC). Those are forbidden in the SM at tree level and suppressed at higher orders. A new production mode for single top quarks via such an anomalous coupling is for example possible by a g-t-q vertex. In this process, a u quark or c quark interacts with a gluon to produce a single top-quark. The strength of the coupling is defined by the parameters κ_{ugt} and κ_{cgt}. Current searches for FCNC single-top quark production set an upper limit of $\sigma_{qg\to t} \times \mathcal{B}(t \to Wb) < 3.9\,\text{pb}$. This result yields a limit on the coupling strength of $\kappa_{ugt}/\Lambda < 6.9 \cdot 10^{-3}\,\text{TeV}^{-1}$ and $\kappa_{cgt}/\Lambda < 1.6 \cdot 10^{-3}\,\text{TeV}^{-1}$ [54].

Extra Heavy Particles

Extensions of the SM postulate the existence of additional heavy gauge bosons, such as a W' for example. The s-channel is sensitive to the exchange of a W' [55] that couples to the top quark and b quark. A positive or negative contribution to the cross-section may arises from the interference with the SM s-channel production mode. Especially a resonant enhancement may arise, if a close to on-shell W' boson is exchanged. In this case a resonance should appear in the invariant mass distribution of the (t,b) system. In contrast, a contribution to the t-channel will be negligible because the exchange of a heavy particle will be suppressed by $1/M^2_{W'}$.

Other theories beyond the SM introduce additional heavy quarks, such as an up-type t' quark or a fourth generation quark pair $(t',\ b')$ [56]. Direct searches for the QCD production of extra quarks, set lower mass limits of $m_{b'} \geq 372\,\text{GeV}$ [57] and $m_{t'} \geq 358\,\text{GeV}$ [58] at 95% CL. The quark-mixing matrix element $V_{tb} \sim 1$ is derived with high precision using the unitarity constraint of the 3×3 CKM matrix. A fourth quark generation could mix with the quarks of the third generation. Hence, in such models V_{tb} can be smaller than 1. Since the single top-quark production cross-section is proportional to $|V_{tb}|^2$, it is sensitive to a fourth quark generation [42]. Thus, the single top-quark cross-section will be reduced proportional to the value of $|V_{tb}|^2$. In this scenario V_{ts} might be as large as 0.55. Therefore, an enhancement of the t-channel cross-section by $\sim 37\%$ is possible because a new production mode opens which is suppressed in the SM. The s-channel cross-section will be reduced by the value proportional to $|V_{tb}|^2$ compared with the SM.

Chapter 2

The ATLAS Detector at the Large Hadron Collider

At the European Centre for Nuclear Research (CERN), located near Geneva, the Large Hadron Collider (LHC) [59] is operated. It reuses the existing infrastructure of the previous Large Electron Positron Collider (LEP) [60], the 26.7 km underground tunnel and the CERN pre-accelerator complex. The LHC is designed to collide proton beams with an maximum energy of 7 T*e*V per beam or lead ions with an energy of 2.56 T*e*V per nucleon.

At four interaction points, six detectors are placed to record the beam collision events. A large ion collider experiment (ALICE) [61] is designed to investigate the properties of the quark-gluon plasma produced in lead-ion collisions. This is a state similar to the very early phase of the universe shortly after the big bang, where quarks and gluons are not confined in hadrons [62]. A second experiment, LHCb [63], is specialised in the physics of b hadrons produced in proton collisions. Precision measurements of CP violation in b-hadron decays might give an indirect evidence for new physics beyond the SM and an insight to the question of the matter-antimatter asymmetry of the universe. The LHC forward detector (LHCf) [64] measures the scattering of particles in the very forward direction. This will provide data for the calibration of hadron-interaction models used for the physics of high-energy cosmic-rays. Another small experiment, Totem [65] studies the total elastic and diffractive proton-proton cross-section. The two general purpose experiments ATLAS [66] and the Compact Muon Solenoid (CMS) [67] are designed to explore the physics at the T*e*V scale. Both detectors have the same physics goals: Testing the SM at the new accessible energy regime, the quest for the Higgs boson, and the search for new unknown phenomena.

This chapter introduces shortly the main components of the CERN accelerator complex and the LHC, which provides the hadron beams for the experiments in the first part. In the second part, the ATLAS detector will be described, as the analysis presented in this thesis is performed with proton-collision data recorded by this detector. Finally, the operating parameters of the LHC as well as the data taking performance of the ATLAS detector are briefly discussed.

2.1 The Large Hadron Collider

The 26.7 km long tunnel of the LHC predecessor is reused to house the LHC. Hence, it adopts the same geometry with eight arcs and eight straight sections. Each of the straight sections is 528 m long. Four of them are the insertion regions (IR) of the main experiments. Here, ATLAS, CMS, LHCb, and ALICE are placed in huge underground caverns. Totem and LHCf share their interaction region with CMS and ATLAS, respectively. The other four IRs are used to install the systems needed to control the beam: Radio-frequency cavities to accelerate the beam and to compensate energy losses, the beam-dump system and collimators to absorb beam particles which deviate from the nominal trajectory and momentum. Each of the eight arcs is equipped with 154 superconducting NbTi dipole magnets to keep the beam on the circular track. Due to the maximum beam energy of 7 T*e*V a dipole field of 8.33 T is needed to bend the beam. To achieve this high field strength, the magnets have to be cooled down to 1.9 K. An optimal beam focusing and corrections of the beam trajectory are attained by 8400 multi-pole magnets.

One important parameter of a collider is the number of events which is produced per second in the interaction point:

$$\dot{N} = \sigma \mathcal{L}. \tag{2.1}$$

Hereby, σ is the cross-section of the considered process and $\mathcal{L}$ the instantaneous luminosity. It is a measure of the number of particles passing through the interaction point per cm^2. Thus, it has the unit of a particle flux density cm^{-2}s^{-1}. The instantaneous luminosity is given by parameters of the accelerator and the beam:

$$\mathcal{L} = \frac{N_b^2 n_b f_{\text{rev}} \gamma_r}{4\pi \epsilon_n \beta^*} F(\theta, \sigma_z). \tag{2.2}$$

It depends on the number of particle bunches n_b, the number of particles per bunch N_b, the revolution frequency f_{rev}, the relativistic gamma factor γ_r, and the size of the beam in the interaction region. That is given by the transverse beam emittance ϵ and the beta function β^* in the collision point. F is a geometric luminosity reduction factor as a function of the bunch length σ_z and the crossing angle θ in the interaction point. The nominal proton beam is formed by 2808 proton bunches separated by a 25 ns gap. Each bunch contains $N_b = 1.15 \times 10^{11}$ protons. With the given beam parameters, a instantaneous luminosity of $10^{34}\,\text{cm}^{-2}\text{s}^{-1}$ can be reached. In case of a heavy ion beam the design luminosity is $10^{27}\,\text{cm}^{-2}\text{s}^{-1}$. The typical beam-lifetime is between 10 and 20 hours.

The hadron beams are prepared in the pre-accelerator complex at CERN. A succession of accelerators increases the energy of the hadron beams step-by-step. Figure 2.1 gives an overview on the accelerator chain. Protons are obtained from a duoplasmatron. Here, protons are obtained from hydrogen-gas, by breaking up the chemical bond and

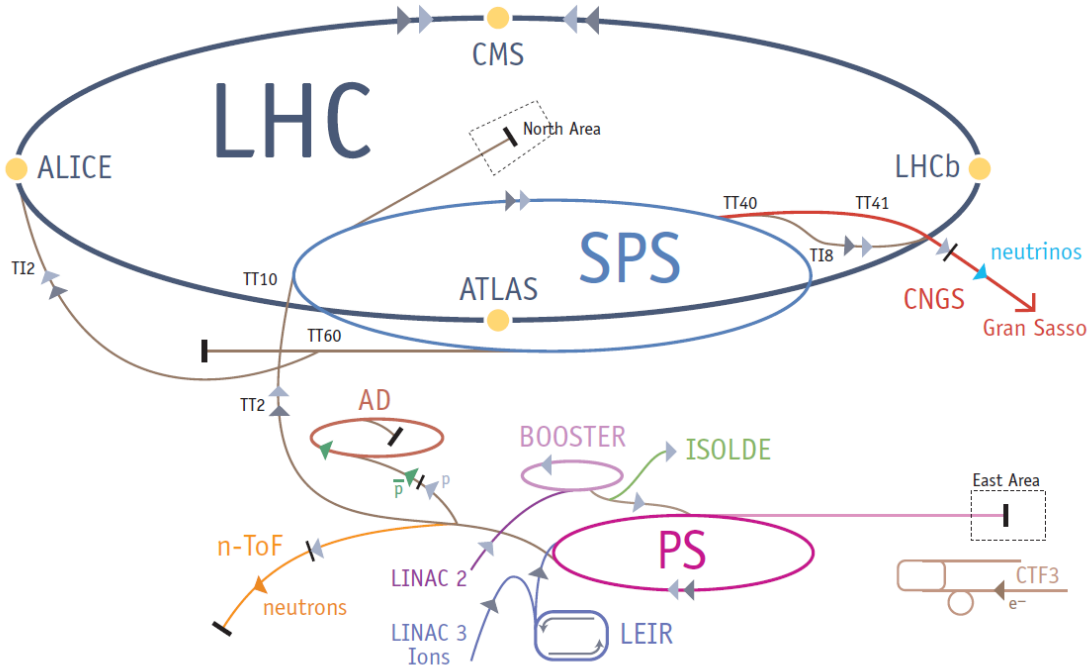

Figure 2.1: *Protons and lead-ions run through various pre-accelerators [68] before being injected to the LHC ring. Protons successively pass the LINAC 2, the PSB, PS and SPS. Before lead-ions are injected into the PS, they are accelerated by LINAC3 and LEIR.*

stripping the electron from the hydrogen atom. The extracted protons are boosted by the linear accelerator (LINAC 2) to an energy of 750 keV. A proton pulse of 30 μs is injected into the Proton Synchrotron Booster (PSB) [69], where the energy is increased to 1.4 GeV. After that, the protons are transferred to the proton synchrotron (PS) [70]. Here, the LHC bunch pattern is formed. Up to six PSB cycles are filled into the PS and split into 72 bunches with a bunch spacing of 25 ns. Additionally the beam is accelerated to 25 GeV. In the subsequent super proton synchrotron (SPS) filled with up to four PS batches the protons are brought to the LHC injection energy of 450 GeV. To achieve the 2808 bunches per beam, twelve SPS [71] cycles are needed for each of the beams. The maximal energy of 7 TeV is reached in the LHC ring. Lead-ions are accelerated in a similar way. They are obtained from an oven, where lead is evaporated and partially ionised. Before being injected into the PS, the lead-ions are accelerated by LINAC 2 and the Low Energy Ion Ring (LEIR) to 4.2 MeV per nucleon and 72 MeV per nucleon, respectively. Full ionisation is achieved during the injection of the lead-ions into the SPS, by a thin Al foil in the PS-SPS transfer line. The injection energy of the LHC after the SPS is 177 GeV per nucleon.

2.2 The ATLAS Detector

At the collision points large detectors are placed to measure the particles produced in the high energetic collisions of the proton beams. Hereby, the design of the ATLAS detector is driven by the requirements of the LHC physics programme. It serves as multiple purpose detector to explore the physics at the TeV scale. Besides the search for new physics, the SM model is studied at this new energy regime. The main benchmark process used to define the detector requirements during the design phase is the SM Higgs boson production. A sophisticated detector design with a fine granularity and fast detector read out is required by the experimental conditions at the LHC with a high luminosity. The main aspects can be summarised as follows: In general a large geometrical acceptance, good charged particle momentum resolution and reconstruction in the inner detector, good vertex reconstruction close to the interaction region, good muon identification and momentum resolution, very good electromagnetic calorimetry for photon and electron identification and an accurate hadronic calorimeter with a fine resolution and a large geometrical acceptance is needed. A detailed overview of the detector is given in Ref. [66].

The origin of the right-handed coordinate system is the nominal interaction point. With an upwards pointing y-axis and the x-axis pointing to the centre of the LHC ring. The

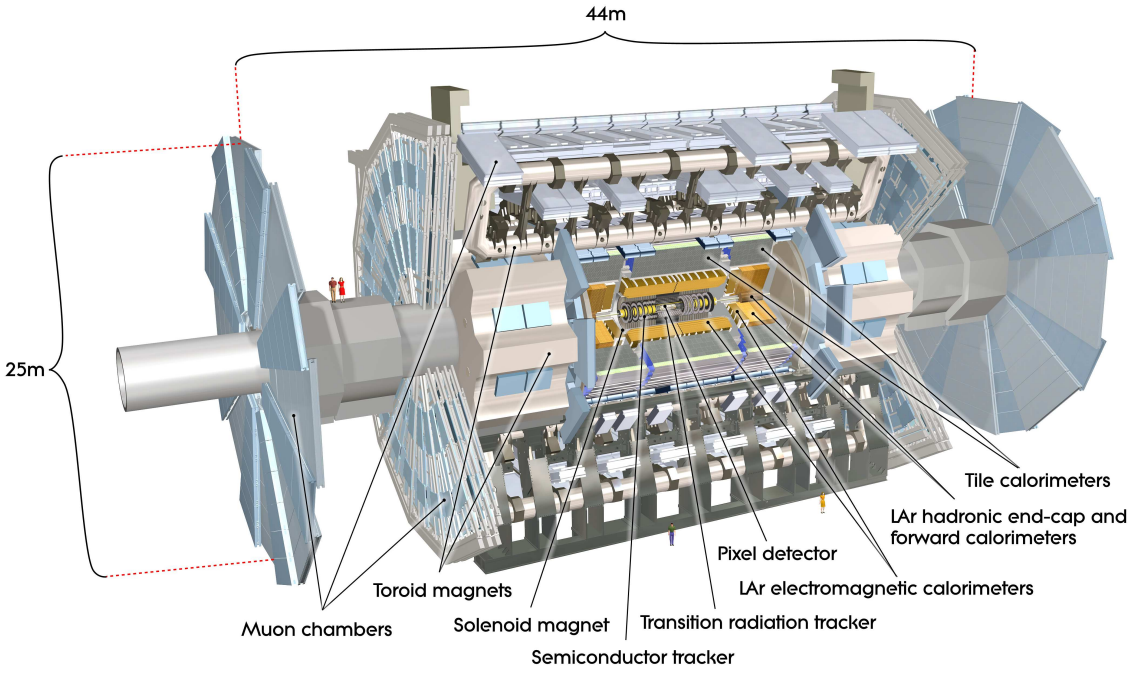

Figure 2.2: *A Perspective view of the ATLAS detector [66]. The detector component closest to the interaction point is the inner tracking system, which is encased by a solenoid magnet. This is surrounded by the electromagnetic and hadronic calorimeter. The outermost detector systems are the air-core toroid magnets with the muon spectrometer.*

z-axis is in beam direction. In the x-y plane the azimuthal angle ϕ is measured from the x-axis. The polar angle is defined in the y-z plane being measured from the z-axis. The pseudorapidity is defined as $\eta = -\ln\tan(\theta/2)$. Distances in the η-ϕ plane are denoted as $R = \sqrt{\Delta\eta^2 + \Delta\phi^2}$. Momentum and energy measured orthogonal with respect to the beam axis are denoted as transverse momentum $p_{\mathrm{T}} = \sqrt{p_{\mathrm{x}}^2 + p_{\mathrm{y}}^2}$ and transverse energy $E_{\mathrm{T}} = E \cdot \sin\theta$.

The main components of the ATLAS detector are shown in Fig. 2.2. Silicon pixel and strip detector techniques as well as a transition-radiation detector are chosen for the inner detector to measure the tracks of charged particles. The inner tracking system is encased by a 2 T solenoid magnet to bend the tracks of the charged particles. The inner tracking system is surrounded by the liquid-argon (LAr) electromagnetic sampling calorimeter and the hadronic calorimetry. The outermost sub-detector is the muon spectrometer. A strong magnetic field is generated by an air-core toroid magnet in this volume to bend the tracks of the muons. The overall dimensions of the ATLAS detector are 25 m in height and 44 m in length, and a total weight of 7000 t. The expected energy and momentum resolutions and geometric acceptances of the sub-detectors explained in the following are summarised in Tab. 2.1.

Detector Component	Required Resolution	η Coverage	
		Measurement	Trigger
Tracking	$\sigma_{p_{\mathrm{T}}}/p_{\mathrm{T}} = 0.05\% \,/\, p_{\mathrm{T}} \oplus 1\%$	± 2.5	-
EM Calorimetry	$\sigma_E/E = 10\% \,/\, \sqrt{E} \oplus 0.7\%$	± 3.2	± 2.5
Hadronic Calorimetry			
Barrel and End-Cap	$\sigma_E/E = 50\% \,/\, \sqrt{E} \oplus 3\%$	± 3.2	± 3.2
Forward	$\sigma_E/E = 100\% \,/\, \sqrt{E} \oplus 10\%$	$3.1 < \lvert\eta\rvert < 4.9$	$3.1 < \lvert\eta\rvert < 4.9$
Muon Spectrometer	$\sigma_{p_{\mathrm{T}}}/p_{\mathrm{T}} = 10\%$ at $p_{\mathrm{T}} = 1$TeV	± 2.7	± 2.4

Table 2.1: *Performance goals of the different subsystems of the ATLAS detector [66].*

2.2.1 Superconducting Magnet System

To bend the tracks of charged particles for momentum measurements and charge identification, a magnetic field is necessary. The magnet system of the ATLAS detector is a hybrid system of four superconducting Al-stabilised NbTi magnets. It comprises one solenoid magnet encapsulating the ID and three toroid magnets. The larger of them in the barrel region of the muon spectrometer and two smaller in the end-caps. The overall dimensions of the system are 22 m in diameter and 26 m in length. Figure 2.3 depicts an overview on the coils configuration of the magnet system. A detailed technical description is given in Ref. [66, 72].

The solenoid magnet provides a 2 T axial field with an inner bore of 2.46 m and an axial length of 5.8 m. An energy of 40 MJ is stored in it. Since the solenoid magnet

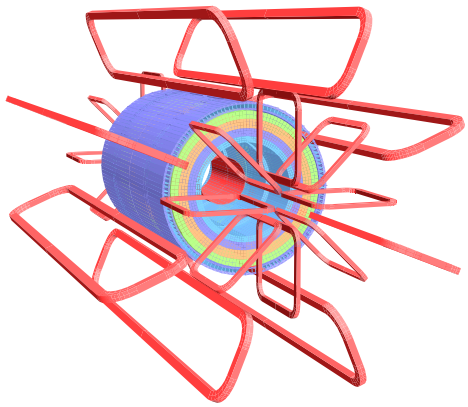

Figure 2.3: *The Geometry of the ATLAS magnet system [66]. The outer part of the system consists of eight barrel toroid magnets accompanied by end-cap coils (red). In the inner part of the detector a solenoid magnet is employed. The tile calorimeter serves as return yoke for this magnet.*

is encapsulated by the calorimeter system, the design is chosen to minimise additional material in front of the calorimeters. Approximately 0.66 radiation lengths are placed in front of the calorimeters due to the magnet. As return yoke of the solenoid field serves the steel of the hadronic calorimeter.

One of the main features of the ATLAS detector are the large toroid magnets of the muon spectrometer. The barrel part consists of eight racetrack-shaped coils with an overall length of 25.3 m. The inner and outer diameter are 9.4 m and 20.1 m. At a nominal current of 20.5 kA the energy stored in the system is 1.1 GJ. Each end-cap of the muon spectrometer is additionally equipped with smaller end-cap toroid magnets. The magnetic field of the toroid system is highly non-uniform. The field strength ranges between 0.5 T and 1 T. A 1 mT accuracy of the B-field strength and 3 mrad in direction is necessary for the required momentum resolution in the muon spectrometer. Thus, the toroid field is monitored by 1840 B-field sensors.

2.2.2 Inner Detector Tracking System

The inner detector system (ID) [73] is located directly around the interaction region. It is build to provide an excellent momentum and position resolution of the tracks of charged particles. Also a very good measurement of primary and secondary vertices for the identification of heavy flavour particle decays is necessary. Due to the high particle flux the detectors need a fine granularity and radiation resistant electronics. Approximately 1000 charged particles emerge from each collision. The dimensions of the ID envelope are 1150 mm in diameter and 7024 mm in length. This covers a pseudorapidity range of $|\eta| < 2.5$. Three independent subsystems form the ID. Closest to the beam pipe a pixel detector with three barrel layers and three end-caps with a very high spatial resolution. A silicon strip tracker (SCT) with four barrel layers

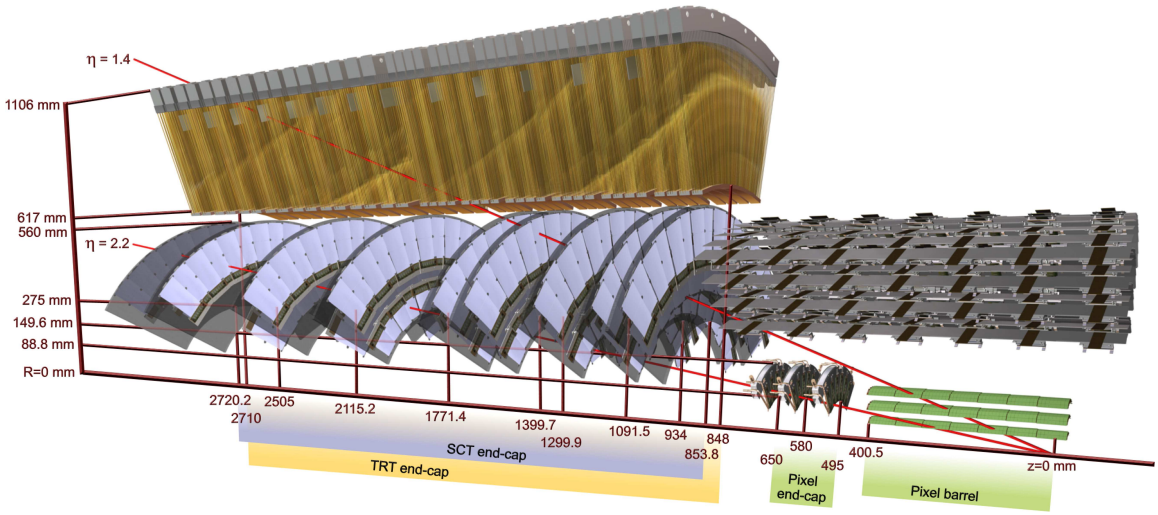

Figure 2.4: *One side of the ATLAS inner detector system [66]. The pixel detector barrel and end-caps are closest to the interaction point, surrounded by the four SCT barrel layers and nine end-caps. Both cover a region up to $|\eta| = 2.5$. The TRT barrel as outermost part of the ID is not shown in this figure, but the TRT end-cap ranging up to $|\eta| = 2$.*

and nine end-cap discs. At lager distances a transition radiation tracker (TRT) with many layers of gas straw tube elements is used which cover a pseudorapidity range of $|\eta| < 2.0$. In addition to track charged particles, the TRT is used to identify electrons. Figure 2.4 gives an overview on the individual components of the ID.

Pixel Detector

The pixel detector [66, 74] is build of three concentric cylindrical barrel layers, located at mean radii of 50.5 mm, 88.5 mm and 122.5 mm around the nominal z-axis with a length of 801 mm. It is enclosed by three end-caps at each side, positioned at $z = \pm 495$ mm, $z = \pm 580$ mm and $z = \pm 650$ mm. 1744 pixel sensors are mounted on 112 barrel staves and 48 disk sectors. Each sensor carries 47232 pixels with a size of $50 \times 400\,\mu\text{m}^2$ (90%) and $50 \times 600\,\mu\text{m}^2$ (10%). The modules are operated with a bias voltage of 150 V to facilitate good charge collection. Depending on ageing effects, a bias voltage up to 600 V is foreseen. The overall area covered by the pixel detector is approximately $1.7\,\text{m}^2$ with $80.4 \cdot 10^6$ pixels in total. To achieve the demanded resolution of the ID the intrinsic axial and azimuthal (R-ϕ) accuracy of the mechanical alignment is required to be $10\,\mu$m and $115\,\mu$m. A charged particle will have 3 space point measurements in the fiducial volume of the pixel detector.

SCT

The silicon strip tracker (SCT) [66, 73] has four cylindrical barrel layers positioned at mean radii between 284 mm and 498 mm with respect to the z-axis. The overall length of the barrel section is 1530 mm. It is supplemented with nine end-cap discs

at each side of the barrel located between 854 mm $< |z| <$ 2720 mm. The whole detector consists of 4088 modules, 2112 modules mounted on the barrel layers and 1976 modules installed on the end-cap discs. On each modules there are two layers of microstrip sensors, which are rotated by $\pm 20\,\mu$rad around their geometrical centre. Each sensor has 768 active strips of 12 cm length and a strip pitch of 80 μm. The strips of the barrel modules are aligned parallel to the beam direction for the measurement of the R-ϕ position of a track. An intrinsic accuracy of 17 μm (R-ϕ) and 580 μm (z) is reached with this geometry. In the end-caps the strip positioning is in radial direction. Hence, an intrinsic accuracy of 17 μm (R-ϕ) and 580 μm (R) is obtained. An overall area of 63 m^2 is almost hermetically covered by the SCT. The layout of the detector provides up to four measured space points per track. The number of readout channels is approximately 6.3 million.

TRT

The transition radiation tracker (TRT) [66] uses the fact, that photon radiation is produced if a charged particle crosses the boundary of two materials with different dielectric constants. This effect can be used for particle tracking and identification. In particular to distinguish charged pions from electrons. Therefore, straw tubes with a diameter of 4 mm are embedded in polyethylene fibres. In the barrel region 52544 of them with a length of 144 cm are aligned parallel to the z-axis in 73 layers. The overall length of the barrel detector is 1560 mm, with an inner and outer radius of 554 mm and 1066 mm. At each side of the barrel, 32 cm long tubes are aligned radially in the end-caps. Those are grouped to 20 end-cap wheels, positioned between 827 mm $< |z| <$ 2744 mm, each with 8 layers, having an inner and outer radius of 615 mm and 1106 mm. In total the end-caps are made up from 319488 tubes. The drift tubes are filled with a gas mixture of 70% Xe, 27% CO_2 and 3% O_2 at 5 to 10 mbar overpressure. A bias voltage of -1530 V is used to operate the cathodes. The TRT covers a pseudorapidity range of $\left|\eta\right| < 2.0$. At least 36 straws will be crossed by a charged particles with $p_T > 0.5$ G*e*V. In the transition region between the barrel and the end-cap ($0.8 < |\eta| < 1.0$) this number is reduced to 22. An electron above 2 G*e*V is expected to have about 10 hits in the TRT.

2.2.3 Calorimetry

The energy of hadronic and electromagnetic interacting particles is measured in the calorimeter system. To deduce the missing energy of particles that are not absorbed by the calorimeter system, a hermetic coverage with a fine granularity is necessary. Figure 2.5 shows a view of the calorimeter system used by the ATLAS detector. Several subsystems are in place to achieve a ϕ-symmetric coverage up to a pseudorapidity of $|\eta| < 4.9$. An electromagnetic liquid argon (LAr) calorimeter [75], matching the ID acceptance range is used for precision energy and position measurements of electrons and photons. Energy and position measurements of hadronic particles are achieved

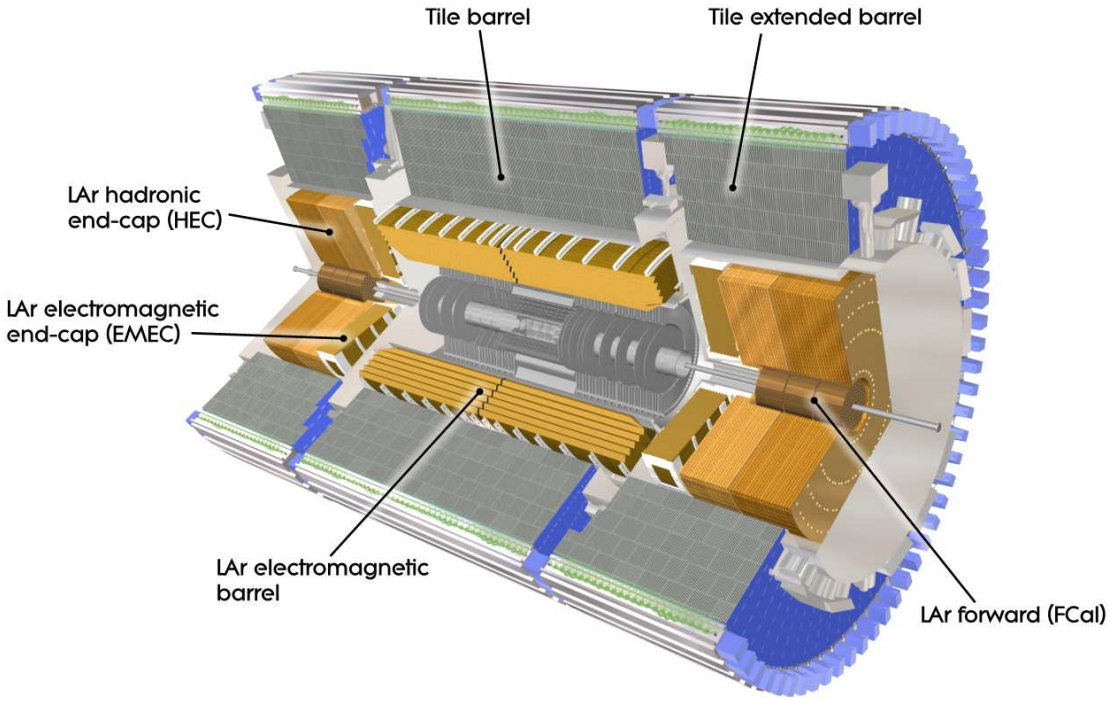

Figure 2.5: *View of the ATLAS calorimetry system [66]. The ID is surrounded by the LAr calorimeter, segmented into a barrel and end-cap. It provides the energy measurement of electromagnetic interacting particles. Hadronic energy is measured by the tile calorimeter, segmented into a barrel and extended barrel. The FCal enables an calorimetry coverage up to* $|\eta| = 4.9$.

with the hadronic calorimeter [75, 76] covering the full η-range. An appropriate choice of the absorber material thickness limits the punch-through of electromagnetic and hadronic showers to the muon system. The energy loss of charged particles in the inner detector and solenoid magnet (corresponding to 1.3 to 1.9 radiation lengths) is measured by a pre-shower LAr calorimeter in a pseudorapidity range of $|\eta| < 1.8$.

Electromagnetic Calorimeter

The transverse energy and position of electromagnetic showers of electrons or photons is measured with a calorimeter based on liquid argon as scintillating material. It provides an intrinsic linear response to the energy deposition and is radiation-hard. Accordion shaped lead plates are used as absorber material. The design of the calorimeter is divided into a barrel part, covering the pseudorapidity region of $|\eta| < 1.475$ and at each side of the barrel, two end-cap wheels to cover the pseudorapidity range of $1.375 < |\eta| < 2.5$ and $2.5 < |\eta| < 3.2$. To reduce the material placed in front of the barrel calorimeter, it shares the cryostat with the solenoid magnet. The accordion geometry of the lead absorbers was chosen to achieve a complete ϕ-symmetry without any cracks in the azimuthal direction. The barrel calorimeter is segmented in

three sections in depth, whereas the end-cap wheels have two segments. In terms of electromagnetic radiation-lengths X_0 the calorimeter has a thickness of $22X_0$ to $33X_0$ and $24X_0$ to $38X_0$ in the barrel and end-cap, respectively. The first layer of the barrel calorimeter has a finest granularity of 0.025×0.1 ($|\eta| < 1.40$) and 0.025×0.025 ($1.40 < |\eta| < 1.475$) in $\Delta\eta \times \Delta\phi$ for precision position measurements. The segmentation of the calorimeter depends on the layer and lateral position of the segments. It ranges up to 0.1×0.1 in $\Delta\eta \times \Delta\phi$ in the end-cap. More detailed information is given in Ref. [66, 75].

Hadronic Calorimeter

The hadronic energy of a collision event is measured with two different types of calorimeters. In the central detector region a tile calorimeter is employed up to a pseudorapidity of $|\eta| < 1.7$. The barrel is enclosed by the hadronic endcap calorimeter (HEC) in a pseudorapidity region of $1.5 < |\eta| < 3.2$. The forward region is covered by the forward calorimeter (FCAL) up to a pseudorapidity of $|\eta| = 4.9$. Detailed information is given in Ref. [66, 75, 76]. The tile calorimeter uses steel plates as absorber material and scintillating tiles. It is subdivided into a barrel for $|\eta| < 1.0$ and an extended barrel for $0.8 < |\eta| < 1.7$. 64 azimuthal segments with three layers in depth are used with a granularity of 0.1×0.1 (first layer) and 0.1×0.2 (other layers) in $\Delta\eta \times \Delta\phi$. The three layers have a depth of 1.5, 4.1 and 1.8 hadronic interaction lengths λ. The total average thickness is $7.4\,\lambda$. The HEC shares the same cryostat with the EMC. At each side of the tile calorimeter the end-cap is formed of two wheels covering a pseudorapidity range of $1.5 < |\eta| < 3.2$. The overlap with the tile calorimeter and forward calorimeter reduces the material drop in the transition region. Copper plates are used as absorber material arranged in 32 wedges in each wheel with two segments in depth. Liquid argon is used as scintillating material. The granularity ranges from 0.1×0.1 to 0.2×0.2. In the very forward direction, the calorimetry is supplemented by the forward calorimeter which is also integrated in the end-cap cryostat to achieve a uniform calorimeter coverage. The segmentation in depth is three layers. Copper plates are used in the first layer as absorber material for electromagnetic measurements, the other two layers utilise tungsten, to measure the hadronic energy. In total the FCAL has a depth of 10λ.

2.2.4 Muon Spectrometer

The largest sub-detector of the ATLAS detector is the muon spectrometer (MS) [66, 77] as outermost layer to detect the tracks of all charged particles which are not absorbed by the calorimeter system. Between the coils of the large air toroid magnets, the tracking chambers of the muon system are mounted. There are three concentric cylinders segmented into eight symmetric octants in ϕ and each in 2 lateral sectors. Their position is at mean radii of 5 m, 7.5 m and 10 m, covering a pseudorapidity up to $|\eta| < 2$. The muon system barrel is enclosed by 4 large wheels at each side at the $z = 7.4$ m,

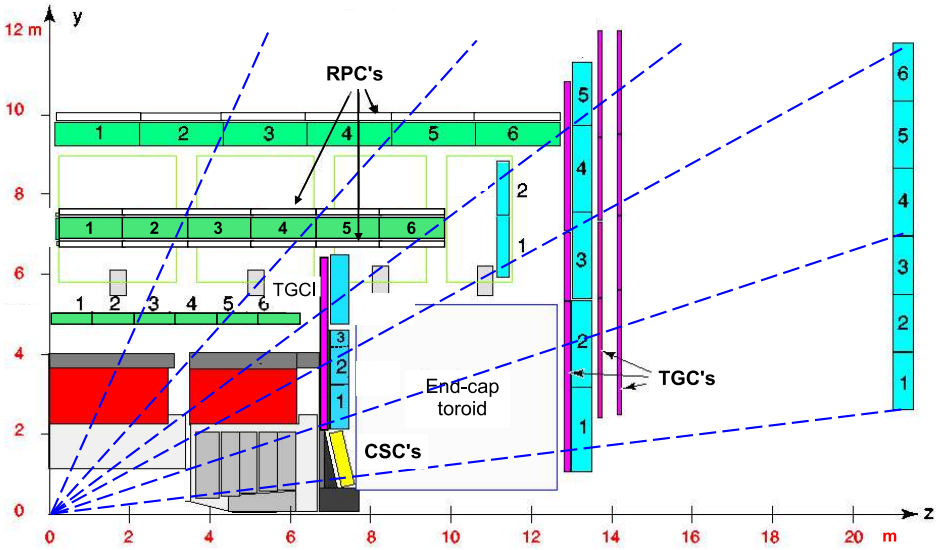

Figure 2.6: *Sketch of the muon spectrometer [66]. Three barrel layers and 4 large wheels at each end of the barrel equipped with MDT chambers (green/azure) are used for measuring muon tracks. CSC chambers (yellow) are utilised for the first wheel where high track densities are expected. For triggering on muon tracks, RPC chambers ($|\eta| < 1.05$) and TGC ($1.05 < |\eta| < 2.4$) chambers are used.*

$z = 10.8\,\text{m}$, $z = 14\,\text{m}$ and $z = 21.5\,\text{m}$, which corresponds to a pseudorapidity range of $2.0 < |\eta| < 2.7$. A schematic sketch of the muon system is depicted in figure 2.6.

Monitored drift tube chambers (MDT) provide a precision momentum measurement of charged tracks with a simple construction in the whole MS. In total, 1088 chambers form the barrel and end-cap wheels. Except the innermost layer of the end-cap, where cathode strip chambers (CSC) are employed due to the high particle flux. An area of $5500\,\text{m}^2$ is covered by MDT chambers. Each of them is equipped with 8 layers of drift tubes, aligned tangentially in ϕ-direction. The drift tubes are operated with a Ar/CO_2 mixture. They measure the coordinate in the bending direction of the magnetic field. Around 20 space points are measured for each track. CSCs are used in the inner wheel of the end-caps in a pseudorapidity range of $2 < |\eta| < 2.7$. These multi-wire proportional chambers with a cathode plane segmented orthogonal into strips provides a η-ϕ measurement. They cover a total area of $65\,\text{m}^2$. The MS is also equipped with Resistive Plate Chambers (RPC) in a pseudorapidity range up to $|\eta| < 1.05$ and thin gap chambers (TGC) in a pseudorapidity range of $1.05 < |\eta| < 2.4$ for a quick identification of muon-tracks. They provide a track information within 15 to 25 ns. Additionally, they complement the MDT spatial measurement by providing a second ϕ-measurement.

2.2.5 Luminosity Detectors

The main system to measure the luminosity in the interaction region is based on a Cerenkov detector. At a position of $\pm 17\,\mathrm{m}$ of both sides of the interaction point the LUCID [66] detector (Luminosity measurement using Cerenkov Integrating Detector) is positioned. Twenty gas-filled Cerenkov tubes cover the pseudorapidity range of $5.6 < |\eta| < 6.0$. They detect the particles of inelastic proton-proton scatterings in the forward direction. The signal amplitude is related to the number of particles passing the detector. A measure of the luminosity in the interaction region is the number of counted particles.

An additional system is the Beam Conditions Monitor (BCM) [78]. Four diamond sensors are placed as horizontal and vertical pair at each side of the interaction point at a position of $|\eta| = 4.2$ around the beam pipe. The main purpose of the detector is to monitor the beam background level to issue an beam abort in case of beam losses. But, the hit rates are also used to measure the bunch-by-bunch luminosity.

A third system is foreseen to measure the absolute luminosity. But the ALFA [66] detector is not yet commissioned. It is located at a distance of 240 m from the interaction point to measure the elastic proton-proton scattering. The optical theorem relates the elastic scattering amplitude in forward direction to the total inelastic cross-section. The aim is to use special data taking runs to calibrate the LUCID detector with this measurement.

2.2.6 Trigger and Data Acquisition

At nominal LHC operation conditions a proton bunch pair collides every 25 ns in the interaction points of ATLAS and CMS. It is impossible to process and store collision data with a frequency of 40 MHz. Fortunately, most of the events are low energetic processes which are not of interest. Thus, it is important to select events with an interesting signature originating from a high energetic inelastic scattering processes. A sophisticated trigger system reduces the amount of data to a manageable size of roughly 200 Hz. Three different levels are implemented in the trigger system with a refined decision in each step. The first step is the Level 1 (L1) trigger system [79], which is operating on custom-made detector electronics. The trigger decision is taken on objects with high transverse momentum detected in the muon system and calorimeters (jets, electrons, photons, missing transverse energy). A fast decision within 2.5 μs after the corresponding bunch crossing is found by taking into account the information of the considered sub-detectors with a reduced granularity. A reduction to 75 kHz is achieved by applying the L1 trigger selection. The result of the L1 trigger is processed by the central trigger processor to enable combinations of different trigger signatures and pre-scaling of trigger signatures for optimal bandwidth usage for the given luminosity and background conditions. Regions of interest (RoI) are defined by the L1 trigger system. Those are used as seed for the Level 2 (L2) trigger system. Before the

L2 processing the data of the RoI is copied to off-detector electronics. On average 2% of the event data have to be processed. The L2 trigger refines the decision by evaluating the information of all sub-detectors with full granularity and precision for the given RoI. The L2 trigger decision is taken within 40 ms and reduces the data rate to 3.5 kHz. During this time, the event data is stored in the detector readout electronics in pipelined buffers. Finally, an event filter is applied after an online reconstruction and processing, which takes approximately 4 s depending on the event complexity. Both, the L2 and event filter are executed on a computer farm. All events passing this final step are copied to a permanent storage. Analysers can access the stored data via the world wide computing grid [80]. An average event rate of 200 Hz can be handled by the data taking system. This corresponds to a data rate of approximately 300 MB/s. It is limited by the computing resources for the data processing and storage system. Under special conditions event rates up to 600 Hz have been achieved [81]. The size of one event which passes the high level trigger (HLT) is approximately 1.3 MB. The data acquisition system (DAQ) is responsible for the full data taking chain and detector configuration during the data taking. The detector hardware is steered by a separate system the detector control system (DCS). Additional information on the trigger and DAQ system can be found in [66, 79, 82].

2.3 LHC Commissioning and ATLAS Data Taking Performance

First proton collisions at the LHC were achieved at a centre-of-mass energy of 900 G*e*V in November 2009, followed by a short run with 2.36 T*e*V. From April 2010 on the protons are collided with an centre-of-mass energy of 7 T*e*V. The energy per beam is limited by the maximum dipole field allowed for safe operation. This limitation is caused by the resistance of the interconnections between the dipole magnets. A total integrated luminosity of $\mathcal{L} = 45\,\text{pb}^{-1}$ was collected during the year 2010. In a data taking period with heavy ion beams at a centre-of-mass energy of 2.76 T*e*V/nucleon a total luminosity of $\mathcal{L} = 9.2\,\mu\text{b}^{-1}$ was collected.

During 2011 the operation continued optimising the beam parameters to increase the instantaneous luminosity. A major improvement was the reduction of the beam size in the interaction point by lowering β^* from 3.5 to 1.5, with a beam emittance of 40 μm and a crossing angle of 240 μrad. The number of maximum bunch pairs colliding in the interaction points of ATLAS and CMS was 1380 with a bunch spacing of 50 ns. A maximum peak luminosity of $3.65 \times 10^{33}\,\text{cm}^{-2}\text{s}^{-1}$ was achieved with the optimised beam parameters. A summary of some operational records by the LHC is shown in Tab. 2.2.

At the end of the data taking period $5.25\,\text{fb}^{-1}$ were recorded by the ATLAS detector, which corresponds to a data taking efficiency of 95% of the detector. Figure 2.7 shows the total integrated luminosity (a) and the peak instantaneous luminosity (b) as a func-

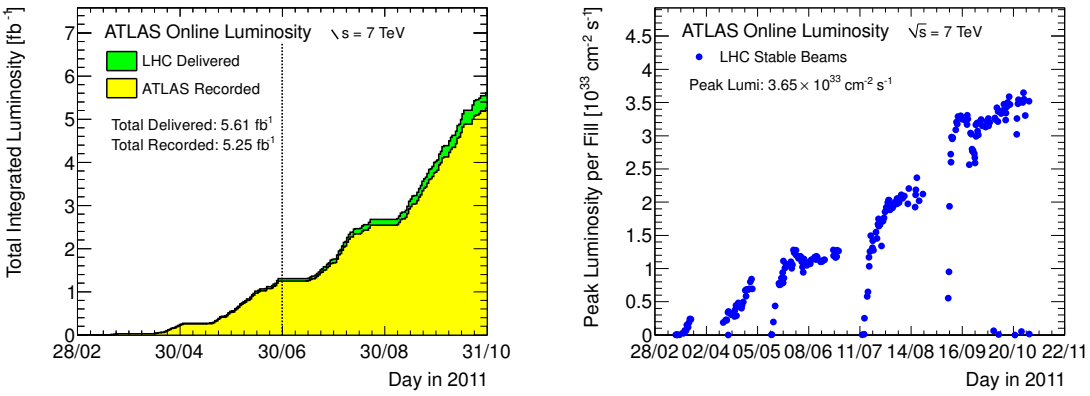

(a) *(b)*

Figure 2.7: *The data delivered by the LHC and stored by the ATLAS detector [85]. The integrated luminosity (a) and peak instantaneous luminosity per fill (b) during the data taking period 2011. Data recorded until the end of June is analysed in this thesis.*

tion of time. The luminosity is calibrated by van der Meer scans [83]. In this method, the beams are moved horizontally and vertically against each other to measure the beam profile, which is an input to the luminosity calculation. Details on the calibration are given in Ref. [84].

In this thesis a subset of the recorded data is used. It falls in the data taking period from April to June and corresponds to a integrated luminosity of $1.04 \pm 0.04\,\text{fb}^{-1}$ after all data quality requirements.

	Record	Date
Peak Stable Luminosity Delivered	$3.65 \times 10^{33}\,\text{cm}^{-2}\text{s}^{-1}$	
Maximum Luminosity Delivered in one Fill	$122.44\,\text{pb}^{-1}$	11/10/16
Maximum Colliding Bunches	1854	11/10/27
Maximum Average Events per Bunch Crossing	32.21	11/10/25
Longest Time in Stable Beams for one Fill	26.0 h	11/08/05
Fastest Turnaround to Stable Beams	2.11 h	11/08/17

Table 2.2: *Operational records achieved by the LHC during the data taking period in 2011.*

Chapter 3

Object Reconstruction

In a collision event, many different particle types are produced. They need to be reconstructed and identified from the traces they leave in the various sub-detector systems. Signals in the inner detector are used to reconstruct the tracks of charged particles. The energy of charged and neutral hadrons, electrons, and photons is measured by the calorimeter system. To distinguish electrons from hadronic jets and photons, the combined information from the tracks and calorimeters is used. Muons are identified by tracks in the muon spectrometer. Neutrinos are particles which are not measured directly. Therefore, they have to be reconstructed indirectly. In this chapter, the algorithms ATLAS uses to identify the different particle types and their kinematics are shortly described. Also the reconstruction of the top-quark decay chain of the t-channel single top-quark production process is presented.

3.1 Track and Vertex Reconstruction

The reconstruction of charged particle tracks is important for the particle identification and to measure the particle momentum. Tracks originating from the interaction region are reconstructed from hits in the inner detector. To reconstruct the primary vertex, where the hard interaction took place, the tracks of the charged particles are used. The primary vertex has to be distinguished from pile-up event vertices in the same bunch crossing. Those are additional scattering processes with a smaller momentum transfer.

3.1.1 Track Reconstruction

Two consecutive approaches are used to reconstruct the tracks of charged particles from the three dimensional hit measurements of the ID layers. A detailed description of the tracking algorithms is given in Ref. [86].

The inside-out method starts with three measured hits of the pixel and SCT detector to construct track seeds. To reduce their number a constraint in z-direction is applied for only selecting tracks pointing to the interaction region. A Kalman filter [87] is used to associate additional hits identified in the search corridor of the track seed to the candidate track by performing a χ^2 fit. Ambiguities of hits being assigned to different

tracks are resolved by scoring the tracks by their quality depending on their parameter quality and χ^2. All tracks are refitted after reassigning the ambiguous hits to the tracks with the highest scoring. Additional space-point measurements from the TRT are added to the track candidates, if it improves the track fit. Otherwise, the previous one is kept and the hits are assigned as outliers to the track. After the inside-out procedure, the outside-in approach is performed, to find additional tracks which were missed by the previous algorithm. Track segments are searched using a Kalman filter in the TRT and tracked back to the silicon detector.

In general, a track in the magnetic field is described by a helix, which is parametrised by the signed transverse (d_0) and longitudinal (z_0) impact parameter and the azimuthal and polar angle θ and ϕ of the track tangent and the charge signed inverse transverse momentum q/p_{T}. For a precise track reconstruction, a good alignment of the detector modules is necessary. A precision of 4 to 10 μm is achieved for the pixel and SCT sensors [88].

3.1.2 Vertex Reconstruction

Besides the primary vertex where the hard scattering process of interest takes place, up to 25 pile-up vertices are expected to happen in one bunch crossing. A high track multiplicity is expected from the primary vertex, but this is not a sufficient identification criterion. Since high-p_{T} objects are produced by the hard interaction, the primary vertex is defined to have the largest sum of the squared transverse momenta Σp_{T}^2 of the tracks associated to this vertex. All tracks matching the luminous region of ATLAS are taken into account in the vertex reconstruction [89] using an adaptive vertex finding algorithm [90]. Vertex seeds are found by searching local maxima in the z-coordinate distribution of the tracks. The compatibility of a track belonging to the candidate vertex is computed from the χ^2 fit. Incompatible tracks are removed on an iterative basis, until the fit converges. The vertex finding through fitting is iteratively done for all remaining tracks, until no more vertices can be constructed. For high track multiplicities (~ 70 tracks) a primary vertex reconstruction resolution of 30 μm in the x/y-direction and 50 μm in the z-direction is found [91].

3.2 Charged Lepton Reconstruction

Charged leptons need to be identified and their energy and momentum needs to be measured. The kinematics of electrons is measured by combining information from the ID track measurement and LAr calorimeter energy measurement. The momentum of muons is measured from the tracks of the inner detector and muon spectrometer. It is necessary to distinguish prompt electrons and muons from the primary interaction from other objects in the detector and charged leptons from secondary decays.

3.2.1 Electron

An electron candidate in the central region of $|\eta| < 2.47$ is defined by a reconstructed energy cluster in the LAr calorimeter and a track pointing to the cluster position. The clusters are found by a sliding window algorithm [92] with seeds in a window of 3×5 calorimeter cells in $\eta \times \phi$ exceeding an energy threshold of 2.5 GeV. Since more than one track can match to the calorimeter position, the track with the best quality criteria is chosen to be associated to the electron candidate. After matching the track and the cluster, the later is recomputed using a 3×7 (5×5) sliding window in the barrel (endcap) with additional energy corrections. To compute the four momentum of the electron, the direction of the track η, ϕ and the energy E of the cluster is used. The transverse energy E_{T} of the electron candidate is defined as $E_{\mathrm{T}} = E/\cosh(\eta)$.

The identification of an electron is refined by applying additional cuts on the electron candidates. Three different sets of cuts are defined with increasing power to reject backgrounds, at which the tighter definition always includes the cuts defined by the looser ones. Table 3.1 gives an overview on the cuts to define the electron categories. The loose electron class includes cuts on the detector acceptance, the shower shape in the middle layer of the LAr calorimeter and on the hadronic leakage. Additional cuts on track quality criteria, the matching between the cluster and the track and variables of the strip layer of the em-calorimeter are required by the medium electron category. The tight electron quality definition applies more stringent cuts on the variables used by the previous definitions and uses an additional cut on the energy-momentum ratio E/p of the electron to distinguish between electrons and charged pions and a requirement on a hit in the b-layer of the pixel detector to reject electrons from photon conversions. Further information from the TRT is used for particle identification. To veto against conversion electrons from photons, all electrons which are reconstructed as photon candidates are rejected.

Besides the cut-based electron identification, a calorimeter and track-based electron isolation is defined to distinguish electrons from hadronic jets or from secondary decays within a jet. The calorimeter isolation defines the energy measured by the calorimeter cells in a cone around the electron cluster with the electron energy removed. A track based isolation accounts for the momentum of additional tracks in a cone around the electron track, with the electron track momentum being removed from this quantity.

The tight quality criterion provides an electron reconstruction efficiency of 72% with a powerful background rejection of $\sim 10^5$ compared to medium electrons, which only have a rejection factor of $\sim 10^3$. The dependence of efficiency of the three electron categories on p_{T} and $|\eta|$ is shown in Fig. 3.1. An energy resolution of 1.2% to 1.8% in the calorimeter barrel and endcap is observed [94]. A detailed description of the algorithms used for the electron reconstruction and identification is presented in Ref. [93].

Type	Description	Variable
	loose	
Detector Acceptance	• $\|\eta\| < 2.47$	
Hadronic Leakage	• Ratio of E_T in the first layer of the hadronic calorimeter to E_T of the EM cluster in the range $\|\eta\| < 0.8$ and $\|\eta\| > 1.37$.	R_{had1}
	• Ratio of E_T in the hadronic calorimeter to E_T of the EM cluster in the range $\|\eta\| > 0.8$ and $\|\eta\| < 1.37$.	R_{had}
Second Layer of EM Calorimeter	• Ratio in η of cell energies in 3×7 versus 7×7 cells.	R_η
	• Lateral width of the shower.	$w_{\eta 2}$
	medium (includes loose)	
Second Layer of EM Calorimeter	• Total shower width.	w_{stot}
	• Ratio of the energy difference associated with the largest and second largest energy deposit over the sum of these energies.	E_{ratio}
Track Quality	• Number of hits in the pixel detector (≥ 1).	
	• Number of hits in the pixel detector and SCT (≥ 7).	
	• Transverse impact parameter (< 5 mm).	d_0
Track Matching	• $\Delta\eta$ between the cluster and the track (< 0.01).	$\Delta\eta_1$
	tight (includes medium)	
b-Layer	• Number of hits in the b-layer(≥ 1).	
Track Matching	• $\Delta\phi$ between the cluster and the track (<0.02).	$\Delta\phi_2$
	• Ratio of the cluster energy to the track momentum.	E/p
	• Tighter $\Delta\eta$ cut (<0.005).	$\Delta\eta_1$
Track Quality	• Tighter transverse impact parameter cut (< 1 mm).	$\Delta\phi_2$
TRT	• Total number of hits in the TRT. The difference between the measured number of hits and the expected average number of hits is required to be within 15 hits. On average, 30 to 35 hits are expected.	
	• Ratio of the number of high threshold hits to the total number of hits in the TRT.	
Conversions	• Electron candidates matching to reconstructed photon candidates are rejected.	

Table 3.1: *Definition of the cuts for the loose, medium, and tight electron categories in the central detector region of* $|\eta| < 2.47$ *[93]*

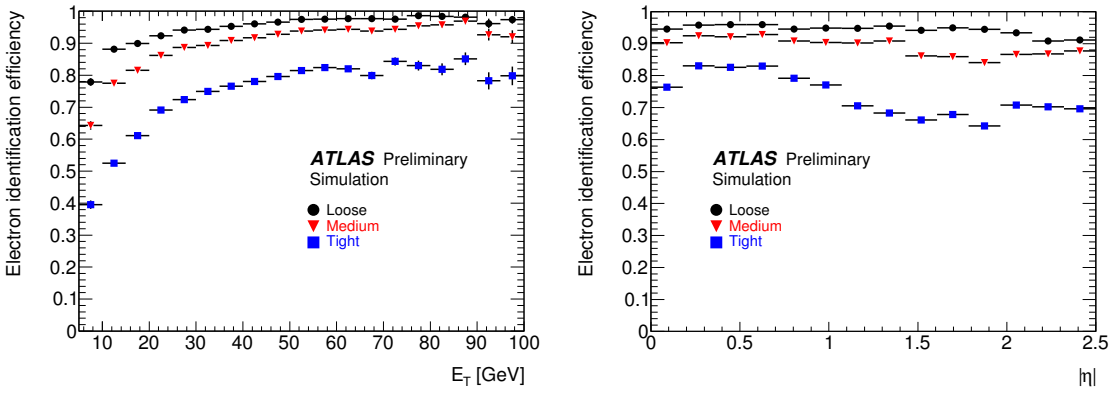

(a) *(b)*

Figure 3.1: *Electron reconstruction efficiency in dependence of p_{T} (a) and $|\eta|$ (b) for the loose, medium and tight electron definition for $Z \rightarrow e^{+}e^{-}$ events [93].*

3.2.2 Muon

Muons are easier to identify than electrons. Hadronically and electromagnetically interacting particles are absorbed by the calorimeter system with very high probability. Hence, a charged particle being measured in the MS is a good muon candidate. The aim of the muon reconstruction is to achieve a momentum resolution below 3.5% for muons having a $p_{\mathrm{T}} \sim 200$ GeV and a resolution of about 10% for high-p_{T} muons up to 1 TeV. Therefore, a combined measurement of tracks from the ID and MS is performed, which limits the geometric acceptance to the acceptance of the ID of $|\eta| < 2.5$. Hereby, the reconstruction efficiency is limited by the MS track reconstruction efficiency due to the transition regions at $|\eta| \sim 0$ and $|\eta| \sim 1.2$. For the muon reconstruction track segments are searched in the MS. Straight line segments are reconstructed from hits in the muon chambers and the corresponding trigger chambers. Track candidates are constructed by a fit, whereas segments in the outermost layer are used as seed for the fit. The track with the most associated hits and the best fit quality is kept. To construct a combined muon, a combined fit of the MS and the matching ID tracks is performed. Figure 3.2 shows the reconstruction efficiency of combined muons in dependence of p_{T} and η. An overall efficiency of $> 96\%$ is observed [95]. To distinguish prompt muons from secondary decay muons or muons within a jet, a track and calorimeter isolation criterion is available to refine the muon definition. A detailed description of the muon reconstruction algorithms and expected performance is given in Refs. [96, 97].

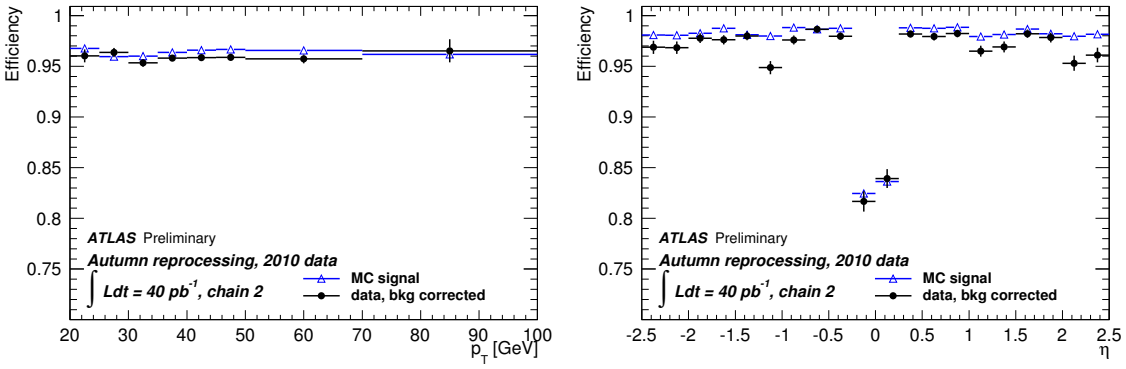

(a) *(b)*

Figure 3.2: *Combined muon reconstruction efficiency in dependence of p_{T} (a) and η (b) for $Z \rightarrow \mu^{+}\mu^{-}$ events [95].*

3.3 Jet Reconstruction

Quarks that originate from the hard process end up in a bunch of collimated hadrons. To measure the initial quark, the bunch of hadrons needs to be measured and related to the initiating particle. On simulated events a jet algorithm is used to cluster all semi-stable hadrons which are close together to one jet. In the calorimeter, the hadrons are measured as energy deposition in the calorimeter cells. From those, topological clusters [92] are constructed, which are the input for the jet algorithm. There are two important requirements a jet algorithm has to fulfil: collinear and infrared safety. The first means that the result of the jet finding should not be affected, if the energy carried by one particle is distributed over two collinear particles. The second, the infrared safety, describes that the result of the jet reconstruction has to be stable under soft energy radiation. Two different categories of jet algorithms can be distinguished: Cone and cluster algorithms. Cone algorithms collect all particles in an area with a fixed cone size. But they are not infrared safe. A cluster algorithm is used by ATLAS to reconstruct jets. It fulfils the infrared and collinear safety requirement. This section describes the jet algorithm used by ATLAS and the jet energy scale (JES) calibration of jets in observed data. Additionally, the identification of jets originating from a b quark is explained, which is an important tool to suppress background events in the analysis.

3.3.1 Jet Algorithm

Cluster algorithms fulfil the requirement of infrared and collinear safety, because their object combination scheme does not depend on a fixed geometrical cone size. It is based on the pairwise combination of objects on basis of a distance measure d_{ij} between two objects i and j as well as the distance d_{iB} between the object i and the beam B. The objects with the minimal distance d_{ij} are combined to become a new object and

all distances are recalculated. All objects are called a jet and removed from the list, if the distance to the beam d_{iB} is the minimum of all distances. The procedure is stopped, if no more objects are left to combine. The following distance measures are used in this context:

$$d_{ij} = \min\left(p_{\mathrm{T}i}^{2p}, p_{\mathrm{T}j}^{2p}\right)\frac{\Delta R_{ij}^2}{R} \tag{3.1}$$

$$d_{iB} = p_{\mathrm{T}i}^{2p}. \tag{3.2}$$

The parameter R is the resolution of the algorithm and defines the size of the jet. ΔR_{ij} is the geometric distance between two objects in the η-ϕ plane. The transverse momentum of an energy cluster or merged object is denoted by $p_{\mathrm{T}i}$.

Depending on the value of p three different cluster algorithms are distinguished, depending on their properties. For the choice of $p = 1$, it is the k_{T} [98] algorithm. Soft objects are clustered before the harder ones are added to the final jet. The area of the jet in the η-ϕ plane has a complex structure. In case of the Cambridge-Aachen [99] algorithm, $p = 0$, only the geometric distance between the objects is considered, not their transverse momentum. The choice ATLAS uses for the jet clustering is the anti-k_t [98] algorithm for $p = -1$ with a parameter $R = 0.4$. The distance d_{ij} is dominated by the geometric distance ΔR_{ij} and the inverse of the transverse momentum. Hence, hard objects collect adjacent soft ones, before the hard objects are clustered. Well separated hard objects will collect all softer objects within a radius smaller than $2R$ and produce conical shaped jets. If two hard objects are located close to each other a more complex shape of the jet area is expected: For $R < \Delta R_{ij} < 2R$, the objects in the overlapping region are associated to one of them depending on the d_{ij}, whereas one jet is produced if both hard objects are within $\Delta R_{ij} < R$. The anti-k_t algorithm has the advantage that it is theoretically well-behaved in terms of infrared- and collinear-safety and a calibration of jets reconstructed in the detector is possible because of their well-defined jet shape.

3.3.2 Jet Energy Calibration

Calorimeter jets are reconstructed from topological clusters which are calibrated on the electromagnetic energy scale. The energy deposit of electromagnetic showers is measured correctly in this calibration scheme, but the energy of the jet has to be corrected to the hadronic energy scale. It has to include all effects due to hadronic particle showers of charged and neutral hadrons in the calorimeter. This is done by comparing the kinematics of measured jets with simulated jets. Different detector effects have to be taken into account: Partial energy measurements due to dead material, calorimeter leakage and the clustering due to the jet algorithm are corrected. Additional energy due to pile-up is removed from the em-scale energy of the jets and the jet-origin is corrected to the primary vertex. The JES is restored by comparing the energy $E_{\mathrm{calo}}^{\mathrm{EM}}$ of

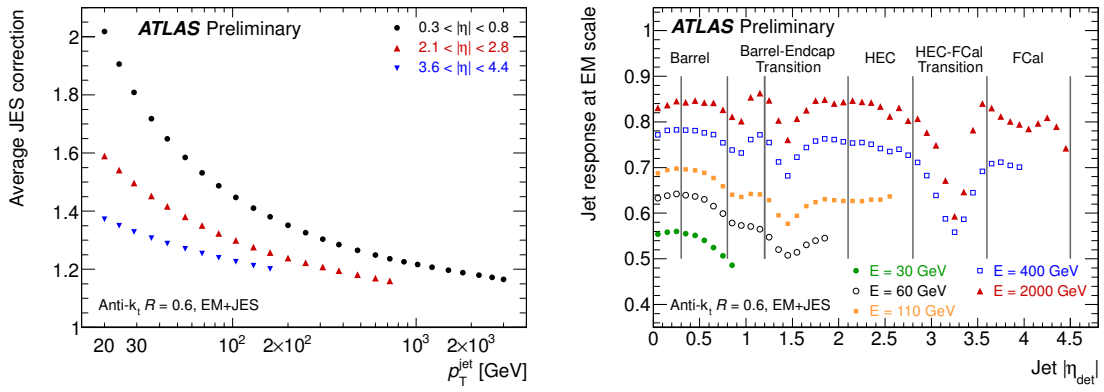

(a) *(b)*

Figure 3.3: *The average JES correction factor as a function of the calibrated transverse momentum for representative detector-$|\eta|$ intervals (a) and the simulated jet energy response on the electromagnetic scale as a function of the detector-$|\eta|$ and selected values of the calibrated jet energy (b). The results are shown for an anti-k_t distance parameter $R = 0.6$. Similar results are obtained by using $R = 0.4$ [100].*

isolated calorimeter jets with the energy E_{truth} of simulated truth jets. The EM-scale energy response $\mathcal{R} = E^{\text{EM}}_{\text{calo}}/E_{\text{truth}}$ is measured in bins of η and p_{T}. The jet energy correction factor is defined as $1/\mathcal{F}_j(E^{\text{EM}}_j, \mathcal{R}_j)$, where $\mathcal{F}_j$ is the calibration function in bins of η and p_{T}. Figure 3.3 shows the average JES correction factor as function of the calibrated transverse momentum $p_{\text{T}}^{\text{EM+JES}}$ for different pseudorapidity-regions (a) and the jet-energy response $\mathcal{R}$ at the em-scale as function of the detector $|\eta|$ for different calibrated jet energies $E^{\text{EM+JES}}$. The results are shown for the distance parameter $R = 0.6$. Similar results are obtained for $R = 0.4$. The uncertainty on the JES calibration depends on the transverse momentum and the calorimeter region. An uncertainty between 2.5% to 4% in the central region, 3.5% to 8% in the calorimeter end-cap and 5% to 14% in the forward calorimeter are obtained. Detailed results on the JES calibration are presented in Ref. [100].

3.3.3 *b*-Quark Jet Identification

The identification of events with jets that originate from b quarks is of crucial importance to isolate signal process events from background processes that do not contain a b quark in the final state. To distinguish b-quark jets from light jets that originate from a gluon or a light quark (u, d, s) or a c quark different techniques are applied which are denoted as b-tagging. An overview is given in Refs. [101, 102]. To identify a b-quark jet, the properties of the b hadron inside the jet are exploited. A b hadron has an average lifetime τ of $\mathcal{O}\left(1.5\,\text{ps}\right)$, which leads to a secondary vertex at a distance of $c\tau \sim 500\,\mu\text{m}$. On average, 5 tracks with a large impact parameter originate from the decay-vertex of the b hadron. Therefore, the misidentification of a light-quark jet

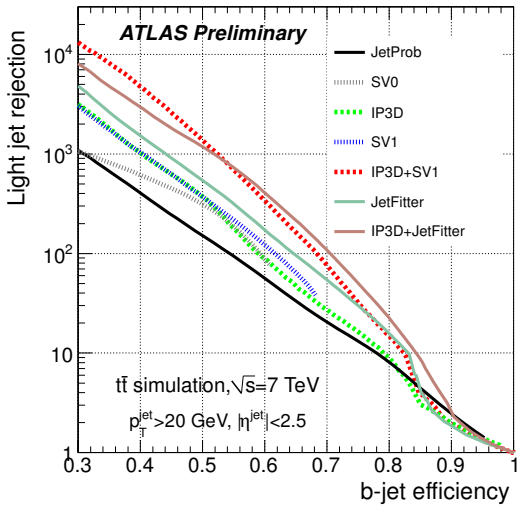

Figure 3.4: *Rejection of light-jets as a function of the b-tagging efficiency for different algorithms, based on simulated $t\bar{t}$ events [102]. The JetFitterCombNN algorithm is denoted as IP3D+JetFitter in the legend of the plot.*

or c-quark jet as b-quark jet is dominated by secondary decays of long lived particles (K_s, Λ) and mismeasurements of tracks. To identify b-quark jets, a combined discriminant of the IP3D and JetFitter algorithms is used in this analysis. The IP3D [101] algorithm uses a likelihood ratio to discriminate between b-quark jets and light-quark jets, based on the information of the signed longitudinal and transverse impact parameter significance of the tracks associated to the jet and the correlation amongst them. The JetFitter [103] algorithm uses a Kalman filter to reconstruct secondary vertices. A fit to the b hadron decay chain, including potentially tertiary vertices from c-quark decays, is performed. The discriminating variables of the IP3D and JetFitter are combined using an artificial neural network to construct the JetFitterCombNN discriminant. A cut on the discriminant above 2.4 defines a working point with a 56% b-tagging efficiency and a light-quark rejection factor of 520 simulated in $t\bar{t}$ events. Figure 3.4 shows the b-tagging efficiency versus the light quark rejection for different algorithms. The combination of the IP3D+JetFitter (JetFitterCombNN) has the best rejection factor for the chosen tagging efficiency. The calibration of the algorithm is performed using the $p_{\mathrm{T}}^{\mathrm{rel}}$-method of Ref. [104]. A subset of b-quark jets is selected that contains a reconstructed muon which is assumed to stem from the b-quark decay and has a relative transverse momentum $p_{\mathrm{T}}^{\mathrm{rel}}$ with respect to the jet axis. The flavour composition is calibrated by fitting template distributions of this variable for light-quark, c-quark and b-quark jets to observed data. A calibration factor between 0.9 and 1.1 is found for jets in the transverse momentum range of 20 GeV to 300 GeV.

3.4 Missing Transverse Energy

The only stable particles that do not interact with the detector material are the neutrinos. Therefore, only an indirect measurement of them is possible. Since the incoming beams have no transverse momentum and energy-momentum conservation holds for the produced particles, the vector sum of all transverse momenta has to be zero. A particle escaping the detector without being measured, leads to an imbalance of the reconstructed transverse momentum. Therefore, the transverse momentum carried by the neutrino is the negative sum of all transverse momenta of the reconstructed particles. At hadron colliders, the p_z component of the neutrino momentum is not accessible since the energy fraction of the colliding partons inside the proton is unknown. The missing transverse momentum is defined by:

$$\vec{E}_{\mathrm{T}}^{\mathrm{miss}} = \begin{pmatrix} E_{\mathrm{x}}^{\mathrm{miss}} \\ E_{\mathrm{y}}^{\mathrm{miss}} \end{pmatrix} \tag{3.3}$$

$$E_{\mathrm{T}}^{\mathrm{miss}} = \left|\vec{E}_{\mathrm{T}}^{\mathrm{miss}}\right| = \sqrt{E_{\mathrm{x}}^{\mathrm{miss}\,2} + E_{\mathrm{y}}^{\mathrm{miss}\,2}} \tag{3.4}$$

The x and y components of the missing momentum are denoted by $E_{\mathrm{x}}^{\mathrm{miss}}$ and $E_{\mathrm{y}}^{\mathrm{miss}}$. The absolute value is denoted as missing transverse energy $E_{\mathrm{T}}^{\mathrm{miss}}$. The energy of all particles absorbed by the calorimeter system is measured at the EM scale. The sum of all cluster energies E_i gives the components of the $E_{\mathrm{T}}^{\mathrm{miss}}$:

$$E_x^{\mathrm{miss}} = -\sum_i^{N_{\mathrm{cell}}} E_i \sin\theta_i \cos\phi_i \tag{3.5}$$

$$E_y^{\mathrm{miss}} = -\sum_i^{N_{\mathrm{cell}}} E_i \sin\theta_i \sin\phi_i. \tag{3.6}$$

Here, the cluster position is given by the polar angle θ_i and azimuthal angle ϕ_i. In the sum of the cluster energies, muons are not taken into account. Thus, their transverse track momentum needs to be subtracted to reconstruct the transverse momentum of the neutrinos. To improve the reconstruction of the $E_{\mathrm{T}}^{\mathrm{miss}}$ the clusters are associated to the reconstructed physics objects and calibrated according to their energy scales. Therefore, the $E_{\mathrm{T}}^{\mathrm{miss}}$ object is composed of different terms corresponding to the reconstructed objects in the detector. The topological calorimeter clusters are associated to electrons $\vec{E}_{\mathrm{T,Electron}}^{\mathrm{miss}}$, jets with low-$p_{\mathrm{T}}$ to $\vec{E}_{\mathrm{T,softJet}}^{\mathrm{miss}}$, and jets with high-$p_{\mathrm{T}}$ to $\vec{E}_{\mathrm{T,Jet}}^{\mathrm{miss}}$. The track momentum of muons is considered as $\vec{E}_{\mathrm{T,Muon}}^{\mathrm{miss}}$. Clusters which are not associated to any physics object are included at the em-scale in the cell-out term $\vec{E}_{\mathrm{T,CellOut}}^{\mathrm{miss}}$:

$$\vec{E}_{\mathrm{T}}^{\mathrm{miss}} = \vec{E}_{\mathrm{T,Electron}}^{\mathrm{miss}} + \vec{E}_{\mathrm{T,Jet}}^{\mathrm{miss}} + \vec{E}_{\mathrm{T,softJet}}^{\mathrm{miss}} + \vec{E}_{\mathrm{T,Muon}}^{\mathrm{miss}} + \vec{E}_{\mathrm{T,CellOut}}^{\mathrm{miss}}. \tag{3.7}$$

All electrons which pass a p_{T} threshold of 10 GeV and fulfil the tight electron requirements are considered in the $\vec{E}^{\mathrm{miss}}_{\mathrm{T,Electron}}$ term. Their energy correction factors, except the out-of-cluster corrections are taken into account. Clusters associated to high-p_{T} jets, that pass a threshold of 20 GeV are calibrated at the JES scale. Whereas the soft-jet term for jets with a p_{T} between 7 GeV and 20 GeV uses the EM scale calibration for the clusters. All muons reconstructed in the full spectrometer acceptance of $|\eta| < 2.7$ are considered by the $E^{\mathrm{miss}}_{\mathrm{T}}$ calculation. Also muons that are found in the crack region of $|\eta| < 0.1$ or $1.0 < |\eta| < 1.3$ are taken into account. Calorimeter clusters associated with muons are included in the cell-out term at EM-scale, except those of non-isolated muons which overlap with a jet ($\Delta R < 0.3$). Here, the clusters are already included in the jet term. A $E^{\mathrm{miss}}_{\mathrm{T}}$ resolution of $\sigma \sim 0.7\sqrt{\Sigma E_{\mathrm{T}}}$ is achieved. A description of the physics object orientated $E^{\mathrm{miss}}_{\mathrm{T}}$ calculation and performance is given in Refs. [105, 106].

3.5 Top Quark Reconstruction

The top quark needs to be reconstructed from its decay products, the b-quark jet, and the charged lepton (ℓ) - neutrino (ν) pair of the W-boson decay. Studies on simulated events have shown that the reconstructed b-tagged jet matches the b quark of the hard process in more than 90% of all t-channel single top-quark production events with one b-tagged jet [107, 108]. Since only the transverse momentum of the neutrino is measured as $E^{\mathrm{miss}}_{\mathrm{T}}$, only the transverse components of the W-boson can be reconstructed. The transverse W-boson mass $m_{\mathrm{T}}(W)$ is defined as:

$$m_{\mathrm{T}}(W \to \ell\nu) = \sqrt{\left(p_{\mathrm{T},\ell} + p_{\mathrm{T},\nu}\right)^2 - \left(p_{\mathrm{x},\ell} + p_{\mathrm{x},\nu}\right)^2 - \left(p_{\mathrm{y},\ell} + p_{\mathrm{y},\nu}\right)^2}. \tag{3.8}$$

To derive the full four momentum of the W boson $p_W = p_\ell + p_\nu$ the z-component of the neutrino momentum needs to be calculated. Since the neutrino stems from a real W-boson decay, its pole mass of $m_W = 80.4\,\mathrm{GeV}/c^2$ can be used as a constraint, leading to a quadratic equation for $p_{\mathrm{z},\nu}$ following the method in Ref. [109]:

$$p^2_{\mathrm{z},\nu} - 2 \cdot \frac{\mu \cdot p_{\mathrm{z},\ell}}{E^2_\ell - p^2_{\mathrm{z},\ell}} \cdot p_{\mathrm{z},\nu} + \frac{E^2_\ell \cdot p^2_{\mathrm{T},\nu} - \mu^2}{E^2_\ell - p^2_{\mathrm{z},\ell}} = 0, \tag{3.9}$$

$$\text{with} \quad \mu = \frac{m^2_W}{2} + p_{\mathrm{T},\ell} \cdot p_{\mathrm{T},\nu} \cdot \cos\Delta\Phi. \tag{3.10}$$

Here, E_ℓ denotes the energy of the charged lepton and $\Delta\Phi$ is the azimuthal angle between the charged lepton and the $\vec{E}^{\mathrm{miss}}_{\mathrm{T}}$. In general, a quadratic equation has two

solutions $p_{z,\nu}^{A,B}$:

$$p_{z,\nu}^{A,B} = \frac{\mu \cdot p_{z,\ell}}{p_{T,\ell}^2} \pm \sqrt{\frac{\mu^2 \cdot p_{z,\ell}^2}{p_{T,\ell}^4} - \frac{E_\ell^2 \cdot p_{T,\nu}^2 - \mu^2}{p_{T,\ell}^2}}. \tag{3.11}$$

For a positive discriminant, the solution with the smaller $p_{z,\nu}$ is chosen. Comparisons with simulated events show, that this solution reproduces the generated neutrino better in $\sim$ 60% of all cases, than the larger $p_{z,\nu}$ solution . A complex solution is obtained in approximately 30% of all cases if the discriminant is negative. This is the case if $m_T(W)$ is larger than m_W due to an imperfect E_T^{miss} measurement. This can be avoided by modifying the E_T^{miss} such, that the discriminant becomes 0, by obeying equation 3.9. The $m_T(W)$ is set to 80.4 GeV/c^2 for such cases. A solution for the quadratic relation between $p_{x,\nu}$ and $p_{y,\nu}$ is obtained by minimising the distance δ between the modified E_T^{miss} and the measured one:

$$\delta_{1/2}\left(p_{x,\nu}\right) = \sqrt{\left(p_{x,\nu} - \not{E}_{T,x}\right)^2 + \left(p_{y_{1/2},\nu}\left(p_{x,\nu}\right) - \not{E}_{T,y}\right)^2}. \tag{3.12}$$

A complex solution for δ is avoided by restricting the values of $p_{x,\nu}$ and $p_{y,\nu}$ to a numerical range which lead to a real solution. The smaller value for δ is taken to calculate the neutrino z-component since it minimises the modification of the E_T^{miss}. The result for $m_T(W)$ is illustrated in Fig. 3.5 (a). The mass constraint on the W boson restricts $m(W)$ to 80.4 GeV/$c^2$for all solutions (b).

To finally reconstruct the top-quark four-vector, the reconstructed four vectors of the neutrino, charged lepton and b-quark jet are added. Additional qualitative studies are presented in Ref. [108].

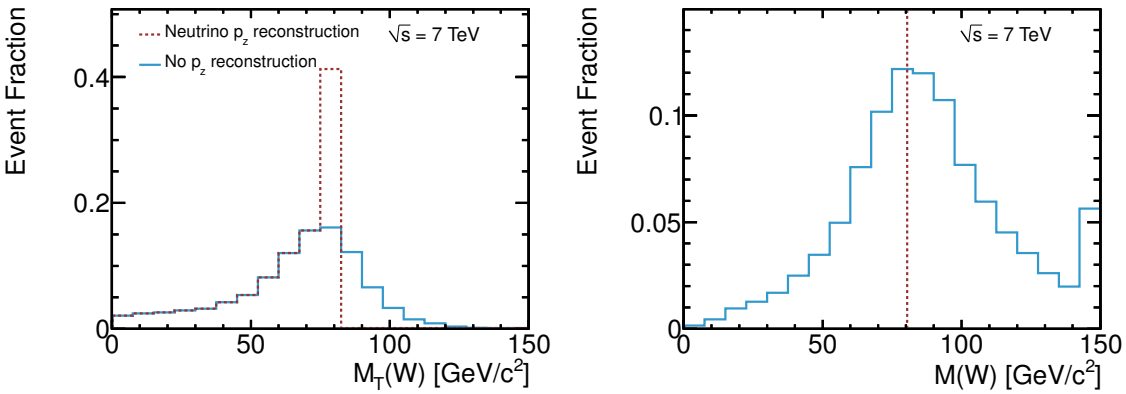

(a) *(b)*

Figure 3.5: *Comparison of $m_T(W)$ (a) and $m(W)$ (b) for the W boson reconstructed from the charged lepton and measured E_T^{miss} or the reconstructed neutrino. A complex solution for the neutrino p_z is obtained if the $m_T(W)$ is larger than the $m(W)$ due to imperfect E_T^{miss} measurements. It is avoided by modifying the E_T^{miss} such that the discriminant becomes 0. In such cases $m_T(W)$ is 80.4 GeV/c^2. In all cases, the mass constraint on the W boson restricts all $m(W)$ to 80.4 GeV/c^2.*

Chapter 4

Modelling of Signal and Background Processes

To understand observed data, the signal and background processes have to be modelled. All physical processes having the same reconstructed final-state particles as the signal process are regarded as background processes. To model the kinematic observables and to understand the selection efficiencies, Monte Carlo (MC) simulations are used to model the processes according to a theoretical model. This chapter briefly introduces the various aspects of MC methods to describe collision events. A summary on the MC programs used to simulate the various background processes and the signal process is given. MC simulations are an important tool to develop particle detectors, analysis strategies and to interpret observed data, but not all background processes can be simulated properly. Thus, also data-driven event models are used for event classes that cannot be simulated properly.

4.1 Event Generation with Monte Carlo Techniques

To study the physics of high energetic particle collisions, one has to understand the structure of the collision event. But its complexity exceeds the possibility of a full quantum mechanical treatment. Too many particles are involved and perturbation theory is no more applicable in some parts to describe the event, such as the transition of partons to hadrons. Therefore, several tools are available to perform a MC simulation of the collision event. In this part, the basics of the MC simulation as well as the tools in use are briefly described. A general introduction to MC methods is given in Ref. [110].

4.1.1 Steps of Monte Carlo Simulation

The simulation of a collision event is subdivided into several steps. A visualisation of the different stages of the MC simulation is depicted in Fig. 4.1. It starts with the generation of the high energetic process characterising the event, followed by the evolution of partons to observable final-state particles. This implies a QCD showering and hadronisation of colour charged objects. In the following each part is briefly described.

Hard Process

The nature of a physical process taking place in a parton scattering is described by the transition matrix element $\mathcal{M}$ of the incoming to the outgoing particles. Due to the high momentum transfer Q^2 perturbation theory is applicable to derive $\mathcal{M}$ at least at the lowest order of the perturbation series. The main characteristics of the physics process are the number and type of outgoing partons and their kinematic distributions, including the information on the spin configuration. A parametrisation of the incoming partons which stem from the proton is given by the parton density function $f\left(x, Q^2\right)$. A subsequent decay of heavy and short-lived outgoing particles like the top quark or W boson may also be treated by the hard scattering. Simulated events are generated by sampling the phase space of the transition matrix element with uniformly distributed random numbers. Hereby, the momentum and position space points, as well as the spin configuration of all particles taking part in the interaction span the phase-space. The square $|\mathcal{M}|^2$ of the matrix element is proportional to the differential cross-section $\mathrm{d}\sigma$, which is the probability of an event to occur in the differential volume $\mathrm{d}\Omega$ of the phase space. No physical meaning can be assigned to an individual event carrying the weight $\mathrm{d}\sigma$. The distribution of an observable is gained by histogramming the weights. This procedure is used by cross-section integrators. Event generators, by contrast, generate unweighted events with a frequency, proportional to their differential cross-section. Those events represent, what might be observed by an experiment. Only a large number of randomly generated unweighted events can be used to predict the distribution of an observable.

Parton Shower

Higher-order QCD corrections are added to the hard process by the application of the parton shower (PS), which is a non-perturbative description since it ranges down to low energy scales, where perturbation theory is no longer applicable. Additional gluons are radiated by the initial-state and final-state quarks ($q \rightarrow q + g$) and gluons ($g \rightarrow g + g$). During the parton shower, gluons are also split into a quark-antiquark pair $g \rightarrow q + \bar{q}$. Whereas the probability of a parton branching is given by the DGLAP splitting functions [111]. The QCD showering is the transition of one parton originating from the hard process to a jet of many partons, which moves approximately in the same direction as the parton initiating the shower. Since a parton shower is a consecutive process, its evolution is described by a time ordering parameter t, the momentum fraction z of the radiated particle and an azimuthal angle ϕ. The shower evolution is terminated at the cut-off parameter t_0. A typical numerical value is an energy of 1 GeV. Collinear parton-splittings and soft-gluon emissions are suppressed to avoid infrared singularities during the parton-shower evolution. In general, the hard process gives a good description of well separated jets with a large transverse momentum, whereas the parton shower models soft, collinear jets well.

To simulate physical processes having a final state X plus n additional jets due to QCD radiation (e.g. the W/Z+n-jets production), exclusive subsamples for each jet

multiplicity are generated. The inclusive sample containing all jet multiplicities is constructed by merging the exclusive subsamples. A phase space overlap of jets emerging from the parton shower and matrix element has to be removed. A final state with m jets might originate from a hard process with m final-state partons which end up in a jet or from a matrix element with $m - n$ partons and n additional extra parton emissions from the parton shower. Thus, a double counting of events from higher-order calculations or hard parton emissions from the shower arises. To eliminate it, the jets after the shower have to be matched to the original partons of the matrix element. Two methods are widely utilised: the CKKW [112] and the MLM [113] algorithms. The former vetoes events featuring parton-shower jet emissions in the phase space of the matrix element. The latter is used for the simulated events of this thesis. At parton level, only events are accepted, that have partons, that are above a transverse energy threshold $E_{\mathrm{T}}^{\mathrm{min}}$ and are well separated $\Delta R_{ij} < \Delta R_{\mathrm{min}}$. After the shower evolution, the particles of the shower are grouped to jets and matched to the partons of the matrix element. Only those events are accepted for a exclusive sample, where all jets match exactly one parton of the hard process. Events with additional jets from the parton-shower emission are rejected. To generate an inclusive sample extra jet emissions are allowed for the highest parton multiplicity of the hard process sample.

Hadronisation and Decay

The quarks, which remain after the showering process, do not exist as free particles, since they carry a colour charge. Therefore, they have to be grouped to colour neutral hadrons. This is done in the hadronisation step. The energy scale of the hadronisation is in the non-perturbative regime. Thus, phenomenological models, which are tuned to observed data, have to be applied. During the hadronisation process, short-lived resonances may be formed. Those have to be decayed to long-lived, stable particles. The lifetimes of hadrons and decay probabilities to other hadrons are well known from experimental measurements.

Underlying Event and Pile-up

The hadron remnants of the two colliding hadrons are colour-connected to the outgoing quarks and gluons of the hard process. This colour connection results in additional particles that are associated to the hard process, the underlying event. Additionally, pile-up events have to be taken into account by the simulation. These are supplementary inelastic hadron-hadron collisions featuring a smaller momentum transfer as the hard process in the same bunch crossing. At the nominal LHC beam conditions up to 25 pile-up events are expected on average per bunch crossing. For the MC production used in this thesis on average 8 pile-up events are added.

Detector Simulation

Besides a well-founded theoretical knowledge of the physical processes taking place

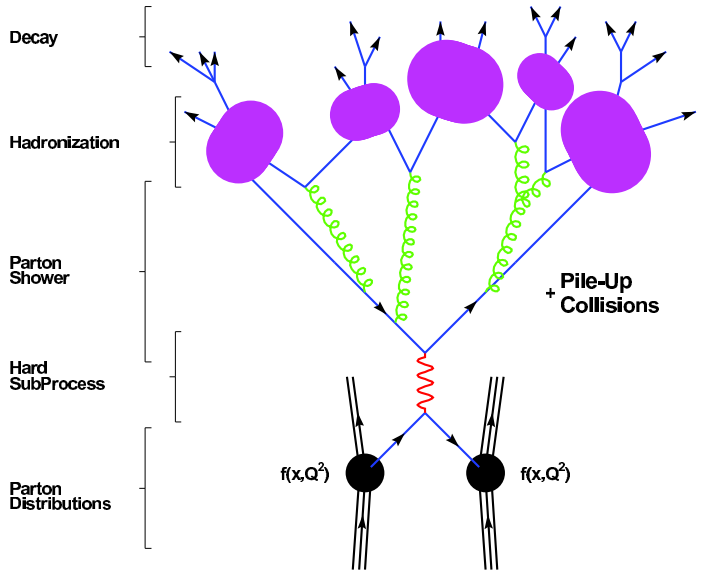

Figure 4.1: *A hadron collision event divided to the different steps of the simulation. Two partons, which are described according to the hadron PDF collide in the hard subprocess. The final-state partons undergo a parton shower, where QCD radiation is added to the event. The partons are evolved to observable hadronic jets. Since partons are no free objects, they are grouped together to hadrons in the hadronisation step, followed by the decay to stable hadrons. Additional to the particles emerging from the hard interaction, pile-up events are added, that originate from additional hadron-hadron collisions at the same bunch crossing. [110].*

in a collision event one needs a precise picture of the detector response to the final-state particles. Therefore, the interaction between the particles and the experimental apparatus has to be modelled, taking into account all information on the detector geometry. The final-state particles of the physics process simulation are passed to the detector simulation performed using the GEANT4 [114] package. A summary of the ATLAS simulation infrastructure is provided by Ref. [115].

4.1.2 ME Generators

As described in the previous section, the first step of an MC simulation is the generation of the hard process. Software for the simulation is available at leading-order and next-to-leading order accuracy. The final-state particles generated by matrix element generators are bare quarks, which have to be processed further by showering programs. A general overview on the MC simulation used for top-quark analysis is given in Ref. [116]. In the following section, the MC programs used to simulate the hard scattering are briefly introduced.

ALPGEN
The simulating of $2 \rightarrow m$ multi-parton final states is provided by the ALPGEN [117] software. In particular it is specialised in the production of additional jets accompanying the physics process due to QCD radiation. A collection of matrix elements is implemented at leading order for the QCD and QED processes. The parton shower has to be simulated with an external showering software. The fixed order QCD calculation gives a better description of the additional jets than a parton shower simulation only. To avoid double counting between events with jets from the parton shower and the matrix element, the MLM algorithm is used.

MC@NLO
Events simulated with NLO accuracy are provided by the MC@NLO [118] package. The hard process is treated with a full NLO calculation in α_s. This treatment improves the modelling of an additional hard jet emission, which is included in the matrix element, whereas the soft and collinear emissions are simulated by the parton shower. A matching between the jet emission from the matrix element and parton shower is necessary. By the time, the implementation of MC@NLO provides a matching to the parton shower and hadronisation of the HERWIG [119, 120] package. To remove the phase space overlap which occurs between the parton-shower emission and hard emission modelled by the NLO matrix element, the parton-shower approximation is subtracted from the NLO calculation. This procedure provides a smooth transition between the hard emission and the parton shower, but introduces negative event weights.

POWHEG
A matrix-element library collection is included in the POWHEG [121, 122] package at NLO accuracy. The main feature of this generator is that the interfacing between the parton shower and NLO calculations is done such, that no negative event weights occur. This is achieved by simulating the hardest emission of QCD radiation first using the exact NLO calculation. The usage of any showering program is possible, that uses a p_{T}-ordered parton shower algorithm.

ACERMC
The ACERMC [123] program provides a collection of selected matrix elements for SM processes as they are typical at the LHC in proton-proton collisions. The matrix elements are generated by the MADGRAPH [124] package in leading order. One feature of the software is that it reaches an efficient event generation due to a phase-space optimisation for LHC conditions. The event simulation can be interfaced to all available showering generators.

4.1.3 PS Generators

Mainly, matrix element MC generators are used to simulate the high energetic part of a physics event. To obtain a realistic event, the QCD showering and hadronisation has to be applied to the partons of the hard process. Specialised tools are available for this task. The application of the QCD shower adds higher-order corrections to the simulated event. Further parts of the simulation such as the hadronisation and decay of hadrons as well as the event structure from the proton remnant are simulated by these programs. The PS generators are also used to generate soft inelastic events that are used to model pile-up events. Those tasks are in a non-perturbative energy regime. Hence, phenomenological models have to be applied, which have to be tuned to the observed data.

PYTHIA

A complete simulation of an event is possible with PYTHIA [125]. It is capable to simulate the ME at the lowest order of the perturbation theory including the subsequent steps of the simulation. But also events produced with other matrix element generators can be processed. PYTHIA can model initial-state and final-state parton showers, multiple parton interactions, treatment of the beam remnants, the hadronisation and particle decays. The parton-shower algorithm relies on a p_{T}-ordered shower evolution. The hadronisation process is simulated using the Lund string fragmentation model [126]. It assumes a linear confinement between two colour charged partons. A colour flux tube is stretched between two partons with an energy potential that linearly increases with the parton distance. As soon as a new $q\bar{q}$ pair can be produced from the stored potential energy, the strings break apart. Therefore, a new colour neutral object is produced.

HERWIG

A library with matrix elements at leading-order perturbation theory is available with the HERWIG [119, 120] package. The matrix elements are already matched to the QCD parton shower. HERWIG can also be used to process events generated by ME generators for the further steps of the simulation. Initial-state and final-state QCD radiation is modelled using an angular ordered scheme, where the energy a parton can radiate, depends on its space-like virtuallity. The parton shower includes an algorithm to achieve a pre-confinement of the partons. To combine the partons into hadrons, the cluster model is used. In the hadronisation step, colourless clusters are formed from nearby partons. Semi-stable clusters are the observable hadrons. Unstable clusters are further processed, until they can be turned into a stable hadron. All hadrons are decayed according to their lifetime. To simulate multiple parton interactions, HERWIG makes use of JIMMY [127].

4.2 Signal Modelling

A simulation of the t-channel signal process which only includes the LO Feynman diagrams does not provide a proper modelling of the final-state particles. The $qb \to tb$ (Fig. 4.2 (a)) process starts with a b quark, which is modelled by the PDF. Originally the b quark stems from a virtual gluon splitting inside the proton $g \to b\bar{b}$. Since the strong interaction obeys flavour conservation, an additional b quark needs to be present in the process. Thus, the second b quark is modelled by the DGLAP backward parton-shower evolution. A feature of this procedure is that the soft p_{T} spectrum is modelled well, whereas the hard p_{T} spectrum of the second b quark is mismodelled. To overcome this problem it is crucial to include at least tree level NLO corrections for the t-channel process for a proper signal modelling. Therefore, the $2 \to 3$ matrix element diagrams have to be taken into account. Those include the gluon splitting in the matrix element by comprising the processes $g + q \to q' + t + \bar{b}$. The contributions of both subprocesses have to be combined in a way that there is no phase space overlap between them. To simulate the t-channel process, AcerMC + Pythia is used. The ACOT [128] matching mechanism is implemented in AcerMC for a proper combination of the $2 \to 2$ and $2 \to 3$ processes. This matching scheme removes the overlap of the LO+PS and NLO events by introducing a subtraction term leading to events having a negative event weight. Figure 4.3 shows the p_{T} and η distributions for the final-state partons of the process: the top quark, the light quark, and the second b quark. The p_{T} distribution of the top quark peaks at 50 GeV (a), its η distribution (b) shows peaks at $|\eta| \sim 2$. The p_{T} distribution of the light-quark jet peaks at 50 GeV (c) and shows distinct peaks in the forward direction at $|\eta| \sim 3$ (d). Compared to the light-quark jet, the second b jet features low p_{T} (e) and is produced centrally (f). To evaluate the

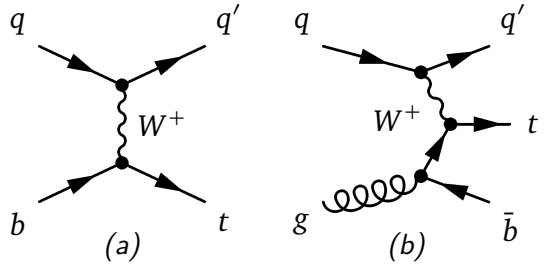

Figure 4.2: *Feynman diagrams of the t-channel signal production at tree level. The LO $2 \to 2$ process starts with a b quark from the PDF. The NLO tree level $2 \to 3$ process starts with a $g \to b\bar{b}$ in the matrix element.*

consistency of the simulated event model, a comparison with a fully differential NLO calculation using MCFM [129] is carried out. The recent version of MCFM employs the four-flavour scheme for the NLO calculation of the signal process. Previous NLO calculations worked with the five-flavour scheme. Here, the $2 \to 2$ Born diagram is calculated at NLO accuracy by assuming a massless b quark. In this approach, possibly large logarithms of the form $\log \frac{Q^2}{m_b^2}$ due to collinear $g \to b\bar{b}$ splittings in the initial state

are absorbed by re-summing them in the b quark PDF. Since the second b quark is modelled by the evolution of the PDF, its kinematic properties are not at NLO accuracy in this scheme. Recent calculations [40] apply the four-flavour scheme to achieve an NLO accuracy for the properties of the second b quark. This is done by an NLO calculation of the $2 \rightarrow 3$ process by keeping the b-quark mass finite. Both schemes are in general agreement.

Comparing the NLO calculation and the distributions generated by AcerMC, an overall good agreement is seen. A simulation with NLO accuracy for the $2 \rightarrow 2$ process is available by MC@NLO together with Herwig. The comparison of the p_{T} and η spectra of the second b quark shows a significant mismodelling of the MC@NLO + Herwig simulation. Too many of the second b quarks are at high $|\eta|$ and low p_{T}. The reason is a problem in the Herwig interface to handle the initial-state b quark from the PDF properly when applying the backward evolution of the parton shower. This problem is solved in more recent versions of Herwig++ which are not available for this study. Due to the wrong b quark kinematics this MC model is not usable for this analysis. Additional kinematic studies and comparisons of MC generators with theoretical calculations can be found in Ref. [107].

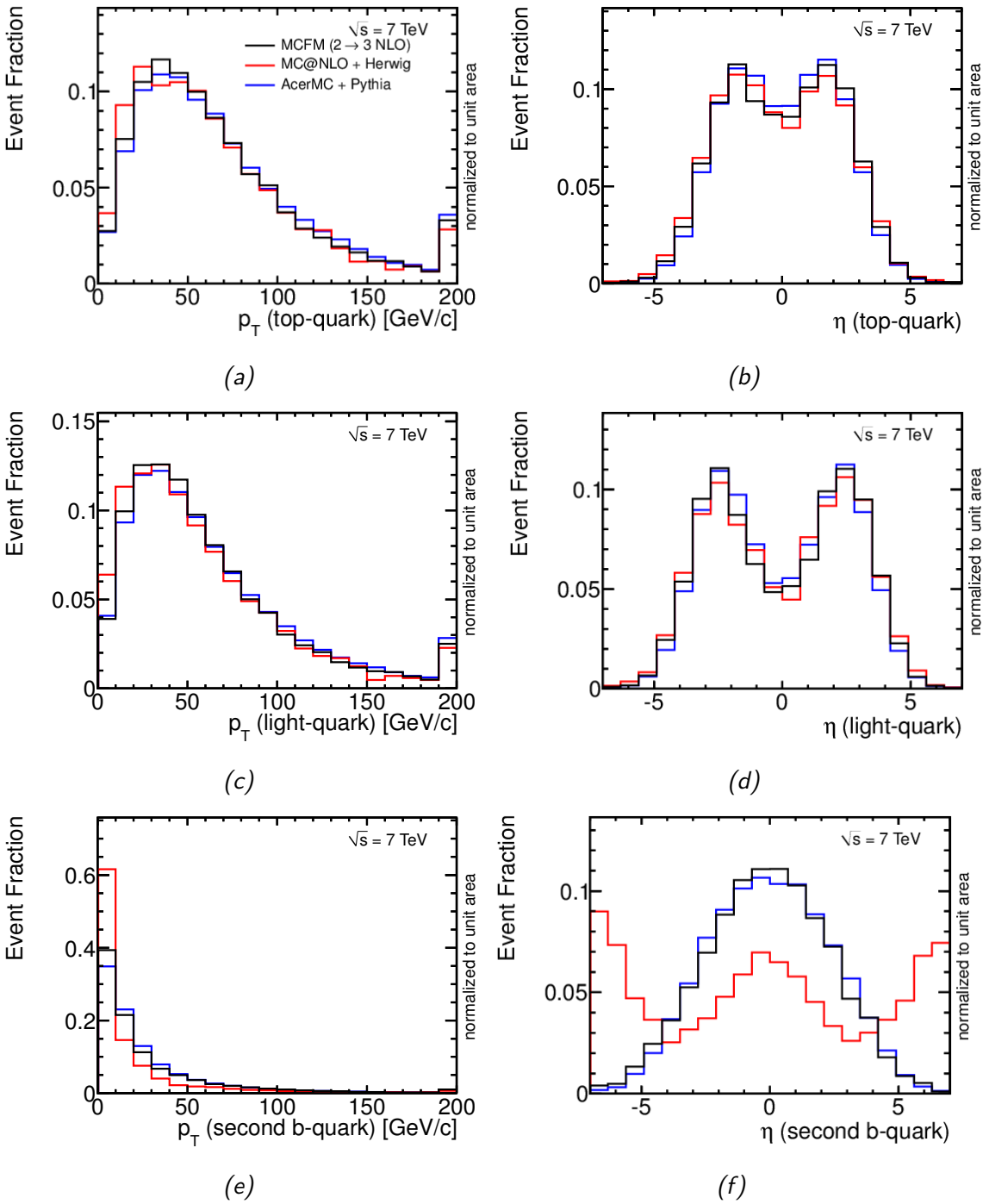

Figure 4.3: *Comparison of the p_T and η distributions of the final-state quarks: the top quark, light quark and second b quark. MC models by* AcerMC+Pythia, MC@NLO+Herwig *and* MCFM *using the four-flavour scheme are compared.* AcerMC+Pythia *and* MCFM *are in good agreement, whereas* MC@NLO+Herwig *shows a severe mismodelling of the second b quark, (e) and (f), due to a problem in the* Herwig *interface, handling the second b quark.*

4.3 Background Event Modelling

Since is not possible to select signal events only, there is always a significant contribution of events having the same final state as the signal process, but originating from a different physical process. Those events have to be considered as background events in the analysis. A profound understanding is important to establish a reliable measurement of the rare signal process. The main background contributions in this analysis are all events that include a real W-boson decay. For example $t\bar{t}$ production events or W+jets events. The background processes are modelled using MC simulated event models as well as data-driven methods. In this section, the different processes considered as background to the signal are described.

4.3.1 Monte Carlo Simulated Background Event Modelling

The classes of MC simulated background events are described in the following. This includes the production of $t\bar{t}$ events, single top-quark s-channel production, single top-quark associated production, the production of W+jets events, Z+jets events, and diboson events.

Top-Quark Background

One important origin of background events is the production of top quarks. The dominant source is the production of $t\bar{t}$ events. It is simulated using MC@NLO + HERWIG. The main contribution stems from the semi-leptonic decay channel (Fig. 4.4 (a)). Additionally, the simulated event sample also includes the di-leptonic decay channel. The $t\bar{t}$ final state mimics the signal event signature if not all decay products are observed due to detector acceptance, reconstruction, and selection efficiencies. An additional background stems from the other single top-quark production modes, the associated-production (Fig. 4.4 (b)) and s-channel (Fig. 4.4(c)) mode. Both processes are simulated with ACERMC + PYTHIA. Due to their smaller production cross-section, the

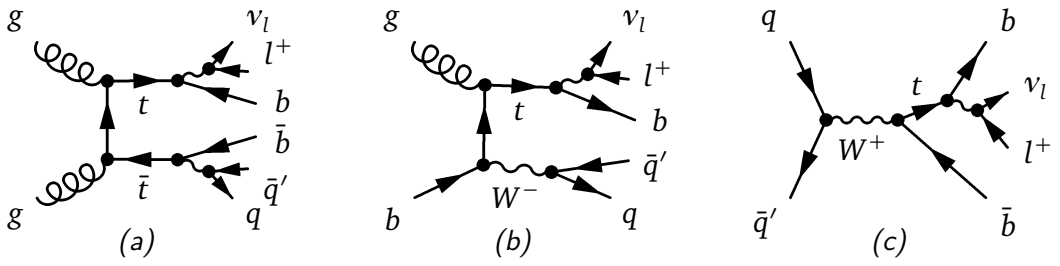

Figure 4.4: *Example Feynman diagrams of background events from top-quark production. The dominant source is the $t\bar{t}$ production in the semi-leptonic decay channel (a). An additional contribution stems from the single top-quark production in the associated production (b) and s-channel production (c) mode, but with smaller rates.*

contribution to the background rates is much smaller that the one of $t\bar{t}$events. In the analysis, background events stemming from real top-quark production are grouped together and denoted as '*top*'-background.

W+jets

One crucial background to the signal process arises from the production of a real W boson in the leptonic (e, μ, τ) decay mode, accompanied by additional hadronic jets. Samples with different parton multiplicities on the matrix-element level are simulated with ALPGEN + HERWIG. Exclusive samples with 0 to 4 partons and one inclusive sample with 5 and more partons are generated. The overlap between partons originating from the matrix element and the parton shower is handled by the MLM matching mechanism. The simulation of the ME only takes into account the production of an extra jet due to a gluon or a light quark. In this context, a light quark is a u, d, s, or c quark, which is considered to be massless. An example Feynman diagram is depicted in Fig. 4.5 (a). Here, b quarks are only produced in the parton shower. Hence, additional samples with massive heavy-flavour quarks (b, c) are simulated. Those include the matrix elements of $W + c\bar{c}/b\bar{b}$+jets, as depicted in Fig. 4.5 (b) and the production of a W boson together with a single c-quark, as depicted in Fig. 4.5 (c). The MC simulation does not include a mechanism to perform a matching of heavy quarks from the ME and PS. Therefore, events of different samples can have the same final-state configuration. To avoid a double counting of events a matching of the MC samples based on the origin of the heavy-flavour quarks is necessary. The used matching procedure exploits the fact, that the ME provides a better description of well separated high-p_{T} quarks than the PS, which models the collinear case well. Thus, the matching criterion is the angular distance ΔR between two heavy partons in the MC event. In the light quark samples, only those events are accepted that have a $\Delta R < R_0$, to select events with collinear c and b quark pairs. The parameter $R_0 = 0.4$ is chosen to be of the same size as the cone-size parameter of the jet algorithm. Events from the samples that produce massive c and b quarks in the matrix elements are kept if the quarks are well separated. Thus a $\Delta R > R_0$ is required. This procedure is called heavy-flavour overlap removal (HFOR) [116]. Additional to the LO cross-section calculated by ALPGEN a k-

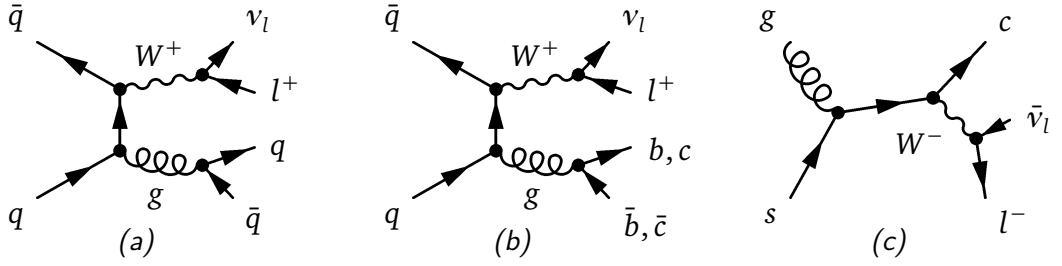

Figure 4.5: *Production of a real W boson in association with jets. Different sets of samples are simulated, those including only light quarks (u,d,s) in the ME (a), and samples including heavy quarks (b, c) in the matrix element (b) and (c). Only the leptonic decay (e, μ, τ) of the W boson is considered.*

factor is taken into account to correct the cross-section to a NLO calculation performed with FEWZ [130]. For all samples 1.2 is used, except the sample simulating the Wc production, which has a NLO scale factor of 1.52. Here, the scale factor is derived using MCFM [116]. In the analysis, the production of a W boson together with light-quark jets is denoted as *'W+light jets'* sample. No events containing heavy-flavour jets from the matrix element or the parton shower are regarded in this event class. Even though, the sample does not include heavy-flavour quarks, a significant amount of events remains due to the large cross-section and b-tagging inefficiencies. All other events featuring heavy quarks from the ME or PS, are referred to as *'W+heavy flavour'*. This is the dominant event class after the application of b-tagging.

Z+jets and Diboson

A small contribution to the background events arises from the production of Z+jets (Fig. 4.6 (a)) and diboson production, which includes the production of a WW, WZ and ZZ, depicted in Fig. 4.6 (b) to (d). To simulate the Z+jets processes ALPGEN + HERWIG is used. An inclusive Z+jets sample is generated from sub-samples with 0 to 5 partons in the final state. The MLM matching is applied to remove double counted events between the sub-samples. Heavy quarks are produced in the parton shower, because the matrix elements only include light quarks. A scale factor of 1.25 derived using FEWZ is taken into account to correct the LO cross-section to the NLO level. The diboson processes are simulated with HERWIG. Their cross-sections are corrected by NLO scale factors derived from a comparison with MCFM and MC@NLO. To mimic the event signature, the production of a heavy-flavour jet is involved. In case of the Z+jets and ZZ production, one of the leptons from the Z-decay needs to be lost or misidentified as a jet due to detector acceptance and reconstruction effects. Both classes of processes are considered together as source of background events and denoted as *'Z+jets, diboson'* background.

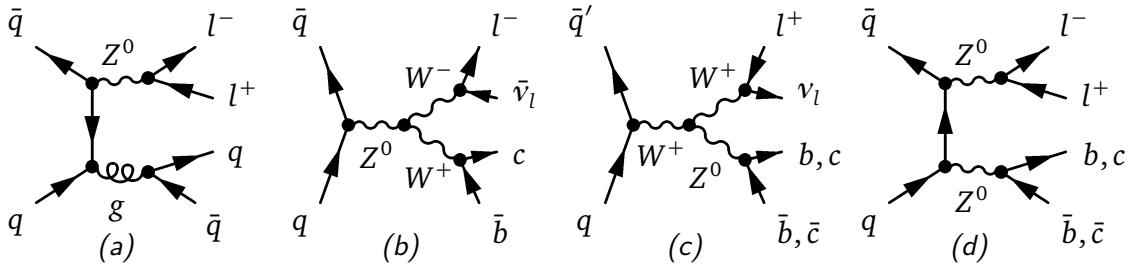

Figure 4.6: *Feynman diagrams of the diboson production Z+jets (a), WW (b), WZ(c), and ZZ production.*

Summary of the MC Simulated Processes

A summary of the MC samples produced for the different physics processes is given in Tab. 4.1. The cross-section and NLO scale factor if available and the size of the event

process	σ[pb]	k-factor	Generator	Events
Wt (all decays)	15.74	1.0	AcerMC + Pythia	300,000
t-channel ($W \to e\nu_e$)	6.94	1.0	AcerMC + Pythia	200,000
t-channel ($W \to \mu\nu_\mu$)	6.83	1.0	AcerMC + Pythia	200,000
t-channel ($W \to \tau\nu_\tau$)	7.26	1.0	AcerMC + Pythia	200,000
s-channel ($W \to e\nu_e$)	0.498	1.0	AcerMC + Pythia	200,000
s-channel ($W \to \mu\nu_\mu$)	0.489	1.0	AcerMC + Pythia	200,000
s-channel ($W \to \tau\nu_\tau$)	0.521	1.0	AcerMC + Pythia	200,000
$t\bar{t}$ (no fully hadronic)	80.1	1.12	MC@NLO + Herwig	12,500,000
$Z \to \ell\ell$ + 0 parton	668	1.25	Alpgen+Herwig	6,620,000
$Z \to \ell\ell$ + 1 partons	134	1.25	Alpgen+Herwig	1,335,000
$Z \to \ell\ell$ + 2 partons	41	1.25	Alpgen+Herwig	405,000
$Z \to \ell\ell$ + 3 partons	11	1.25	Alpgen+Herwig	110,000
$Z \to \ell\ell$ + 4 partons	2.9	1.25	Alpgen+Herwig	30,000
$Z \to \ell\ell$ + 5 partons	0.8	1.25	Alpgen+Herwig	10,000
$W \to \ell\nu$ + 0 parton	6,920	1.2	Alpgen+Herwig	3,460,000
$W \to \ell\nu$ + 1 partons	1,300	1.2	Alpgen+Herwig	642,000
$W \to \ell\nu$ + 2 partons	380	1.2	Alpgen+Herwig	3,770,000
$W \to \ell\nu$ + 3 partons	100	1.2	Alpgen+Herwig	1,010,000
$W \to \ell\nu$ + 4 partons	26	1.2	Alpgen+Herwig	250,000
$W \to \ell\nu$ + 5 partons	7	1.2	Alpgen+Herwig	70,000
$W \to \ell\nu + b\bar{b}$ + 0 parton	47	1.2	Alpgen+Herwig	475,000
$W \to \ell\nu + b\bar{b}$ + 1 partons	36	1.2	Alpgen+Herwig	360,000
$W \to \ell\nu + b\bar{b}$ + 2 partons	17	1.2	Alpgen+Herwig	175,000
$W \to \ell\nu + b\bar{b}$ + 3 partons	7	1.2	Alpgen+Herwig	70,000
$W \to \ell\nu + c\bar{c}$ + 0 parton	128	1.2	Alpgen+Herwig	1,275,000
$W \to \ell\nu + c\bar{c}$ + 1 partons	105	1.2	Alpgen+Herwig	1,050,000
$W \to \ell\nu + c\bar{c}$ + 2 partons	52	1.2	Alpgen+Herwig	525,000
$W \to \ell\nu + c\bar{c}$ + 3 partons	17	1.2	Alpgen+Herwig	170,000
$W \to \ell\nu + c$ + 0 parton	644	1.52	Alpgen+Herwig	6,500,000
$W \to \ell\nu + c$ + 1 partons	205	1.52	Alpgen+Herwig	2,070,000
$W \to \ell\nu + c$ + 2 partons	51	1.52	Alpgen+Herwig	520,900
$W \to \ell\nu + c$ + 3 partons	11	1.52	Alpgen+Herwig	115,000
$W \to \ell\nu + c$ + 4 partons	3	1.52	Alpgen+Herwig	30,000
WW	11.5	1.48	Herwig	250,000
WZ	3.46	1.60	Herwig	250,000
ZZ	0.97	1.30	Herwig	250,000

Table 4.1: *MC samples used for the analysis. The cross-section column includes the branching ratios. The cross-sections of the top-quark processes are the NLO theory predictions. NLO correction k-factors have to be applied on top of the cross-section of the other background processes.*

samples are documented. For the processes involving the production of a top quark, additional MC samples are available for systematic studies. They are presented in Tab. 4.2. The additional samples are produced using alternative MC generators and PS models. Additional $t\bar{t}$ samples are produced using PowHeg+Herwig and PowHeg+Pythia. To study the effect of the parton shower modelling on the single top-quark production processes, samples using AcerMC+Herwig are generated. The parton shower parameters are varied to investigate the effect of increased or reduced QCD radiation from initial-state and final-state particles.

process	σ[pb]	k-factor	Generator	Events
Wt (all decays)	15.74	1.0	AcerMC + Herwig	300,000
t-channel ($W \to e\nu_e$)	6.94	1.0	AcerMC + Herwig	200,000
t-channel ($W \to \mu\nu_\mu$)	6.83	1.0	AcerMC + Herwig	200,000
t-channel ($W \to \tau\nu_\tau$)	7.26	1.0	AcerMC + Herwig	200,000
s-channel ($W \to e\nu_e$)	0.498	1.0	AcerMC + Herwig	200,000
s-channel ($W \to \mu\nu_\mu$)	0.489	1.0	AcerMC + Herwig	200,000
s-channel ($W \to \tau\nu_\tau$)	0.521	1.0	AcerMC + Herwig	200,000
$t\bar{t}$ no fully hadronic	80.1	1.12	PowHeg+Herwig	3,000,000
$t\bar{t}$ no fully hadronic	80.1	1.12	PowHeg+Pythia	3,000,000
initial-state and final-state variation samples				
$t\bar{t}$ (no fully hadronic)	80.1	1.12	AcerMC+Pythia	1,000,000
Wt (all decays)	15.74	1.0	AcerMC+Pythia	200,000
t-channel ($W \to e\nu_e$)	6.94	1.0	AcerMC+Pythia	200,000
t-channel ($W \to \mu\nu_\mu$)	6.83	1.0	AcerMC+Pythia	200,000
t-channel ($W \to \tau\nu_\tau$)	7.26	1.0	AcerMC+Pythia	200,000
s-channel ($W \to e\nu_e$)	0.498	1.0	AcerMC+Pythia	200,000
s-channel ($W \to \mu\nu_\mu$)	0.489	1.0	AcerMC+Pythia	200,000
s-channel ($W \to \tau\nu_\tau$)	0.521	1.0	AcerMC+Pythia	200,000

Table 4.2: *MC samples used for studies of systematic uncertainties. The cross-section column includes the branching ratios. The cross-section of the top-quark processes are the NLO theory predictions.*

4.3.2 Data Driven QCD model

Another source of background events arises from QCD multijet events that are misidentified as lepton+jets events. Signal leptons stem from a prompt W-boson decay taking place in the hard process of the collision. Whereas non-prompt leptons are produced in leptonic decays of a b or c hadron within a hadronic jet. Those may be selected as isolated electron or muon if they are well separated from the hadronic jet. Thus, they can be misinterpreted as a lepton originating from the hard process. An example of such a multijet event is direct $b\bar{b}$ production, depicted in Fig. 4.7 (a). Those events are the main source of muon-fake events. Another possibility of faking a lepton is the misidentification of a hadronic jet as electron. The event signature of such multijet events is shown in Fig. 4.7 (b). An additional source of non-prompt electrons are electrons from photon conversions. These event classes have a similar signature as the signal events if a simultaneous mismeasurement of $E_{\mathrm{T}}^{\mathrm{miss}}$ takes place.

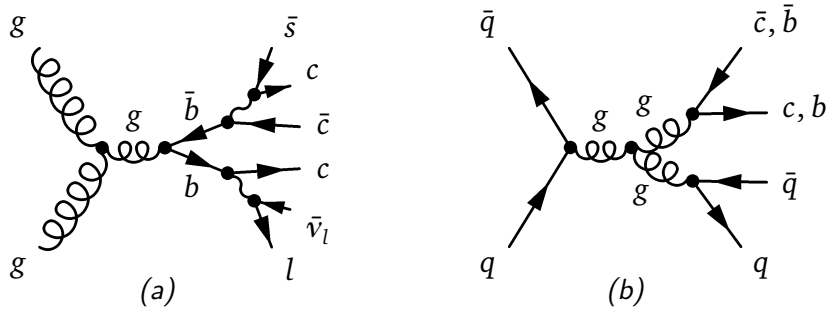

Figure 4.7: *Feynman diagrams of QCD multijet events. The semileptonic b decay of $b\bar{b}$ events can lead to fake-lepton events. The production of pure multijet events (b) contributes due to jets being misidentified as electron.*

Since the origin of a fake lepton is the misidentification of a jet as lepton or a non-prompt lepton originating from a jet, it has to be understood on the basis of the detector simulation and object reconstruction. Also, a mismeasurement of the $E_{\mathrm{T}}^{\mathrm{miss}}$ depends on the performance of the calorimeter system during the data taking period and is challenging to model correctly. These instrumental effects are difficult to include in the detector simulation. Thus, it is difficult to model fake-lepton events using MC simulated QCD multijet events. The probability of misidentifying a jet as a lepton is of the order of 10^{-4}. Despite the small fake rate, the large cross-section of QCD multijet events which is $\sim 1\,\mathrm{m}b$ [131] leads to a significant amount of fake-lepton events. The adequate solution to address those difficulties is a data-driven model which selects events from collision data with the typical kinematic properties of QCD multijet events. In the context of this analysis the 'jet-electron' model was developed. The ansatz is to select pure QCD multijet events, satisfying the signal selection criteria, but instead of a signal lepton, one of the jets in the event that fulfils certain criteria is used to model the lepton. Using a jet instead of a lepton is motivated by the fact, that misidentified jets are the source of fake-electrons. The jet-electron model is also used as a model for events having a fake muon. This is justified, since QCD multijet events faking a muon

due to a heavy-flavour decay within a jet and QCD multijet events where one jet is misidentified as an electron have the same event kinematics.

The events of the model are selected from a jet-triggered data sample. The jet which is used to model the lepton, the jet-electron, has to pass the kinematic acceptance cuts of the signal leptons in p_T and η. The energy of the jet-electron is calibrated at the em-scale to match the electron energy-scale. This requires a recalculation of the E_T^{miss}, including the jet at the em-scale with a calibration factor of $0.90 \cdot$ emjes. Hereby, emjes denotes the original JES calibration factor of the jet. The constant calibration factor of 0.9 is necessary since a jet is used as an electron, which has a different calibration scheme in the E_T^{miss} calculation. It is empirically derived by comparing the low mass range of the $m_T(W)$ distribution of observed data events which is dominated by selected fake-lepton events to the distribution predicted by the jet-electron model. Additional requirements on the jet are a high electromagnetic energy fraction f_{EM} between 0.8 and 0.95 and having at least 4 tracks to avoid selecting real electrons from photon conversions. An additional veto against signal leptons prevents selecting real lepton events. In Tab. 4.3 the selection criteria to define the jet-electron sample are summarised. Figure 4.8 shows a comparison of the E_T^{miss} distribution (a) and transverse W-boson mass (b), the difference of the azimuth angle between the lepton and the E_T^{miss} (c) and the p_T of the lepton (d) for simulated events with real W bosons and the jet-electron model. Typically, fake-lepton events have a small E_T^{miss} and $m_T(W)$ because the origin of the E_T^{miss} is instrumental. Additionally, the p_T of the jet-electron is softer than the p_T of a lepton originating from a W-boson decay. Another property is, that the jet-electron is parallel to the $\vec{E}_T^{miss}$ in the transverse plane, whereas both are back-to-back for events with a real W-boson decay. In the analysis the fake-lepton events are denoted as *'multijets'* background.

Variable	Cut
Trigger	EF_j20_a4_EFFS, EF_J20_a4tc_EFFS, EF_j15_a4tc_EFFS, EF_j10_a4tc_EFFS, EF_fj20_a4tc_EFFS, EF_fj15_a4tc_EFFS, EF_fj10_a4tc_EFFS
Transverse Energy of the Jet	$E_T > 25$ GeV
η of the Jet (electron)	$\lvert\eta\rvert < 2.47$, no CRACK region
η of the Jet (muon)	$\lvert\eta\rvert < 2.5$
EM Fraction	$0.8 < f_{EM} < 0.95$
Number of Tracks within the Jet	$n_{tracks} > 3$

Table 4.3: *The jet-electron model is selected from a generic jet-trigged sample. Additional requirements are applied to the jet which is used to model the lepton. This jet has to fulfil the lepton (e or μ) kinematic acceptance cuts at the em-scale.*

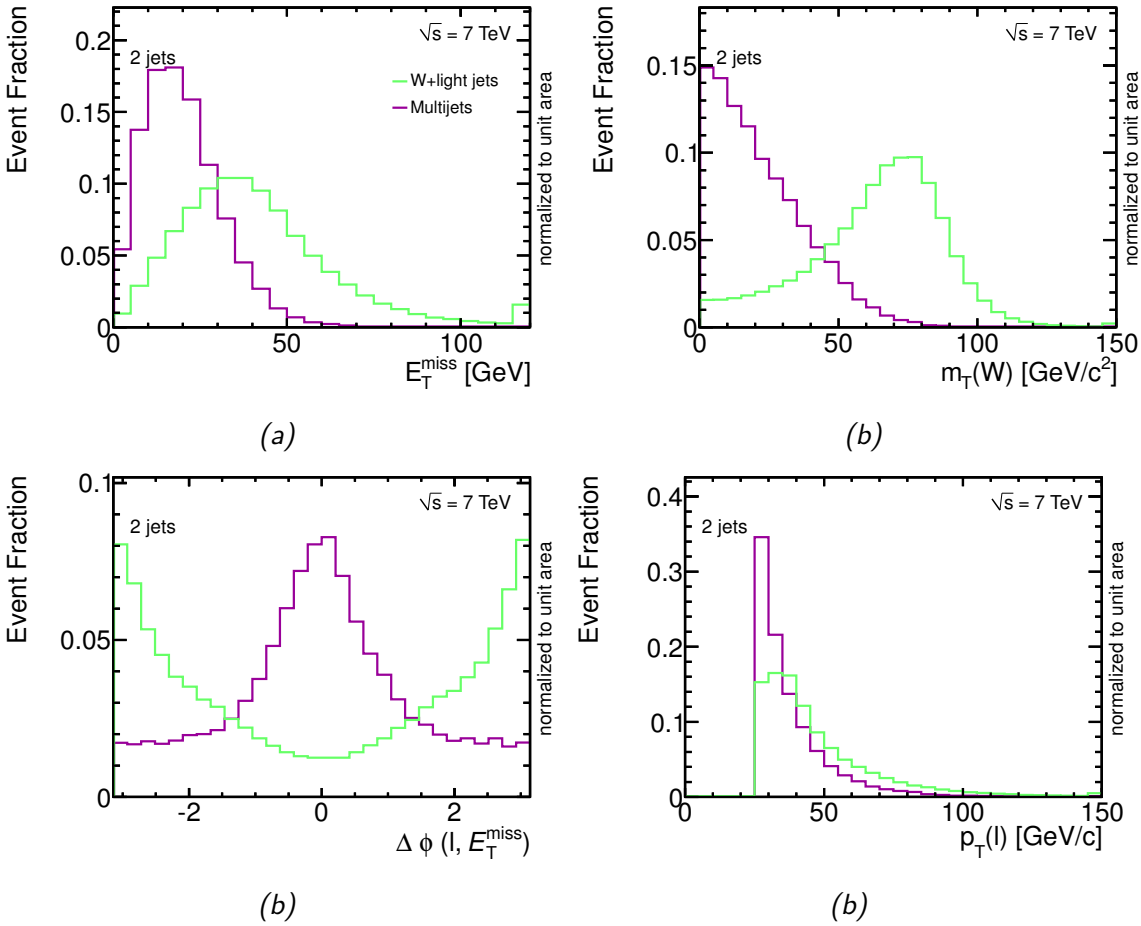

Figure 4.8: *Characteristic distributions that distinguish fake-lepton events modelled by the jet-electron model from real W events, the $E_{\mathrm{T}}^{\mathrm{miss}}$ (a), $m_T(W)$ (b), $\Delta\phi(\ell, E_{\mathrm{T}}^{\mathrm{miss}})$ (c) and the $p_T(\ell)$ (d). Typically, fake lepton events have a small $E_{\mathrm{T}}^{\mathrm{miss}}$, $m_T(W)$ and $p_T(\ell)$. The ϕ-direction of the $E_{\mathrm{T}}^{\mathrm{miss}}$ and lepton is back-to-back for real lepton events and parallel for fake-lepton events.*

Chapter 5

Event Selection and Event Yield

In this chapter, the event selection criteria of the signal region and control datasets are defined. The number of expected events after the selection cuts for the MC simulated background models and data-driven background model is estimated differently. A binned maximum-likelihood fit is employed to derive the amount of fake-lepton events in the signal region, whereas the event yields of the different processes are calculated from the theoretically predicted cross-sections and the selection efficiencies obtained from simulated events; Hereby, correction factors have to be taken into account for different reconstruction and identification efficiencies in observed events and the simulation. The event yield is presented for an integrated luminosity of $1.04\,\text{fb}^{-1}$ for the 2 and 3 jet signal and control region.

5.1 Lepton + Jets Event Selection

Candidate events of the t-channel signal process from simulated events and observed data are selected in the lepton+jets dataset. The signal event signature is characterised by the leptonic decay mode $e\nu$ or $\mu\nu$ of the W boson stemming from the top quark. Thus, events with one isolated high-p_{T} electron or muon and large $E_{\text{T}}^{\text{miss}}$ due to the neutrino are selected. Also events with a $W \to \tau\nu$ decay contribute to the selected events, if the τ decays to an isolated electron or muon. Two or three jets are expected to be present in the signal events. Exactly one of them has to be identified as a jet originating from a b quark. One important characteristic of the signal process is the light-quark jet in the forward direction. Thus, the full pseudorapidity coverage of the hadronic calorimeter up to $|\eta| = 4.5$ is used to select jets. By contrast to standard $t\bar{t}$ analyses which only use the central region of the calorimeter in a pseudorapidity range up to 2.5. Additional cuts on the event topology are applied to reduce the background from fake leptons. In the following the selection cuts applied to the reconstructed physics objects are described in detail. Table 5.1 presents an overview on the kinematic event cuts.

Electrons

In the electron channel one isolated high-p_{T} electron is required to be present in the

Cut	Value
	Electron
Trigger	EF_e20_medium
Transverse Momentum	$p_{\mathrm{T}} > 25\,\mathrm{GeV}$
Fiducial Region	$\lvert\eta_{\mathrm{cl}}\rvert < 2.47$, $1.37 < \lvert\eta_{\mathrm{cl}}\rvert < 1.52$ excluded
Quality and Isolation	tight, ptcone30/$p_{\mathrm{T}} < 0.10$, etcone30/$p_{\mathrm{T}} < 0.15$
	Muon
Trigger	EF_mu18
Transverse Momentum	$25\,\mathrm{GeV} < p_{\mathrm{T}} < 150\,\mathrm{GeV}$
Fiducial Region	$\lvert\eta_{\mathrm{cl}}\rvert < 2.5$
Jet Overlap	$\Delta R(\mathrm{jet}, \mu) > 0.4$
Quality and Isolation	tight, ptcone30/$p_{\mathrm{T}} < 0.10$, etcone30/$p_{\mathrm{T}} < 0.15$
	Jet
Transverse Momentum	$p_{\mathrm{T}} > 25\,\mathrm{GeV}$
Fiducial Region	$\lvert\eta\rvert < 4.5$
Electron Overlap	$\Delta R(\mathrm{jet}, e) > 0.2$
Quality	no bad jet with $p_{\mathrm{T}} > 10\,\mathrm{GeV}$
	Event Level
Anti-QCD	$m_{\mathrm{T}}(W) > 60 - E_{\mathrm{T}}^{\mathrm{miss}}$
$E_{\mathrm{T}}^{\mathrm{miss}}$	$E_{\mathrm{T}}^{\mathrm{miss}} > 25\,\mathrm{GeV}$
Primary Vertex	more than one with at least 4 associated tracks
b-tag	one jet with JetFitterCombNN discriminator > 2.4
Jets	2 or 3 jets
Charged Lepton	one isolated electron or muon

Table 5.1: *Cuts for selecting the physics objects in the event and the candidate events. Events having exactly one isolated electron and muon with 2 or 3 jets with one of them b-tagged are considered as signal events.*

event. It has to pass the EF_e20_medium [132] event filter chain. An electromagnetic cluster energy of 20 GeV is demanded for the electron trigger object. The efficiency of the electron trigger $\epsilon_{\mathrm{trigger}}$ is measured using $Z \to ee$ and $W \to e\nu$ events. At the plateau of the trigger turn-on-curve above 25 GeV an efficiency of $\simeq 98\%$ is achieved. Therefore, for a constant trigger efficiency, a reconstructed electron needs a transverse momentum larger than 25 GeV. The trigger efficiency of simulated events and observed data agrees with unity [133]. The fiducial region of a selected electron is defined by the position of the calorimeter cluster (cl) associated to the electron. A pseudorapidity range of $\lvert\eta_{\mathrm{cl}}\rvert < 2.47$ is required. The transition region of the electromagnetic calorimeter of $1.37 < \lvert\eta_{\mathrm{cl}}\rvert < 1.52$ is excluded from the fiducial region.

Due to a dead region in the LAr calorimeter, electrons in the rectangular region of $(-0.74 < \phi < 0.64) \times (0 < \eta < 1.4)$ are not measured in observed data. This problem exists for 85% of the observed dataset studied in this analysis. Roughly 10% of the observed events are rejected by removing events, where the reconstruction is affected. In simulated events, electrons in this detector region are not reconstructed as an electron. For a clean electron identification the track and cluster properties need to fulfil the tight identification requirements, which have a selection efficiency of $\sim 75\%$ [134]. Additionally, an isolation of the electron is demanded to reduce the background from fake-electrons. Thus, an extra energy in the calorimeter (etcone) and additional track momenta (ptcone) not associated to the electron in a cone of ΔR around the electron track are determined. A relative isolation criterion is applied to the etcone30 and ptcone30 variables. An additional cluster energy of 15% and track momentum of 10% of the electron p_{T} is allowed in a cone of $\Delta R < 0.3$ around the electron. It was studied that the relative isolation reduces the background from misidentified electrons by a factor of 2 to 3 in comparison to an absolute cluster-isolation criterion smaller than 3.5 G*e*V. Correction factors are measured for the differences of the trigger and electron identification between data and simulated events as described in Ref. [135]. The energy scale of observed electrons is corrected according to studies based on results of the $Z \rightarrow ee$ analysis [136].

Muons

In the muon channel of the analysis, events having one isolated high-p_{T} muon are selected. This has to pass the EF_mu18 event filter chain, which demands a muon-trigger object with a p_{T} larger than 18 G*e*V. A trigger efficiency of roughly 80% is observed. The identification of reconstructed combined muons is based on the tight track quality requirements described by Ref. [137]. Muons with a geometric coverage of $|\eta| < 2.5$ in the transverse momentum range between 25 G*e*V and 150 G*e*V are selected. The p_{T} range is restricted by the measurements of the reconstruction efficiency due to statistical limitations. The loss of observed events and expected signal events due to the upper p_{T} cut is negligible. To reduce the contamination of non-prompt muons from heavy-flavour decays within hadronic jets, different isolation criteria are applied. A relative track (ptcone30) and calorimeter (etcone30) isolation is required within a cone of $\Delta R < 0.3$ around the muon direction. An extra calorimeter energy of 15% and track momentum of 10% of the muon p_{T} is allowed, which is not associated to the muon. Additionally, muons overlapping with a hadronic jet within a cone of $\Delta R < 0.4$ are rejected. Jets with a p_{T} above the threshold of 20 G*e*V are considered. The efficiencies of the muon trigger and reconstruction are derived from $Z \rightarrow \mu\mu$ events with the techniques described in Ref. [138]. The efficiencies in simulated events and observed data are compatible.

Jets and $E_{\mathrm{T}}^{\mathrm{miss}}$

Jets are reconstructed using the anti-k_{T} algorithm with a cone-width parameter of 0.4.

The jets are calibrated at the EM+JES energy scale. Jets with a p_{T} larger than 25 GeV are selected. Their fiducial region is defined by the position of the calorimeter cluster associated to the jet of $|\eta_{cl}| < 4.5$. Events having a jet with an uncalibrated p_{T} above 10 GeV and bad quality criteria due to calorimeter noise bursts or non-collision backgrounds [139] are rejected, because they would lead to a mismeasurement of the $E_{\mathrm{T}}^{\mathrm{miss}}$. Since the jet reconstruction algorithm forms jets from all topological calorimeter clusters, also electrons are reconstructed as jets. Thus, the jet closest to a selected electron candidate is removed from the jet list, if it overlaps with the reconstructed and isolated electron within a cone of $\Delta R < 0.2$. Events featuring a jet fulfilling the above quality criteria with $p_{\mathrm{T}} > 20$ GeV that is in the dead rectangular region of LAr calorimeter $(-0.74 < \phi < 0.64) \times (0 < \eta < 1.4)$ are rejected on simulated events and observed data. In the pseudorapidity range of $|\eta| < 2.5$ the JetFitterCombNN algorithm is used to identify jets originating from a b quark. A jet is defined as tagged jet if the discriminator exceeds a value of 2.4.

Events having 2 or 3 jets are selected. Exactly one of them is required to be a b-tagged in the tagged dataset. In the pretag dataset, one of the jets has to have a $|\eta_{\mathrm{cl}}| < 2.5$. To select events with neutrinos from the W-boson decay, the missing transverse energy has to exceed 25 GeV.

Anti-QCD

Using tight quality and isolation criteria for electrons and muons reduces the amount of events with lepton fakes significantly. For a further reduction, the kinematic properties of fake-lepton events are exploited. The $E_{\mathrm{T}}^{\mathrm{miss}}$ of those events stems from an instrumental mismeasurement or a semi-leptonic b hadron or c hadron decay in a jet. Thus, they are characterised by a small $E_{\mathrm{T}}^{\mathrm{miss}}$ and small $m_{\mathrm{T}}(W)$. Hence, a triangular cut on $m_{\mathrm{T}}(W) > 60 - E_{\mathrm{T}}^{\mathrm{miss}}$ is performed to reject this event class. In the pretag dataset, the performance of the triangular cut can be studied since it is dominated by the production of W+jets events. Figure 5.1 illustrates the distribution of events in the

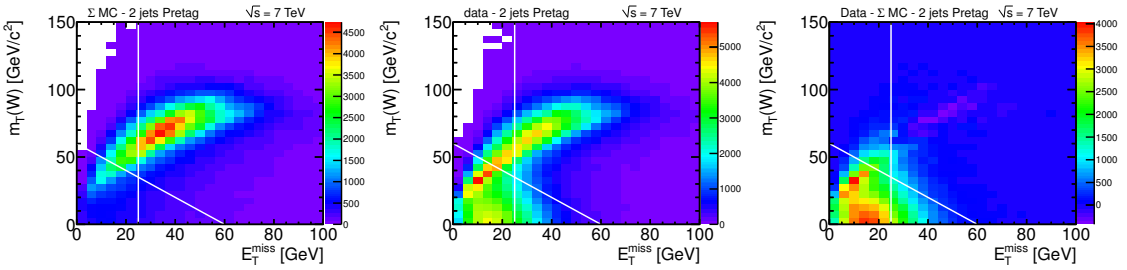

(a) *(b)* *(c)*

Figure 5.1: *Simulated real W events (a), observed data events (b) and the difference between the observed data and the MC expectation (c) for the two jet pretag selection. The triangular and $E_{\mathrm{T}}^{\mathrm{miss}}$ cut were omitted in the selection. White lines are used to illustrate both cuts. The difference between the simulated and observed events shows the event class of fake lepton events in the low $E_{\mathrm{T}}^{\mathrm{miss}}$ and low $m_{\mathrm{T}}(W)$ region.*

two-dimensional $E_{\mathrm{T}}^{\mathrm{miss}}$-$m_{\mathrm{T}}(W)$ plane in the pretag dataset. The the sum of all simulated real W-boson events is shown in Fig. 5.1 (a). The observed data events are displayed in Fig. 5.1 (b) and the difference between the observed data and simulated events in Fig. 5.1 (c). The triangular cut and the $E_{\mathrm{T}}^{\mathrm{miss}}$ cut are omitted for this selection and indicated by the white lines. The remaining events in the low $E_{\mathrm{T}}^{\mathrm{miss}}$ and $m_{\mathrm{T}}(W)$ region are suspected to be fake-lepton events and are rejected by the triangular cut. In the tagged dataset the efficiency on the t-channel signal events is roughly 95%, on observed data about 85%. Alternative cut scenarios ($\Delta\phi(j_1, E_{\mathrm{T}}^{\mathrm{miss}})$ vs. $E_{\mathrm{T}}^{\mathrm{miss}}$, $\Delta\phi(j_2, E_{\mathrm{T}}^{\mathrm{miss}})$ vs. $E_{\mathrm{T}}^{\mathrm{miss}}$, $\Delta\phi(\ell, E_{\mathrm{T}}^{\mathrm{miss}})$ vs. $E_{\mathrm{T}}^{\mathrm{miss}}$, $\Delta\phi(\ell, E_{\mathrm{T}}^{\mathrm{miss}})$ vs. p_{T}^{ℓ}, and $m_{\mathrm{T}}(W)$ vs. p_{T}^{ℓ}) were studied, but the rejection of fake-lepton events was less powerful.

Signal and Control Dataset

Figure 5.2 shows the jet multiplicity distribution of the signal events after all selection cuts: 45% and 30% of the simulated signal events are selected in the 2 jets and 3 jets channel, respectively. Therefore, these two channels are regarded as signal channels in the analysis. The 1-jet and 4-jet channel only have a small contribution of signal events compared to the background processes. The data sample of the signal region, where the b-jet identification requirement is applied, is called 'tagged dataset'. An additional control sample, the 'pretag dataset', without any requirements on b-jet identification is defined. Here, one of the jets is required to be in the pseudorapidity region of $|\eta| < 2.5$, which is the pseudorapidity range of a b-tagged jet.

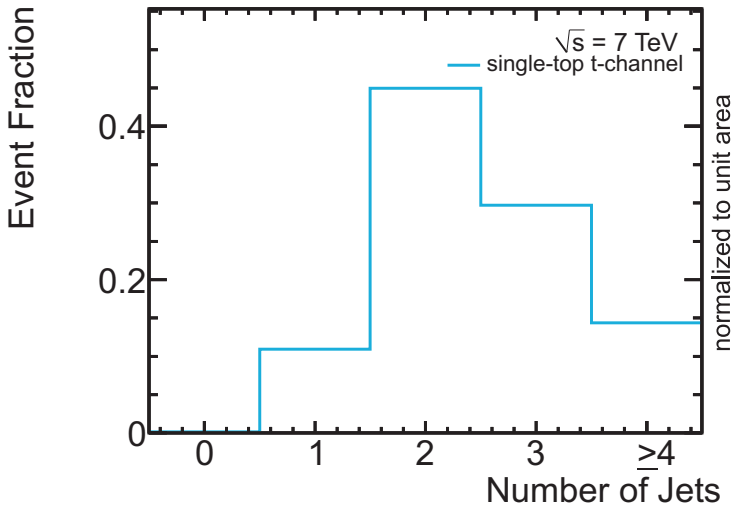

Figure 5.2: *Distribution of the jet multiplicity after all selection cuts for the t-channel signal sample.*

5.2 Data-Driven QCD Estimate

A binned maximum-likelihood fit is utilised to estimate the normalisation of the QCD-multijet background. The kinematic shapes of multijet events are obtained from the data-driven jet-electron model. Simulated events are used for the shapes of real W-boson and Z-boson events. Several kinematic distributions were tested to perform the fit. Finally, the $E_{\mathrm{T}}^{\mathrm{miss}}$ distribution turned out to be the most sensitive one. All event selection cuts, except the $E_{\mathrm{T}}^{\mathrm{miss}}$ cut are applied to define the datasets on which the fits are performed. Thus, the full range of the $E_{\mathrm{T}}^{\mathrm{miss}}$ distribution is used, including the sideband between 0 and 25 G*e*V to increase the discrimination power between lepton-fake events which accumulate in the low energy region and real-W events. Since the statistical uncertainty on the multijet event yield is not used in the further analysis, the full $E_{\mathrm{T}}^{\mathrm{miss}}$-range can be fitted.

The performance of the method has been investigated in Ref. [140] using pseudo-data from simulated events. In this study, the jet-electron model is also constructed from simulated events. Good agreement of the fitted number of multijet events and the real contamination in the pseudo-data was found. Additionally, a comparison with an alternative model, that constructs the multijet event model by inverting the electron identification cuts is in good agreement within the uncertainty of the fit.

The binned maximum-likelihood fit is performed separately in the electron and muon channel. For the tagged dataset, the jet-electron model with the pretag selection is used to avoid statistical fluctuations of the model, to ensure smooth event shapes. Both, the shape of the tagged and pretag model are very similar and agree within their statistical fluctuations. A shape comparison is given in Appx. A.1. The number of multijet events in the signal region above 25 G*e*V is determined from the fit. Table 5.2 shows the re-

	Pretag Events		Tagged Events	
Jet Bin	QCD	QCD Fraction [%]	QCD	QCD Fraction [%]
		Electron Channel		
2-Jet	14860 ± 500	11	710 ± 90	14
3-Jet	5980 ± 330	15	580 ± 60	16
		Muon Channel		
2-Jet	6800 ± 420	5	440 ± 70	8
3-Jet	1660 ± 270	4	270 ± 60	7

Table 5.2: *Estimate of the QCD-multijet background in the electron and muon channel in the 2-jet and 3-jet dataset for pretag and tagged events. The yield and the event fraction of the multijet events is given in the signal region with $E_{\mathrm{T}}^{\mathrm{miss}} > 25$ GeV. The uncertainty of the yield is the statistical uncertainty of the fit.*

sults for both lepton channels for events with 2 or 3 jets, separately.

Figure 5.3 depicts the fit results of the two jet bin for the electron and muon channel. The pretag dataset is shown in 5.3 (a) and 5.3 (c), the tagged dataset is shown in 5.3 (b) and 5.3 (d). In the electron channel, a slight mismodelling of the $E_{\mathrm{T}}^{\mathrm{miss}}$ sideband region is visible. Additional kinematic control variables in the pretag dataset are presented in Fig. 5.4 and Fig. 5.5. In general good agreement between observed data and the fit result is found for the kinematic variables. The low-p_{T} region of the electron channel Fig. 5.4 (d) shows a small deviation. Appxs. A.2 to A.5 show all fit results and pretag control plots for the electron and muon channel. In the electron channel, a QCD fraction of 14% and 16% is found for the 2-jet and 3-jet signal region. A smaller contamination is measured in the muon channel, accounting to 8% and 7% for 2-jet and 3-jet events, respectively.

The effect of different pile-up conditions is evaluated by dividing the jet-electron sample into a high pile-up sample having six and more primary vertices and a low pile-up sample having less than six vertices. Each of the sample is used to re-estimate the event yield. A variation within $\pm 20\%$ with respect to the nominal jet-electron sample is observed in the different channels. Additionally, the results are checked by performing the fits in a less sensitive variable, the transverse W-boson mass. Here, a variation within $\pm 50\%$ is seen. The detailed results are shown in Appx. A.6. Conclusively, a systematic uncertainty of 50% is assigned to the fit results.

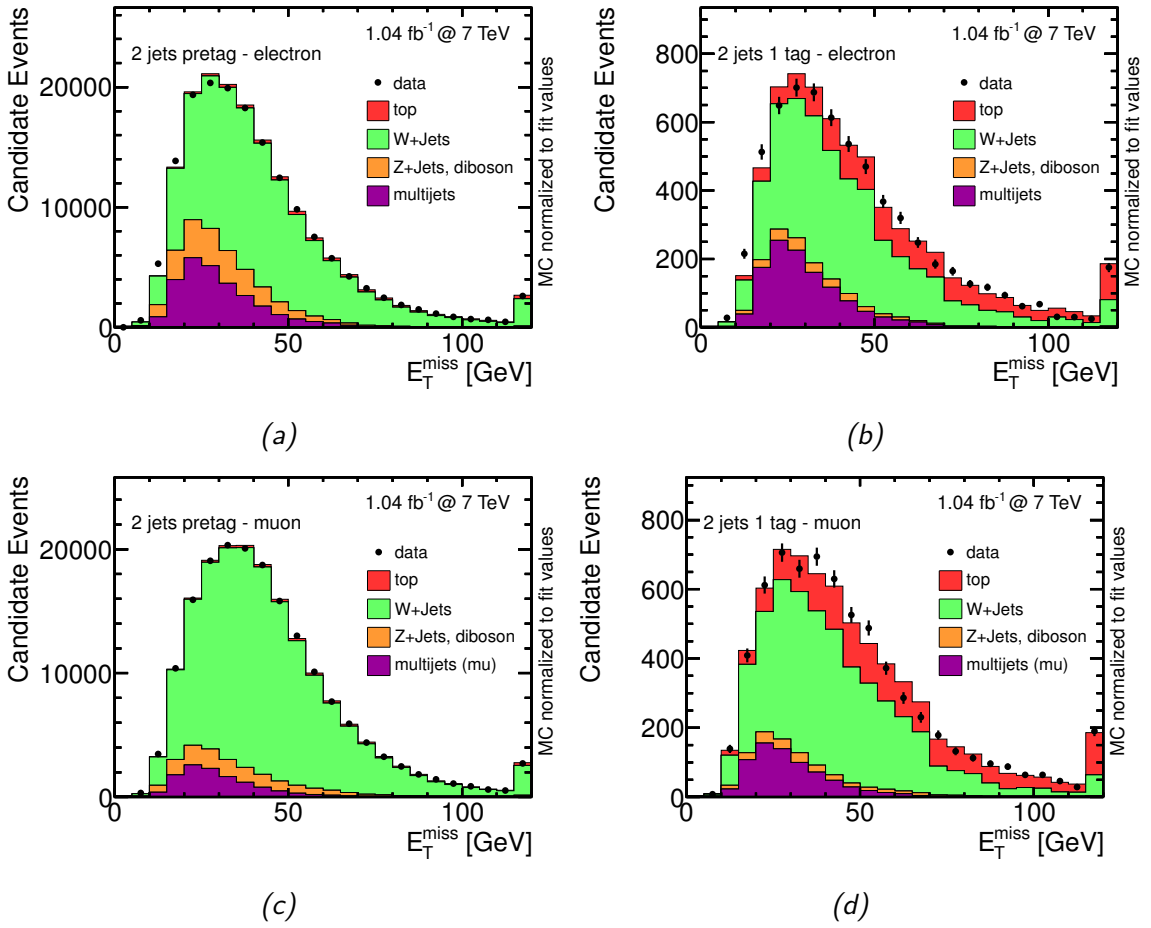

Figure 5.3: *Fits to the $E_{\mathrm{T}}^{\mathrm{miss}}$-distribution in the 2 jet pretag (a) and tagged (b) dataset for the electron channel and the 2 jet pretag (c) and tagged (d) dataset of the muon channel.*

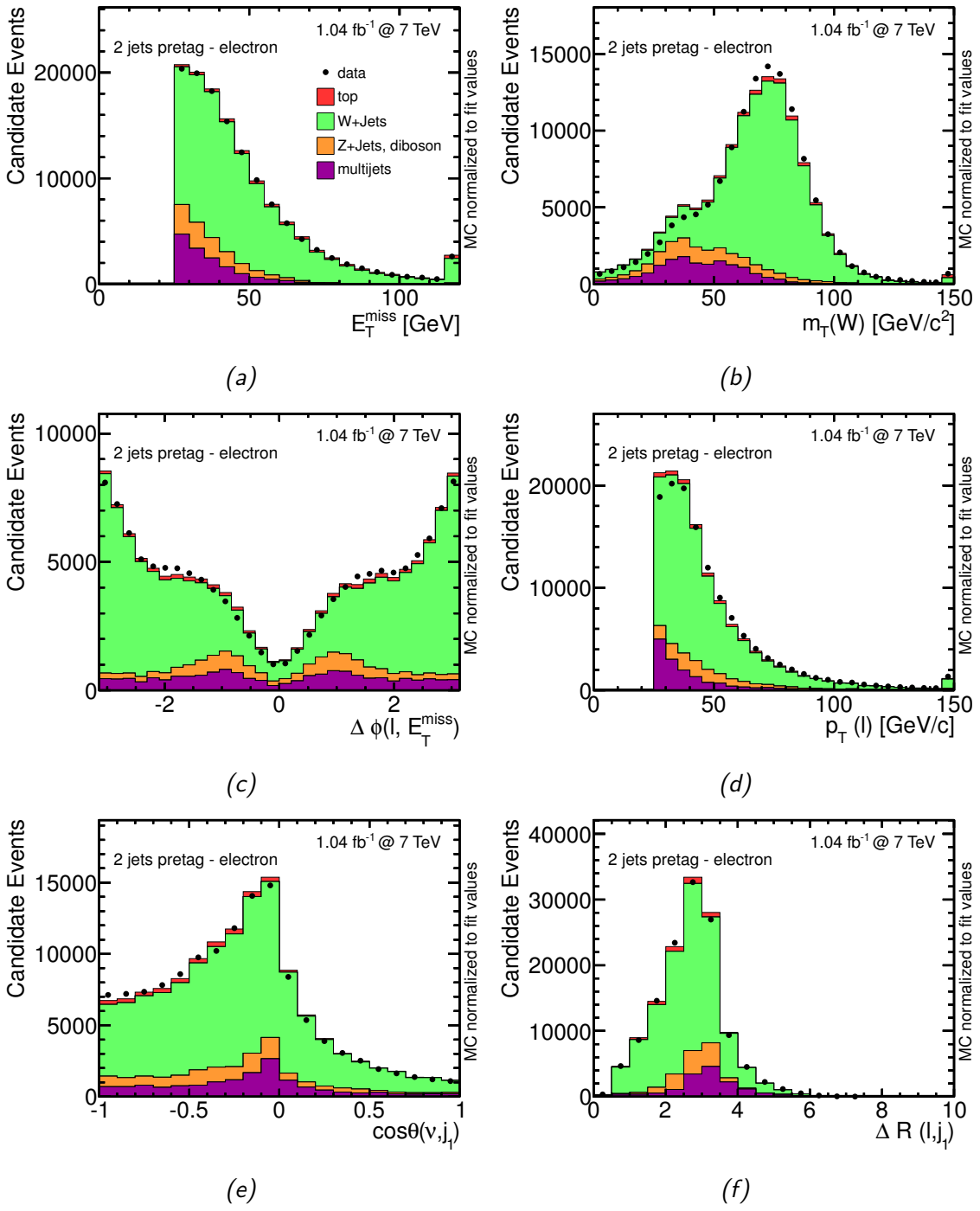

Figure 5.4: *Control plots for the fit of the jet-electron model after all cuts in the signal region (pretag) for the electron channel in the 2-jet bin. Distribution of the $E_{\mathrm{T}}^{\mathrm{miss}}$ (a), the reconstructed transverse W-boson mass (b), the $\Delta\phi$ between the charged lepton and the $\vec{E}_{\mathrm{T}}^{miss}$ (c), the p_{T} of the charged lepton (d), the $\cos\theta$ between the leading jet and the reconstructed neutrino (e), the ΔR between the charged lepton and the leading jet (f).*

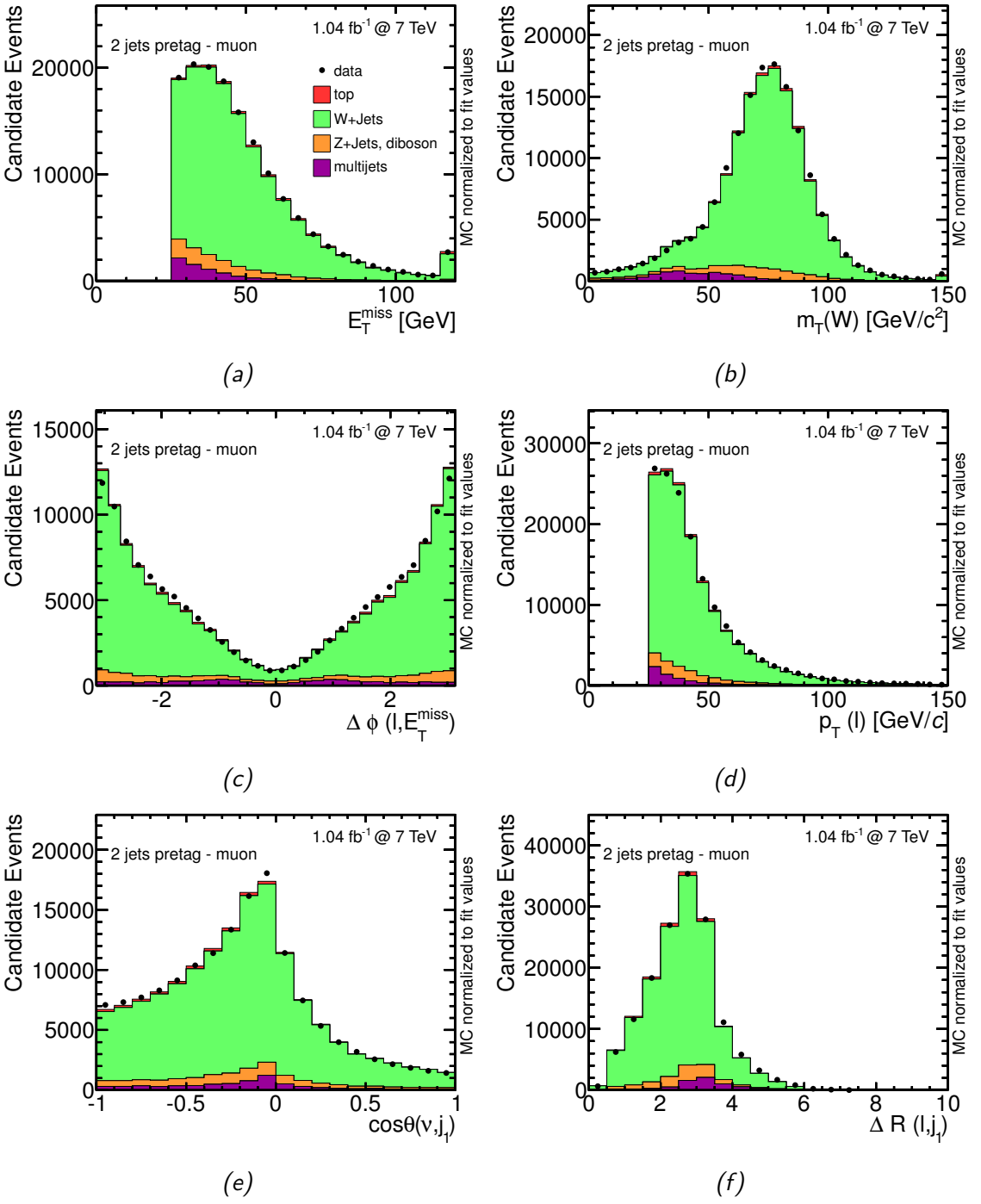

Figure 5.5: *Control plots for the fit of the jet-electron model after all cuts in the signal region (pretag) for the muon channel in the 2-jet bin. Distribution of the $E_{\mathrm{T}}^{\mathrm{miss}}$ (a), the reconstructed transverse W boson mass (b), the $\Delta\phi$ between the charged lepton and the $\vec{E}_{\mathrm{T}}^{miss}$ (c), the p_{T} of the charged lepton (d), the $\cos\theta$ between the leading jet and the reconstructed neutrino (e), the ΔR between the charged lepton and the leading jet (f).*

5.3 Event Yield

The number of expected events for the simulated signal and background processes is given by the theoretical cross-section σ of each process, the event selection efficiency ϵ_{evt} and the integrated luminosity $\mathcal{L}_{\text{int}} = \int L dt$. Thus, it is important that the cross-section calculation and kinematic distributions are theoretically well understood. Some of the backgrounds events rates are difficult to predict. Therefore, they need to be normalised using observed data. This is done for W+jets events in the final analysis by simultaneously fitting the signal and background rates. The theoretical prediction serves as rough approximation of the estimate for the W+light and W+heavy flavour events. The event yield of multijet events is also measured from observed data as described in the previous section. Taking all together, the number of expected events $\hat{\nu}$ is given by:

$$\hat{\nu} = \sigma^{\text{theory}} \cdot \epsilon_{\text{evt}} \cdot \mathcal{L}_{\text{int}} \tag{5.1}$$

$$\epsilon_{\text{evt}} = \epsilon_{\text{BR}} \cdot \epsilon_{\text{MC}} \cdot \epsilon_{\text{trigger}} \cdot \epsilon_{\text{reco}} \cdot \epsilon_{b-\text{tagging}} \cdot \epsilon_{\text{pile-up}}. \tag{5.2}$$

The total event detection efficiency ϵ_{evt} is the product of several efficiencies and correction factors. For events featuring a leptonic W-boson decay, the leptonic branching ratio of the W boson $\epsilon_{\text{BR}} = 0.324$ has to be taken into account. Simulated events are used to determine the event selection efficiency ϵ_{MC} by taking the ratio of all selected event weights to the sum of all weights in the simulated sample. The branching ratio ϵ_{BR} takes into account that only specific decay modes are considered in the simulated event samples. Additional correction factors have to be considered to adjust different selection efficiencies in simulated events and observed data. Those are derived for the trigger efficiency $\epsilon_{\text{trigger}}$, lepton reconstruction ϵ_{reco} and the b-tagging $\epsilon_{b-\text{tagging}}$. Also, the simulated events are reweighed according to the different pile-up conditions in observed data and the event simulation, which is accounted for in $\epsilon_{\text{pile-up}}$.

Table 5.3 and 5.4 show the event yields for an integrated luminosity of $1.04\,\text{fb}^{-1}$ for the pretag and tagged dataset with 2 or 3 jets. The uncertainties on the event yield are due to the theoretical prediction and experimental measurements. The theoretical uncertainty on the signal process is $^{+4}_{-3}$%. The uncertainty on the processes composing the top background is of theoretical nature. It is $^{-10}_{-7}$% [38] on $t\bar{t}$, 7% on the single-top Wt channel and 4% on the single-top s-channel [5, 6]. Uncertainties on the background normalisation of W+heavy-flavour jet of 50% and W-light jet production of 30% are derived from an experimental measurement [141]. An uncertainty of 5% is assigned to the diboson background [142] and one of 60% to the Z+jets background. The multijet background has an uncertainty of 50%. In the tagged dataset, the main source of background events is the production of W+heavy flavour events and $t\bar{t}$ events. W+light jet events, which are the vast background in the pretag dataset are rejected significantly by the application of the b-jet identification. After all event selection cuts, 940 ± 20 and 620 ± 20 t-channel signal events are expected in the 2 and 3 jet channel. This cor-

responds to a signal-to-background ratio of 11.2% and 9.0%. The total event selection efficiency for signal events is 4.3% and 2.8% in the 2 and 3 jets channel, respectively.

	Pretag			
	2-Jets		3-Jets	
	$\epsilon_{\text{evt}}[\%]$	$\hat{\nu}$	$\epsilon_{\text{evt}}[\%]$	$\hat{\nu}$
t-channel	2.8	1890 ± 50	1.6	1100 ± 30
top	1.0	3330 ± 290	1.9	6670 ± 580
W+light	0.6	196440 ± 58930	0.1	44950 ± 13480
W+heavy flavour	0.9	54510 ± 32700	0.3	15890 ± 9530
Z+jets, Diboson	1.7	19200 ± 11520	0.6	6280 ± 3770
Multijets	–	21660 ± 10830	–	7640 ± 3820
Total Exp.		297020 ± 92990		82520 ± 23640
S/B		0.6		1.4
DATA		272286		73751

Table 5.3: *Event yield for the pretag dataset of* $1.04\,\text{fb}^{-1}$ *with 2 and 3 jets. The QCD multijet event estimation is from the fitting method. All the other expectations are derived using theoretical cross-sections. The uncertainties are due to the uncertainty on the predicted cross-section.*

	b-Tagged Dataset			
	2-Jets		3-Jets	
	$\epsilon_{\text{evt}}[\%]$	$\hat{\nu}$	$\epsilon_{\text{evt}}[\%]$	$\hat{\nu}$
t-channel	1.4	940 ± 20	0.9	620 ± 20
top	0.3	1160 ± 100	1.0	3380 ± 300
W+light	0.003	1010 ± 300	0.001	390 ± 120
W+heavy flavour	0.06	4800 ± 2400	0.03	2080 ± 1040
Z+jets, Diboson	0.03	330 ± 200	0.02	180 ± 110
Multijets	–	1150 ± 570	–	850 ± 420
Total Exp.		9390 ± 2770		7490 ± 1280
S/B		11.2		9.0
DATA		10613		7507

Table 5.4: *Event yield for the tagged dataset of* $1.04\,\text{fb}^{-1}$ *with 2 and 3 jets. The QCD multijet event estimation is from the fitting method. All the other expectations are derived using theoretical cross-sections. The uncertainties are due to the uncertainty on the predicted cross-section.*

Chapter 6

Candidate Event Classification

After the event selection, a signal-to-background ratio of 11.2% and 9.0% in the 2-jet and 3-jet channel is expected for the tagged dataset. The strategy used in this analysis to isolate signal events from background events is to combine several topological variables with an artificial neural network (NN) to one distribution having more discrimination power than the individual variables. An NN exploits not only the individual separation power of a single variables but also the correlations amongst them. In this analysis, the NEUROBAYES [143, 144] package is used to train a classifier that discriminates t-channel single top-quark signal events from all background processes. Simulated events are used to create template distributions which are fitted to the classifier output of observed data. One advantage is, that the background normalisation and signal extraction can be done in a combined binned maximum-likelihood fit to the observed output distribution of the NN. In a classical approach of isolating a signal enriched sample space by applying additional cuts the background normalisation has to be derived from additional measurements in control regions. In this chapter the general functionality of an NN and the specialities of NEUROBAYES are explained. Additionally, the selection of discriminating variables and the validation of the NN classifier is presented.

6.1 Neural Networks

The NEUROBAYES package combines a three-layer feed forward NN with a complex and robust preprocessing of the input variables. In general, a neural network consists of neurons arranged in different layers, where each neuron of one layer is connected to all neurons of the previous layer. Finally, the output calculated by each neuron in the previous layer is merged together by one output neuron. It provides a continuous distribution that separates signal and background events. After a successful training, the network can be used to classify the observed events. In this section, the preprocessing of the input variables and the technique of neural networks is explained.

6.1.1 Preprocessing of the Input Variables

Before the input variables x_i are processed by the NN, each single variable undergoes a complex preprocessing. It includes variable transformations and a linear decorrelation from the other input variables. The individual preprocessing of an input variable starts with flattening the distribution to be uniformly distributed for the sum of signal and background events. A uniform distribution is achieved by applying a monotonous non-linear transformation. Technically, this is done using the cumulative probability distribution of x_i, to create a histogram having the same number of events in each bin. Hence, a variable bin width is obtained. This procedure prevents that extreme outliers saturate a neuron of the network and dominates its final output. A conditional probability of an event being a signal or background event $P(x_{i,j}|\text{signal})$ in each bin j of the histogram is derived from the flattened distribution. It is given by the purity distribution $p_j = N_{i,j}^{\text{signal}}/(N_{i,j}^{\text{signal}} + N_{i,j}^{\text{background}})$. Here, $N_{i,j}^{\text{signal}}$ and $N_{i,j}^{\text{background}}$ are the number of signal and background events in each bin of the histogram. To avoid statistical fluctuations of the purity distribution, a spline fit is applied for smoothing. The numerical range of the input variables is standardised by transforming the purity distribution to a Gaussian distribution with mean zero. By doing so, all input variables have a similar dynamic range. Thus, numerical problems are avoided in the network training and evaluation.

After this procedure, all input variables are decorrelated to achieve an optimal network training. A Jacobi transformation [145] is applied for a linear decorrelation of the input variables. Correlations at higher order still remain. Finding the n-dimensional rotation matrix, that diagonalises the correlation matrix, is a difficult task. Thus, it is approximated by consecutive 2-dimensional rotations until the correlation matrix is close to a diagonal form.

To find an optimal set of input variables in terms of the separation power of the network, an importance ranking of the variables is calculated at the end of the preprocessing. This helps to select variables having major separation power and remove those, that would not contribute significantly to the network. Adding a variable that is highly correlated to an other one for instance does not increase the separation power of the network. To determine the variable ranking, the total correlation to the training target is calculated using the correlation matrix. The training target is defined as the classification of an event to belong to the signal or background hypothesis. Each variable is removed once from the set of n input variables, to calculate the correlation to the training target of the remaining $n-1$ variables. This is done for all variables. The least important variable is identified by the smallest loss in the correlation to the target of the remaining variables. Hence, this variable is removed and the procedure is repeated with the set of $n-1$ variables to find the least important amongst them.

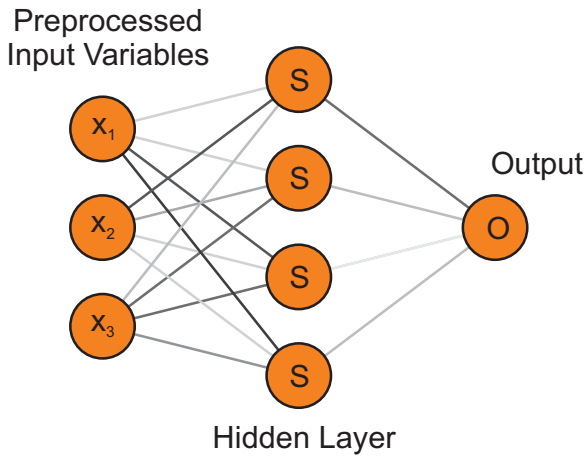

Figure 6.1: *Schematic sketch of a simple three-layer feed forward NN topology. The preprocessed input variables x_i are fed to the network via input nodes. Those are connected to all hidden layer nodes, with individual weights. Its strength is denoted by the different grayscales of the connection lines. The output of one hidden node is calculated by the transfer function S. The output of all hidden layer neurons is combined to one output variable.*

6.1.2 Neural Network Technique

In general, the topology of an artificial neural network is comparable with a mesh, which nodes are denoted as neurons. The strength of the connection between two neurons is given by an individual weight. For classification problems NeuroBayes utilises a three-layer feed-forward network. Here, the output of one neuron is propagated only in direction of the output node as input of the subsequent nodes. In the first layer, the input variables feed to the network, plus an additional bias node. All nodes of the input layer are connected to each neuron of the hidden layer. Thereby, an arbitrary number of hidden layer nodes can be chosen for the network architecture. Their output is combined to one single value of the output neuron. A simple sketch of such a topology is depicted in Fig. 6.1.

The input of an internal neuron j is the weighted sum $a_j(\vec{x})$ of all input variables x_i. The strength of the connections of the internal neuron j to the input node i is given by the weight w_{ij}:

$$a_j(\vec{x}) = \sum_i^D w_{ij} x_i + \mu_j. \tag{6.1}$$

A constant bias μ_j can be used to shift the weighted sum. NeuroBayes facilitates a shifted sigmoid function $S(a_j)$ to compute the output of a neuron:

$$S\left(a_j\right) = \frac{2}{1+e^{-a_j}} - 1. \tag{6.2}$$

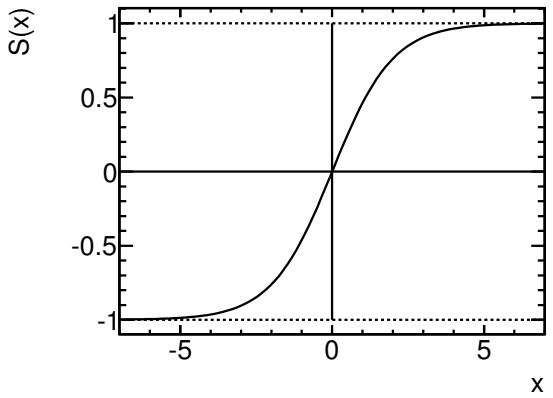

Figure 6.2: *The transfer function of the neurons to calculate their output is a shifted sigmoid function. It is sensitive for input values around zero and saturates for large values.*

It maps the input value range $]-\infty,\infty[$ to the output value range $[-1,1]$. A visualisation of the sigmoid function is depicted in Fig. 6.2. It is sensitive for values around zero and has an asymptotic behaviour for large values. The bias constant μ_j is used to shift the weighted sum of the input variables to the sensitive region of the sigmoid function to avoid saturation effects.

The final output of a network with M hidden nodes and D input variables is given by the weighted sum of all hidden layer node outputs:

$$o = S\left(\sum_j^M \cdot S\left(\sum_i^D w_{ij}x_i + \mu_j\right)\right). \tag{6.3}$$

Since the output of the network is passed through a sigmoid function, its target values for the classification of background events are -1 and $+1$ for signal events. A mapping of the continuous output to the range between 0 and 1 allows an interpretation as conditional probability for an event to be signal or background like. The weights that connect the network nodes have to be adjusted by a network training for each classification task.

6.1.3 Training of the Neural Network

The training procedure of the neural network adjusts the weights connecting the neurons such, that a complex pattern is recognised by the network to discriminate between two event classes. The aim of the learning procedure is to minimise the difference between the network classification with respect to the true event class of the training sample. Therefore, adjusting the weights is equivalent with a minimisation problem. The numerical quantity that is used to define the error of the network output is the

entropy loss function:

$$E_D = \sum_k \log\left(\frac{1}{2}\left(1 + T_k \cdot o_k + \epsilon\right)\right). \tag{6.4}$$

Hereby, T_k denotes the training target of the problem for event k, which is a binary value of -1 for background and $+1$ for signal events. The current output of the network for this event is o_k. A small regularisation constant ϵ avoids numerical problems at the beginning of the training. It decreases with each training iteration. Using the entropy loss function has the advantage, that completely wrong classifications will have an infinite large value. Thus, they are avoided in the very early iterations of the training. Finding the minimum of a complex multidimensional surface is a numerically non-trivial problem. Since the network has a complex structure and the target values of the hidden nodes are unknown, the back-propagation algorithm is used for this task. This algorithm propagates the input pattern through the network to calculate the current response and error. Since the target values of the hidden values is not known, the weight update of the connections to the hidden layer is propagated backwardly through the network. The weight update is calculated by the gradient of the current surface point:

$$\Delta w_{ij}^{\text{new}} = -\gamma \frac{\partial E}{\partial w_j} + \mu \Delta w_{ij}^{prev}. \tag{6.5}$$

The change of the weight is given by the gradient $\frac{\partial E}{\partial w_j}$ and a constant γ, which regulates the learning speed. To avoid getting stuck in local minima of steep valleys or flat plateaus, a momentum term is added. It depends on the previous weight update and a constant term μ to steer the strength of the momentum term.

Special care needs to be taken during the training of a neural network to avoid an overtraining, which degenerates the generalisation ability of the classifier. The NeuroBayes package uses Bayesian regularisation techniques to enhance the generalisation ability of the network. Using a Bayesian minimisation technique involves a simultaneous minimisation of the network entropy and the network weights [146] to improve the generalisation ability of the NN. Hereby, insignificant connections between neurons or even full neurons that do not have significant connections are removed from the network. Thus, the number of free parameters of the minimisation problem are reduced. After a successful network training, the final network topology represents the optimal solution for the given training dataset.

6.1.4 Training Sample

To train the NN an example dataset needs to be presented to the network. In this analysis the training dataset is composed of simulated events only. The data-driven multijet

event model is not included in the training of the network. The available number of events of the model limits the possibility of an adequate training. To simulate the expected data as close as possible in the training dataset, the relative ratios of the simulated event samples are according to their theoretical expectation. But for a proper training, it is better to enhance the importance of the signal process in the training dataset such, that it consists of 50% signal and 50% background events. In doing so, the signal process is as important as all background processes together in the network training. The network gets 50% of the information to learn from the signal process and 50% from the background processes. Otherwise, the learning would be dominated by the background process information. The relative fractions among the background processes is according to their theoretical prediction. Selecting a random subset of the available simulated event sample of each process, whose amount corresponds to the relative ratios, has the problem that the MC sample with the smallest statistics limits the size of the training sample. To avoid the problem of dropping events, all available simulated events that pass the event selection are used to construct the training dataset. By introducing additional event weights for the different processes, the desired fractions are achieved. The advantage of this method is that all available events from the full phase-space are used instead of randomly dropping events. The composition of the training dataset in the 2-jet and 3-jet channel is presented in Tab. 6.1. In the training dataset, 12k and 9k signal events and 135k and 245k background events are available for the 2-jet and 3-jet channel, respectively. All simulated processes are

	2 jets			3 jets		
Process	Events	Σw	Fraction [%]	Events	Σw	Fraction [%]
Diboson	6075	3835	0.76	2953	3642	0.4
Z+jets	823	6828	1.4	530	8729	1.0
W+light jets	1646	33103	6.6	785	27117	3.2
W+c+ jets	7738	86406	17	1565	57261	6.8
$W + c\bar{c}/b\bar{b}$+jets	7468	70890	14	4332	87334	10.4
$t\bar{t}$	93707	39632	7.9	224246	206749	24.7
s-channel	15120	2590	0.5	6631	2429	0.3
Wt	2652	8782	1.7	3496	25699	3.1
$\sum$ Background	135229	252066	50	244538	418960	50
t-channel	12465	252066	50	9009	418960	50

Table 6.1: *Composition of the dataset used for the NN training. The relative composition of the signal to background events is 50:50. All background events are weighted according their expected rate. Here, the available number of simulated events, the sum of the event weights w and the relative fraction is given for the 2-jet and 3-jet dataset. The fraction of the background events refers to the sum of all background events.*

included separately in the training. The main contribution to the training sample stems from W + heavy flavour events and $t\bar{t}$ production.

6.2 Discriminating Variables

Many variables are considered as potential discriminators between the signal process and background processes. The emphasis is set to variables providing a good separation, which are well modelled in control regions. Quantities directly measured in the detector, as well as reconstructed objects are considered. Simple kinematic distributions like the p_T or η of the reconstructed jets or the charged lepton belong to the first category. More complex reconstructed properties to the second one. Such as the properties of the b-tagged jet. The event kinematics is described with variables combining several physics objects, like the reconstructed top-quark mass, $m_{\mathrm{T}}(W)$, invariant masses of the jets, and the transverse sum of all object momenta H_{T}. Angular variables between the reconstructed jets, the charged lepton, and $E_{\mathrm{T}}^{\mathrm{miss}}$ such as ΔR, $\Delta\phi$, $\Delta\eta$ are evaluated. In total, more than 80 variables were tested in each channel of the analysis. The best separating and well modelled variables were chosen as input to the neural network discriminant. Quantities, that do not add a significant improvement of the separation power to the network are not regarded.

6.2.1 Discriminating Variables in the 2-Jet Channel

Twelve variables are used in the neural network training of the 2-jet channel to discriminate between the t-channel signal and the background processes. The kinematic distributions of the discriminating variables are presented in Figs. 6.3 and 6.4. They are normalised to unit area for each process. It is advantageous for the network training to take the absolute value of symmetric distributions to increase the statistics in the bins of the variable used for the training. The reconstructed objects used to construct the discriminating variables are the b-tagged jet (b), the untagged jet (j), the charged lepton (ℓ), missing transverse momentum $E_{\mathrm{T}}^{\mathrm{miss}}$ the reconstructed neutrino (ν), and the reconstructed W boson (W). The reconstruction of the neutrino is described in Sec. 3.5.

- $\boldsymbol{m(\ell\nu b)}$: The four-vector of the top quark is reconstructed from the charged lepton, the neutrino, and the b-tagged jet of the event. The mass of the top quark is defined by the invariant mass of the three objects. Figure 6.3 (a) depicts the shape distributions of this variable for all processes. Signal events have a sharp peak around the top-quark mass. The distribution of top-quark events is broader due to the combinatorial ambiguity in the top-quark reconstruction of $t\bar{t}$ events. The other backgrounds peak at the threshold of the distribution around 110 to 120 GeV, due to the kinematic selection cuts on the jet, lepton and $E_{\mathrm{T}}^{\mathrm{miss}}$.

- $|\eta(j)|$: One of the main characteristics of the single top-quark t-channel process is that the light-quark jet is produced mainly in the forward direction. Thus, the distribution of the absolute value of the pseudorapidity of the untagged jet distinguishes the signal from background events. Figure 6.3 (b) shows the corresponding shapes for the signal and background processes. A good separation between the signal, the top-quark background and the W+jets background is evident. The untagged jet of the background processes is in the central region. The shape of the fake-lepton model is very similar to the signal shape. Thus, a separation between signal events and multijet events is difficult in this variable.
- $E_{\mathrm{T}}(j)$: The transverse energy of the untagged jet. A discrimination is possible between light jets from top-quark processes which have more transverse energy than light jets from multijet or W+jets backgrounds. The shape distributions are depicted in Fig. 6.3 (c).
- $|\Delta\eta(b, W)|$: The absolute value of the pseudorapidity difference between the b-tagged jet and the reconstructed W boson is shown in Fig. 6.3 (d). Here, the distributions of the top-quark processes are similar. A separation between those and the other background processes is possible. The $|\Delta\eta|$ between the W boson and b quark is smaller for events with a real top quark, since both objects originate from the top-quark decay. For W+heavy flavour events, the W and b quark are not correlated through the top-quark decay.
- $|\Delta\eta(j, b)|$: The absolute value of the pseudorapidity difference between untagged jet and b-tagged jet in the event. For the signal process, the b-tagged jet is expected to be centrally distributed. Together with the characteristic forward jet, a large η difference is expected. The $|\Delta\eta|$ distribution of the simulated background processes peaks at zero, because the jets are expected to be centrally distributed. Only a small separation is achievable between the signal and the multijet model with this variable. The shapes of the distributions are depicted in Fig. 6.3 (e).
- $p_{\mathrm{T}}(\ell)$: The p_{T} distribution of the charged lepton is depicted in Fig. 6.3 (f). A softer spectrum than the signal one is observed for the multijet background and W+light jet events. The other backgrounds show a slightly more energetic distribution.
- H_{T}: The scalar sum of the p_{T} of the jets, the charged lepton, and the $E_{\mathrm{T}}^{\mathrm{miss}}$. As shown in Fig. 6.4 (a) the distribution of top-quark background events peaks at 330 GeV, whereas the other backgrounds peak just below 200 GeV close to the threshold of the distribution due to the kinematic p_T cut on the objects. The peak of the signal process is in between the two classes of background.
- $m_{\mathrm{T}}(W)$: The transverse mass of the reconstructed W boson, which is reconstructed from the charged lepton and $\vec{E}_{\mathrm{T}}^{miss}$. The transverse mass is calculated according to Eqn. (3.8). Figure 6.4 (b) shows the discrimination between non-W events such as Z+jets and multijet events and those containing real W bosons.

The shapes of the signal events and the W+jets event classes are similar, whereas the top-quark background shape is broader due to the larger $E_{\mathrm{T}}^{\mathrm{miss}}$ of $t\bar{t}$ events.

- $\boldsymbol{\eta(\ell)}$: The pseudorapidity distribution of the charged lepton is shown in Fig. 6.4 (c). Charged leptons from top-quark decays show a central distribution, whereas the other backgrounds tend to have a flat pseudorapidity distribution.
- $\boldsymbol{m(b)}$: The mass of the four-vector of the b-tagged jet is depicted in Fig. 6.4 (d). A difference between b-jets from the top-quark decay which have a larger mass and b-tagged jets from W+jets events can be seen. The origin of this effect are light jets or c jets from the W+light jets and W+heavy flavour sample which are misidentified as a b-tagged jet.
- $\boldsymbol{E_{\mathrm{T}}^{\mathrm{miss}}}$: The reconstructed missing transverse momentum is shown in Fig. 6.4 (e). A difference can be clearly seen between events having fake $E_{\mathrm{T}}^{\mathrm{miss}}$, such as it is the case for non-W events as the multijet and the Z+jet background. Top-quark events tend to have a larger $E_{\mathrm{T}}^{\mathrm{miss}}$ than W+jet events. The signal process can also be distinguished from $t\bar{t}$ production which has a larger $E_{\mathrm{T}}^{\mathrm{miss}}$.
- $\boldsymbol{m(jb)}$: The invariant mass of the untagged jet and b-tagged in the event. Figure 6.4 (f) shows the shapes for the different processes. The resulting distribution depends on the underlying structure of the event. If the two jets stem from the same physical object, for example from a hadronically decaying W boson or Z boson, it is the invariant mass of the boson. In case of top-quark events a distribution with larger values is seen. In particular, the distribution of the signal process shows a broad peak featuring a long tail. Here, the invariant mass is constructed from two high-p_{T} objects having a large pseudorapidity difference. The light-jet of the signal process is characteristically scattered in the forward direction, whereas the b-tagged jet is produced centrally. For the W+jets background the invariant mass is smaller, since both jets stem from an initial state gluon radiation.

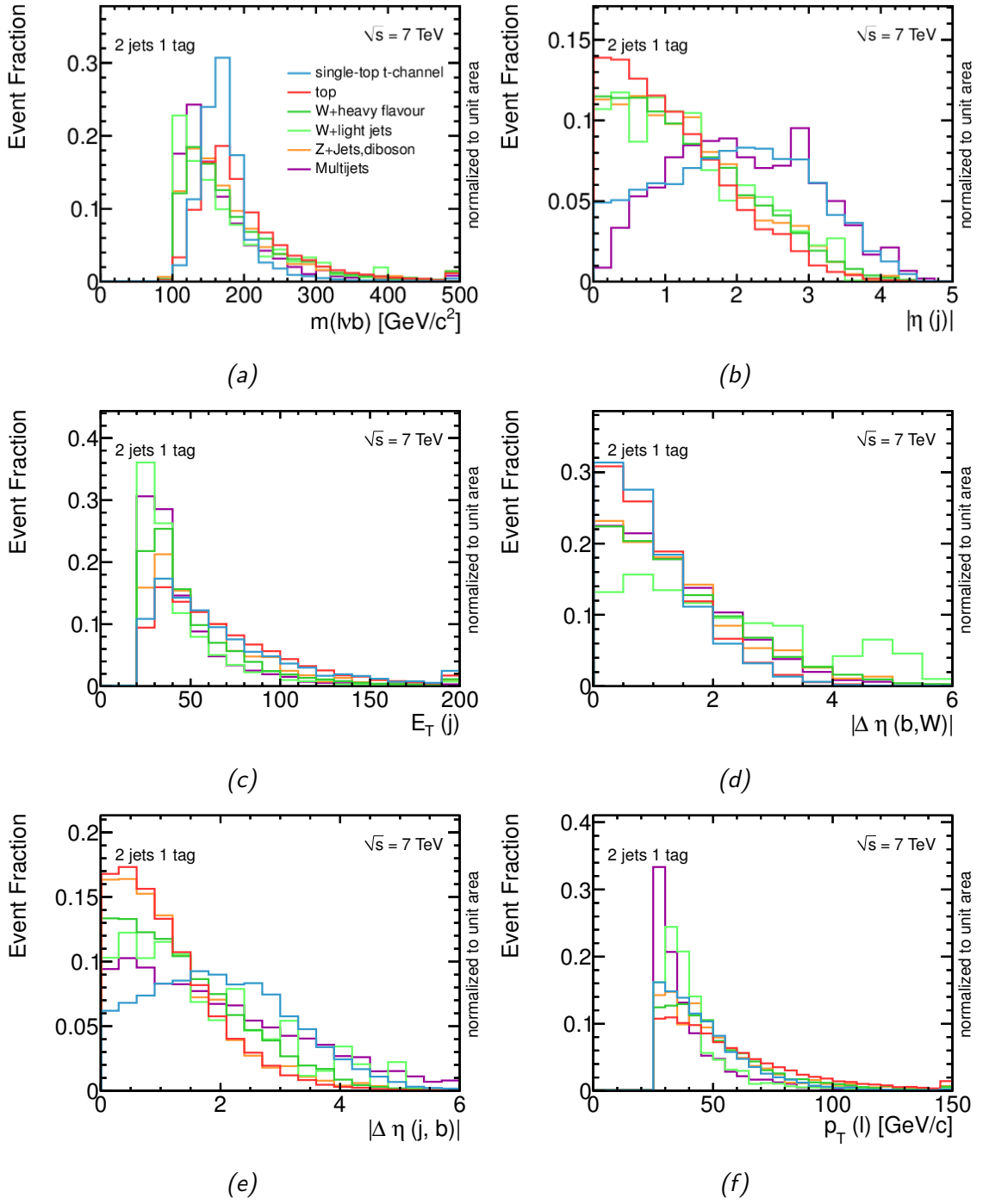

Figure 6.3: *Comparison of the kinematic distributions normalised to unit area of the different processes used for the NN training in the 2-jet channel. The reconstructed top-quark mass $m(\ell\nu b)$(a), the $|\eta|$ of the untagged jet (b), the transverse energy E_{T} of the untagged jet (c), the $|\Delta\eta|$ between the tagged jet and the reconstructed W boson (d), the $|\Delta\eta|$ between the untagged and tagged jet (e), and the p_{T} of the charged lepton (f).*

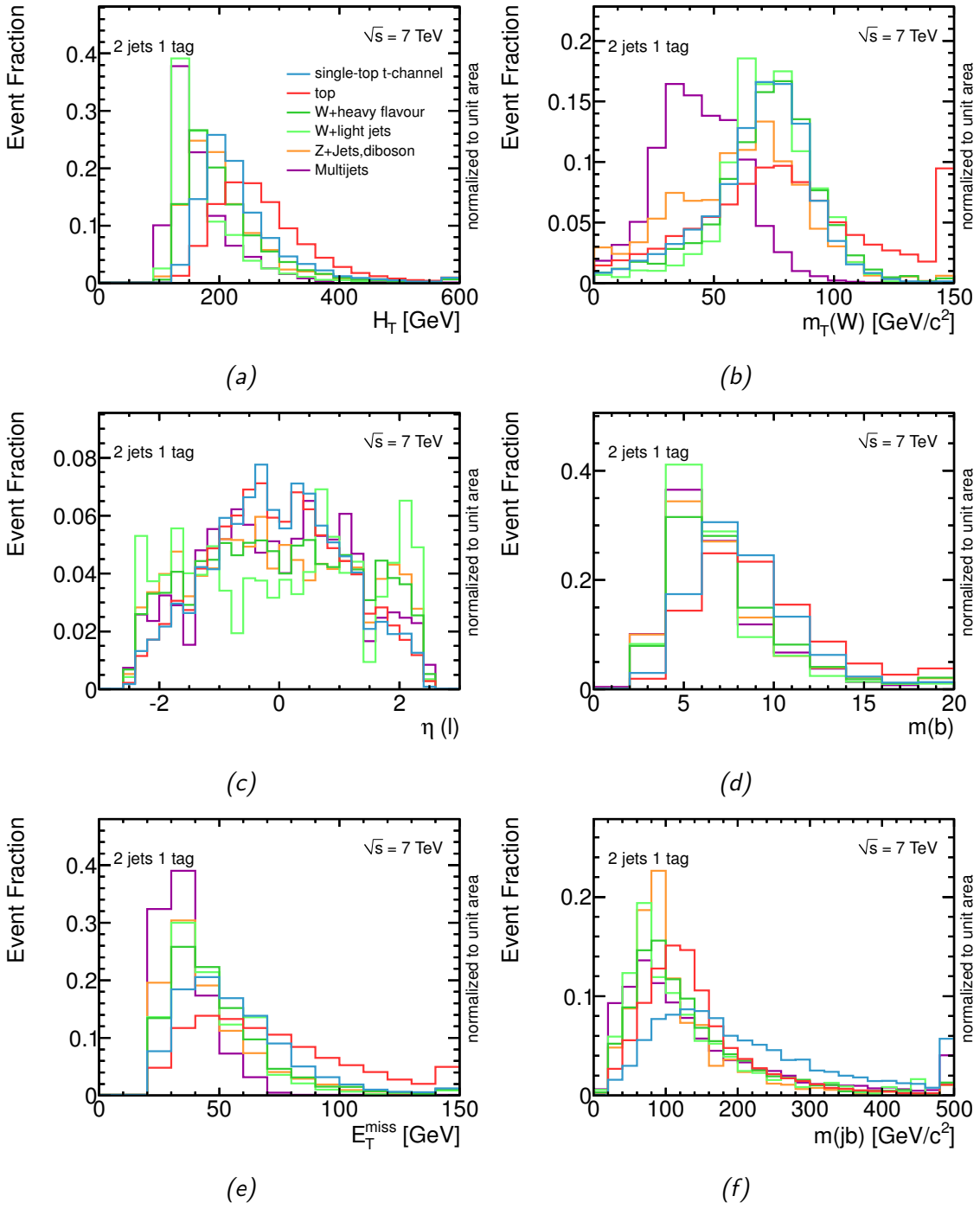

Figure 6.4: *Comparison of the kinematic distributions normalised to unit area of the different processes used for the NN training in the 2-jet channel. The scalar sum of the transverse momenta H_T of the jets, the charged lepton and the missing transverse momentum (a), the reconstructed transverse mass of the W boson (b), the pseudorapidity of the charged lepton (c), the mass of the four vector of the tagged jet (d), the missing transverse momentum (e), and the invariant mass of the tagged and untagged jet (f).*

6.2.2 Discriminating Variables in the 3-Jet Channel

In total, 18 variables are used in the neural network training of the 3-jet channel to discriminate between the t-channel signal and the background processes. The shapes of the kinematic distributions of the discriminating variables are presented in in Figs. 6.5, 6.6, and 6.7. The reconstructed objects used to construct the discriminating variables are the b-tagged jet (b), the charged lepton (ℓ), missing transverse momentum $E_{\mathrm{T}}^{\mathrm{miss}}$ the reconstructed neutrino (ν), the reconstructed W boson (W), and the jets. Jets are labelled according to their transverse momentum, the jet having the largest p_{T} is denoted as j_1, the second leading jet as j_2, and the jet with the smallest p_{T} as j_3.

- $\boldsymbol{m\left(j_1 j_2\right)}$: The invariant mass of the two jets having the largest and second largest p_{T} is depicted in Fig. 6.5 (a). For the signal process, a larger and broader distribution than for the backgrounds is observed. The background processes peak at approximately 100 GeV for the top-quark background and below for the other backgrounds.
- $\boldsymbol{m\left(\ell\nu b\right)}$: The reconstructed top-quark mass is shown in Fig. 6.5 (b). Signal events have a sharp peak around the top-quark mass. The distribution of top-quark background events is broader due to the combinatorial ambiguity in the top-quark reconstruction of $t\bar{t}$ events. The other backgrounds peak at much smaller values.
- $\boldsymbol{|\Delta\eta\left(j_1, j_3\right)|}$: The absolute value of the pseudorapidity difference between the jet having the largest and smallest p_{T} is shown in Fig. 6.5 (c). The background processes show a smaller $|\Delta\eta|$ than the signal process because the jets of the background processes are produced centrally.
- $\boldsymbol{|\Delta\eta\left(j_2, j_3\right)|}$: The absolute value of the pseudorapidity difference of the second leading and lowest p_{T} jet in the event is depicted in Fig. 6.5 (d). Background processes tend to have centrally produced jets. Thus, a discrimination of the signal is possible, which has a large $|\Delta\eta|$ due to the forward jet.
- $\boldsymbol{m_{\mathrm{T}}(W)}$: The transverse mass of the reconstructed W boson is shown in Fig. 6.6 (e).
- $\boldsymbol{H_{\mathrm{T}}}$: Scalar sum of the transverse momenta of the jets, the charged lepton and the missing transverse energy in the event is depicted in Fig. 6.5 (f).
- $\boldsymbol{|\Delta\eta(\ell, b)|}$: The absolute value of the pseudorapidity difference of the charged lepton and the b-tagged jet is shown in 6.6 (a). On average, events from top-quark background processes show a smaller pseudorapidity difference between the charged lepton and the b-tagged jet, than the other backgrounds. This is the case since the b-jet and charged lepton stem from the top-quark decay. Therefore, both are boosted in its direction.
- $\boldsymbol{|\Delta\eta\left(j_1, j_2\right)|}$: The absolute value of the pseudorapidity difference between the two jets having the largest and second largest p_{T} is depicted in Fig. 6.6 (b).

The signal process has a large opening angle between the two jets, whereas the background processes have a smaller one.

- $\boldsymbol{p_{\mathrm{T}}(\ell)}$: Transverse momentum of the charged lepton is presented in 6.6 (c).
- $\boldsymbol{\eta(\ell)}$: The pseudorapidity of the charged lepton is shown in Fig. 6.6 (d).
- $\boldsymbol{m(b)}$: The invariant mass of the b-tagged jet is depicted in Fig. 6.6 (e).
- $\boldsymbol{m(j_1 j_3)}$: The invariant mass of the jet having the largest and the smallest p_{T} in the event is shown in Fig. 6.6 (f). On average, the invariant mass has larger values for signal events than for the background events.
- $\boldsymbol{|\Delta\eta(b, W)|}$: The absolute value of the pseudorapidity difference between the b-tagged jet and the reconstructed W boson is shown in Fig. 6.7 (a).
- $\boldsymbol{\cos\theta^*}$: The cosine of the helicity angle of the W boson decay, where θ^* is defined as the angle between the momentum of the charged lepton in the W-boson rest-frame and the momentum of the W boson as seen in the top-quark rest-frame. It is shown in Fig. 6.7 (b).
- $\boldsymbol{E_{\mathrm{T}}^{\mathrm{miss}}}$: The reconstructed missing transverse energy is shown in Fig. 6.7 (c).
- $\boldsymbol{|\Delta\eta(\ell, j_3)|}$: The absolute value of the pseudorapidity difference between the charged lepton and the jet having the smallest transverse momentum is shown in Fig. 6.7 (d).
- $\boldsymbol{|\Delta\eta(\ell, j_2)|}$: The absolute value of the pseudorapidity difference between the second leading jet and the charged lepton (ℓ) is shown in Fig. 6.7 (e).
- $\boldsymbol{m(j_1 j_2 j_3)}$: The invariant mass of the three jets present in the event is shown in Fig. 6.7 (f). This variable shows a good separation power since the $t\bar{t}$ process events have a sharp peak around 200 GeV with a tail to larger values, whereas the other background processes have a broader peak at lower values. The signal process shows a harder distribution than the background processes with a large tail.

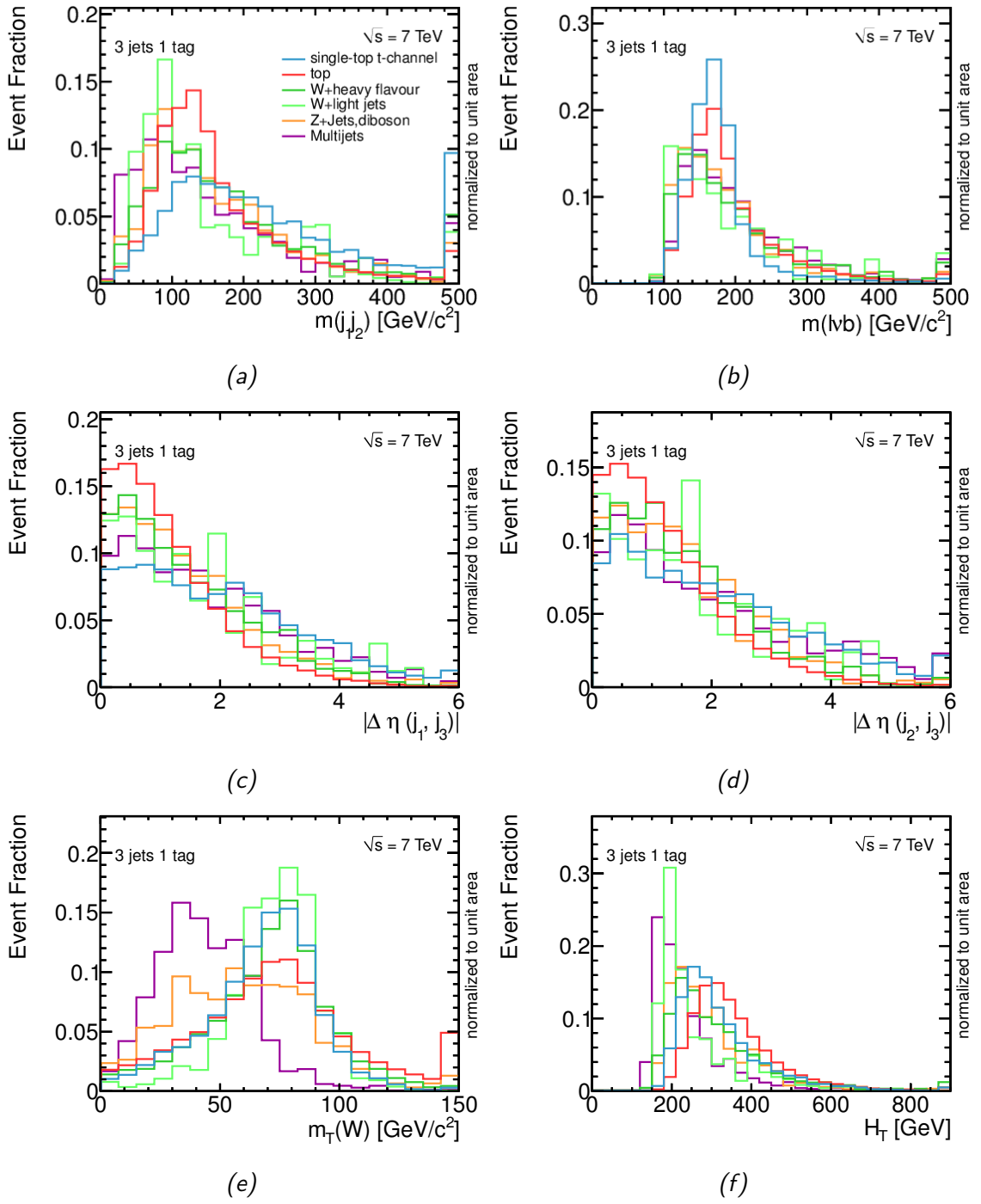

Figure 6.5: *Comparison of the kinematic distributions normalised to unit area of the different processes used for the NN training in the 3-jet channel. The invariant mass of the leading and second leading jet (a), the reconstructed top-quark mass $m(\ell\nu b)$ (b), the $|\Delta\eta|$ between the leading and third leading jet (c), the $|\Delta\eta|$ between the second and third leading jet (c) (d), the reconstructed transverse mass of the W boson (e), and the scalar sum of the p_T of the jets, the charged lepton, and the $\vec{E}_T^{miss}$ (f).*

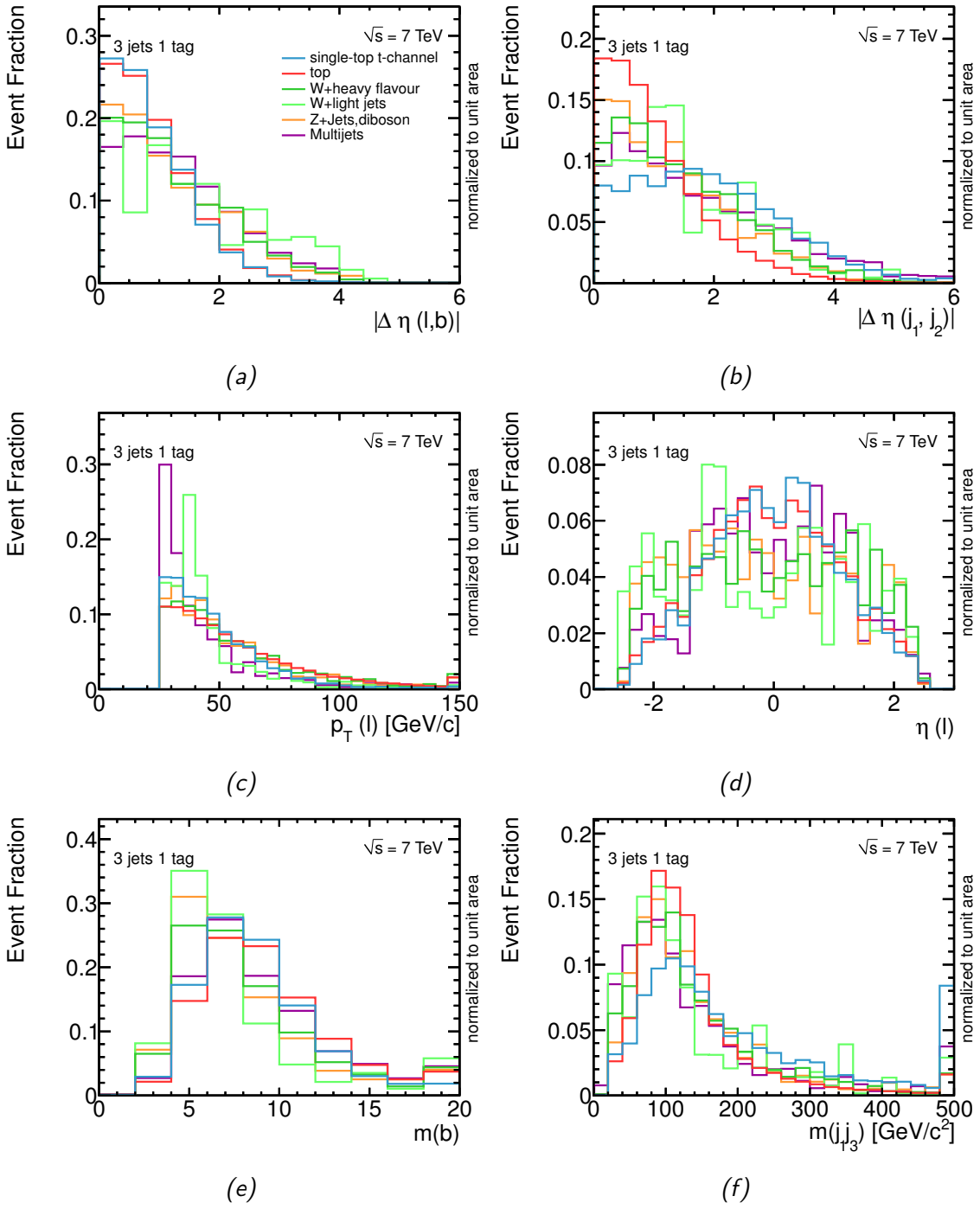

Figure 6.6: *Comparison of the kinematic distributions normalised to unit area of the different processes used for the NN training in the 3-jet channel. The $|\Delta\eta|$ between the charged lepton and the b-tagged jet (a), the $|\Delta\eta|$ between the leading and second leading jet (b), the p_{T} of the charged lepton (c), the η of the charged lepton (d), the invariant mass of the b-tagged jet (e), and the invariant mass of the leading and third leading jet (f).*

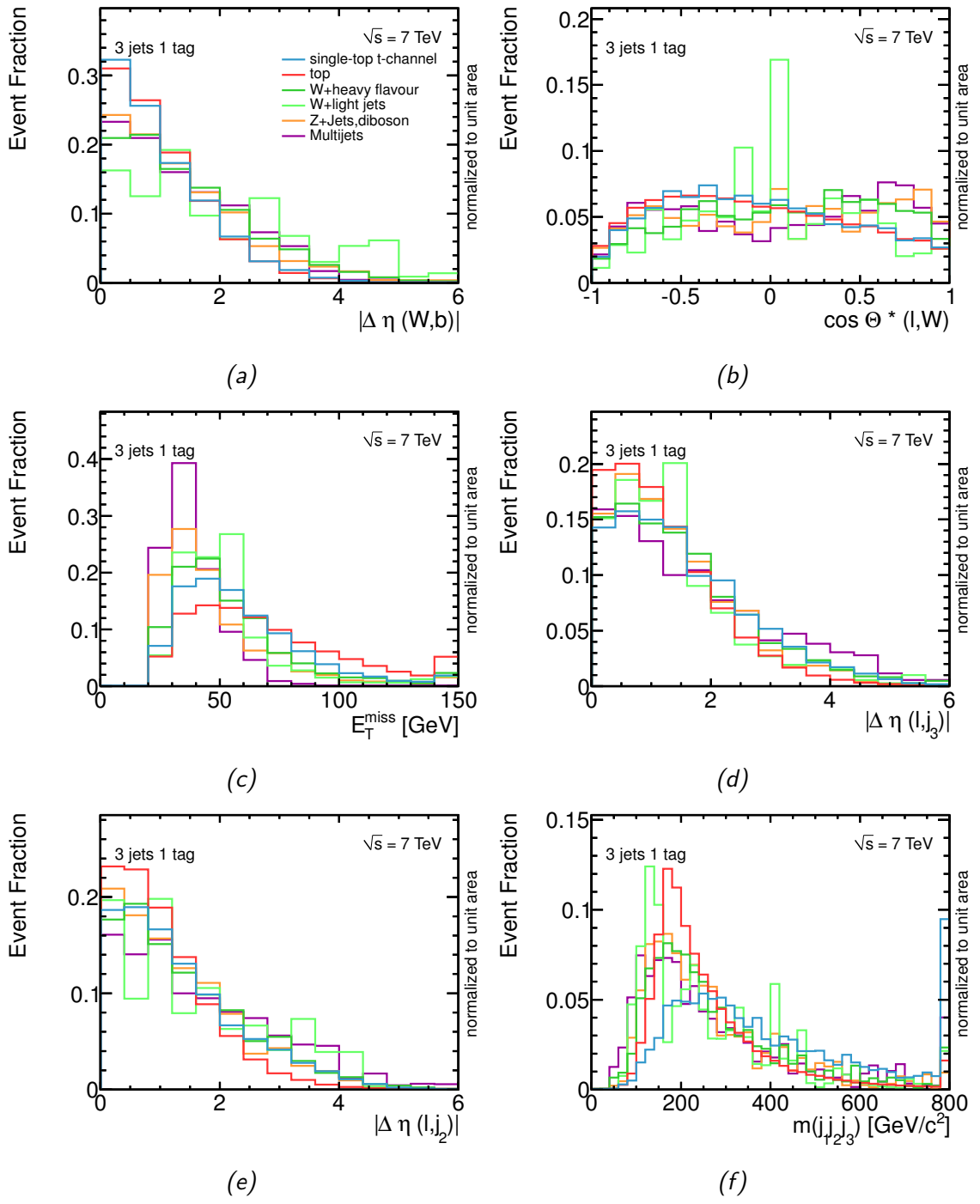

Figure 6.7: *Comparison of the kinematic distributions normalised to unit area of the different processes used for the NN training in the 3-jet channel. The $|\Delta\eta|$ between the reconstructed W boson and the b-tagged jet (a), the helicity angle of the W-boson decay (b), the missing transverse momentum (c), the $|\Delta\eta|$ between the charged lepton and the third leading jet (d), the $|\Delta\eta|$ between the charged lepton and the second leading jet (e), and the invariant mass the three jets in the event (f).*

6.3 Input Variable Validation

The input variables of a NN have to be checked carefully to ensure the reliability of the classification power of the NN. Thus, the event model is validated for each input variable in a control region. In this analysis, the pretag dataset, which is dominated by W+jets events, is chosen as control dataset. Here, the contribution of the signal process is insignificant compared to the number of background events. Since no requirement on a b-tagged jet is defined in the pretag dataset and many variables use the properties of the b-tagged jet, an alternative definition for a 'tagged jet' is necessary. The most central jet is used to model the b-tagged jet in the pretag dataset, because the signal process expects the jet originating from a b quark in the central region. To be compatible with the fiducial region of b-taggable jets, the central jet is required to be in the pseudorapidity range of $|\eta| < 2.5$.

To check the event model of the observables used as input to the NN it has to be compared to observed data. Thus, the shapes of the model are scaled to the theoretical prediction of each process and stacked on top of each other. The shape of the overall event model for a kinematic observable is checked against observed events by scaling the stacked histogram to the number of observed events, respecting the relative ratios of the processes. Deviations of the event model from the observed distributions have to be covered by the systematic uncertainty on the model description. For this check the uncertainty on the JES is chosen, because it involves the larges variations on the reconstructed four-vector of the jets and $E_{\mathrm{T}}^{\mathrm{miss}}$. The effect on the acceptance as well as on the shape of the distributions are considered when evaluating the JES uncertainty. Variables that do not show a reasonable modelling within this uncertainty are not used in the network training.

Exemplarily, three input variables of the 2-jet and 3-jet channel are depicted in Fig. 6.8. All input variables are documented in Appxs. B.1 and B.2. In general, good agreement between the distributions of collision events and the event model is found. A small mismodelling of the forward jet in the 2-jet channel, depicted in Fig. 6.8 (c) is visible in the region of $|\eta| \sim 3$. It is still covered by the JES, but as it is shown in section 7.3 an additional systematic uncertainty is introduced to account for this effect. Since neural networks also exploit the correlation information between the input variables, the correlation of the input variables are also checked. The correlation variable κ between the input variables i and j is defined as:

$$\kappa_{ij} = \frac{x_i - \bar{x}_i}{\sigma_{x_i}} \cdot \frac{x_j - \bar{x}_j}{\sigma_{x_j}} \tag{6.6}$$

The mean of the observable is denoted by $\bar{x}_i$ and the width by σ_{x_i}. Figure 6.9 shows the distributions of the correlation variable between the most important and the three next important variables for the 2-jet and 3-jet channel. The ranking of the input variables is discussed in the next section.

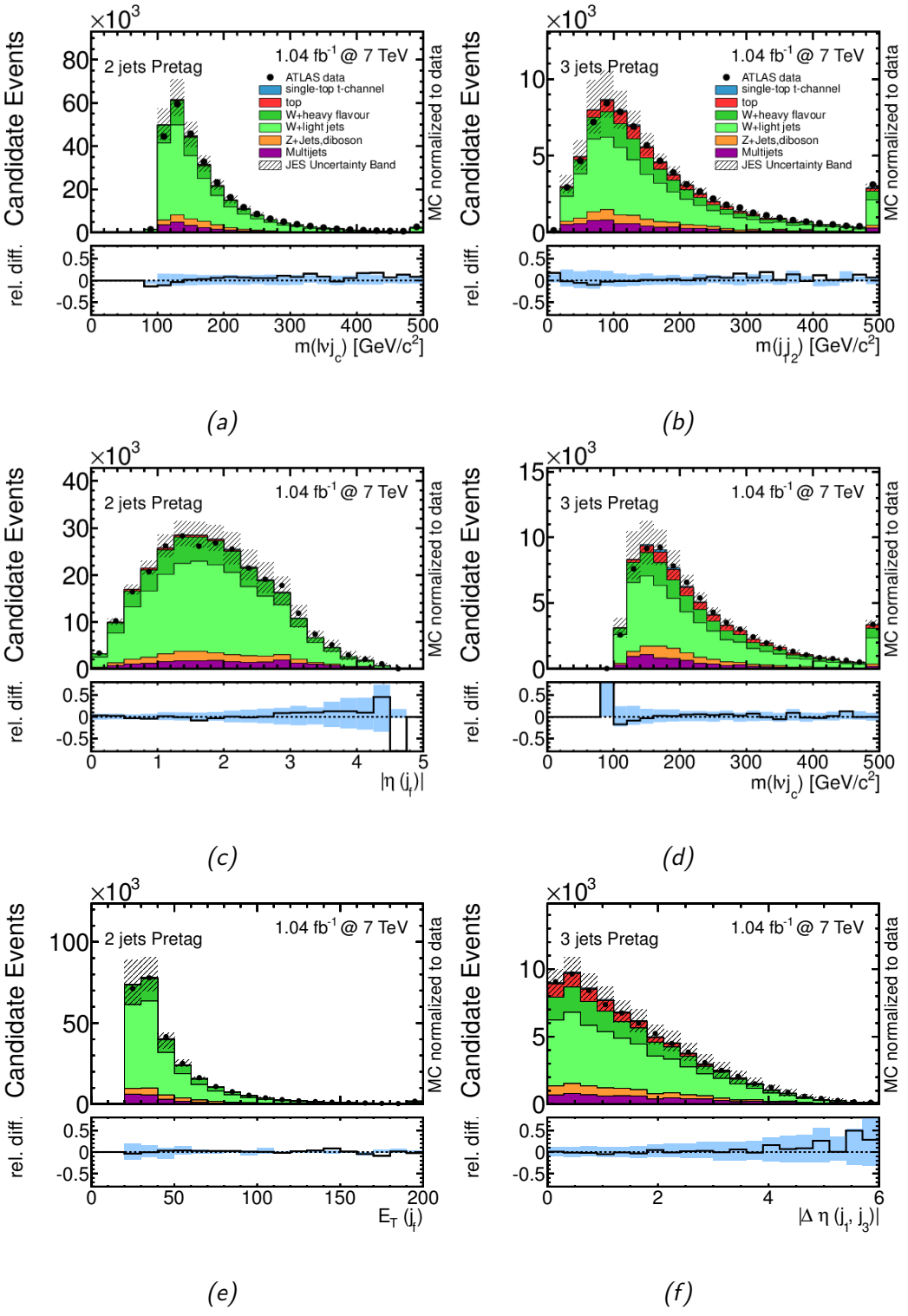

Figure 6.8: *Validation of the discriminating variables in the pretag dataset. The overall MC expectation is scaled to the number of observed data events by respecting the individual cross sections. The error band is due to the uncertainty of the JES for all MC processes. The reconstructed top-quark mass (a), the $|\eta|$ of the untagged jet (c), and the transverse energy of the untagged jet (e) of the 2-jet channel. The invariant mass of the leading and second leading jet (b), the reconstructed top-quark mass (d), and the $|\Delta\eta|$ of the leading and third leading jet (f) of the 3-jet channel.*

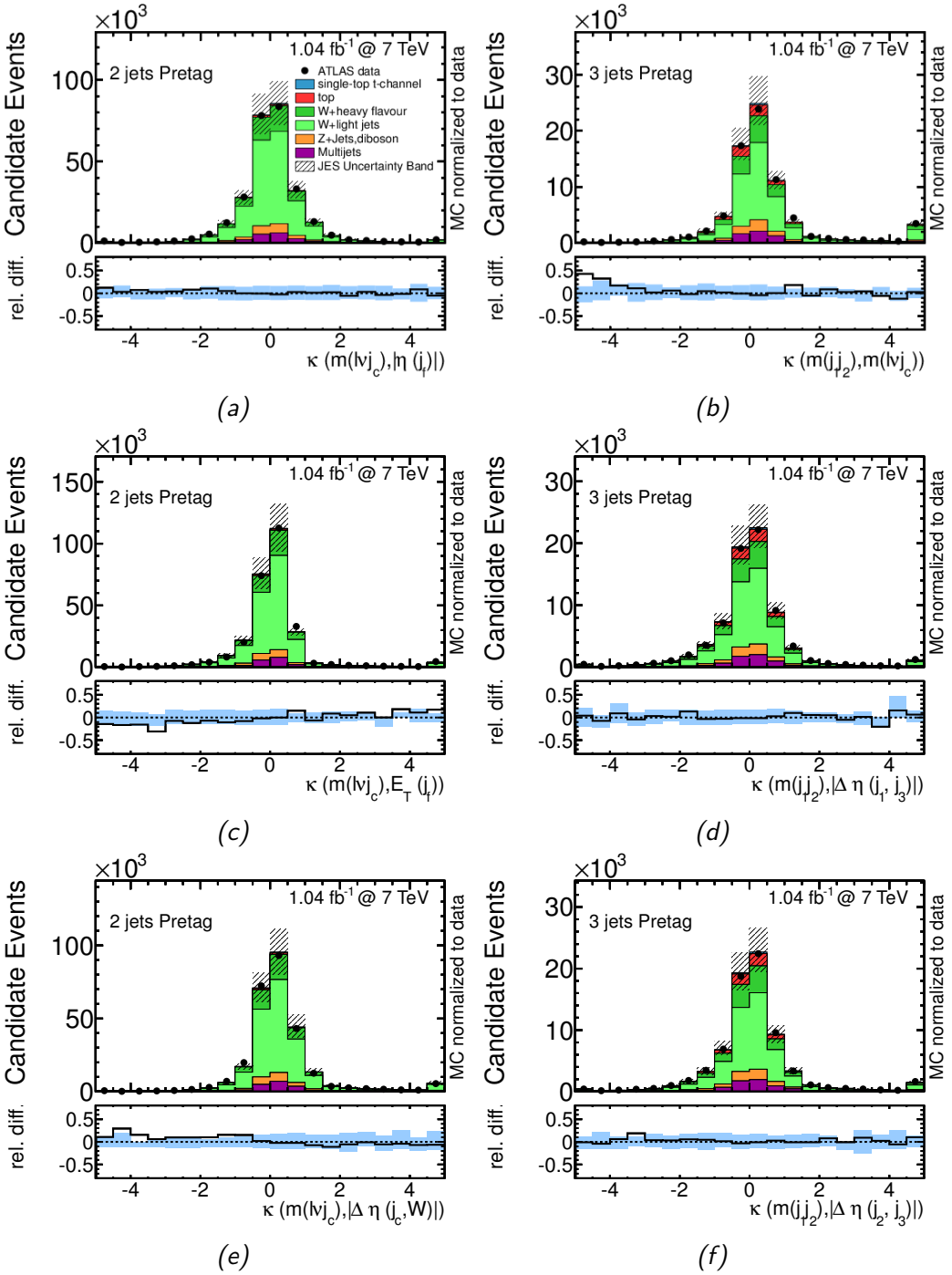

Figure 6.9: *Validation of the correlation between the discriminating variables in the pretag dataset. The overall MC expectation is scaled to the number of observed data events by respecting the individual cross sections. The error band is due to the uncertainty of the JES for all MC processes. In the 2-jet channel, the correlation between the reconstructed top-quark mass and the $|\eta|$ of the light jet (a), the transverse energy of the light jet (c), and the $|\Delta\eta|$ between the central jet and the reconstructed W boson (e) is shown. In the 3-jet channel the correlation between the invariant mass of the leading and second leading jet and the reconstructed top-quark mass, the $|\Delta\eta|$ between the leading and third leading jet (d), and the $|\Delta\eta|$ between the second and third leading jet (f) is shown.*

6.4 Result of the Neural Network Training

Two separate neural networks are trained for the 2-jet and 3-jet channel of the tagged dataset. The samples of simulated events are used to construct template distributions according to the network output of each process. Templates of processes that have a similar shape are combined to one template. For example the templates of the associated production and $t\bar{t}$ production are not distinguishable. Finally, five background templates plus one additional template for the signal sample are constructed. The background templates are W+heavy flavour jets, W+light jets, Z+jets and diboson, multijets, and the background processes involving the production of top quarks, as described in section 4.3.

The neural network infrastructure used for the training includes 33 hidden layer nodes. Studies have shown, that the number of hidden nodes does not influence the separation power of the network significantly. The parameters of the preprocessing are the same for all input variables. All input variables are flattened and smoothed by a regularised spline fit and decorrelated.

The preprocessing procedure provides a ranking of the input variables by their importance for the separation power of the network. The separation power is expressed in terms of the correlation of the input variables to the training target of the classification problem. Table 6.2 provides an overview of the variable ranking for the 2-jet (a) and 3-jet (b) channel training, respectively. The quantity used for the variable ranking is the significance σ, which is determined from the iterative method described in section 6.1.1. It expresses the additional gain of the network in terms of correlation to the training target by including this variable. The correlation of each individual variable to the training target is given by the significance of this single variable σ_{only}. In general, the variable with the largest significance is the most important of the network training. It might happen, if two variables that have a large individual significance but are highly correlated do appear in the ranking as most important and least important variable. Thus, the loss of significance σ_{loss} of each variable is given when it is removed from the training sample. The global correlation κ to all other variables has a big influence on the ranking of the input variables. For example, in the training of the 2-jet channel $|\eta(j)|$ and $m(jb)$ have a similar individual correlation to the training target, but $m(jb)$ is the least important, whereas $|\eta(j)|$ is the second most important variable. The reason for this is the loss of information if one of the two variables is removed from the training. Due to the large correlation to the other variables, the information loss by removing $m(jb)$ is much smaller than by removing $|\eta(j)|$.

The result of the training is depicted in Fig. 6.10. The shape distributions of the neural network output are shown in Fig. 6.10 (a) for the two jet and Fig. 6.10 (b) for the 3-jet channel of the tagged dataset. A validation of the neural network classifier is done in the pretag dataset. It is shown in Fig. 6.10 (c) and Fig. 6.10 (d) for the two analysis channels. The agreement between the shape of the observed and simulated event distribution is acceptable within the uncertainty of the JES. The event model of the

tagged dataset is shown in Fig. 6.10 (e) and Fig. 6.10 (f) in the 2-jet and 3-jet channel. The event model of the different processes is normalised to their expected event yield of Tab. 5.4. As it is shown in the next chapter, the overall normalisation of the signal and background processes is derived from a combined binned maximum-likelihood fit of the NN shape distributions to the observed data. A normalisation of the W+light jets and W+heavy flavour jets background from observed data is necessary since the theoretical predictions are associated with a large uncertainty.

Variable	σ	σ_{only}	σ_{loss}	κ
$m(\ell\nu b)$	264	264	159	39
$\lvert\eta(j)\rvert$	206	244	111	62
$E_{\text{T}}(j)$	136	140	54	72
$\lvert\Delta\eta(b,W)\rvert$	86	157	66	44
$\lvert\Delta\eta(j,b)\rvert$	97	206	41	83
$p_{\text{T}}(\ell)$	71	85	52	38
H_{T}	63	190	39	63
$m_{\text{T}}(W)$	59	89	62	32
$\eta(\ell)$	53	115	52	36
$m(b)$	47	147	38	49
$E_{\text{T}}^{\text{miss}}$	37	94	39	39
$m(jb)$	26	249	26	86

(a)

Variable	σ	σ_{only}	σ_{loss}	κ
$m(j_1j_2)$	246	246	60	93
$m(\ell\nu b)$	225	222	122	43
$\lvert\Delta\eta(j_1,j_3)\rvert$	213	252	54	87
$\lvert\Delta\eta(j_2,j_3)\rvert$	137	227	63	82
$m_{\text{T}}(W)$	126	150	89	31
H_{T}	113	138	82	41
$\lvert\Delta\eta(\ell,b)\rvert$	86	121	34	69
$\lvert\Delta\eta(j_1,j_2)\rvert$	74	277	80	75
$p_{\text{T}}(\ell)$	68	158	67	41
$\eta(\ell)$	69	116	61	30
$m(b)$	44	105	44	24
$m(j_1j_3)$	37	234	39	93
$\lvert\Delta\eta(b,W)\rvert$	33	108	33	68
$\cos\theta^*$	28	63	30	26
$E_{\text{T}}^{\text{miss}}$	30	89	29	30
$\lvert\Delta\eta(\ell,j_3)\rvert$	29	101	30	58
$\lvert\Delta\eta(\ell,j_2)\rvert$	16	66	16	46
$m(j_1j_2j_3)$	15	315	15	97

(b)

Table 6.2: *The ranking of the 12 input variables of the 2-jet channel (a) and the 18 input variables of the 3-jet channel (b), which are used in the neural network training ordered by their importance. The significance σ is the gain in total correlation to the training target by adding the n-th variable to the existing set of (n-1) variables. If this variables is removed from the set of input variables, the loss is given by σ_{loss}. The correlations of each individual variable to the training target is denoted by σ_{only} and κ gives the correlation of each variable to the others. .*

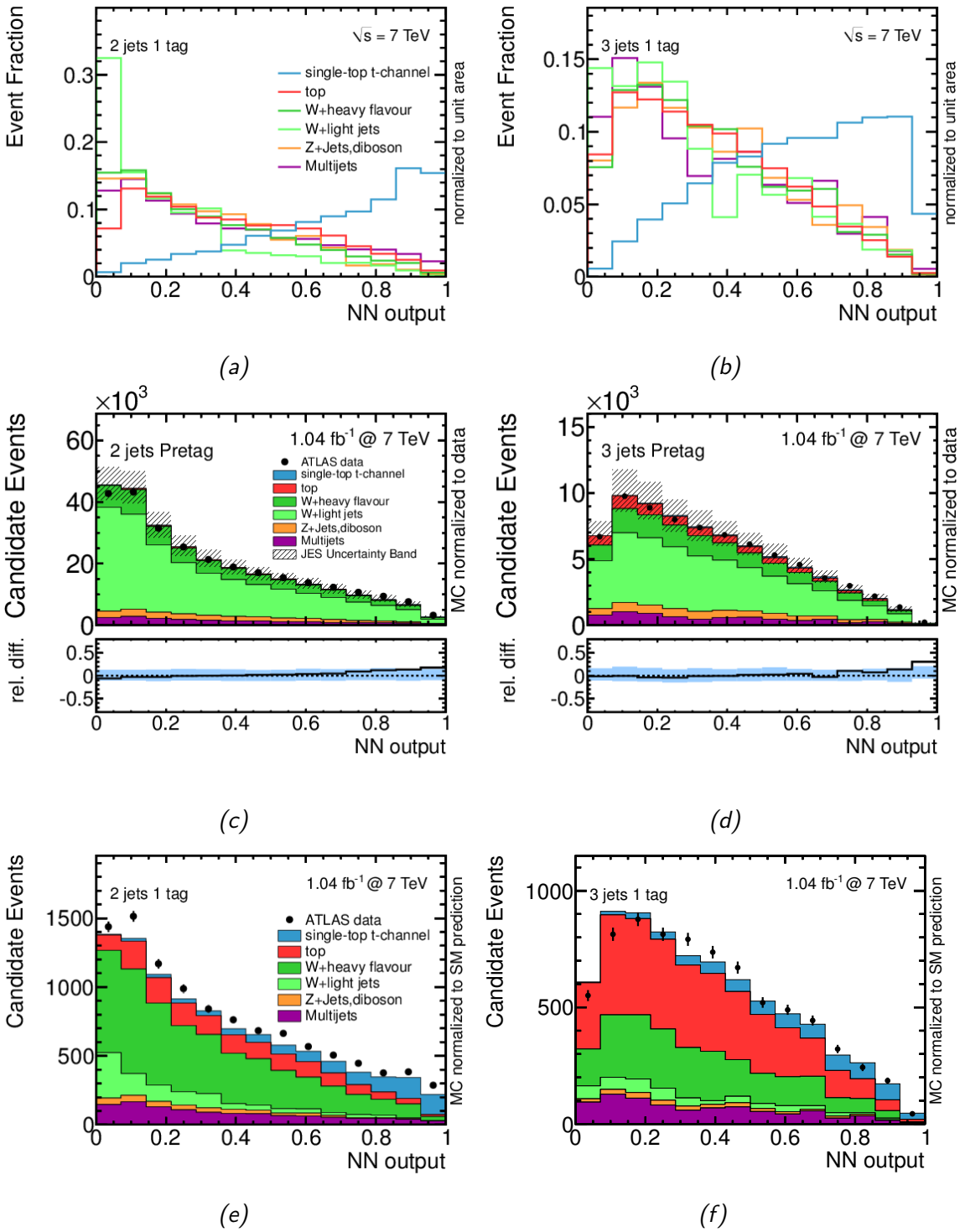

Figure 6.10: *Result of the network training. The shapes of the NN output distribution are shown in (a) for the 2-jet channel and (b) for the 3-jet channel of the tagged dataset. A validation of the classifier is done in the pretag dataset, by scaling the overall MC expectation to the number of observed events, by respecting the individual cross sections. A comparison of the event model and observed events is shown in (e) and (f) for the two channels in the tagged dataset. The MC model is normalised to the SM expectation.*

Chapter 7

Analysis

The aim of the analysis is the measurement of the t-channel single top-quark production cross-section. A binned maximum-likelihood fit of the NN output distribution templates to the observed data is used to extract the number of signal events. A crucial part of the analysis is the identification and evaluation of the impact of systematic uncertainties on the cross-section measurement. They affect the number of expected events and the shape of the template distributions of each process. Different sources of systematic uncertainties due to residual differences between MC simulations and observed data, as well as the modelling of the signal and background processes are discussed. In this chapter, the statistical methods used in this analysis are introduced. The method of a binned maximum-likelihood fit is explained, as well as the treatment of the systematic uncertainties using a frequentist method. Additionally, the statistical significance of the measurement is evaluated using a hypothesis test based on a likelihood ratio. The final result of the cross-section measurement including the impact of the different systematic uncertainties is presented.

7.1 Statistical Methods

In this section, the mathematical formulation of the likelihood function used to fit the template distributions to the observed data is explained. Additionally, the treatment of the impact of the systematic uncertainties on the shape of the NN output distributions, as well as on the normalisation of the different processes is illustrated. The statistical significance of the measurement is derived from a hypothesis test based on a likelihood-ratio technique.

7.1.1 Binned Likelihood Function

The number of observed single-top t-channel events is determined by a binned maximum-likelihood fit of the NN output distributions to the distribution of observed data. In practise, MINUIT [147] is used to minimise the negative log-likelihood function. Two parts build the likelihood function. First, a product of Poisson terms with each single term reflecting the probability to observe n_k events in bin k of the histogram with M

bins. The second part contains Gaussian terms to constrain the normalisation of the background processes due to prior knowledge:

$$L(\beta^s;\beta_1^b,\ldots,\beta_B^b) = \prod_{k=1}^{M} P(n_k;\mu_k) \cdot \prod_{j=1}^{B} G(\beta_j^b;1.0,\Delta_j). \tag{7.1}$$

The parameters of the likelihood function are the scale factors β^s for the signal process and β_j^b for each of the background processes j. The number of background processes is labelled by B. The scale factors are varied by MINUIT in the fit to the observed data such, that they minimise the log-likelihood function. They are the ratio of the observed cross-section $\sigma^{s,b}_{\text{obs},j}$ to the expected cross-section $\sigma^{s,b}_{\text{SM},j}$, defined as $\beta_j^{s,b} = \sigma^{s,b}_{\text{obs},j}/\sigma^{s,b}_{\text{SM},j}$. A value of $\beta = 1$ corresponds to the SM expectation. The Poisson term of the likelihood function in the bin k is defined by:

$$P(n_k;\mu_k) \;=\; \frac{e^{-\mu_k}\cdot\mu_k^{n_k}}{n_k!}. \tag{7.2}$$

Hereby, μ_k denotes the number of expected events and n_k the number of observed data events in the bin k. The number of expected events is given by the sum over the expected number of background events μ_{jk}^b for each background process j plus the number of expected signal events μ_k^s:

$$\mu_k = \mu_k^s + \sum_{j=1}^{B}\mu_{jk}^b\,, \quad \mu_k^s = \beta^s\cdot\tilde{\nu}^s\cdot\alpha_k^s\,, \quad \text{and} \quad \mu_{jk}^b = \beta_j^b\cdot\tilde{\nu}_j^b\cdot\alpha_{jk}^b\,. \tag{7.3}$$

The number of predicted events is denoted by $\tilde{\nu}^s$ for the signal process and $\tilde{\nu}_j^b$ for each background process j. The fraction of events in each bin of the histogram is defined by the template fraction α_k^s for the signal process and α_{jk}^b for the background processes j. Each template distribution needs to obey the normalisation condition $\sum_{k=1}^{M}\alpha_k^{s,b} = 1$.

To improve the robustness of the fit, Gaussian penalty terms limit the variation of the background scale factors β^b to account for a-priori knowledge on the background rates:

$$G(\beta_j^b;1.0,\Delta_j) \;=\; \frac{1}{\sqrt{2\pi\Delta_j^2}}\cdot\exp\frac{-\left(\beta_j^b-1\right)^2}{2\Delta_j^2}. \tag{7.4}$$

Those Gaussian priors have a mean of one and a width of Δ_j, which is the relative uncertainty on the production cross-section of the background processes.

7.1.2 Treatment of Systematic Uncertainties

A frequentist approach is used to evaluate the effect of systematic uncertainties on the precision of the cross-section measurement. Variations on the shape of the neural network template distributions, as well as on the acceptance of the signal and background processes are considered. In pseudo-experiments, those effects are estimated by creating a set of pseudo-data with variations according to the systematic shifts, following the idea of Refs. [148, 149]. The whole set of pseudo-experiments is interpreted as the available phase space due to the systematically limited knowledge of nature. In each set of pseudo-data, randomly altered by the systematic variations, the signal measurement is performed to obtain an estimator β^s of the possible outcomes of the signal measurement. The expected uncertainty on the cross-section measurement is the root-mean-square (RMS) of the β^s-distribution of the pseudo-experiments using the predicted cross-sections as input. The uncertainty on the actual measurement is estimated by using the scale factors $\hat{\beta}$ after the fit to observed data for the generation of the pseudo-data.

Cross-Section Uncertainties

In each pseudo experiment, the expectation values of the backgrounds $\tilde{\nu}_j$ are randomly varied according to a multiplicative factor β_j^{gen} following a log normal distribution:

$$\mathcal{N}\left(x;\mu,\sigma\right) \;=\; \frac{1}{x\sqrt{2\pi\sigma^2}}\exp\left\{\frac{-\left(\ln x-\mu\right)^2}{2\sigma^2}\right\} \tag{7.5}$$

Using a log-normal distribution has the advantage of avoiding unphysical negative expectation values for the background processes by construction. A Gaussian prior by contrast does not avoid negative values for the expected event yield. To obtain a log-normal distribution having an expectation value of one and a variance of Δ_j by choosing the parameters $\mu = -\sigma^2/2$ and $\sigma^2 = \ln(\Delta_j^2 + 1)$. For the cross-section measurement, the β^s of the signal process is not varied according to its theoretical uncertainty, since the signal cross-section is measured. The systematic uncertainties on the cross-section measurement are evaluated exactly at the predicted cross-section.

Monte Carlo Statistics

To take into account the limited amount of simulated events, the template distributions are morphed according to the statistical uncertainty on the number of simulated events in each bin, following a Gaussian distribution.

Acceptance Uncertainties

Each systematic variation i of a process alters its acceptance. The systematic shifts are denoted by ϵ_{ij+} for an upward and ϵ_{ij-} for a downward variation of the acceptance

of the signal and background processes j. Those are included by varying the expectation values $\tilde{\nu}^s$ and $\tilde{\nu}_j^b$ accordingly for each source of systematic uncertainty i. The total number of considered systematic uncertainties is S. This is done by drawing a random number δ_i from a Gaussian distribution with mean of zero and width of one for each source of systematic uncertainty in each pseudo experiment. The constant values of ϵ_{ij+} and ϵ_{ij-} correspond to the one-sigma deviation from the nominal expectation value and the random value δ_i is equal to the strength of the variation in the pseudo experiment. The altered expectation value used for the generation of a pseudo experiment is given by:

$$\nu_j^{\text{gen}} = \tilde{\nu}_j \cdot \beta_j^{\text{gen}} \cdot \left\{ 1 + \sum_{i=1}^{S} |\delta_i| \cdot \left(\cdot H(\delta_i) \cdot \epsilon_{ij+} + H(-\delta_i) \cdot \epsilon_{ij-} \right) \right\}. \tag{7.6}$$

Hereby, H denotes the Heaviside step function, to define whether an upward or downward fluctuation of the systematic i is generated in the pseudo experiment. The β_j^{gen} are randomly drawn from a log-normal distribution as explained before. Finally, the number of events n_j for each process in the pseudo experiment is drawn from a Poisson distribution with mean ν_j^{gen}.

Shape Uncertainties

Systematic effects on the shapes of the NN output distribution α_{jk} are gained by evaluating the NN with the systematically altered event model. Thus, a new set of shapes α_{jk}^+ and α_{jk}^- for the upward and downward shift is obtained for all processes and each systematic uncertainty. To include the systematic shifts on the shape of the classifier, new template distributions α_{jk}^{gen} are generated. A linear interpolation between the nominal shape and the systematically shifted shape is done in each pseudo experiment. The strength of the shift is given by the random value δ_i, which is 100% correlated to the strength of the acceptance variation for each systematic i. The new, generated shape is given by:

$$\alpha_{jk}^{\text{gen}} = \alpha_{jk} + \sum_{i=1}^{S} |\delta_i| \cdot \left\{ (\alpha_{jki}^+ - \alpha_{jk}) \cdot H(\delta_i) + (\alpha_{jki}^- - \alpha_{jk}) \cdot H(-\delta_i) \right\}. \tag{7.7}$$

The distribution of the process j in the pseudo experiment is gained by drawing n_j events from the new shape α_{jk}^{gen}, including the systematic shifts with random strength.

7.1.3 Hypothesis Testing

A hypothesis test needs to be carried out, to determine the significance of the cross-section measurement. It will answer the question, if the observed signal events are significantly distinguishable from a background fluctuation. Thus, two hypotheses are investigated. The null hypothesis H_0 assumes, that the signal process does not exist.

The alternative hypothesis H_1 assumes, the production of the signal process with the predicted rate of the SM. In both cases, an ensemble test is carried out to determine the probability of the observed signal events being only a background fluctuation. Additional to all sources of systematic uncertainties, the theoretical uncertainty on the cross-section of the signal process is included in each ensemble. The pseudo-data of H_0 does not include the signal process, whereas it is included in the ensemble data of H_1. According to the Neyman-Pearson lemma [150], a likelihood-ratio test is the most powerful test statistic:

$$Q = -2 \cdot \ln \frac{L\left(\beta^s = 1; \hat{\beta}_1^b, \ldots, \hat{\beta}_B^b\right)}{L\left(\beta^s = 0; \hat{\hat{\beta}}_1^b, \ldots, \hat{\hat{\beta}}_B^b\right)} \tag{7.8}$$

To construct the quantity Q of the hypothesis test, the likelihood function is fitted twice to each ensemble test, first by including the signal process in the fit by setting $\beta^s = 1$ and second by only fitting the background process templates using $\beta^s = 0$. The values $\hat{\beta}_j$ and $\hat{\hat{\beta}}_j$ are the observed results of each background process j. The significance is obtained from the overlap of the two Q-value distributions, q_0 for the null-hypothesis and q_1 for the alternative hypothesis, defined by the p-value:

$$p\left(Q_0\right) = \frac{1}{I_q} \int_{-\infty}^{Q_0} q_0\left(Q'\right) dQ', \tag{7.9}$$

$$I_q = \int_{-\infty}^{\infty} q_0(Q') dQ'. \tag{7.10}$$

The p-value is the fraction of pseudo-experiments of the q_0 distribution in the range of $-\infty$ to Q_0. For the expected p-value, Q_0 is defined as the median of the q_1 distribution. In case of the observed p-value, it is the Q-value of the likelihood fits to the observed data. Under the assumption that H_1 is correct, an observed p-value smaller than p is found with a probability of 50%.

Commonly, the significance of a method is expressed in terms of standard deviations σ of a normal distribution, which is comparable to the probability of rejecting the null hypothesis although it is true. It is the one sided integral of the Gaussian distribution:

$$\sigma = \sqrt{2} \cdot \mathrm{Erf}^{-1}\left(1 - 2 \cdot \left(1 - p\right)\right), \tag{7.11}$$

$$\mathrm{Erf} = \frac{2}{\sqrt{\pi}} \int_0^z e^{-t^2} dt, \tag{7.12}$$

Two numerical values are of vital importance. An evidence for a signal process is claimed for an observed significance of 3σ. This corresponds to $p < 1.35 \cdot 10^{-3}$. One speaks of an observation of a signal process, if the significance of the measurement exceeds 5σ with a p-value smaller than $2.87 \cdot 10^{-7}$.

7.2 Result of the Binned Likelihood Fit

As a result of the fit the scale factors $\hat{\beta}^s$ of the signal process and $\hat{\beta}^b_j$ of the background processes j , which minimise the likelihood function, are obtained. The whole NN output distribution is used in the fit to exploit the background enriched region to constrain the rates of the background processes in conjunction with the signal measurement. Using the 2-jet and 3-jet channel in a simultaneous fit adds additional constraints to the background processes due to the different composition of the backgrounds. Since the background from top-quark events is the dominant one in the 3-jet channel, it adds an additional constraint to the rates of the top-quark background in the 2-jet channel. Prior knowledge on the background rates is added to the fit by including the Gaussian constraints Δ_j shown in Tab. 7.1 for the different processes. The constraints of Z+Jets, diboson and top-quark processes are taken from the theoretical prediction, whereas the constraints on the W+heavy flavour and W+light jets is taken from the uncertainties found in an auxiliary measurement [141]. Since the multijet background yield was already measured in the signal region by the $E_{\mathrm{T}}^{\mathrm{miss}}$-fit described in section 5.2 it is set to this result and is not varied in the fit.

To check the consistency of the binned maximum-likelihood fit, a linearity check is implemented. Technically, this is done by constructing sets of pseudo data using the expected SM rates of the background processes but different scale factors β^S_{input} for the signal process, which are varied between 0.4 and 1.6 for each pseudo dataset. A com-

Background Process	Δ_j
W+heavy flavour	0.50
W+light jets	0.30
Z+jets, diboson	0.60
top	0.087
Mulitjets	fixed

Table 7.1: *The relative uncertainties Δ_j on the background processes are applied as Gaussian constraints in the binned likelihood fit. The constraints on the Z+Jets, diboson, and top-quark processes are taken from the theoretical prediction. W+heavy flavour and W+light jets processes are constrained by the results of auxiliary measurements [141]. Moreover, the multijet background is set to the result of the $E_{\mathrm{T}}^{\mathrm{miss}}$-fit and not varied.*

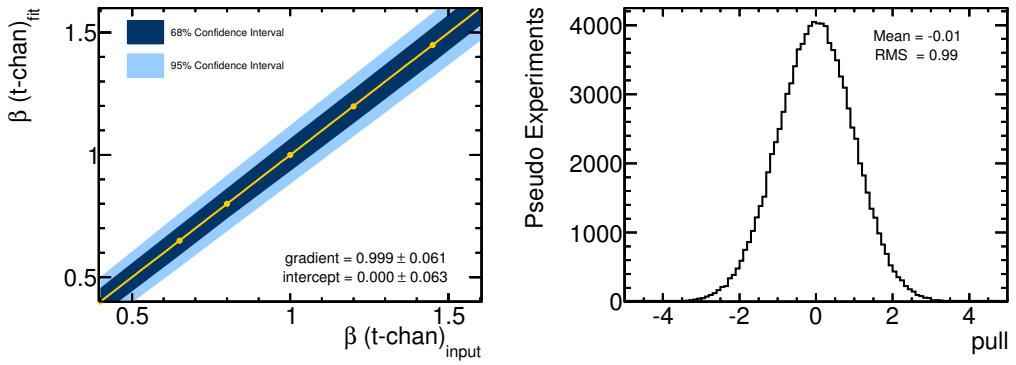

(a) *(b)*

Figure 7.1: *Linearity check of the fit (a). Different expected cross-sections for the t-channel signal process are compared with the fit result. The input cross-section β^s_{input} is varied between 0.4 and 1.6 of the SM expectation. It shows the expected linear dependence. The pull distribution (b) for the scenario with the SM expectation. The pull is defined as $(\beta^s_{\text{fit}} - \beta^s_{\text{input}})/\Delta\beta^s_{\text{fit}}$.*

parison of the signal scale factor used in the pseudo dataset and the result β^S_{fit} obtained by the fit is shown in Fig. 7.1 (a). In the tested range, a perfect linear behaviour of the fit without any bias is found. Also the 68% and 95% C.L. intervals of the pseudo experiments are shown, which are of statistical nature only.

As additional check for a bias, the average deviation of the β^S_{fit} from the true β^S_{input} of the pseudo experiments is tested. For this purpose, the pull distribution is defined:

$$\text{pull}(\beta^s_{\text{fit}}) \quad = \quad \frac{\beta^s_{\text{fit}} - \beta^s_{\text{input}}}{\Delta\beta^s_{\text{fit}}}. \tag{7.13}$$

The statistical uncertainty on the fit result is denoted by $\Delta\beta^s_{\text{fit}}$. An unbiased method expects the pull distribution to be a Gaussian distribution with mean zero and width one. A pull distribution for the SM scenario assuming a $\beta^s_{\text{input}} = 1$ is shown in Fig. 7.1 (b). The pull distribution shows that the fit does not induce a bias. A width of one proofs, that the average deviation of the fit result from the input is compatible with the statistical uncertainty of the fit.

Table 7.2 presents the results of fitting the NN template distributions to observed collision data. The estimated event yield after the fit is denoted by $\hat{\nu}_j$. It is calculated by $\hat{\nu}_j = \hat{\beta}_j \cdot \tilde{\nu}_j$, whereas $\hat{\beta}_j$ is the estimator of the fit. The uncertainties on the expected yield $\tilde{\nu}_j$ are the ones used for the Gaussian constraints (see Tab. 7.1), whereas the uncertainties on the observed yield $\hat{\nu}_j$ are the statistical uncertainties of the fit to observed data. A scale factor of $\hat{\beta}^s = 1.28$ for the signal process is found. To estimate the

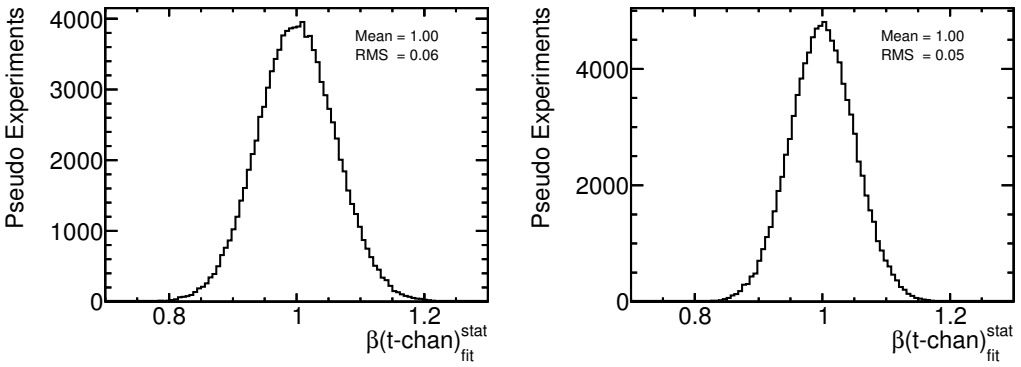

(a) *(b)*

Figure 7.2: *Distributions of the fitted $\hat{\beta}^s$ value from experiments for the expected (a) and observed (b) numbers. The width of the distribution is the statistical uncertainty due to the size of the dataset.*

uncertainty due to the data statistics in the selected data set, pseudo experiments are employed by varying the event yields according to a Poisson distribution. The width of the resulting β^s distribution of the ensemble is the relative statistical uncertainty. Two sets of pseudo experiments are carried out. First for the expected number of events $\tilde{\nu}_j$ and second for the observed event numbers $\hat{\nu}_j$. Both distributions are depicted in Fig. 7.2. For the expected SM cross-section of $64.6 \pm 3.9\,(\text{stat})\,\text{pb}$ a relative statistical uncertainty of 6% is expected. Using the fitted scale factor $\hat{\beta}^s$ the observed t-channel single top-quark production cross-section yields $82.6 \pm 4.2\,(\text{stat})\,\text{pb}$. A relative statistical uncertainty of 5% is observed.

Both, the quality of the fit and the quality of the background model can be judged by comparing the observed distribution of the NN classifiers and input variables to the signal and background model from simulated events, normalised to the fit result. Figure 7.3 (a) shows the 2-jet channel and (b) for the 3-jet channel of the NN output distribution. Good agreement between observed data and the event model is found in the 2-jet channel. A small mismodelling is present in the background region of the 3-jet channel. It is acceptable since it does not influence the signal region and is covered by the systematic uncertainties. The three most important input variables in both channels are shown in Fig. 7.4. In general, good agreement between the event model normalised to the fit result and observed data is seen. A deviation between the simulated model and observed data is noted in the 2-jet channel for the pseudorapidity distribution of the untagged jet. Since the deviation is in the central region $|\eta| \sim 0$, which is highly background enriched, it is covered by the systematic uncertainties. All input variables used in the 2-jet and 3-jet channel are shown in Appx. C.1 for the 2-jet channel and Appx. C.2 for the 3-jet channel.

To check the input variables of the 2-jet channel in a highly signal enriched phase space events having a NN output value larger than 0.875 are selected. The event

model is normalised to the $\hat{\beta}$-scale factors of the binned maximum-likelihood fit. The normalisation of the multijet background is estimated by the cut efficiency on the NN output value. In Fig. 7.5 the reconstructed top-quark mass (a), the $|\eta|$ of the untagged jet (b), the transverse energy E_{T} of the untagged jet (c), the reconstructed transverse mass of the W boson (d), the scalar sum of the transverse momenta of the jets, charged lepton, and missing transverse momentum (e), and the p_{T} of the charged lepton (f) are shown. An overall reasonable agreement of the event model and observed data is seen. The untagged jet shows a small mismodelling in the very forward direction in the $|\eta|$ range between 3 and 4 and in the low E_{T} range of 25 G*e*V to 40 G*e*V. Both seem to be correlated, because the jets in the very forward direction are expected to have a small E_{T}.

Process	$\tilde{\nu}$(2Jets)	$\tilde{\nu}$(3Jets)	$\hat{\beta}$	$\hat{\nu}$(2Jets)	$\hat{\nu}$(3Jets)
t-channel	940 ± 20	620 ± 20	1.28 ± 0.07	1200 ± 60	800 ± 40
			nuisance parameters		
$W+$ heavy flavour	4800 ± 2400	2080 ± 1040	1.22 ± 0.06	5850 ± 290	2530 ± 130
$W+$ light jets	1010 ± 300	390 ± 120	0.72 ± 0.16	740 ± 160	280 ± 60
$Z+$ jets, diboson	330 ± 200	180 ± 110	0.84 ± 0.56	270 ± 180	150 ± 100
top	1160 ± 100	3380 ± 300	0.88 ± 0.03	1370 ± 50	2960 ± 120
Multijets	1150 ± 570	850 ± 420	–	1150 ± 570	850 ± 420
Total sum	9390 ± 2770	7490 ± 1280	–	10570 ± 760	7570 ± 490
Total observed	–	–	–	10613	7507

Table 7.2: *Input and result of the binned maximum-likelihood fit. The SM expectations $\tilde{\nu}$ of all processes including their uncertainty Δ_j are the input of the fit. The event yield of the multijet background is estimated using the $E_{\mathrm{T}}^{\mathrm{miss}}$-fit. The estimators of the likelihood function parameters are denoted by $\hat{\beta}$ and the estimated event yield after the fit $\hat{\nu}$. Their quoted uncertainties are statistical, only.*

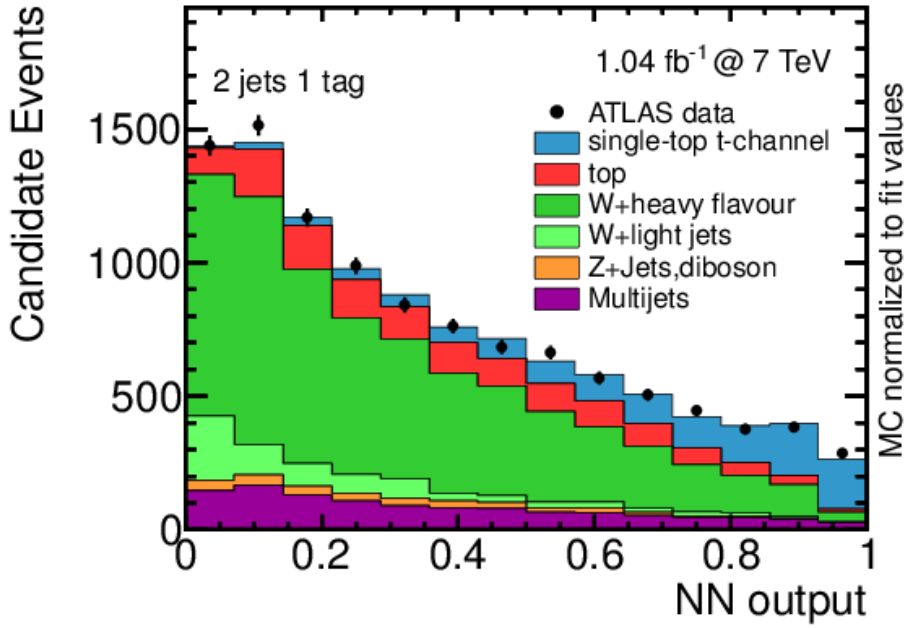

(a)

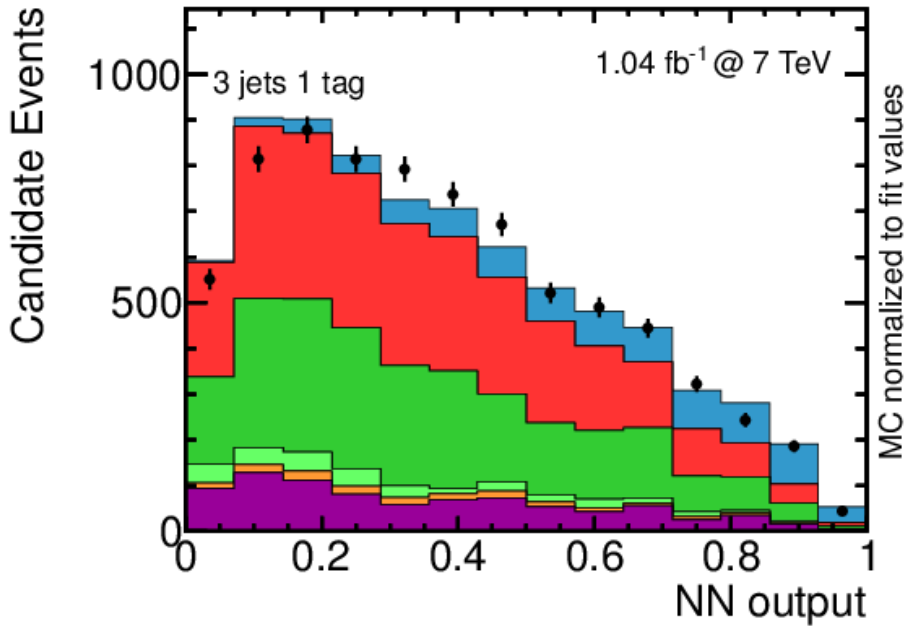

(b)

Figure 7.3: *The Neural network output distribution of the 2-jet (a) and 3-jet (b) signal region with one b-tagged jet. The simulated event model is normalised to the results of the binned maximum-likelihood fit.*

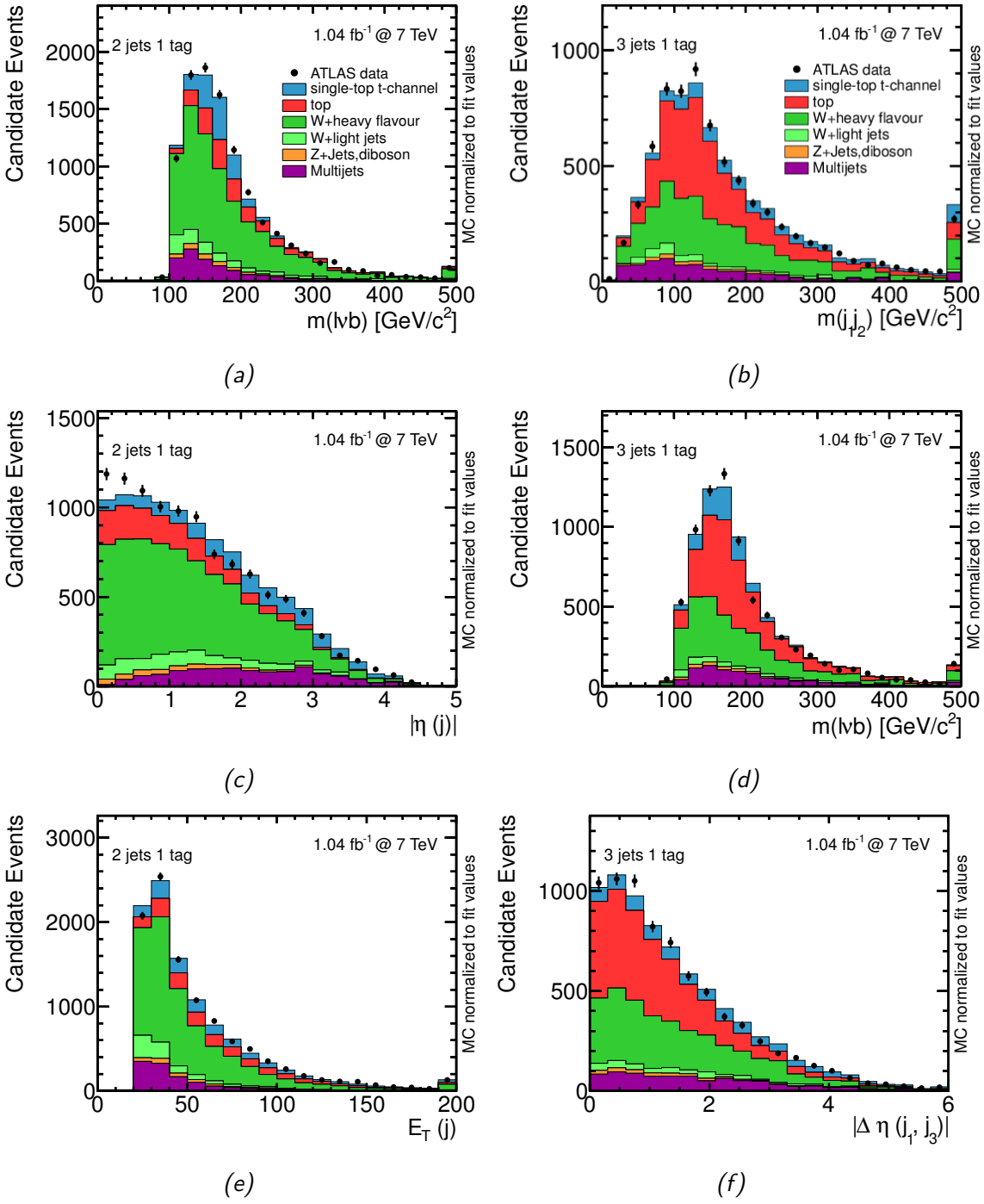

Figure 7.4: *The three most important variables of the 2-jet channel are the reconstructed top-quark mass (a), the $|\eta|$ of the untagged jet (c), and the transverse energy E_{T} of the untagged jet (e). The three most important variables of the three jet channel, the invariant mass of the leading and second leading jet (b), the reconstructed top-quark mass (d), and the $|\Delta\eta|$ between the leading and third leading jet (f). The event model is normalised to the result of the binned maximum-likelihood fit.*

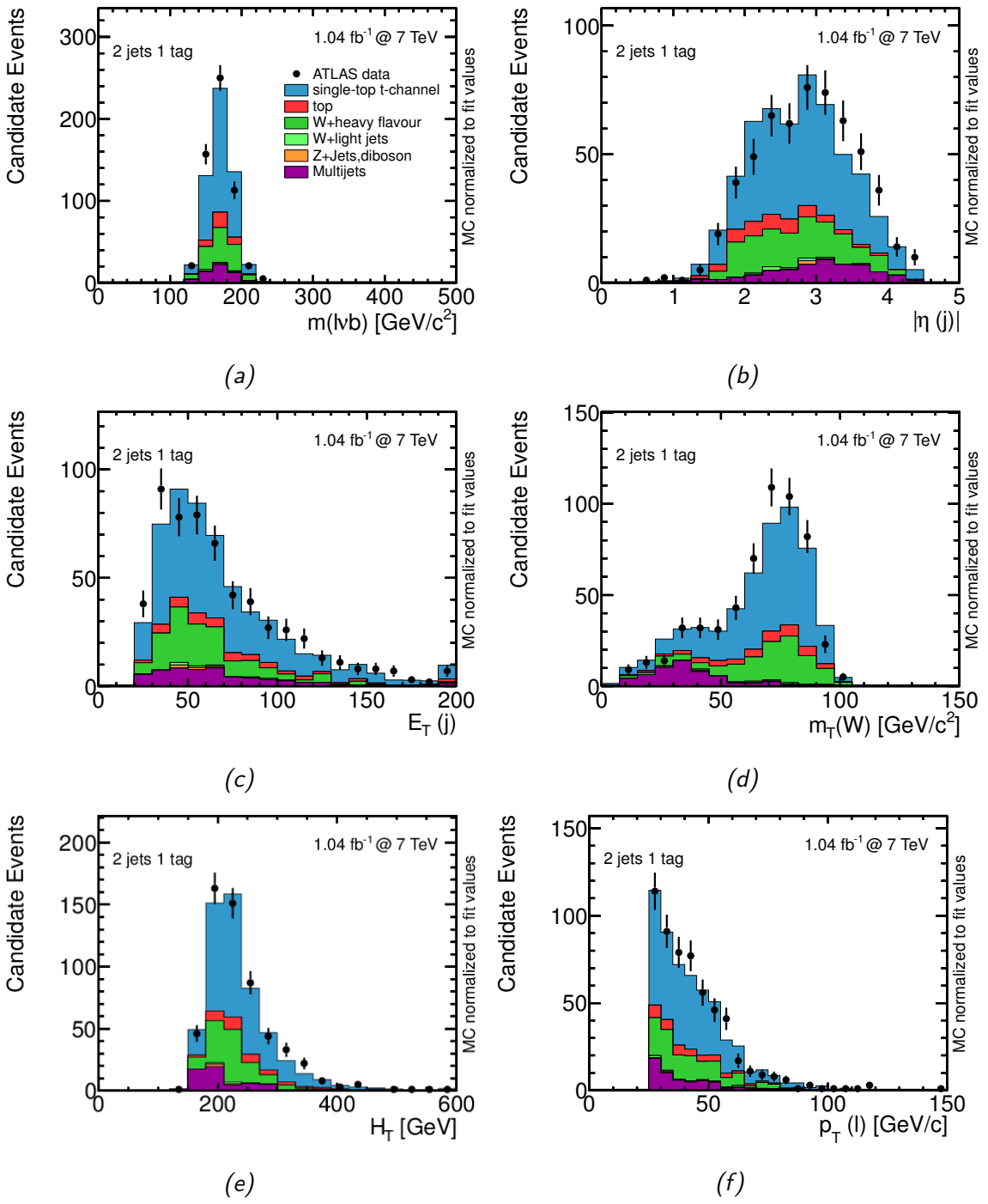

Figure 7.5: *Kinematic distributions in the 2-jet channel in a highly signal enriched phase space by cutting on the NN value larger than 0.875. The event model is normalised with the scale factors obtained by the binned maximum-likelihood fit. The reconstructed top-quark mass (a), the $|\eta|$ of the untagged jet (b), the transverse energy E_{T} of the untagged jet (c), the reconstructed transverse mass of the W boson (d), the scalar sum of the transverse momenta of the jets, missing transverse momentum and lepton (e), and the p_{T} of the charged lepton (f).*

7.3 Systematic Uncertainties

In this section, the different sources of systematic uncertainties taken into account for the measurement of the single top-quark t-channel production cross-section are explained. First, different sources of systematic uncertainties and their impact on the normalisation of the signal and background processes as well as on the shape of the NN output distribution are investigated. Second, the size of the systematic uncertainties on the measurement is evaluated.

7.3.1 Sources of Systematic Uncertainties

Many sources of systematic uncertainties are considered affecting the precision of the single top-quark t-channel production cross-section measurement. Two categories of systematic uncertainties are be distinguished. The first category comprises uncertainties affecting the modelling of physics objects due to residual differences between observed data and simulated events, such as the energy scale calibration of jets or leptons. The second category includes uncertainties dealing with the modelling of simulated events, such as the difference between MC generators or different parton shower models. The systematic effects explained in this section have an impact on the normalisation of all simulated processes by changing their acceptance. Table 7.3 and 7.4 present the relative rate uncertainties for the different processes for the 2-jet and 3-jet channel, respectively. Since template distributions are used in a binned maximum-likelihood fit to extract the signal cross-section, the impact on the shapes of the neural network output has to be taken into account, too. Figure 7.7 and 7.8 show exemplarily the shape uncertainties due to the JES for the 2-jet and 3-jet channel. All shape uncertainties are documented in Ref. [151]. In the following, all sources of systematic uncertainties considered in the analysis are specified.

Lepton Energy Scale and Resolution

The impact of the lepton energy scale uncertainty on the simulated event samples is evaluated by scaling the p_T of the lepton up or down by 1σ of the uncertainty and re-applying the event selection. Also, the lepton energy resolution is investigated by smearing the lepton energy with a random number from a Gaussian distribution. Both, the lepton momentum scale and resolution is measured using $Z \to \ell\ell$ events [93, 97]. The effect on the acceptance and shape of the NN distribution is considered.

Lepton ID and Trigger Efficiency Scale Factors

Scale factors are applied to match the trigger and lepton identification efficiencies in observed data and simulated events. These scale factors have associated uncertainties. Their impact on the cross-section measurement is assessed by reweighting the selected events according to the uncertainty on the scale factor depending on the lepton p_{T} and

η. The scale factor uncertainties are around 3%. Both, the impact on the shape and event yield is considered.

Jet Energy Scale
The uncertainty on the JES depends on the p_{T} and η of the reconstructed jet [152]. The MultijetJESUncertaintyProvider tool is used to scale the energy of each jet up or down by 1σ of the uncertainty. It varies between 2.5% and 8% (3.5% and 14%) in the central (forward) region of the calorimeter. An additional uncertainty on the JES is applied to b-tagged jets. Hereby, the b-jets are selected by their true flavour from the simulated event information. It is provided in 5 p_{T} bins and the uncertainty ranges from 2.5% to 0.76% for low-p_{T} and high-p_{T} jets. Since the JES is calibrated with 2010 collision data, an extra uncertainty to the JES due to the different pile-up conditions in 2011 data ranging from 1% to 5% as function of the jet p_{T} is added. The additional uncertainties are added in quadrature to the JES uncertainty. This change is propagated to the calculation of the missing transverse momentum. Reapplying the object and event selection reveals the effect on the normalisation of each simulated process and the shapes of the NN output.

Jet Energy Resolution
The energy resolution of jets (JER) is measured using di-jet collision data. An agreement at the level of 10% is found between collision data and simulated events [153]. The impact of the uncertainty on the JER is evaluated by smearing the p_{T} of the jets in simulated events with a normal distribution having a width of the resolution, depending on the p_{T} and η of the jet. Since it is an one-sided uncertainty, it is symmetrised by taking half of the difference as up- and downward fluctuation of the acceptance. The symmetrised shape uncertainty is constructed by adding half the difference between the altered and nominal shape to the nominal shape for the upward fluctuation. In case of the downward fluctuation half of the difference is subtracted from the nominal shape.

Jet Reconstruction Efficiency
The jet reconstruction efficiency (jet reco) is measured using minimum bias and QCD di-jet events. An uncertainty of 2% on the reconstruction efficiency on jets with $p_{\mathrm{T}} < 30\,\mathrm{GeV}$ is found by comparing the selection efficiencies in collision data and simulated event samples. For jets with a larger p_{T} it is negligible [152]. To study the impact of the jet reconstruction efficiency on the analysis, jets are randomly dropped from the nominal simulated event samples. The uncertainty on the acceptance and the shape of the NN output distribution is symmetrised.

***b*-Jet Identification Efficiency**
Different b-tagging efficiencies between observed data and simulated events are cor-

rected by scale factors. The uncertainty on the scale factor for b-tagged b-jets is denoted as 'b-tagging scale-factor' and is at the level of 10% to 20%. The scale factor uncertainty on light-jets, as well as c-jets misidentified as b-jets is denoted as 'mistag scale-factor'. An uncertainty of 20% to 50% or 20% to 40% is assigned on the scale factor for mistagged light- and c-jets, respectively. The uncertainties depend on the p_{T} and η of the jet [102]. To evaluate the uncertainties in the analysis, the jet flavour is taken from the MC truth information for each jet to identify true b-tagged jets and mistagged jets to apply the corresponding scale factor variation. Both uncertainties, the b-tagging scale factor and the mistag scale factor have an impact on the acceptance and the shape of the classifier distribution.

MC Generator

An uncertainty due to the MC generator model for the important top-quark processes is taken into account. Therefore, different MC generators are compared to study the impact on the acceptance and on the shape of the processes. In case of the $t\bar{t}$ process, events generated with MC@NLO+HERWIG and POWHEG+HERWIG are compared. The resulting uncertainty on the shape and acceptance is symmetrised. The generator uncertainty on the signal sample is estimated by comparing on parton level the acceptance difference between the nominal signal sample simulated using ACERMC+PYTHIA and a simulated sample using MCFM. Hereby, a cut of $p_{\mathrm{T}} > 20\,\mathrm{GeV}$ is required for the second b quark and the light quark. In doing so, an acceptance uncertainty of 7.5% is found. This uncertainty is symmetrised.

Parton Shower Modelling

Two different models used for the parton shower and hadronisation are compared to evaluate a systematic uncertainty due to the model used. Since the signal process is simulated using ACERMC+PYTHIA, it is compared to ACERMC+HERWIG. In case of the $t\bar{t}$ sample, POWHEG+HERWIG is compared with POWHEG+PYTHIA. Technically, the shape difference between the two samples is transferred to the shape of the MC@NLO+HERWIG sample to create the systematic sample used in the pseudo experiment generation. Since the parton shower model uncertainty is a one-sided one, it is symmetrised for the acceptance and shape uncertainty.

Initial-State and Final-State Radiation

The dependence of the signal process and the other top-quark background processes on the initial-state radiation (ISR) and final-state radiation (FSR) settings of the parton shower model are evaluated. The uncertainty on the model is estimated from a set of ACERMC+PYTHIA samples for the top-quark processes generated with a variation of the corresponding parameters. In order to alter the ISR, the PYTHIA settings PARP(64)=1 and PARP(67)=1 are changed. The former corresponds to a variation of the strong evolution scale proportional to $1/\Lambda^{\mathrm{ISR}}_{\mathrm{QCD}}$. Its value is varied to increase (decrease) the ISR to 4 (0.25). The later limits the maximum virtuallity of partons in space-like parton

showers. Here, the values are changed to 0.5 (6) to decrease (increase) the radiation of partons. To change the activity of the FSR, the PYTHIA parameters PARP(72)=192 and PARJ(82)=1 are modified. The first is the energy scale $\Lambda_{\mathrm{QCD}}^{\mathrm{FSR}}$ for time-like parton showers in the final state. It is changed to 0.092 (0.384) to increase (decrease) the probability of the radiation of a parton in the final state. The second is the low-p_{T} cutoff for an FSR branching. It is varied to 2 (0.5) to increase (decrease) the amount of FSR. The simulated sample with the simultaneous up- and downward variation of the ISR and FSR parameters is used. The shape difference due to the ISR/FSR variation is transferred to the shapes of the nominal simulated event samples. Since a different MC generator set is used than for some of the nominal samples, the observed shape uncertainty is transferred to the nominal shapes to create the templates used for the pseudo experiments.

Parton Distribution Functions

An uncertainty due to the parametrisation of the PDF is taken into account for the top quark related processes. The nominal MC samples are reweighted according to an alternative PDF parametrisation. As uncertainty, the largest deviation due to the alternative parametrisation is taken. The PDF sets taken in consideration are: MSTW2008nlo68cl [154], CTEQ6.6 [155]. The rate uncertainty ranges from 3% to 8%, depending on the process and channel of the analysis. An impact on the shape of the NN output distribution is negligible and not regarded.

Theoretical Cross Section Normalisation

In this analysis, the event yields of the $t\bar{t}$, Z+jets, diboson and the single-top s-channel and associated production background processes are estimated using the acceptance from MC simulated events and the theoretically predicted cross-sections. The cross-section uncertainty on the $t\bar{t}$ cross-section is $^{+10}_{-7}$% [38]. For the Wt and s-channel single-top processes a 7% and 4% uncertainty on the cross-section is assigned [5, 6]. An uncertainty of 5% is assigned to the diboson background [142] and one of 60% to the Z+jets background. These uncertainties account for scale variations, PDFs, and the imperfect knowledge of α_S. The uncertainties of processes that are combined in the final analysis are added linearly to incorporate a correlation of the uncertainties.

QCD Background Normalisation

The QCD background is normalised to data through fitting the $E_{\mathrm{T}}^{\mathrm{miss}}$ distribution for the electron and the muon channel. As described in section 5.2 a systematic uncertainty of 50% is assigned to the normalisation based on studies comparing results of fitting in $m_{\mathrm{T}}(W)$ and comparing the impact of different pileup conditions on the model.

W+jets Background Uncertainty

The theoretical prediction of the W+light jet production and W+heavy-flavour jet pro-

duction provides only an approximation of the normalisation of these processes. Thus, the normalisation of the W+light jet production is associated with an uncertainty of 30%. An uncertainty of 50% is considered on the normalisation of the W+heavy-flavour jet production. These numbers are estimated in the frame of the single top-quark t-channel cross-section measurement using a cut-based approach [141], which extracts the signal region by applying more stringent cuts. Here, the W+jets normalisation is estimated from sidebands in the pretag and tagged dataset using the event counting method by solving a set of equations to normalise the W+light jets and W+heavy-flavour jets and processes. The uncertainties associated with this method are used for this analysis.

Luminosity

The uncertainty on the integrated luminosity for the 2011 data is 3.7%. It is based on dedicated *van der Meer* scans taken in May 2011 and constantly validated using calorimeter-based techniques during the data-taking period [84].

Forward Jet η-Reweighting

To evaluate uncertainties due to the mismodelled η distribution of the forward jet c.f. Fig. B.1 (b) for the 2-jet pretag dataset, especially for high η regions, alternative MC distributions are generated by a reweighting procedure. The reweighting histograms are obtained from the pretag data samples in the 2-jet or 3-jet dataset. The η distribution of observed events is divided by the distribution taken from simulation. The reweighting histograms are shown in Fig. 7.6.

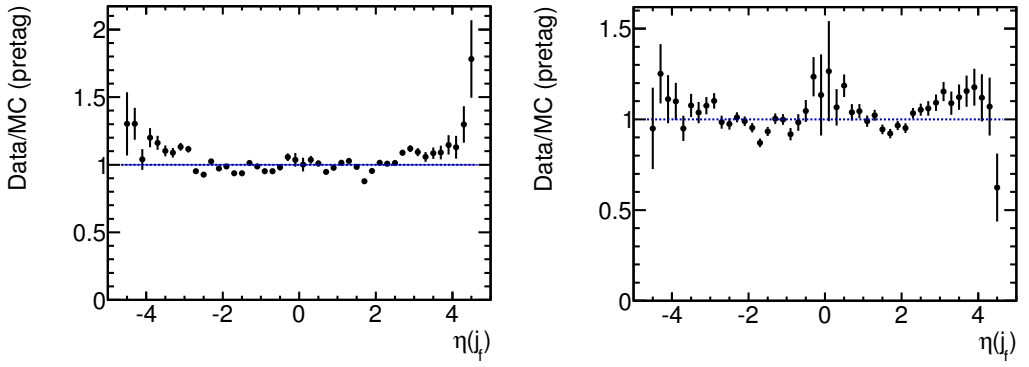

(a) *(b)*

Figure 7.6: *Reweighting histogram determined in the pretag sample for the 2-jet (a) and 3-jet (b) dataset by dividing the η distribution of the forward jet obtained from observed events by the distribution taken from simulated events.*

MC Statistics

An uncertainty due to the limited statistics of simulated events is included as described before.

W+Jets Shape Uncertainty

An uncertainty is assigned to the shapes of the W+jets background based on varying several ALPGEN parameters in the generation of the W+jets MC. The MLM matching threshold of the jets PTJMIN is changed to $p_{\mathrm{T}} = 10\,\mathrm{GeV}$ compared to the nominal value of $p_{\mathrm{T}} = 15\,\mathrm{GeV}$. Another variation is changing the factorisation scale (IQOPT) from $Q^2 = m_W^2 + \Sigma m_{\mathrm{T}}^2$ to $Q^2 = m_W^2 + p_{\mathrm{T}}^2(W)$. Hereby, m_W is the mass of the W boson and m_{T} the transverse mass of a final-state particle. The nominal W+jets samples are reweighted according to the resulting change of these variations. The largest variation is considered as systematic uncertainty.

E_T^{Miss}

An additional uncertainty to the $E_{\mathrm{T}}^{\mathrm{miss}}$ calculation is introduced from calorimeter cells that are not associated to any jet (cell-out) and from soft jets that are included in the $E_{\mathrm{T}}^{\mathrm{miss}}$ calculation. Soft jets are defined as jets with a p_{T} larger than 7 GeV and smaller than 20 GeV. The contribution from the soft-jets and cell-out term are treated fully correlated. The impact on the shape and acceptance are regarded.

Pileup E_T^{Miss}

A flat variation of 10% is applied to the cell-out and soft-jet term of the $E_{\mathrm{T}}^{\mathrm{miss}}$ calculation to take into account an additional uncertainty due to pile-up events on the $E_{\mathrm{T}}^{\mathrm{miss}}$-composition. This uncertainty affects the shape of the distributions as well as the acceptance.

Liquid Argon

Due to a hardware failure in the LAr calorimeter read-out electronics, a rectangular region of $(-0.74 < \phi < 0.64) \times (0 < \eta < 1.4)$ was not read out during the data taking runs 180614 to 185353. Thus, events featuring a jet with $p_{\mathrm{T}} > 20\,\mathrm{GeV}$ which is in this calorimeter region are rejected. A systemtic uncertainty is is evaluated by varying the p_{T} threshold of those jets by $\pm 4\,\mathrm{GeV}$.

Source		t-ch.	top	W+lj	W+hf	Z+j, diboson
Jet Energy Scale	up	−6.65	−13.05	+14.84	+6.53	+7.40
	down	+2.75	+14.30	−15.15	−6.97	−8.82
Jet Energy Resolution	up	−0.73	−0.82	+0.97	+1.14	+0.10
	down	+0.73	+0.82	−0.97	−1.14	−0.10
Jet Reconstruction	up	−0.01	+0.04	−1.00	+0.07	+0.60
	down	+0.01	−0.04	+1.00	−0.07	−0.60
Lepton Efficiencies	up	+2.71	+3.27	+2.58	+2.91	+2.88
	down	−2.68	−3.24	−2.56	−2.89	−2.86
Lepton Energy Resolution	up	+0.11	−0.00	+0.30	+0.04	−0.20
	down	−0.09	−0.05	+0.31	+0.05	+0.08
Electron Energy Scale	up	−0.01	+0.11	+0.35	+0.30	+0.29
	down	−0.21	−0.14	+0.17	−0.09	+0.30
b-tagging Scale Factor	up	+10.21	+6.33	+2.12	+16.54	+12.11
	down	−10.40	−7.48	−2.14	−16.67	−12.30
Mistag Scale Factor	up	+0.01	+0.09	+21.35	+0.68	+6.05
	down	−0.01	−0.09	−21.37	−0.68	−6.05
PDF	up	+3.20	+6.40	−−	−−	−−
	down	−3.00	−5.60	−−	−−	−−
MC Generator	up	+3.55	−13.05	−−	−−	−−
	down	−3.55	+14.30	−−	−−	−−
Parton Shower	up	+5.68	−3.97	−−	−−	−−
	down	−5.68	+3.97	−−	−−	−−
ISR/FSR	up	−9.26	−5.61	−−	−−	−−
	down	+18.70	+13.69	−−	−−	−−
η-Reweighing		+1.22	−1.41	−1.80	−0.95	−1.33
Luminosity	up	+3.70	+3.70	−−	−−	+3.70
	down	−3.70	−3.70	−−	−−	−3.70
$E_{\mathrm{T}}^{\mathrm{miss}}$	up	+0.03	−0.05	−0.54	+0.35	+0.98
	down	−0.36	+0.03	−2.10	−0.21	+1.74
Pileup $E_{\mathrm{T}}^{\mathrm{miss}}$	up	+0.12	−0.04	−0.22	+0.25	+0.49
	down	−0.34	+0.00	−1.66	−0.28	+1.99
Liquid Argon	up	+0.74	+1.09	+0.73	+0.77	+1.18
	down	−1.00	−1.54	−1.15	−0.81	−0.98

Table 7.3: *The relative rate uncertainties of the tagged 2-jet dataset given in per cent.*

Source		t-ch.	top	W+lj	W+hf	Z+j, diboson
Jet Energy Scale	up	+4.94	−6.48	+23.79	+12.80	+20.97
	down	−5.65	+6.49	−11.55	−13.69	−13.48
Jet Energy Resolution	up	−0.19	−0.57	+6.93	−0.60	+1.88
	down	+0.19	+0.57	−6.93	+0.60	−1.88
Jet Reconstruction	up	−0.08	+0.07	+0.41	−0.29	+1.42
	down	+0.08	−0.07	−0.41	+0.29	−1.42
Lepton Efficiencies	up	+2.77	+3.28	+2.41	+3.01	+3.26
	down	−2.75	−3.26	−2.39	−2.99	−3.23
Lepton Energy Resolution	up	+0.01	−0.02	+0.84	+0.14	+1.03
	down	−0.12	−0.01	+0.56	+0.21	+0.02
Electron Energy Scale	up	+0.14	+0.12	+0.78	+0.14	−0.24
	down	−0.20	−0.01	+0.60	+0.07	+0.73
b-tagging Scale Factor	up	+6.35	+3.28	+3.03	+14.97	+12.08
	down	−7.32	−5.03	−3.04	−15.32	−12.30
Mistag Scale Factor	up	−0.01	+0.03	+21.63	+0.90	+5.93
	down	+0.01	−0.03	−21.67	−0.91	−5.94
PDF	up	+3.00	+7.55	−−	−−	−−
	down	−3.00	−6.66	−−	−−	−−
MC Generator	up	+3.55	−6.48	−−	−−	−−
	down	−3.55	+6.49	−−	−−	−−
Parton Shower	up	−4.50	−3.69	−−	−−	−−
	down	+4.50	+3.69	−−	−−	−−
ISR/FSR	up	−1.94	−4.69	−−	−−	−−
	down	−4.87	+11.50	−−	−−	−−
η-Reweighing		+1.58	−0.63	−0.44	−0.59	−1.33
Luminosity	up	+3.70	+3.70	−−	−−	+3.70
	down	−3.70	−3.70	−−	−−	−3.70
$E_{\mathrm{T}}^{\mathrm{miss}}$	up	−0.11	+0.12	+0.28	+0.21	−0.23
	down	+0.13	−0.01	+1.82	−0.05	+2.46
Pileup $E_{\mathrm{T}}^{\mathrm{miss}}$	up	−0.20	+0.09	+0.12	+0.35	+0.47
	down	+0.04	−0.01	+1.79	+0.30	+2.71
Liquid Argon	up	+0.63	+1.14	+1.64	+0.43	+1.61
	down	−1.14	−1.40	+0.41	−1.47	−1.12

Table 7.4: *The relative rate uncertainties of the tagged 3-jet dataset given in per cent.*

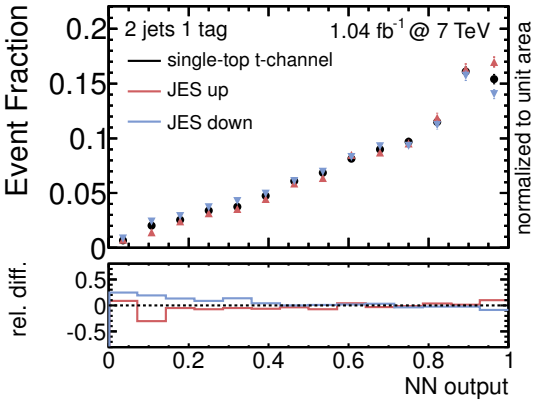

(a) t-channel

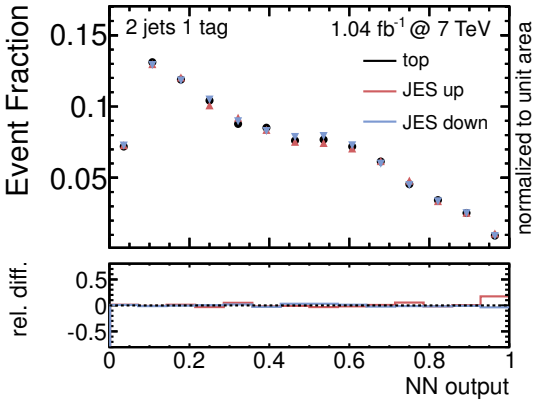

(b) top

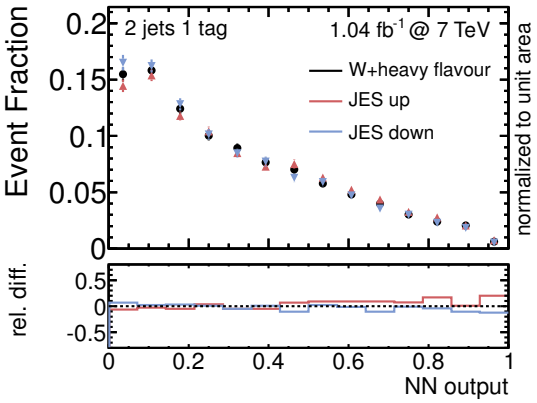

(c) W+heavy flavour

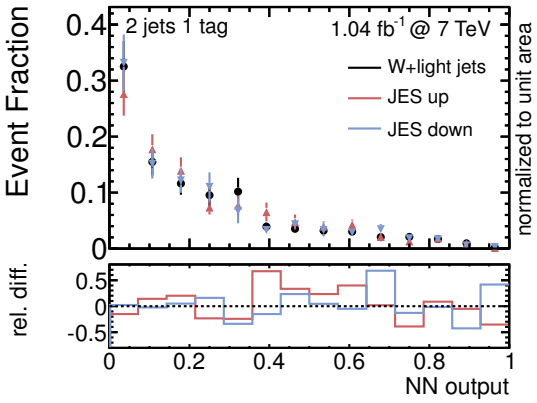

(d) W+light flavour

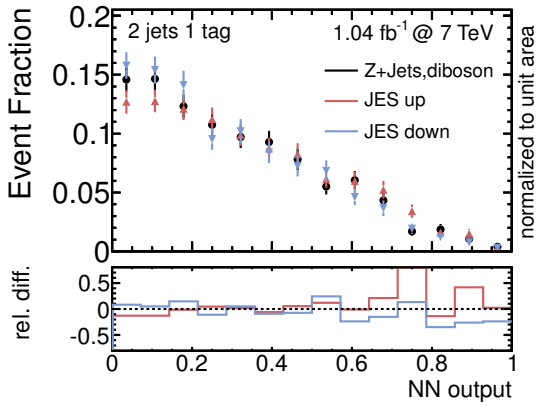

(e) Z+jets, diboson

Figure 7.7: *The shape variation of the neural network discriminant for the JES variation in the 2-jet channel. The nominal shape is shown by the black points. Red denotes the shape with the JES shifted up and the blue histograms show the neural network response for a JES shifted down. The relative difference is defined as (shifted - nominal)/nominal.*

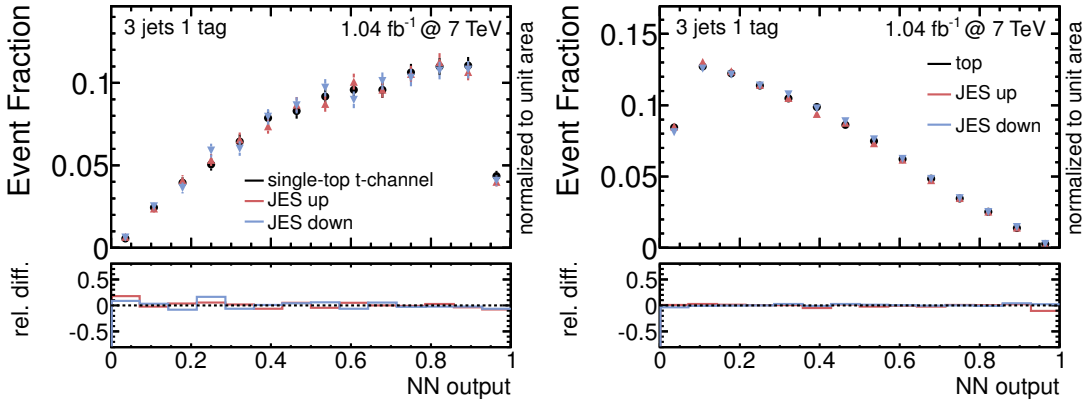

(a) t-channel

(b) top

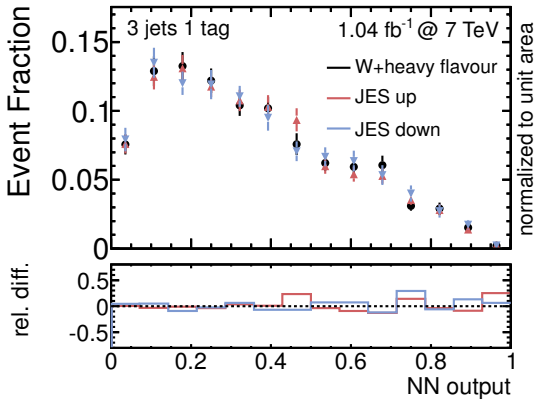

(c) W+heavy flavour

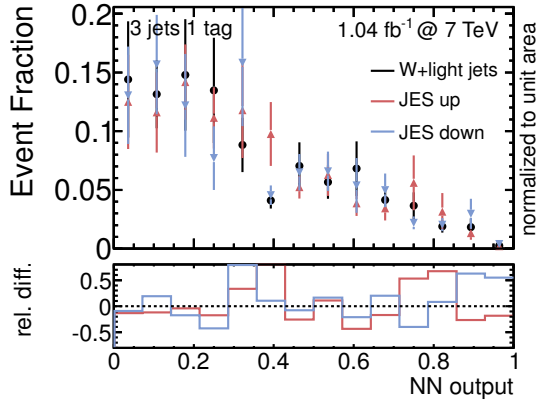

(d) W+light flavour

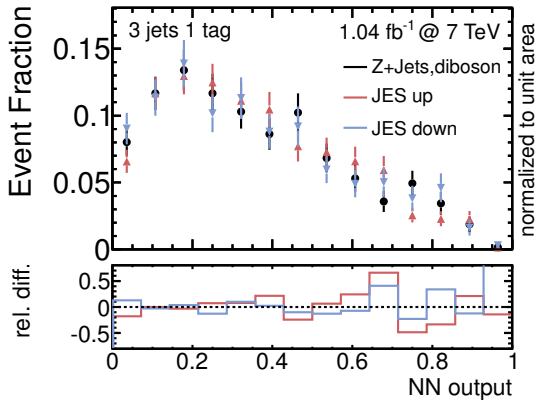

(e) Z+jets, diboson

Figure 7.8: *The shape variation of the neural network discriminant for the JES variation in the 3-jet channel. The nominal shape is shown by the black points. Red denotes the shape with the JES shifted up and the blue histograms show the neural network response for a JES shifted down. The relative difference is defined as (shifted - nominal)/nominal.*

7.3.2 Evaluation of Systematic Uncertainties

Ensemble tests are carried out in order to evaluate the impact of the systematic uncertainties on the precision of the cross-section measurement. Those include all systematic shifts on the normalisation and shape of the NN output distribution, which are explained in the previous section. The effect of each single uncertainty on the precision is deduced by running pseudo experiments which varies only this single effect. To estimate the expected and observed uncertainties, the SM expectations $\tilde{\nu}$ and the result $\hat{\nu}$ of the template fit are used, respectively. The result of the pseudo experiments is the distribution of measured cross-sections $\hat{\beta}^s$. It is interpreted as estimator of the probability density function of all possible results of a cross-section measurement under the assumed systematic effects. The uncertainty on the actual measurement is estimated from the RMS of the distribution. A potentially positive or negative bias due to the systematic uncertainties is added in quadrature to the positive or negative uncertainty. Thus, asymmetric uncertainties can arise.

The impact of each single systematic uncertainty due to the different sources originating from the object modelling, the event modelling, and the normalisation of the backgrounds is listed in Tab. 7.5. It shows the relative uncertainties $\Delta\sigma/\sigma$ on the expected and the observed cross-section measurement. Hereby, $\Delta\sigma$ denotes the absolute uncertainty of the measurement. Figure 7.2 depicts the probability density function of the $\hat{beta}^s$-value, using 100k pseudo experiments for the ensemble tests of the expected (a) and observed (b) cross-section measurement. The RMS of this distributions is the relative uncertainty. Including all systematic uncertainties and the statistical uncertainty, a total relative uncertainty of $^{+26}_{-24}$% (expected) and $^{+24}_{-24}$% (observed) is found. The uncertainty due to systematic effects only is $^{+25}_{-24}$% (expected) and $^{+24}_{-23}$% (observed). They dominate over the uncertainty due to the data statistics ±6.1% (expected) and ±5.1% (observed). An asymmetric uncertainty is found, since the mean of the $\hat{\beta}^s$ distribution is shifted by 8% (expected) and 6% (observed) to larger values, respectively. Since the bias is small compared to the size of the uncertainty, it has no influence on the total observed uncertainty. The main sources of the bias are ISR/FSR and the forward jet η-reweighting.

The dominant uncertainties belonging to the object modelling category are the uncertainty on the b-tagging calibration, the JES uncertainty, and the lepton efficiencies. A relative uncertainty of ±13.4% (expected) and ±13.0% (observed) due to the b-tagging calibration is found. The relative JES uncertainty on the measurement accounts to ±5.7% (expected) and ±4.4% (observed). The efficiencies on the lepton identification and reconstruction yield a relative uncertainty of ±1.9% (expected) and ±2% (observed). All other sources of systematic uncertainties play a minor role. Their values are in the range of 0.5% to 2%.

In the event-modelling category, the largest uncertainties are due to ISR/FSR, parton-shower modelling, and the forward jet η-reweighting. ISR/FSR is the largest individual uncertainty with ±14% (expected/observed). An additional large uncertainty is

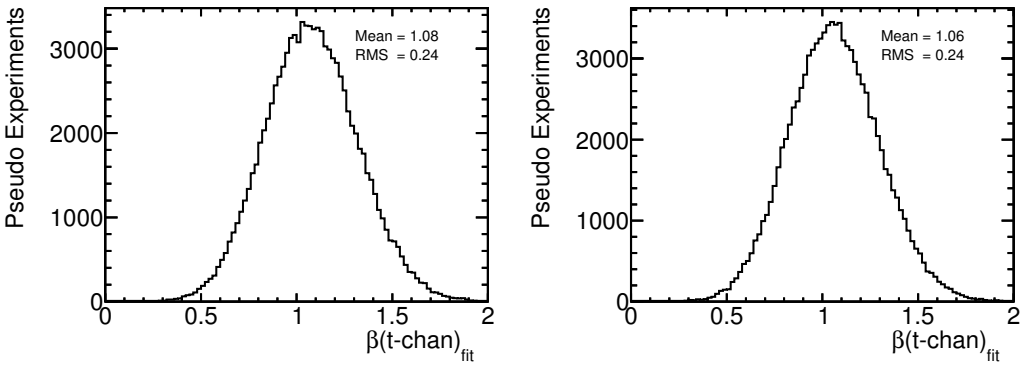

(a) *(b)*

Figure 7.9: *Distributions of the fitted $\hat{\beta}^S$ value from pseudo experiments for the expected (a) and observed (b) event yields. In the pseudo experiments, all sources of systematic uncertainties are included.*

due to the forward jet η-reweighting, accounting for $^{+6.9}_{-4.2}$% (expected) and $^{6.4}_{-3.9}$% (observed). Comparing different parton shower models yields a relative impact of ±4.5% (expected) and ±5% (observed) on the cross-section measurement. Uncertainties due to MC generator models and the PDF parametrisation ranging from 0.5% to 3.5% can be regarded as small compared to the other uncertainties in the event-modelling category.

The dominant uncertainty on the background normalisation is the uncertainty on the event yield of the multijet background. It results in an uncertainty of ±4.7% (expected) and ±5.3% (observed) on the measurement.

To improve the precision of the cross-section measurement, a better understanding of the object and event modelling is needed. It is crucial, to tackle the largest uncertainties which are the uncertainty due to the ISR/FSR modelling and on the b-tagging calibration. Both are roughly 2.5 times larger than the other uncertainties of major importance. If one assumes both uncertainties to be at a level of 7%, the total expected uncertainty would roughly improve to a 18% level. To reduce the uncertainty of the b-tagging calibration, a better understanding on the b-tagging efficiencies in simulated events and observed data is necessary. A future reduction of the ISR/FSR uncertainty will be possible based on $t\bar{t}$ cross-section measurements that derive constraints on the additional jet activity due to high energetic QCD radiation. A measurement and comparison to theoretical models is performed in Ref. [156]. Those results will be available to constrain the ISR/FSR uncertainty for future analyses.

Source	$\Delta\sigma_{\text{exp}}/\sigma_{\text{exp}}$ [%]	$\Delta\sigma_{\text{obs}}/\sigma_{\text{obs}}$ [%]
Data Statistics	±6.1	±5.1
MC Statistics	±3.8	±3.4
Object Modelling		
Jet Energy Scale	±4.7	±5.3
Jet Energy Resolution	±1.7	±1.5
Jet Reconstruction	±0.5	±0.2
b-Tagging Scale Factor	±13	±13
Mistag Scale Factor	±0.6	±0.4
Lepton Efficiencies	±1.9	±2.0
Lepton Energy Resolution	±0.4	±0.3
Electron Energy Scale	+0.5/−0.6	0.2/−0.4
E_T^{Miss}	±1.0	±0.8
Pileup E_T^{Miss}	±1.0	±0.9
Liquid Argon	±0.9	±0.9
Event Modelling		
PDF	±3.3	±3.3
W Shape	+0.5/−0.3	+0.5/−0.3
Top Generator	±3.3	±2.3
t-Channel Generator	±3.5	±3.5
ISR/FSR	±14	±14
Parton Shower	±4.5	±5.0
η-Reweighting	+6.9/−4.2	+6.4/−3.9
Normalisation		
Background Normalisation	±1.1	±0.9
QCD	±5.7	±4.4
Luminosity	±3.9	±3.8
Total Systematic	+25/−24	+24/−23
Total Systematic + Statistic	+26/−24	+24/−24

Table 7.5: *Breakdown of the major contributions to the relative systematic uncertainties on the expected $\Delta\sigma_{\text{exp}}/\sigma_{\text{exp}}$ and observed $\Delta\sigma_{\text{obs}}/\sigma_{\text{obs}}$ t-channel cross-section measurement.*

7.4 Results

In this analysis an integrated luminosity of $1.04\,\text{fb}^{-1}$ of data recorded by the ATLAS detector at a centre-of-mass energy of 7 T*e*V is studied. The cross-section of the single top-quark t-channel production is measured in a signal enriched dataset having two or three jets. Exactly one of the jets is required to be b-tagged. Also, one high p_T electron or muon and large $E_{\text{T}}^{\text{miss}}$ is demanded to be present in the event. The significance of the measurement is determined to distinguish the interpretation of the observed events as signal from a statistical fluctuation of the background processes. Using the result of the cross-section measurement, the absolute value of the CKM matrix element V_{tb} is extracted.

Cross-Section Measurement

The single top-quark t-channel cross-section is measured by a simultaneous binned maximum-likelihood fit of the NN output distributions to the NN distribution of observed data in the 2-jet and 3-jet channel. Using the SM expectations and the results of the systematic uncertainties evaluation as presented in section 7.3.2 the expected measurement yields

$$\sigma_{\text{expected}}^{t-\text{channel}} = 65 \pm 4\,(\text{stat.})\,^{+16}_{-15}\,(\text{syst.})\,\text{pb} = 65\,^{+17}_{-16}\,\text{pb}. \tag{7.14}$$

Since the systematic uncertainties are much larger than the uncertainty due to the data statistics, the precision of the measurement is limited by the impact of the systematic uncertainties. The fit to observed data yields an observed cross-section of

$$\sigma_{\text{observed}}^{t-\text{channel}} = 83 \pm 4\,(\text{stat.})\,^{+20}_{-19}\,(\text{syst.})\,\text{pb} = 83 \pm 20\,\text{pb}. \tag{7.15}$$

A result, which is 28% larger than the SM expectation is found. But, the observed result is compatible with the theoretical cross-section value within the statistical and systematic uncertainties.

Significance

To distinguish the interpretation of the observed result as signal from a fluctuation of background events, a test statistic based on a likelihood ratio is used. A detailed description of the method is given in section 7.1.3. To compute the significance, $2.1 \cdot 10^9$ pseudo experiments are generated including all sources of systematic uncertainties. The Q-value distributions of the null- and alternative hypothesis are shown in Fig. 7.10. Only two pseudo experiments are smaller than the expected Q-value of $Q_{\text{exp}} = -415$. Thus, the expected p-value is $9.7 \cdot 10^{-10}$. It corresponds to a significance of 6σ in

terms of standard deviations, which exceeds the 5σ threshold of a measurement to be statistically significant.

The fit to observed data obtains a Q-value of $\tilde{Q}_0 = -530$. No single pseudo experiment of the q_0 distribution has a Q-value smaller than $\tilde{Q}_0$. To deduce the observed significance an approximation is necessary, because it is not feasible to create more pseudo experiments. For a sufficient statistics to populate the tails of the q_0 distribution roughly 10 times more pseudo experiments are necessary, which is very CPU time consuming. Thus, a Gaussian function is used to extrapolate the tail of the q_0 distribution for Q-values smaller than 0. Using the extrapolation, a p-value of $3.9 \cdot 10^{-13}$ corresponding to 7.2σ is observed. Summarising the results of the hypothesis test for the given dataset, the expected and observed significance of the measurement are 6σ and 7.2σ, respectively. This result shows the statistical significance of the single top-quark t-channel production cross-section measurement.

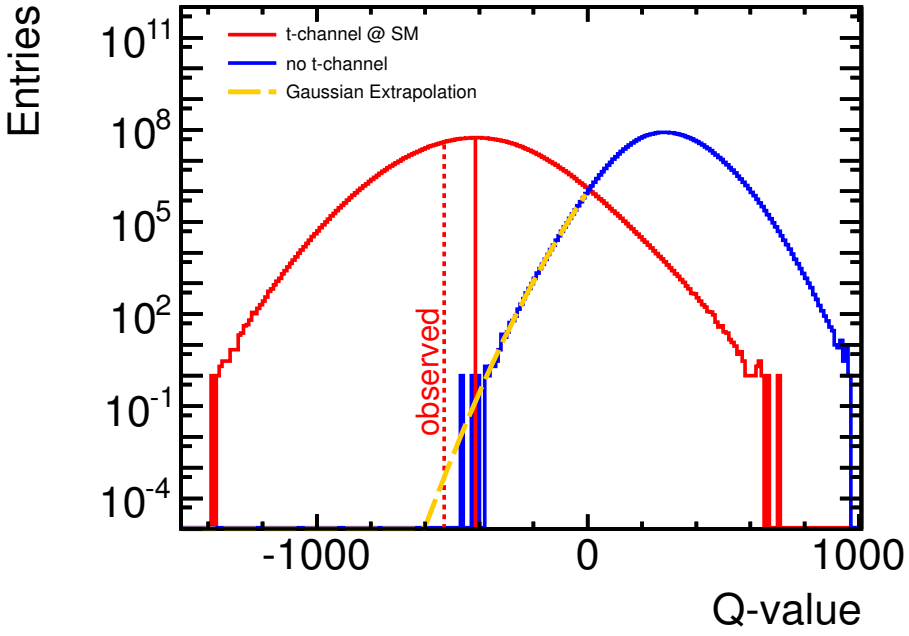

Figure 7.10: *The Q-value distributions the signal hypothesis (red) and the background only hypothesis (blue) are shown. The expected Q-value is the median of the signal hypothesis distribution, whereas the observed Q-value is obtained from the fit to collision data. The tail of the background hypothesis is extrapolated using a Gaussian function.*

Extraction of V_{tb}

The t-channel production cross-section of singly produced top quarks involves the W-t-b vertex. Thus, it is proportional to the CKM-matrix element $|V_{tb}|^2$. In the SM with three generations of quarks, the V_{tb} matrix element is close to one. It is only obtained indirectly due to the unitarity constraint of the CKM matrix. Using the observed cross-section, the absolute value of $|V_{tb}|$ can be extracted independently of the assumption of

three generations of quarks and the unitarity constraint. Contributions of new physics processes may alter the W-t-b coupling to significantly larger values. Only two assumptions have to be made for the extraction. The first assumption is the left handedness of the weak interaction. The second assumption is that the top quark predominantly decays to b quarks. For a measurement of $|V_{tb}|^2$ being independent of the b-tagging requirement of the analysis, it has to be assumed that $|V_{tb}| \gg |V_{td}|, |V_{ts}|$. This assumption is tested by measuring the branching ratio of top quarks decaying into b-jets $\mathcal{B}(t \to Wb)$ to all jet flavours $\mathcal{B}(t \to Wq)$ defined as $R = \mathcal{B}(t \to Wb)/\mathcal{B}(t \to Wq)$ by counting the number of b-tagged jets in selected $t\bar{t}$ events. A ratio of $R = 0.98 \pm 0.04$ being compatible with the SM expectation is observed [157].

The numerical value of $|V_{tb}|$ is obtained from the square root of the ratio of the observed σ^{obs} to the expected cross-section σ^{theo}.

$$|V_{tb}^{\text{obs}}| = \sqrt{\frac{\sigma^{\text{obs}}}{\sigma^{\text{theo}}}} \tag{7.16}$$

The extraction of $|V_{tb}|$ from the cross-section measurement yields a result of $|V_{tb}| = 1.13^{+0.14}_{-0.13}$. The experimental and theoretical uncertainties are added in quadrature. The result is still compatible with the assumptions of the SM. Assuming the SM constraints on $|V_{tb}|$ by requiring $0 < |V_{tb}| < 1$, a lower limit of $|V_{tb}| > 0.75$ at the 95% C.L.is found. Figure 7.11 shows the posterior probability density function of $|V_{tb}|^2$.

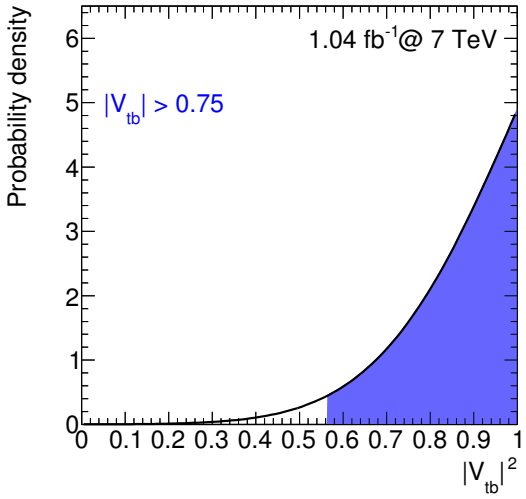

Figure 7.11: *Probability density function of the CKM matrix element* $|V_{tb}|^2$.

Conclusion and Outlook

In the presented analysis, $1.04\,\mathrm{fb}^{-1}$ of data, recorded by the ATLAS experiment during the 2011 data-taking period, are analysed to measure the t-channel single top-quark production cross-section. The final state of the signal process is characterised by a light-quark jet produced predominantly in the forward direction and the decay of the top quark to a W boson and a b quark, $t \to W\,b$. The W boson is reconstructed in the $W \to e\nu$ and $W \to \mu\nu$ mode. Thus, events having missing transverse momentum and an isolated high-p_{T} charged lepton are selected. Some acceptance to $\tau\nu$ events, where the τ decays leptonically, is also contained in the dataset. Additionally, two or three jets are required, whereas one of them is identified as a jet originating from a b quark. Studies on simulated events show that 45% and 30% of the signal events are selected in the 2-jet and 3-jet channel, respectively. The dominant contributions of background events stem from the production of a W boson in association with heavy quark jets and $t\bar{t}$ events. A signal-to-background ratio of roughly one to ten is expected after the final event selection.

The signal and background processes are modelled using MC techniques. Additionally, a data driven method was developed for QCD multijet events, that are misidentified as lepton + jets events. In the context of this analysis the jet-electron model was developed. Here, pure QCD multijet events are selected from a jet-triggered dataset. One of the jets, fulfilling certain requirements is used to model the charged lepton in the event. The amount of selected QCD multijet events in the signal region is estimated by fitting the MC event models and the data-driven model to the missing transverse momentum distribution. It was studied that the amount of multijet background events can be reduced by a factor 2 to 3 by tightening the lepton identification and isolation requirements. In the signal region, a contribution of 8% to 16% is found.

A neural network is trained using the simulated event model to separate signal from background events. In the 2-jet and 3-jet channel, a separate network is trained utilising characteristic kinematic event observables. Template distributions are constructed from the output for the signal and background processes. The signal cross-section is extracted by a combined binned log-likelihood fit of the template distributions to observed data. The fit simultaneously extracts the signal cross-section and the normalisation of the background processes. Especially, the normalisation of the W+heavy flavour process is not predicted well by theory. The influence of the systematic uncertainties on the cross-section measurement is estimated using a frequentist method. Hereby, the effect on the normalisation and the shapes of the NN output distribution is considered for the different sources of systematic uncertainties. In this analysis, a

single-top quark t-channel production cross-section of

$$\sigma^{t-\text{channel}}_{\text{observed}} = 83 \pm 4\,(\text{stat.})\,^{+20}_{-19}\,(\text{syst.})\,\text{pb} = 83 \pm 20\,\text{pb}.$$

is measured. A significance of 7.2σ is observed for the measurement, whereas 6σ are expected. The measured cross-section is 28% larger than the expected cross-section of $64.6\,^{+2.7}_{-2.0}$ pb, but compatible within the uncertainties. The precision of the measurement is limited by the size of the systematic uncertainties of $^{+24}_{-23}$% compared to the statistical uncertainty of 5.1%. Hereby, the dominant uncertainties are ISR/FSR accounting for 14% and the b-tagging calibration accounting for 13%. Systematic uncertainties because of the object modelling, event modelling, and background normalisation are of the size of 4% to 7%. To improve the measurement, the uncertainties on the ISR/FSR and b-tagging calibration have to be reduced. Future measurements will profit from a better understanding of the b-tagging efficiencies in observed data and simulated events, and constraints on the ISR/FSR uncertainty from $t\bar{t}$ measurements studying the additional jet activity of high energetic QCD radiation [156].

Using the measured cross-section to extract $|V_{tb}|$ under the assumption of $|V_{tb}| \gg |V_{td}|, |V_{ts}|$, with the result of $|V_{tb}| = 1.13^{+0.14}_{-0.13}$ is obtained. Within the uncertainty, the result is compatible with the Standard Model value of $|V_{tb}| \approx 1$. Under the assumption of $0 < |V_{tb}| < 1$ a lower limit of $|V_{tb}| > 0.75$ is set at the 95% C.L.

Two alternative methods have analysed the same dataset, a cut-based analysis [141] and an analysis employing a boosted decision tree (BDT) [158]. In the cut-based analysis, a signal enriched region is defined by more stringent cuts on the phase space. The BDT analysis selects a signal enriched region by cutting on the output of the BDT. The cut based analysis observes a cross-section of $\sigma_t = 92 \pm 7\,(\text{stat.})\,^{+28}_{-25}\,(\text{syst.})\,\text{pb} = 92^{+29}_{-26}\,\text{pb}$. A result of $\sigma_t = 97 \pm 7\,(\text{stat.})\,^{+30}_{-29}\,(\text{syst.})\,\text{pb} = 97^{+31}_{-30}\,\text{pb}$ is found by the BDT analysis. All analyses are in agreement within their systematic and statistical uncertainties. The NN analysis presented in this thesis is the most precise measurement among the three ATLAS measurements.

The CMS collaboration has presented preliminary results on the t-channel production cross-section. Here, a dataset of $1.14\,\text{fb}^{-1}$ ($1.51\,\text{fb}^{-1}$) recorded in 2011 is studied in the electron (muon) channel. The signal cross-section is extracted by a likelihood fit to the $|\eta|$-distribution in a signal enriched region having two jets with one of them being identified as b-jet. A signal cross-section of $70 \pm 5.2\,(\text{stat.})10.4 \pm\,(\text{syst.}) \pm 3.4\,(\text{lumi})\,\text{pb}$ is observed [10]. The total uncertainty amounts to 17%. The uncertainty of the CMS measurement is smaller than the one presented in this thesis mostly due to a smaller uncertainty on ISR/FSR of ±7% on the signal process and a smaller b-tagging uncertainty of ±3.1%. The extraction of the $|V_{tb}|$ matrix elements yields $|V_{tb}| = 1.04 \pm 0.09(\text{exp.}) \pm 0.02(\text{th.})$, under the same assumptions as stated above. The CMS measurement is in agreement with the Standard Model prediction and the ATLAS results. A summary of the measurements is given in Fig. 8.12.

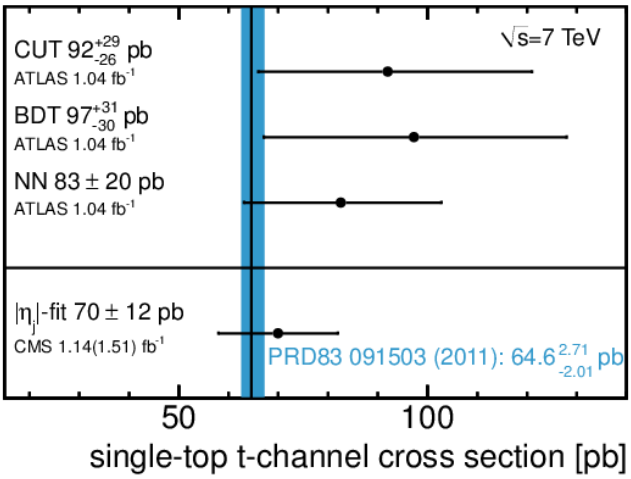

Figure 8.12: *Summary of the ATLAS and CMS single top-quark t-channel cross-section results. The experimental ATLAS results are documented in [141, 151, 158], the CMS result in [10], and the theoretical prediction is obtained from [4].*

For future measurements, the systematic uncertainties have to be revisited to improve the precision of the measurement. With a larger amount of observed data, the cross-section measurement can be redone for the t and $\bar{t}$ production separately or the cross-section ratio $\sigma_t/\sigma_{\bar{t}}$. Since a b quark is in the initial state of the process, the cross-section ratio measurement is sensitive to constrain the b-quark PDF. The NN can be used to select a highly signal enriched region by cutting on large NN output values. Thus, the kinematic event model of the signal process can be validated.

Appendix A

QCD estimation and control distributions

A.1 Comparison of the jet-electron event shapes in the tagged and pretag dataset

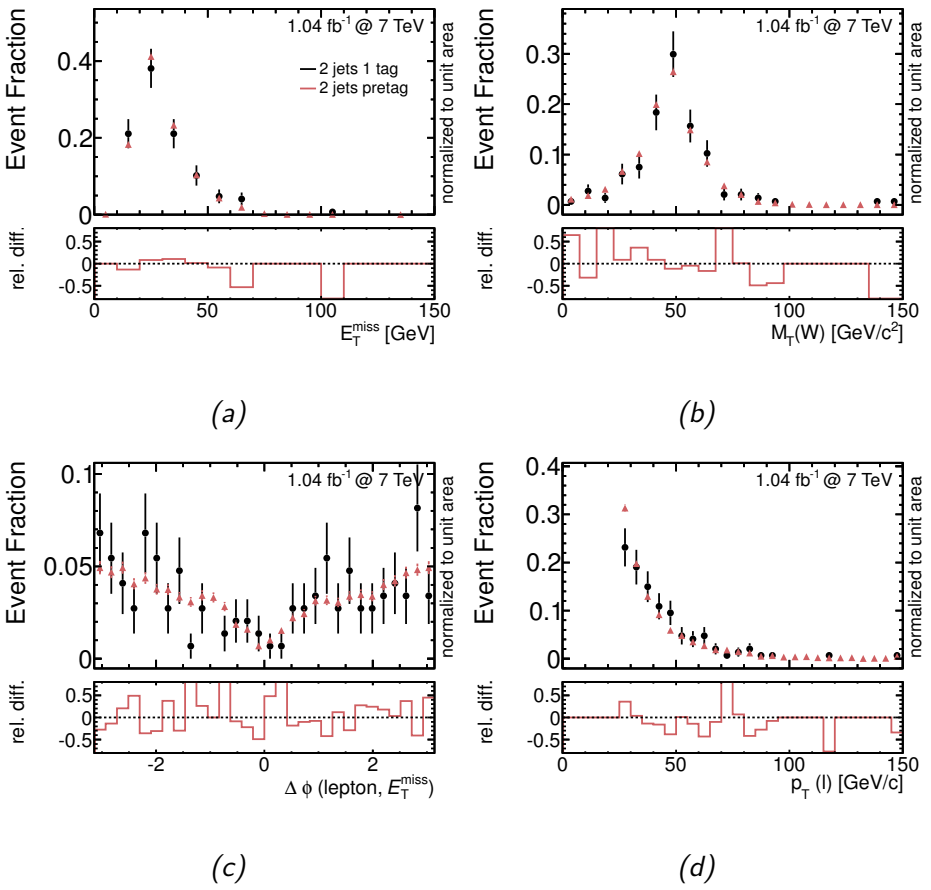

Figure A.1: *Comparison of the jet-electron model in the tagged and pretag dataset with 2 jets. The tagged jet electron model is limited by low statistics. It is compatible with the pretag model within the statistical uncertainty. No* $E_{\mathrm{T}}^{\mathrm{miss}}$ *cut is applied.*

A.2 Fitted $E_{\mathrm{T}}^{\mathrm{miss}}$ distributions in the electron channel

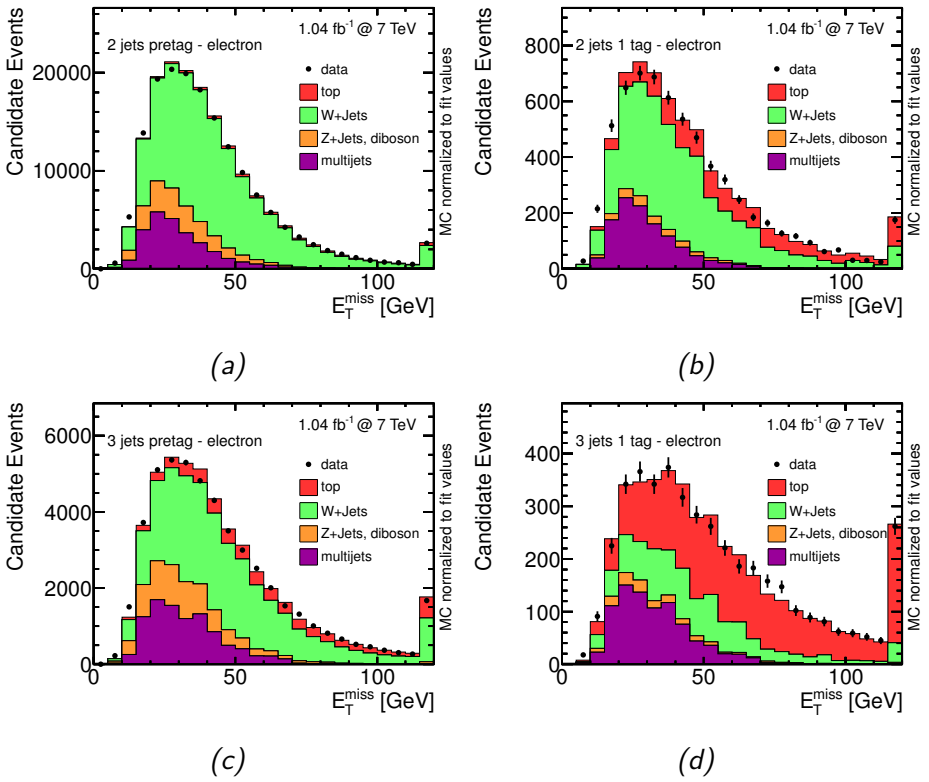

Figure A.2: *$E_{\mathrm{T}}^{\mathrm{miss}}$ distribution of the pretag dataset (a) and (c), and tagged dataset (b) and (d) for the 2-jet and 3-jet electron channel. A binned maximum-likelihood fit was performed to determine the fraction of QCD-multijet events. The shape of the QCD-multijet background is modelled by the jet-electron model. The fit is performed after the triangular cut in the pretag and in the tagged dataset.*

A.3 Control distributions for the fit of the jet-electron model in the electron channel

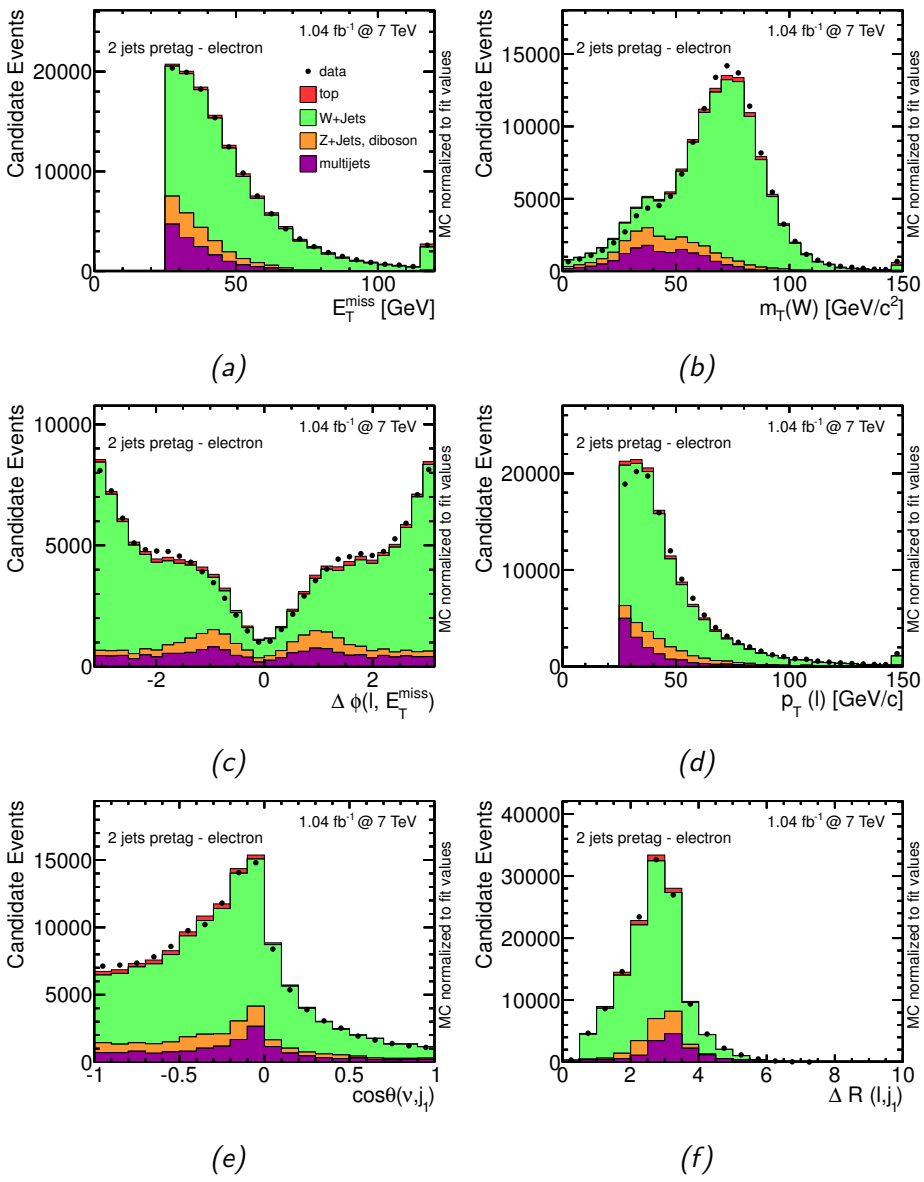

Figure A.3: *Control Plots for the jet-electron model after all cuts in the signal region (pretag) for the electron channel in the 2-jet channel. The $E_{\mathrm{T}}^{\mathrm{miss}}$ (a), the reconstructed transverse W boson mass (b), the $\Delta\phi$ between the charged lepton and the $\vec{E}_{\mathrm{T}}^{miss}$ (c), the p_{T} of the charged lepton (d), the $\cos\theta$ between the leading jet and the reconstructed neutrino (e), the ΔR between the charged lepton and leading jet (f).*

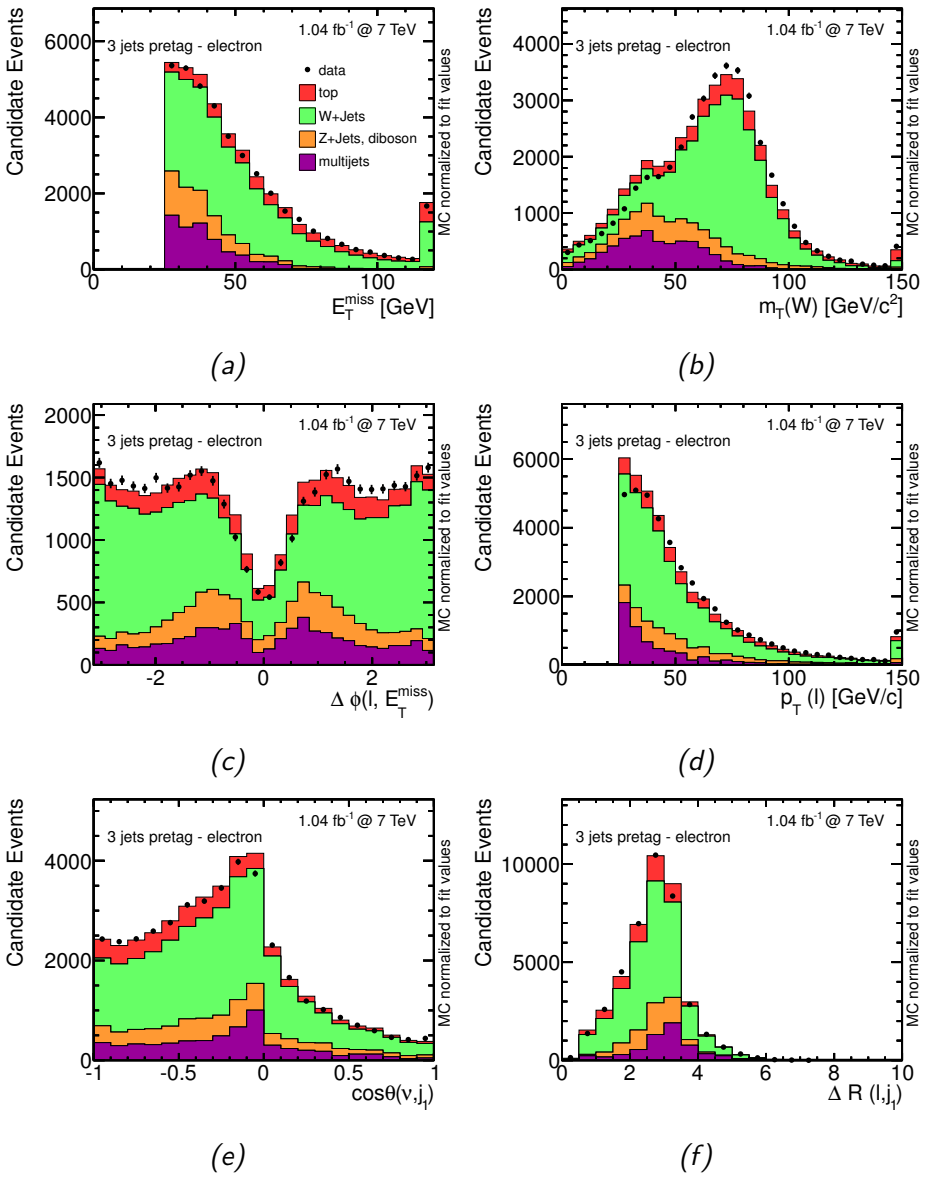

Figure A.4: *Control Plots for the jet-electron model after all cuts in the signal region (pretag) for the electron channel in the 3-jet channel. The $E_{\mathrm{T}}^{\mathrm{miss}}$ (a), the reconstructed transverse W boson mass (b), the $\Delta\phi$ between the charged lepton and the $\vec{E}_{\mathrm{T}}^{miss}$ (c), the p_{T} of the charged lepton (d), the $\cos\theta$ between the leading jet and the reconstructed neutrino (e), the ΔR between the charged lepton and leading jet (f).*

A.4 Fitted $E_{\mathrm{T}}^{\mathrm{miss}}$ distributions in the muon channel

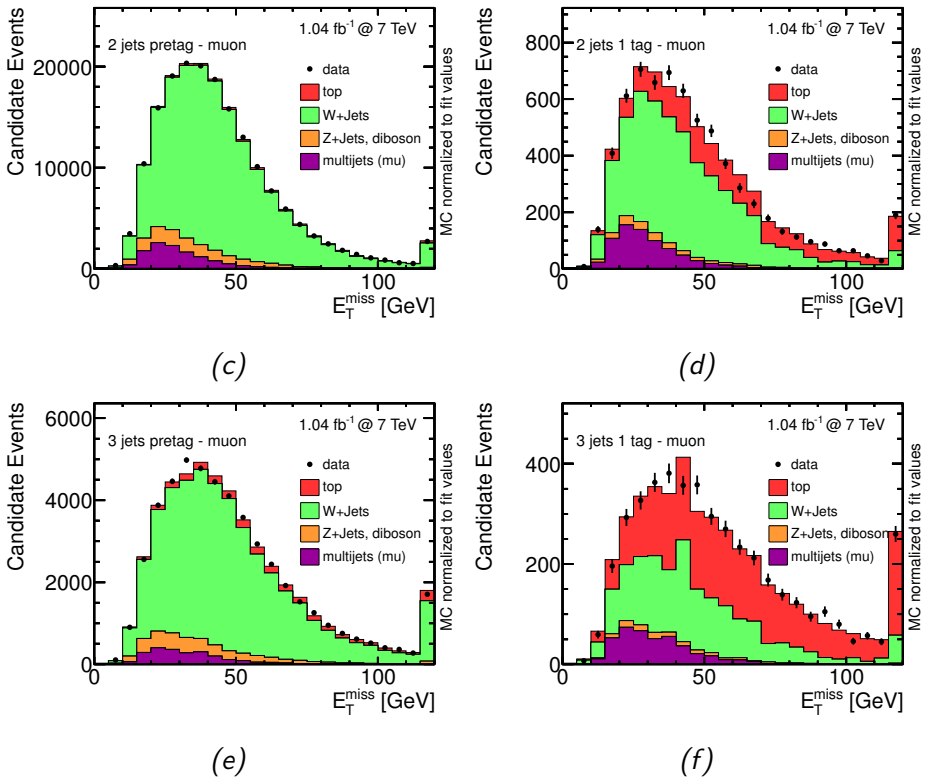

Figure A.5: *$E_{\mathrm{T}}^{\mathrm{miss}}$ distribution for the pretag dataset (a) and (c), and tagged dataset (b) and (d) for the 2-jet and 3-jet muon channel. A binned maximum-likelihood fit was performed to determine the fraction of QCD-multijet events. The shape of the QCD-multijet background is taken from the jet-electron model. The fit is performed after the triangular cut in the pretag and in the tagged dataset.*

A.5 Control distributions for the fit of the jet-electron model in the muon channel

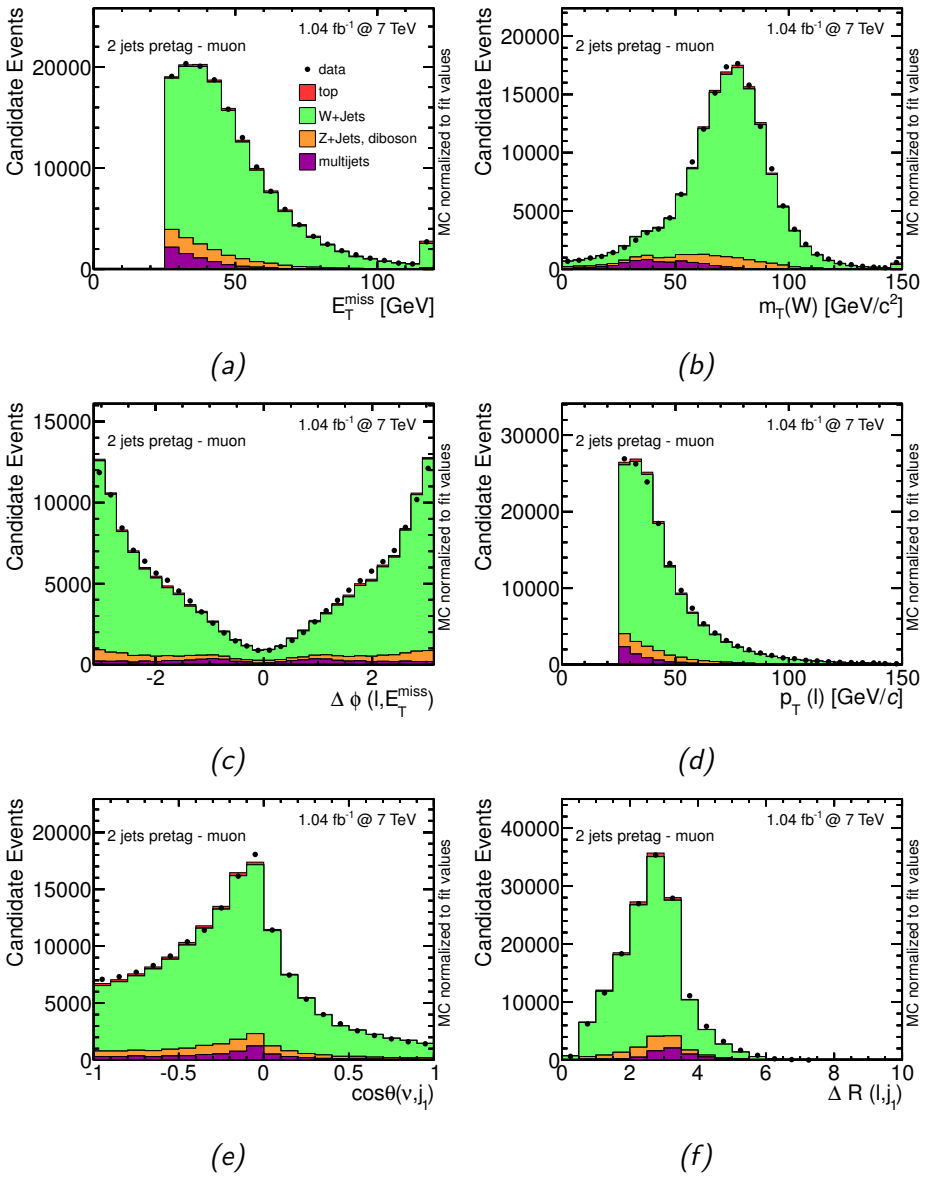

Figure A.6: *Control Plots for the fit of the jet-electron model after all cuts in the signal region (pretag) for the muon channel in the 2-jet channel. The $E_{\mathrm{T}}^{\mathrm{miss}}$ (a), the reconstructed transverse W boson mass (b), the $\Delta\phi$ between the charged lepton and the $\vec{E}_{\mathrm{T}}^{miss}$ (c), the p_{T} of the charged lepton (d), the $\cos\theta$ between the leading jet and the reconstructed neutrino (e), the ΔR between the charged lepton and leading jet (f).*

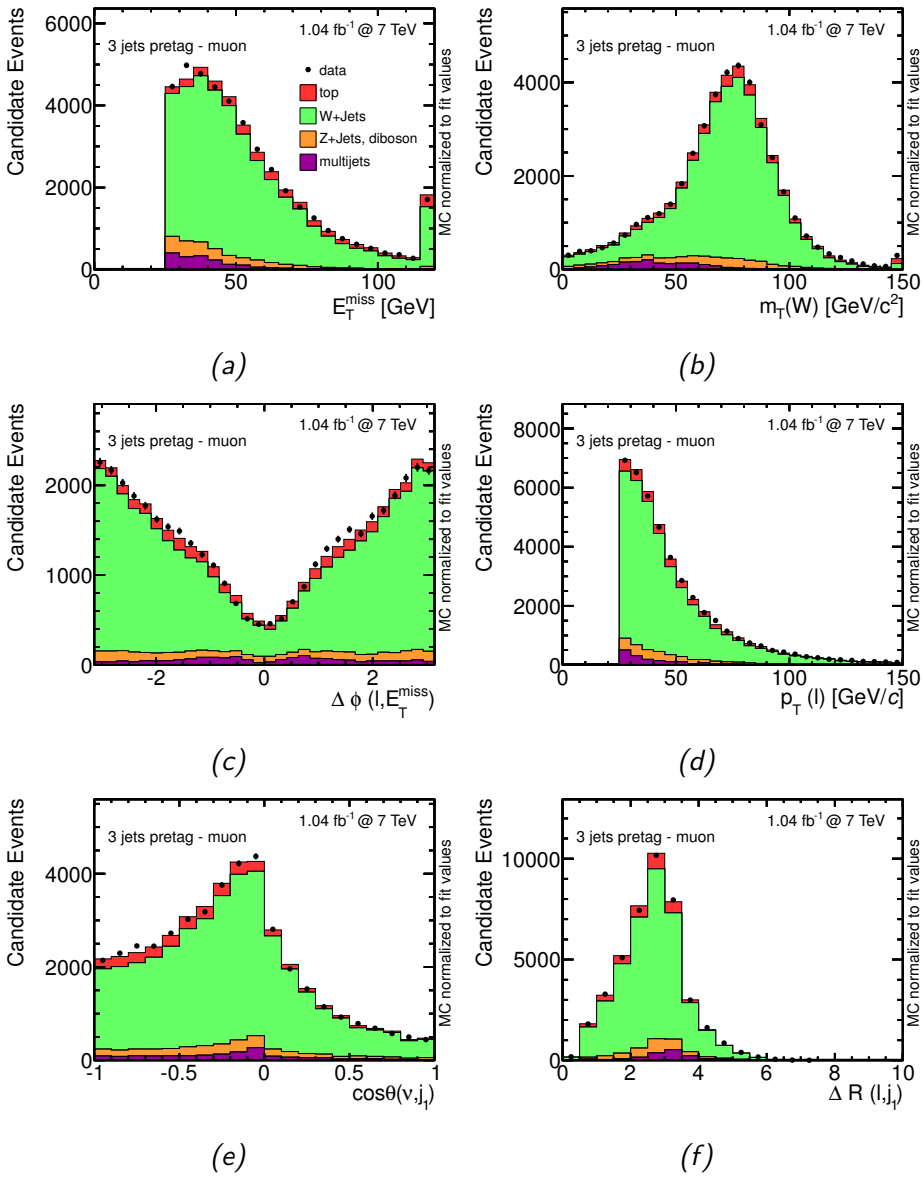

Figure A.7: *Control Plots for the fit of the jet-electron model after all cuts in the signal region (pretag) for the muon channel in the 3-jet channel. The $E_{\mathrm{T}}^{\mathrm{miss}}$ (a), the reconstructed transverse W boson mass (b), the $\Delta\phi$ between the charged lepton and the $\vec{E}_{\mathrm{T}}^{miss}$ (c), the p_{T} of the charged lepton (d), the $\cos\theta$ between the leading jet and the reconstructed neutrino (e), the ΔR between the charged lepton and leading jet (f).*

A.6 Systematic Uncertainty Evaluation

To evaluate the uncertainty on the multijet event yield, the sensitivity to the amount of pile-up events in the events selected for the model is tested. The jet-electron sample is divided into two subsets one with less than six primary vertices and one with six or more primary vertices. The fit to the $E_{\mathrm{T}}^{\mathrm{miss}}$ distribution is redone for each sample separately. In the electron and muon channel, a variation between ±20 % is observed. The results are shown in Tab. A.1 and A.2.

Additionally, the fit is redone after all selection cuts, including the cut on $E_{\mathrm{T}}^{\mathrm{miss}} > 25\,GeV$ in the $m_{\mathrm{T}}(W)$ distribution. Here, the comparison with the nominal results shows a variation within ±50%. Thus, a rate uncertainty of 50% is assigned to the result of the multijet background event yield.

	2 Jets		3 Jets	
	Pretag [%]	Tagged [%]	Pretag [%]	Tagged [%]
Number of Vertices ≥ 6	−8	−17	−15	21
Number of Vertices < 6	−17	8	12	8
$m_{\mathrm{T}}(W)$	48	38	53	−49

Table A.1: *Variation of the multijet event yield in the electron channel, obtained by fitting the jet-electron sample constructed with events having six and more primary vertices and less than six primary vertices. The fit is also done in the $m_{\mathrm{T}}(W)$-distribution with the nominal jet-electron sample to estimate the uncertainty of the method. The deviation is with respect to the event yield obtained from the default procedure.*

	2 Jets		3 Jets	
	Pretag [%]	Tagged [%]	Pretag [%]	Tagged [%]
Number of Vertices ≥ 6	−12	−22	−32	−23
Number of Vertices < 6	18	16	0.4	13
$m_{\mathrm{T}}(W)$	24	−16	29	20

Table A.2: *Variation of the multijet event yield in the muon channel, obtained by fitting the jet-electron sample construes with events having six and more primary vertices and less than six primary vertices. The fit is also done in the $m_{\mathrm{T}}(W)$-distribution with the nominal jet-electron sample to estimate the uncertainty of the method. The deviation is with respect to the event yield obtained from the default procedure fitting the $E_{\mathrm{T}}^{\mathrm{miss}}$-distribution.*

Appendix B

Validation of the Input Variables

B.1 Discriminating Variables in the 2-Jet Pretag Channel

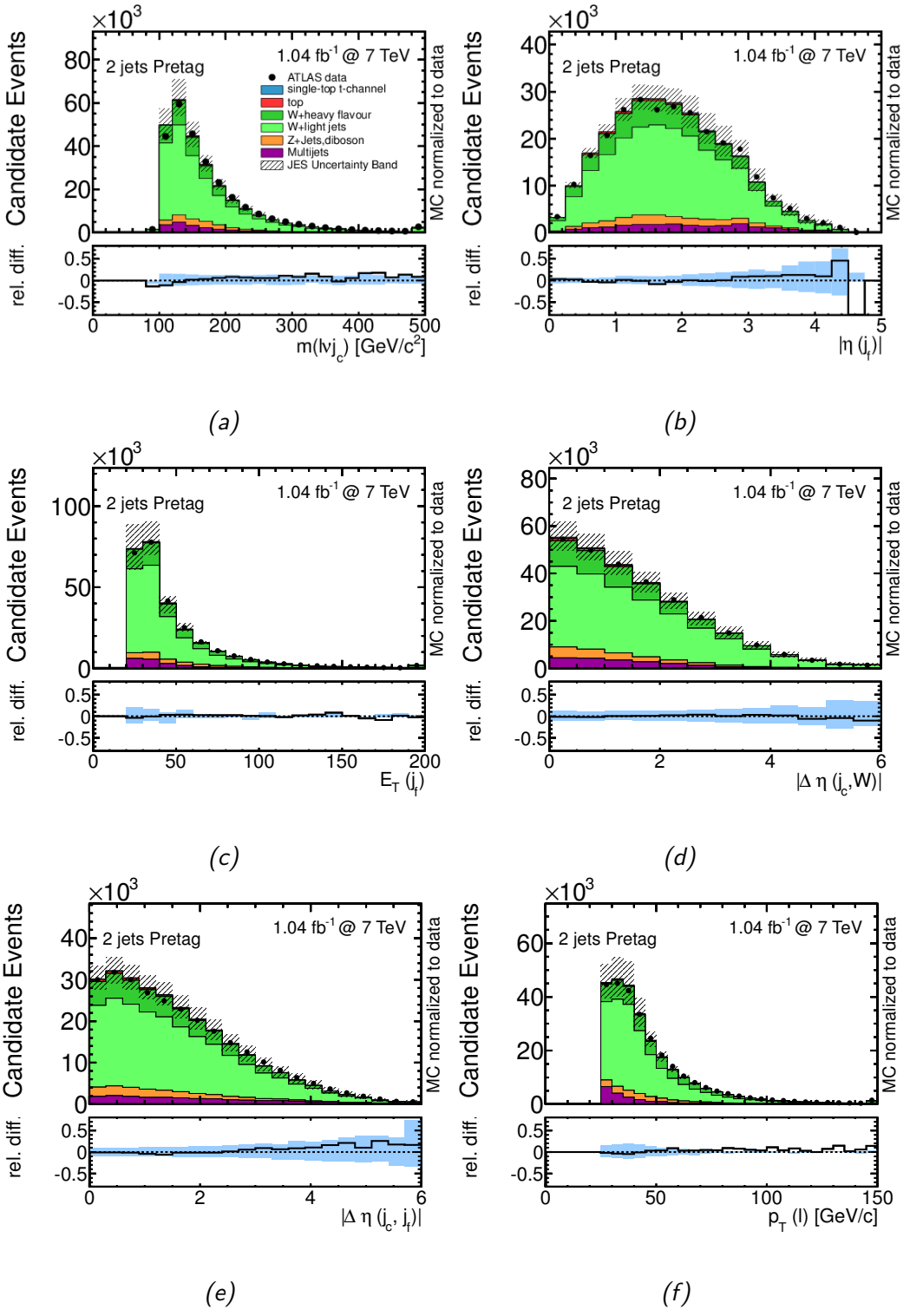

Figure B.1: *Validation of the discriminating variables in the pretag dataset. The overall MC expectation is scaled to the number of observed data events by respecting the individual cross sections. The error band is due to the uncertainty of the JES for all MC processes. The reconstructed top-quark mass (a), the $|\eta|$ of the untagged jet (b), the transverse energy E_{T} of the untagged jet (c), the absolute value of the $|\Delta\eta|$ between the central jet and the reconstructed W boson (d), the absolute value of the $|\Delta\eta|$ between the central jet and untagged jet (e), and the p_{T} of the charged lepton (f).*

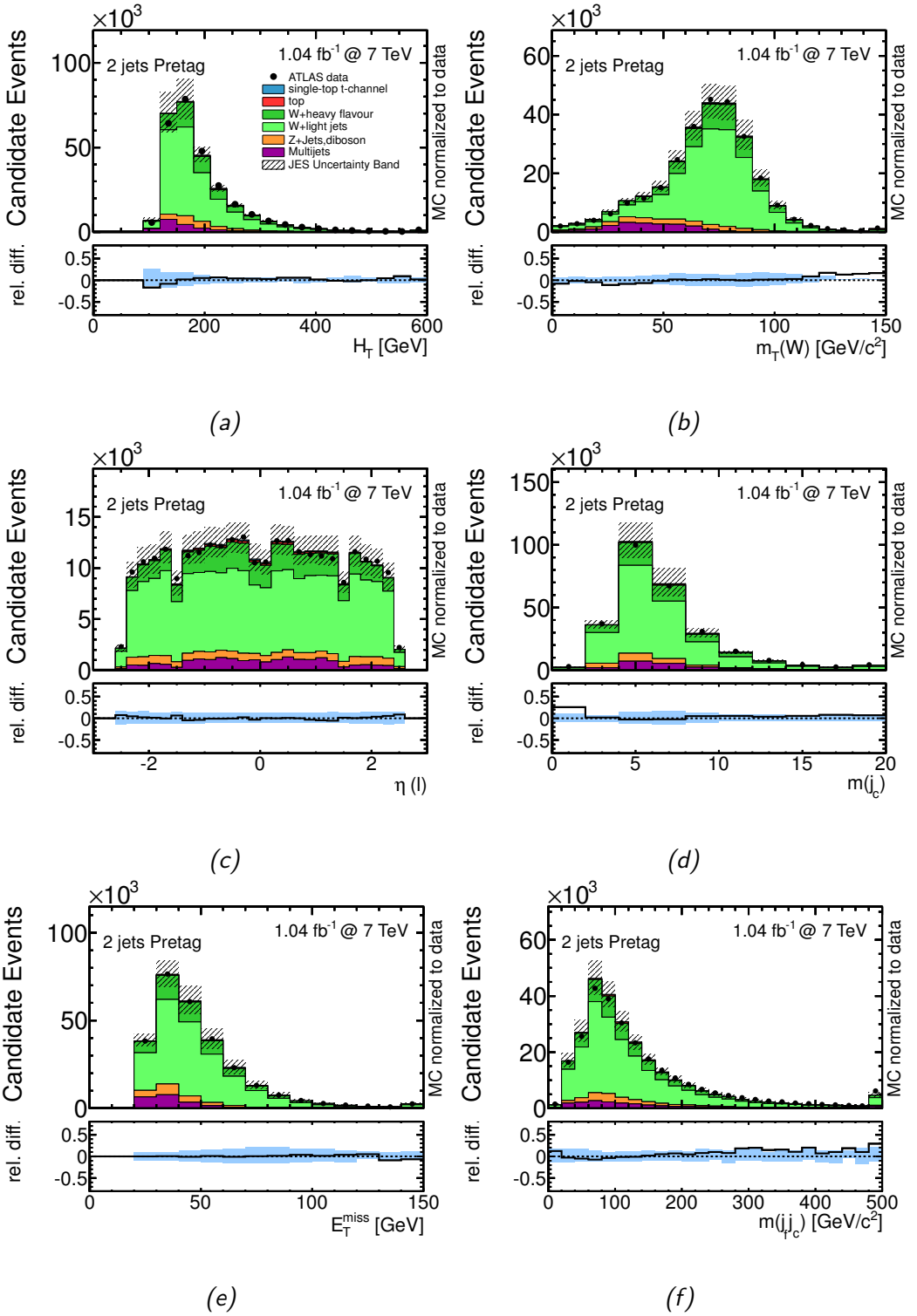

Figure B.2: *Validation of the discriminating variables in the pretag dataset. The overall MC expectation is scaled to the number of observed data events by respecting the individual cross sections. The error band is due to the uncertainty of the JES for all MC processes. The scalar sum of the transverse momenta of the jets, missing transverse momentum and lepton (a), the reconstructed transverse mass of the W boson (b), the pseudorapidity of the charged lepton (c), the mass of the central jet (d), the missing transverse momentum (e), and the invariant mass of the central jet and untagged jet (f).*

B.2 Discriminating Variables in the 3-Jet Pretag Channel

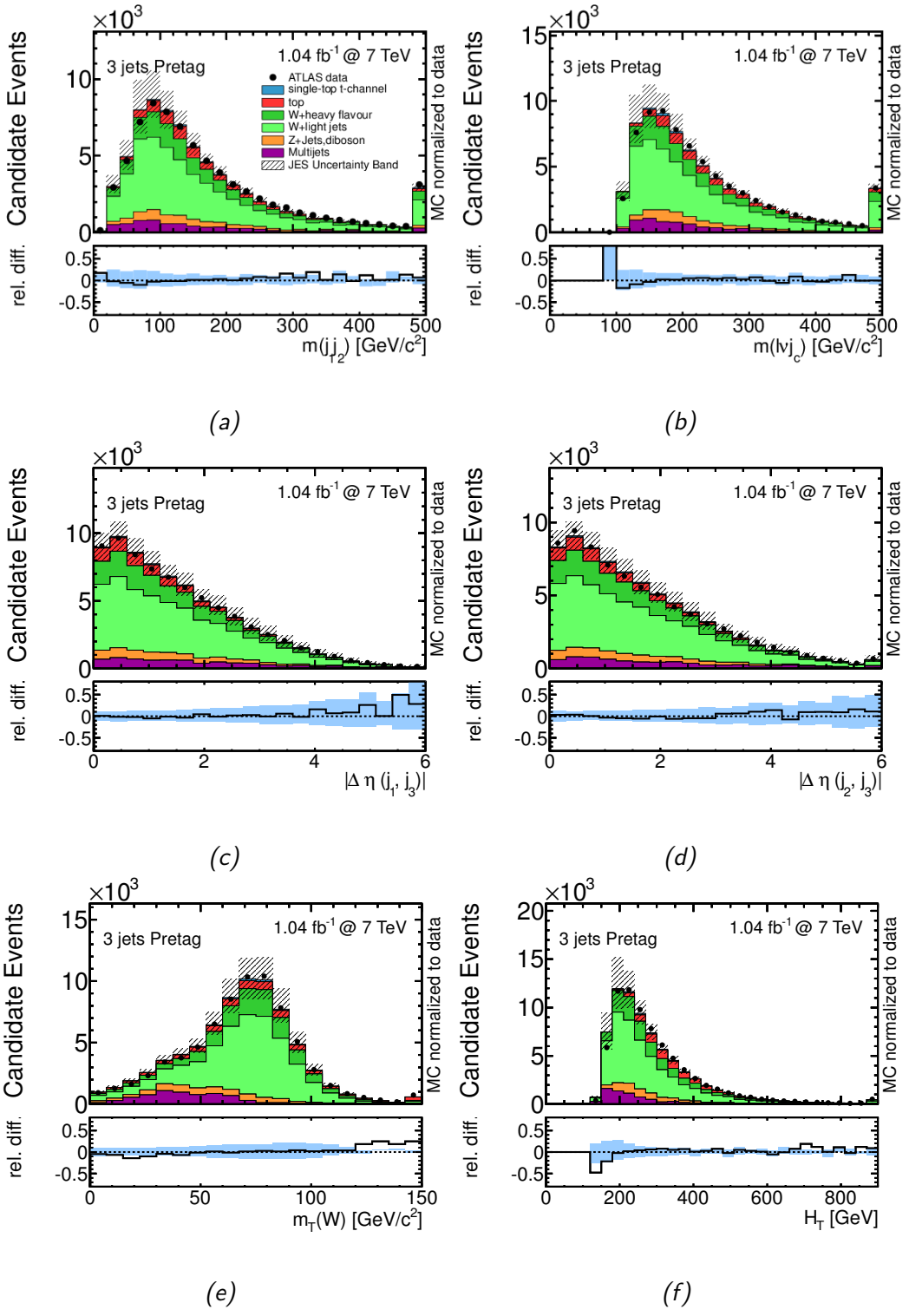

Figure B.3: *Validation of the discriminating variables in the pretag dataset. The overall MC expectation is scaled to the number of observed data events by respecting the individual cross sections. The error band is due to the uncertainty of the JES for all MC processes. The invariant mass of the leading and second leading jet (a), the reconstructed top-quark mass (b), the $|\Delta\eta|$ between the leading and third leading jet (c), the $|\Delta\eta|$ between the second and third leading jet (c) (d), the reconstructed transverse mass of the W boson (e), and the scalar sum of the p_{T} of the jets, the lepton and the $\vec{E}_{\mathrm{T}}^{miss}$ (f).*

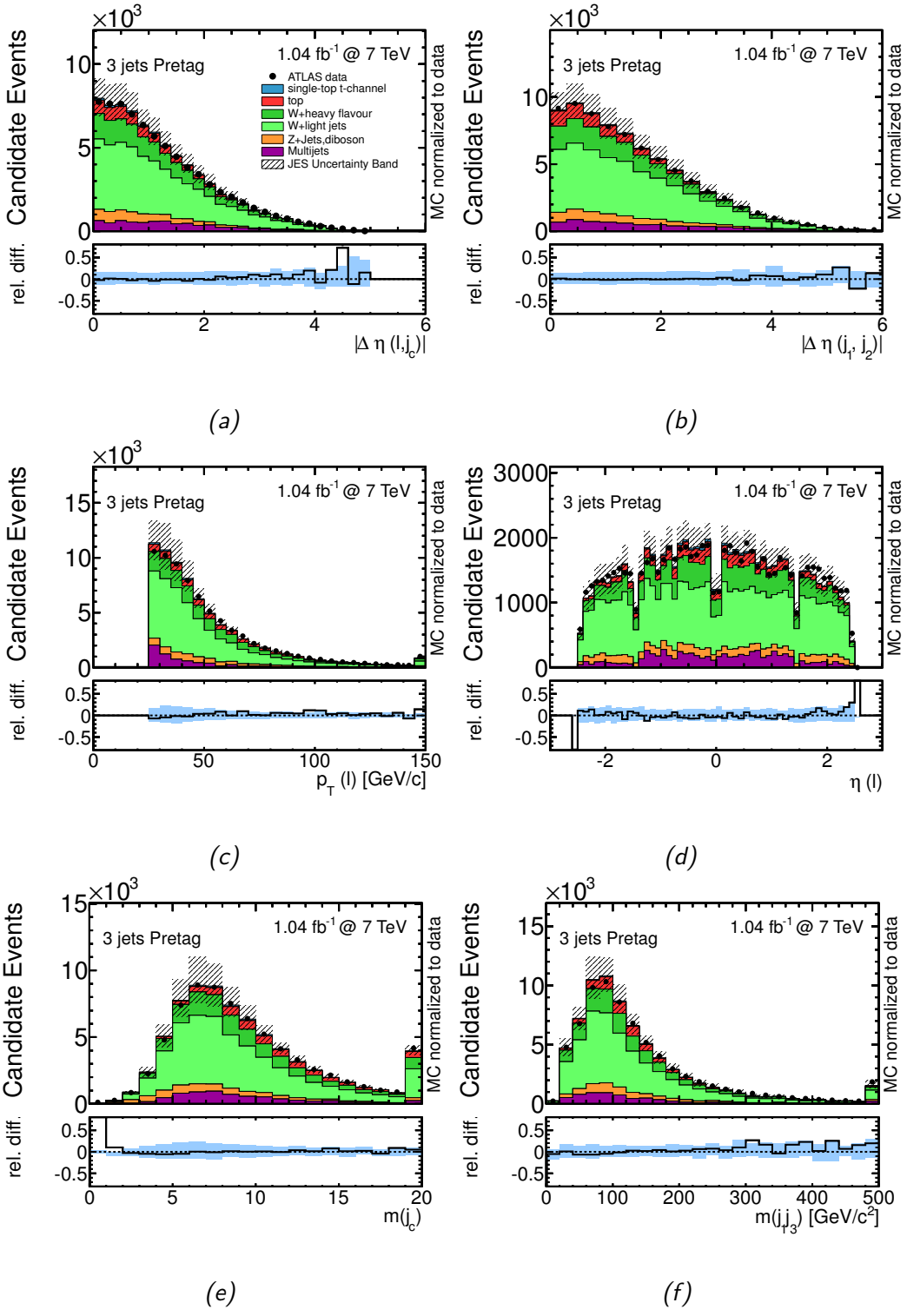

Figure B.4: *Validation of the discriminating variables in the pretag dataset. The overall MC expectation is scaled to the number of observed data events by respecting the individual cross sections. The error band is due to the uncertainty of the JES for all MC processes. The $|\Delta\eta|$ between the charged lepton and the central jet (a), the $|\Delta\eta|$ between the leading and second leading jet (b), the p_T of the charged lepton (c), the η of the charged lepton (d), the mass of the four vector of the central jet (e), and the invariant mass of the leading and third leading jet (f).*

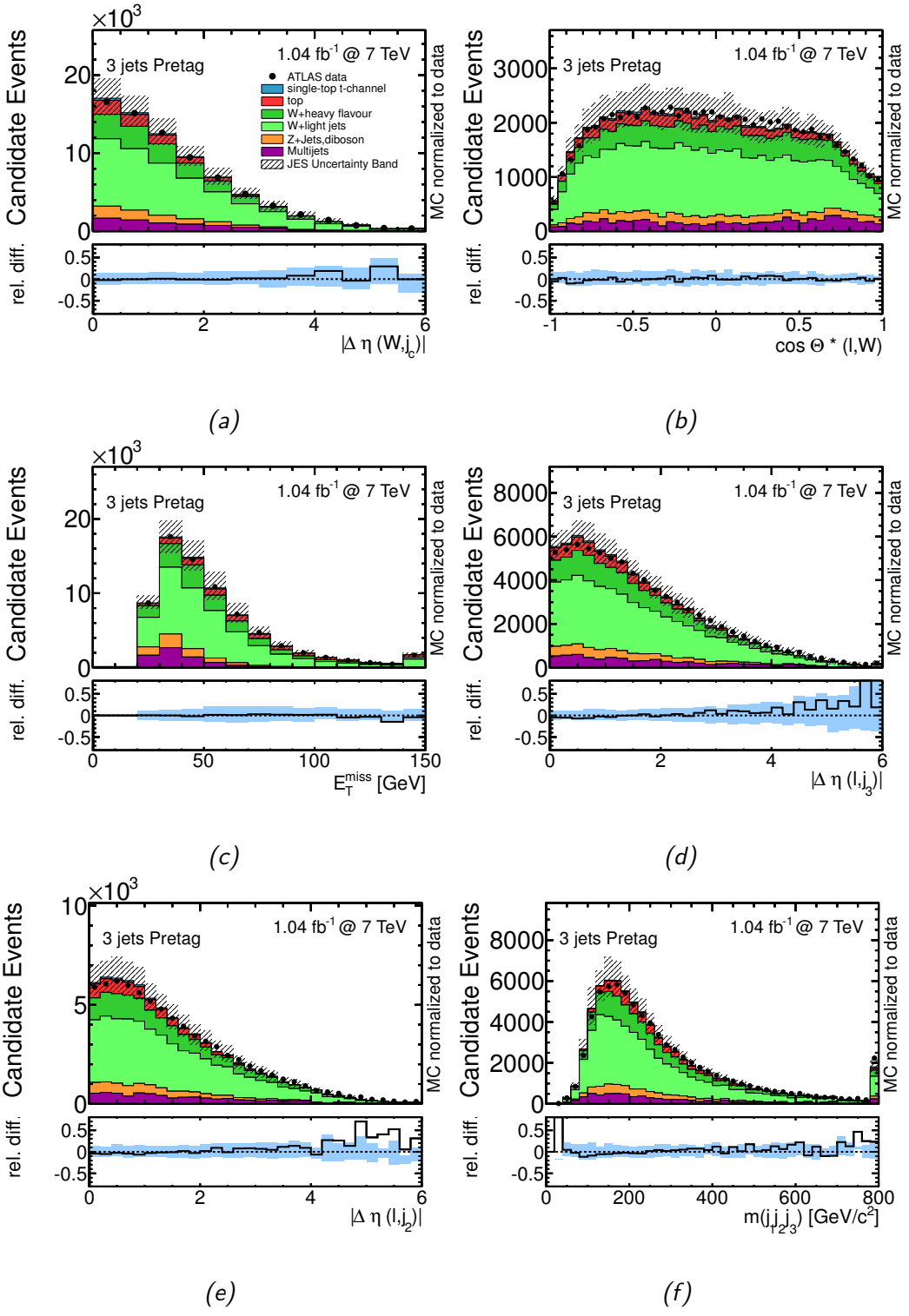

Figure B.5: *Validation of the discriminating variables in the pretag dataset. The overall MC expectation is scaled to the number of observed data events by respecting the individual cross sections. The error band is due to the uncertainty of the JES for all MC processes. The $|\Delta\eta|$ between the reconstructed W boson and the central jet (a), the helicity angle of the W boson decay (b), the missing transverse momentum (c), the $|\Delta\eta|$ between the charged lepton and the third leading jet (d), the $|\Delta\eta|$ between the charged lepton and the second leading jet (e), and the invariant mass the three jets in the event (f).*

Appendix C

Input Variables Normalised to Fit Result

C.1 Discriminating Variables in the Two Jets Channel

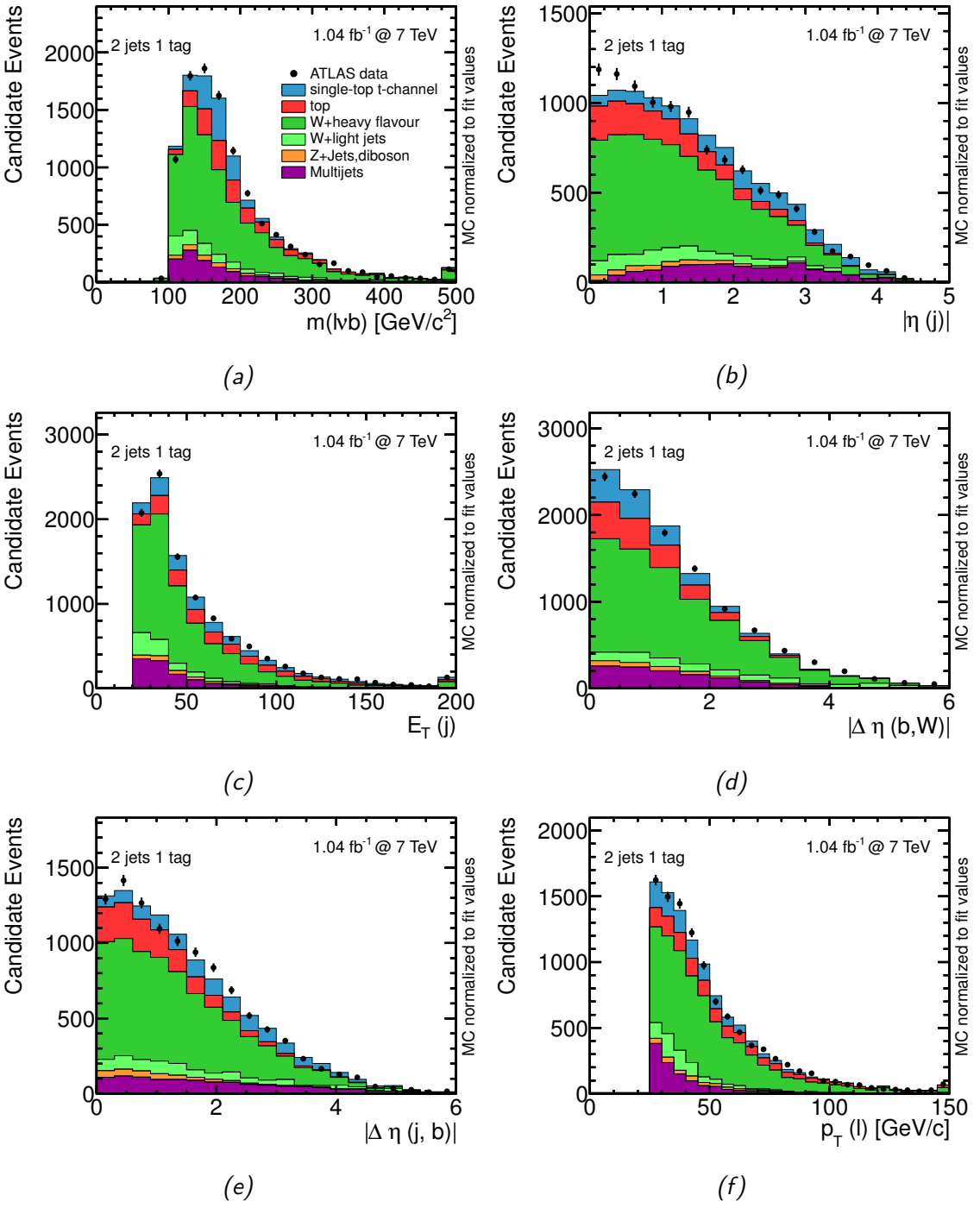

Figure C.1: *The input variables of the two jet NN. The simulated event model is normalised to the result of the binned likelihood fit. The reconstructed top-quark mass (a), the $|\eta|$ of the untagged jet (b), the transverse energy E_{T} of the untagged jet (c), the $|\Delta\eta|$ between the b-tagged jet and the reconstructed W boson (d), the $|\Delta\eta|$ between the untagged and b-tagged jet (e), and the p_{T} of the charged lepton (f).*

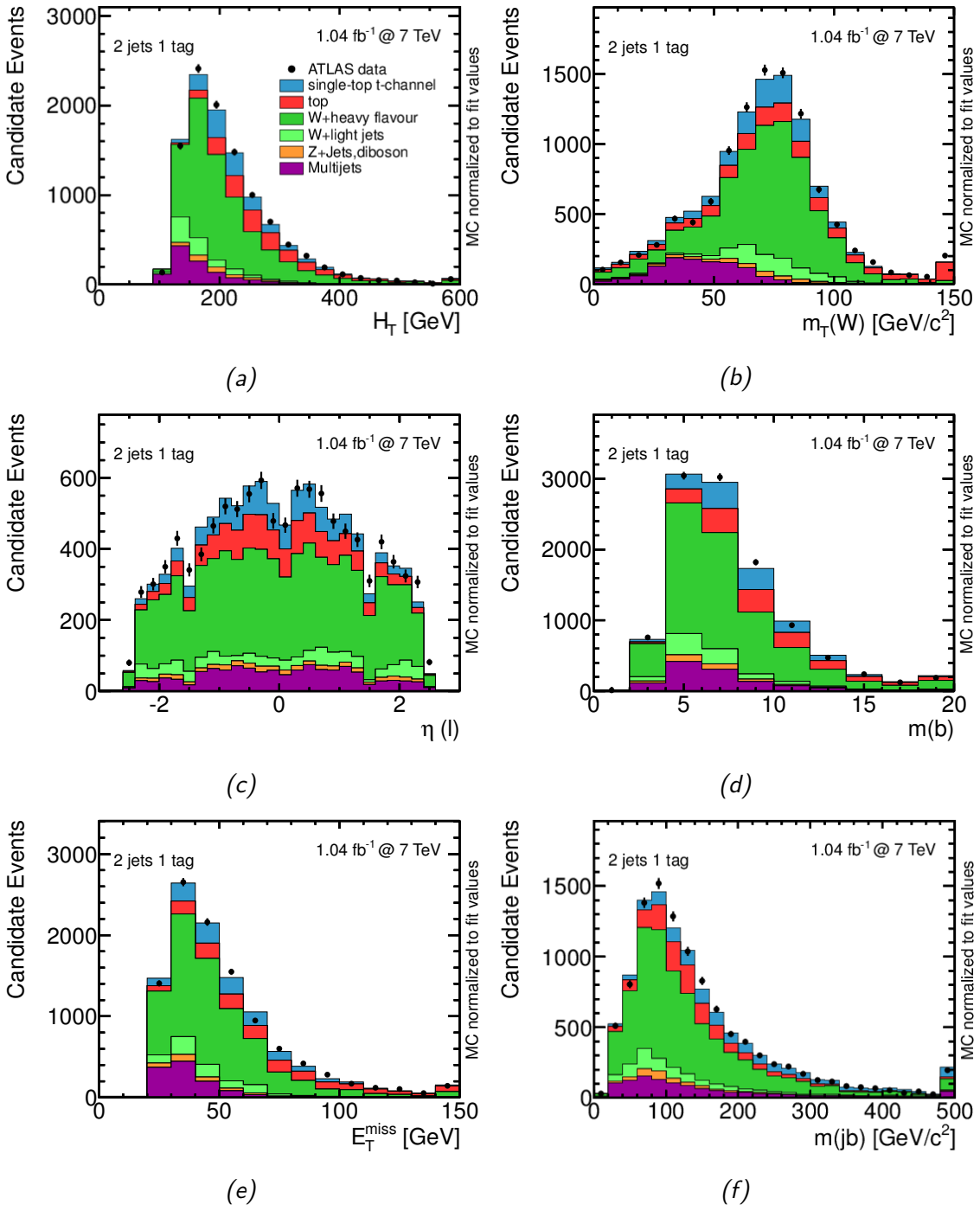

Figure C.2: *The input variables of the two jet NN. The simulated event model is normalised to the result of the binned likelihood fit. The scalar sum of the missing transverse momentum and the transverse momenta of the jets and the charged lepton (a), the reconstructed transverse mass of the W boson (b), the pseudorapidity of the charged lepton (c), the mass of the b-tagged jet (d), the missing transverse momentum (e), and the invariant mass of the b-tagged and untagged jet (f).*

C.2 Discriminating Variables in the Three Jets Channel

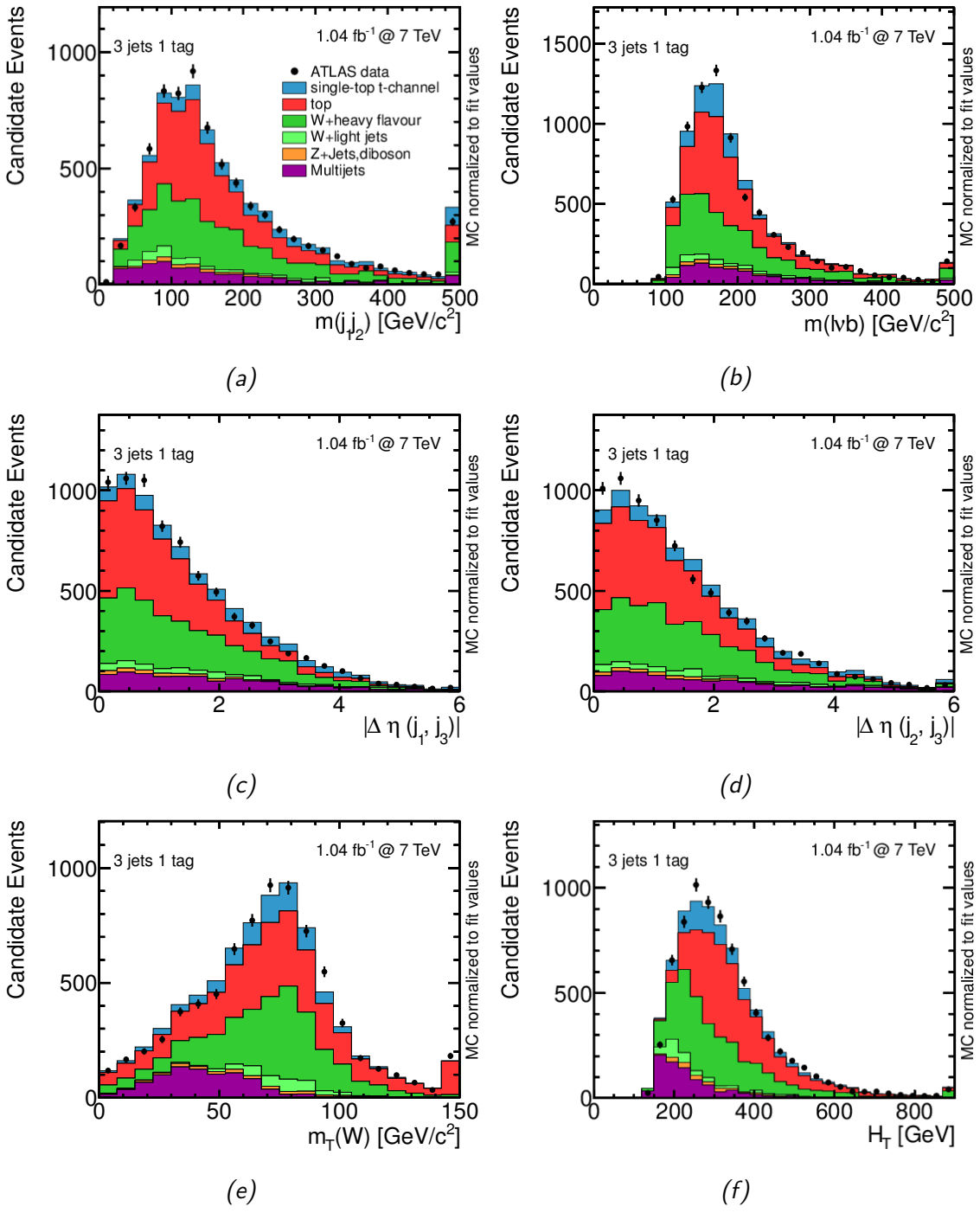

Figure C.3: *The input variables of the three jet NN. The simulated event model is normalised to the result of the binned likelihood fit. The invariant mass of the leading and second leading jet (a), the reconstructed top-quark mass (b), the $|\Delta\eta|$ between the leading and third leading jet (c), the $|\Delta\eta|$ between the second and third leading jet (c) (d), the reconstructed transverse mass of the W boson (e), and the scalar sum of the p_{T} of the jets, the charged lepton, and the $\vec{E}_{\mathrm{T}}^{miss}$ (f).*

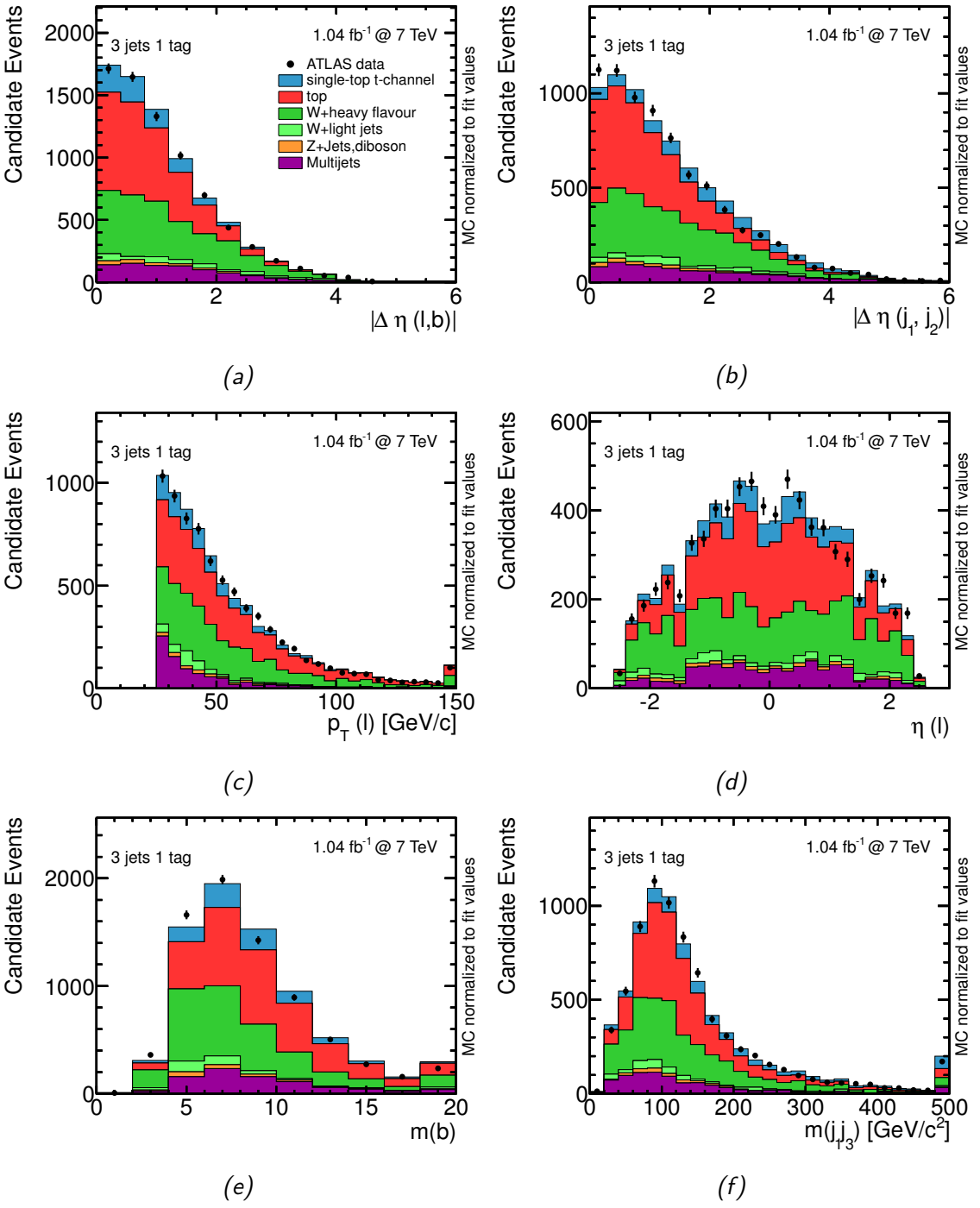

Figure C.4: *The input variables of the three jet NN. The simulated event model is normalised to the result of the binned likelihood fit. The $|\Delta\eta|$ between the charged lepton and the b-tagged jet (a), the $|\Delta\eta|$ between the leading and second leading jet (b), the p_{T} of the charged lepton (c), the η of the charged lepton (d), the mass of the b-tagged jet (e), and the invariant mass of the leading and third leading jet (f).*

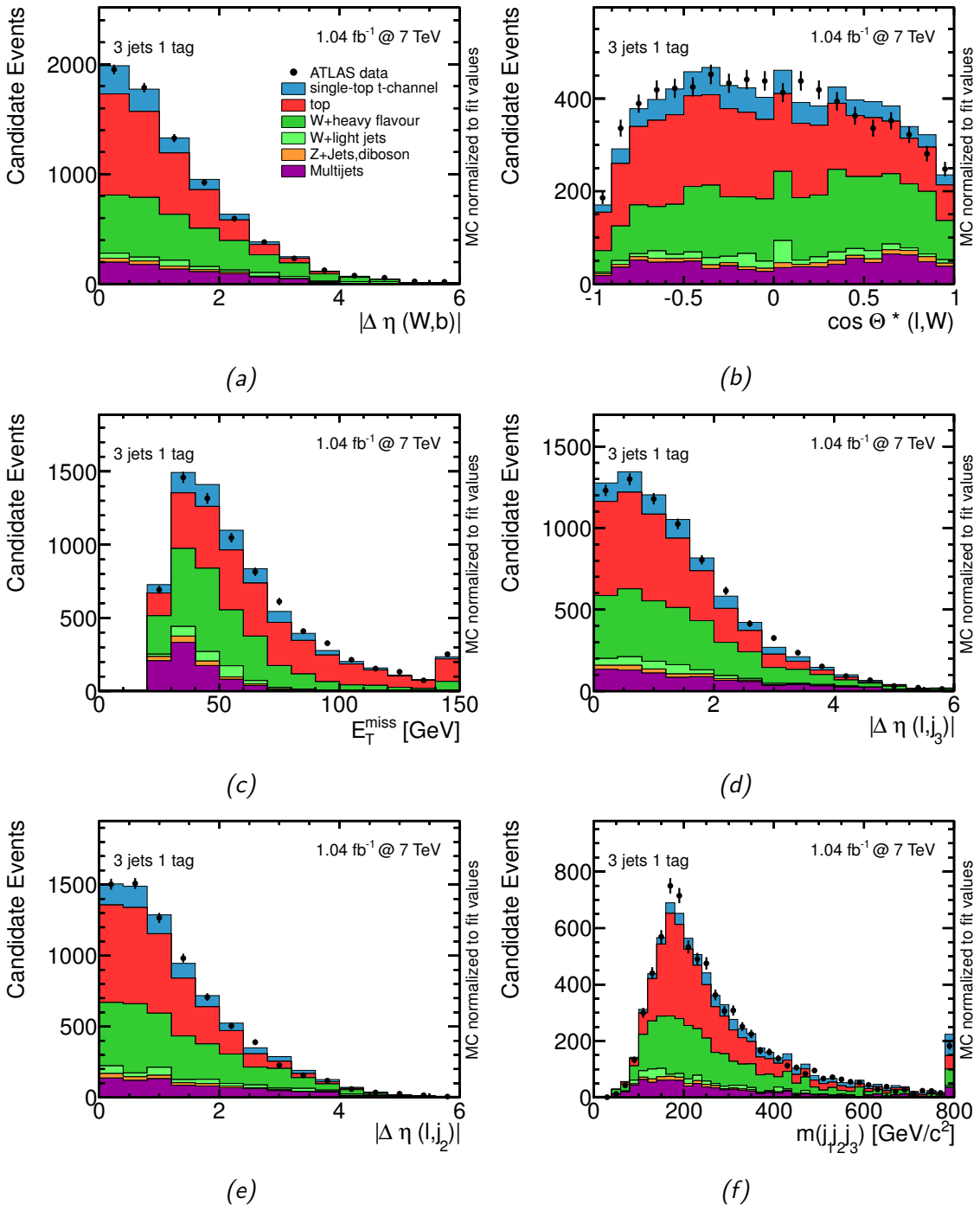

Figure C.5: *The input variables of the three jet NN. The simulated event model is normalised to the result of the binned likelihood fit. The $|\Delta\eta|$ between the reconstructed W boson and the b-tagged jet (a), the helicity angle of the W-boson decay (b), the missing transverse momentum (c), the $|\Delta\eta|$ between the charged lepton and the third leading jet (d), the $|\Delta\eta|$ between the charged lepton and the second leading jet (e), and the invariant mass the three jets in the event (f).*

Bibliography

[1] CDF Collaboration, T. Aaltonen et al., "Observation of Top Quark Production in $P\bar{P}$ Collisions", *Phys. Rev. Lett.* 74 (1995) 2626–2631, arXiv:hep-ex/9503002.

[2] DØ Collaboration, S. Abachi et al., "Observation of the Top Quark", *Phys. Rev. Lett.* 74 (1995) 2632–2637, arXiv:hep-ex/9503003.

[3] Tevatron Electroweak Working Group, for the CDF and DØ Collaborations, "Combination of CDF and DØ results on the mass of the top quark using up to 5.8, fb^{-1} of data", arXiv:1107.5255.

[4] N. Kidonakis, "Next-to-next-to-leading-order collinear and soft gluon corrections for t-channel single top quark production", *Phys. Rev.* D83 (2011) 091503, arXiv:1103.2792.

[5] N. Kidonakis, "Two-loop soft anomalous dimensions for single top quark associated production with a W- or H-", *Phys. Rev.* D82 (2010) 054018, arXiv:1005.4451.

[6] N. Kidonakis, "NNLL resummation for s-channel single top quark production", *Phys. Rev.* D81 (2010) 054028, arXiv:1001.5034.

[7] CDF Collaboration, T. Aaltonen et al., "First Observation of Electroweak Single Top Quark Production", *Phys. Rev. Lett.* 103 (2009) 092002, arXiv:0903.0885.

[8] DØ Collaboration, V.M. Abazov et al., "Observation of Single Top Quark Production", *Phys. Rev. Lett.* 103 (2009) 092001, arXiv:0903.0850.

[9] ATLAS Collaboration, G. Aad et al., "Observation of t Channel Single Top-Quark Production in pp Collisions at $\sqrt{s} = 7\,\text{TeV}$ with the ATLAS detector", *ATLAS-CONF-2011-088* (Jun, 2011).

[10] CMS Collaboration, S. Chatrchyan et al., "Measurement of the single top t-channel cross section in pp collisions at $\sqrt{s} = 7\,\text{TeV}$", *CMS-PAS-TOP-11-021* (2012).

[11] S. Weinberg, "What is quantum field theory, and what did we think it is?", arXiv:hep-th/9702027.

[12] K. Nakamura, Particle Data Group, "Review of Particle Physics", *Journal of Physics G: Nuclear and Particle Physics 37* (2010), no. 7A, 075021.

[13] SNO Collaboration, Q. R. Ahmad et al., "Measurement of the rate of $\nu_e + d \rightarrow p + p + e^-$ interactions produced by B-8 solar neutrinos at the Sudbury Neutrino Observatory", *Phys. Rev. Lett.* 87 (2001) 071301, arXiv:nucl-ex/0106015.

[14] Y. Ashie, et al., "Measurement of atmospheric neutrino oscillation parameters by Super-Kamiokande I", *Phys. Rev. D* 71 (Jun, 2005) 112005.

[15] M. L. Perl, E. R. Lee, D. Loomba, "A Brief review of the search for isolatable fractional charge elementary particles", *Mod. Phys. Lett.* A19 (2004) 2595–2610.

[16] G. 't Hooft, "Renormalizable Lagrangians for Massive Yang-Mills Fields", *Nucl. Phys. B 35* (1971) 167–188.

[17] G. 't Hooft, M. Veltman, "Regularization and Renormalization of Gauge Fields", *Nucl. Phys. B 44* (1972) 189–213.

[18] E. Noether, "Invariante Variationsprobleme", *Nachr. d. König. Gesellsch. d. Wiss. zu Göttingen, Math-phys. Klasse, Seite 235-157* (1918).

[19] H. Fritzsch, M. Gell-Mann, H. Leutwyler, "Advantages of the Color Octet Gluon Picture", *Phys. Lett.* B47 (1973) 365–368.

[20] D. J. Gross, F. Wilczek, "Asymptotically Free Gauge Theories. I", *Phys. Rev. D* 8 (Nov, 1973) 3633–3652.

[21] D. J. Gross, F. Wilczek, "Asymptotically free gauge theories. II", *Phys. Rev. D* 9 (Feb, 1974) 980–993.

[22] M. Kobayashi, T. Maskawa, "CP-Violation in the Renormalizable Theory of Weak Interaction", *Progress of Theoretical Physics* 49 (1973), no. 2, 652–657.

[23] N. Cabibbo, "Unitary Symmetry and Leptonic Decays", *Phys. Rev. Lett.* 10 (Jun, 1963) 531–533.

[24] S. L. Glashow, "Partial Symmetries of Weak Interactions", *Nucl. Phys.* 22 (1961) 579–588.

[25] S. Weinberg, "A Model of Leptons", *Phys. Rev. Lett.* 19 (Nov, 1967) 1264–1266.

[26] A. Salam, J. C. Ward, "Electromagnetic and weak interactions", *Phys. Lett.* 13 (1964) 168–171.

[27] F. Englert, R. Brout, "Broken Symmetry and the Mass of Gauge Vector Mesons", *Phys. Rev. Lett.* 13 (1964) 321–323.

[28] G. S. Guralnik, C. R. Hagen, T. W. B. Kibble, "Global Conservation Laws and Massless Particles", *Phys. Rev. Lett.* 13 (Nov, 1964) 585–587.

[29] P. W. Higgs, "Broken Symmetries and the Masses of Gauge Bosons", *Phys. Rev. Lett.* 13 (Oct, 1964) 508–509.

[30] P. W. Higgs, "Spontaneous Symmetry Breakdown without Massless Bosons", *Phys. Rev.* 145 (May, 1966) 1156–1163.

[31] LEP Working Group for Higgs boson searches, ALEPH Collaboration, DELPHI Collaboration, L3 Collaboration, OPAL Collaboration, R. Barate et al., "Search for the standard model Higgs boson at LEP", *Phys.Lett.* B565 (2003) 61–75, arXiv:hep-ex/0306033.

[32] ATLAS Collaboration, G. Aad et al., "Combined search for the Standard Model Higgs boson using up to 4.9 fb^{-1} of pp collision data at $\sqrt{s} = 7\,\mathrm{TeV}$ with the ATLAS detector at the LHC.", *CERN-PH-EP-2012-019* (2012).

[33] P. M. Nadolsky, H.-L. Lai, Q.-H. Cao et al., "Implications of CTEQ global analysis for collider observables", *Phys. Rev.* D78 (2008) 013004, arXiv:0802.0007.

[34] ATLAS Collaboration, G. Aad et al., "Measurement of the top quark-pair production cross section with ATLAS in pp collisions at $\sqrt{s} = 7\,\mathrm{TeV}$.", *Eur. Phys. J. C* 71 (2010) 1577.

[35] CMS Collaboration, S. Chatrchyan et al., "First Measurement of the Cross Section for Top-Quark Pair Production in Proton-Proton Collisions at $\sqrt{s} = 7\,\mathrm{TeV}$", *Phys. Lett. B* 695 (Oct, 2010) 424–443 . 26 p.

[36] I. I. Y. Bigi et al., "Production and Decay Properties of Ultraheavy Quarks", *Phys. Lett.* B181 (1986) 157.

[37] U. Langenfeld, S. Moch, P. Uwer, "Measuring the running top-quark mass", *Phys. Rev.* D80 (2009) 054009, arXiv:0906.5273.

[38] M. Aliev, H. Lacker, U. Langenfeld et al., "HATHOR: HAdronic Top and Heavy quarks crOss section calculatoR", *Comput. Phys. Commun.* 182 (2011) 1034–1046, arXiv:1007.1327.

[39] ATLAS Collaboration, G. Aad et al., "Measurement of the ttbar production cross-section in pp collisions at $\sqrt{s} = 7\,\mathrm{TeV}$ using kinematic information of lepton+jets events", *ATLAS-CONF-2011-121* (2011).

[40] J. M. Campbell, R. Frederix, F. Maltoni, F. Tramontano, "Next-to-Leading-Order Predictions for t-Channel Single-Top Production at Hadron Colliders", *Phys. Rev. Lett.* 102 (May, 2009) 182003.

[41] B. W. Harris, Eric Laenen, L. Phaf, Z. Sullivan, S. Weinzierl, "The Fully differential single top quark cross-section in next to leading order QCD", *Phys. Rev.* D66 (2002) 054024, arXiv:hep-ph/0207055.

[42] J. Alwall, R. Frederix, J.-M. Gerard et al., "Is V(tb) = 1?", *Eur.Phys.J.* C49 (2007) 791–801, arXiv:hep-ph/0607115.

[43] A. D. Martin, W. J. Stirling, R. S. Thorne, G. Watt, "Parton distributions for the LHC", *Eur.Phys.J.* C63 (2009) 189–285, arXiv:0901.0002.

[44] S. S. D. Willenbrock, D. A. Dicus, "Production of heavy quarks from *W* -gluon fusion", *Phys. Rev. D* 34 (Jul, 1986) 155–161.

[45] A. Heinson, A. S. Belyaev, E. E. Boos, "Single top quarks at the Fermilab Tevatron", *Phys. Rev.* D56 (1997) 3114–3128, arXiv:hep-ph/9612424.

[46] C. D. White, S. Frixione, E. Laenen, F. Maltoni, "Isolating Wt production at the LHC", *JHEP* 0911 (2009) 074, arXiv:0908.0631.

[47] S. Frixione, E. Laenen, P. Motylinski, B. R. Webber, C. D. White, "Single-top hadroproduction in association with a W boson", *JHEP* 0807 (2008) 029, arXiv:0805.3067.

[48] T. Stelzer, Z. Sullivan, S. Willenbrock, "Single-top-quark production at hadron colliders", *Phys. Rev. D* 58 (Oct, 1998) 094021.

[49] G. Mahlon, S. J. Parke, "Single top quark production at the LHC: Understanding spin", *Phys.Lett.* B476 (2000) 323–330, arXiv:hep-ph/9912458.

[50] T. M. P. Tait, C.-P. Yuan, "Single top quark production as a window to physics beyond the standard model", *Phys. Rev. D* 63 (Dec, 2000) 014018.

[51] N. Greiner, S. Willenbrock, C. Zhang, "Effective Field Theory for Nonstandard Top Quark Couplings", *Phys.Lett.* B704 (2011) 218–222, arXiv:1104.3122.

[52] J. A. Aguilar-Saavedra, "A Minimal set of top-Higgs anomalous couplings", *Nucl. Phys.* B821 (2009) 215–227, arXiv:0904.2387.

[53] J. A. Aguilar-Saavedra, "Single top quark production at LHC with anomalous Wtb couplings", *Nucl. Phys.* B804 (2008) 160–192, arXiv:0803.3810.

[54] ATLAS Collaboration, Georges Aad et al., "Search for FCNC single top-quark production at $\sqrt{s} = 7$ TeV with the ATLAS detector", *Phys.Lett.* B712 (2012) 351–369, arXiv:1203.0529.

[55] E. H. Simmons, "New gauge interactions and single top-quark production", *Phys. Rev. D* 55 (May, 1997) 5494–5500.

[56] E. Arik, O. Çakir, S. A. Çetin, S. Sultansoy, "Consequences of the extra SM families on the Higgs boson production at Fermilab Tevatron and CERN LHC", *Phys. Rev. D* 66 (Aug, 2002) 033003.

[57] CDF Collaboration, T. Aaltonen, et al., "Search for Heavy Bottomlike Quarks Decaying to an Electron or Muon and Jets in $p\bar{p}$ Collisions at $\sqrt{s} = 1.96$ TeV", *Phys. Rev. Lett.* 106 (Apr, 2011) 141803.

[58] CDF Collaboration, T. Aaltonen et al., "Search for a Heavy Top-Like Quark in $p\bar{p}$ Collisions at $\sqrt{s} = 1.96$ TeV", *Phys. Rev. Lett.* 107 (2011) 261801, arXiv:1107.3875.

[59] L. Evans, P. Bryant, "LHC Machine", *Journal of Instrumentation* 3 (2008), no. 08, S08001.

[60] *LEP design report*. CERN, Geneva, 1984.

[61] ALICE Collaboration, K. Aamondt et al., "The ALICE experiment at the CERN LHC", *JINST 3 S08002* (2008).

[62] H. Satz, "The Quark-Gluon Plasma", Nucl.Phys.A862-863:4-12,2011, 2011.

[63] LHCb Collaboration, A. Alves Jr et al., "The LHCb Detector at the LHC", *JINST 3 S08005* (2008).

[64] The LHCf Collaboration, "The LHCf detector at the CERN Large Hadron Collider", *Journal of Instrumentation* 3 (2008), no. 08, S08006.

[65] TOTEM Collaboration, G. Antchev et al., "The TOTEM detector at LHC", *NIM Phys. Res. 617* (2010) 62–66.

[66] ATLAS Collaboration, The ATLAS Collaboration, "The ATLAS Experiment at the CERN Large Hadron Collider", *JINST 3 S08003* (2008).

[67] CMS Collaboration, S. Chatrchyan et al., "The CMS experiment at the CERN LHC", *JINST 3 S08004* (2008).

[68] C. Lefevre, "LHC: the guide (English version). Guide du LHC (version anglaise)", Feb, 2009.

[69] K. Schindl, "The PS Booster as Pre-Injector for LHC", Tech. Rep. CERN-PS-97-011-DI, CERN, Geneva, Apr, 1997.

[70] M. et al. Benedikt, "The PS complex produces the nominal LHC beam",.

[71] P. et al. Collier, "The SPS as Injector for LHC: Conceptual Design", Tech. Rep. CERN-SL-97-007-DI, CERN, Geneva, Mar, 1997.

[72] The ATLAS Collaboration, *ATLAS magnet system: Technical Design Report, 1*. CERN, Geneva, 1997.

[73] The ATLAS Collaboration, *ATLAS inner detector: Technical Design Report, 2*. CERN, Geneva, 1997.

[74] N. Wermes, G. Hallewel, *ATLAS pixel detector: Technical Design Report*. CERN, Geneva, 1998.

[75] The ATLAS Collaboration, *ATLAS liquid-argon calorimeter: Technical Design Report*. CERN, Geneva, 1996.

[76] The ATLAS Collaboration, *ATLAS tile calorimeter: Technical Design Report*. CERN, Geneva, 1996.

[77] The ATLAS Collaboration, *ATLAS muon spectrometer: Technical Design Report*. CERN, Geneva, 1997.

[78] V. Cindro et al., "The ATLAS Beam Conditions Monitor", *Journal of Instrumentation* 3 (2008), no. 02, P02004.

[79] The ATLAS Collaboration, *ATLAS level-1 trigger: Technical Design Report*. CERN, Geneva, 1998.

[80] The ATLAS Collaboration, *ATLAS computing: Technical Design Report*. CERN, Geneva, 2005.

[81] The ATLAS Collaboration, "Performance of the ATLAS Trigger System in 2010.", *Eur. Phys. J. C* 72 (Oct, 2011) 1849. 63 p.

[82] P. Jenni, M. Nessi, M. Nordberg, K. Smith, *ATLAS high-level trigger, data-acquisition and controls: Technical Design Report*. CERN, Geneva, 2003.

[83] S. van der Meer, "Calibration of the effective beam height in the ISR. oai:cds.cern.ch:296752", Tech. Rep. CERN-ISR-PO-68-31. ISR-PO-68-31, CERN, Geneva, 1968.

[84] ATLAS Collaboration, G. Aad et al., "Luminosity Determination in pp Collisions at $\sqrt{s} = 7\,\mathrm{TeV}$ using the ATLAS Detector in 2011", Tech. Rep. ATLAS-CONF-2011-116, CERN, Geneva, Aug, 2011.

[85] ATLAS Collaboration, The ATLAS Collaboration, "Luminosity Public Results", `https://twiki.cern.ch/twiki/bin/view/AtlasPublic/LuminosityPublicResults`, 2011.

[86] T. Cornelissen, M. Elsing, S. Fleischmann et al., "Concepts, Design and Implementation of the ATLAS New Tracking (NEWT)", Tech. Rep. ATL-SOFT-PUB-2007-007, CERN, Geneva, Mar, 2007.

[87] R. E. Kalman, "A new approach to linear filtering and prediction problems", *Journal Of Basic Engineering* 82 (1960), no. Series D, 35–45.

[88] ATLAS Collaboration, G. Aad, et. al, "Alignment of the ATLAS Inner Detector Tracking System with 2010 LHC proton-proton collisions at $\sqrt{s} = 7\,\mathrm{TeV}$", Tech. Rep. ATLAS-CONF-2011-012, CERN, Geneva, Mar, 2011.

[89] G. Piacquadio, K. Prokofiev, A. Wildauer, "Primary vertex reconstruction in the ATLAS experiment at LHC", *Journal of Physics: Conference Series* 119 (2008), no. 3, 032033.

[90] W. Waltenberger, R. Frühwirth, P. Vanlaer, "Adaptive vertex fitting", *Journal of Physics G: Nuclear and Particle Physics* 34 (2007), no. 12, N343.

[91] ATLAS Collaboration, G. Aad, et. al, "Performance of primary vertex reconstruction in proton-proton collisions at $\sqrt{s} = 7\,\mathrm{TeV}$ in the ATLAS experiment", Tech. Rep. ATLAS-CONF-2010-069, CERN, Geneva, Jul, 2010.

[92] W. Lampl, S. Laplace, D. Lelas et al., "Calorimeter Clustering Algorithms: Description and Performance", Tech. Rep. ATL-LARG-PUB-2008-002, CERN, Geneva, Apr, 2008.

[93] ATLAS Collaboration, G. Aad, et. al, "Expected electron performance in the ATLAS experiment", Tech. Rep. ATL-PHYS-PUB-2011-006, CERN, Geneva, Apr, 2011.

[94] ATLAS Collaboration, G. Aad et al., "Electron performance measurements with the ATLAS detector using the 2010 LHC proton-proton collision data", *Eur. Phys. J.* C72 (2012) 1909, arXiv:1110.3174.

[95] ATLAS Collaboration, G. Aad, et. al, "Muon reconstruction efficiency in reprocessed 2010 LHC proton-proton collision data recorded with the ATLAS detector", Tech. Rep. ATLAS-CONF-2011-063, CERN, Geneva, Apr, 2011.

[96] ATLAS Collaboration, G. Aad et al., "Expected Performance of the ATLAS Experiment - Detector, Trigger and Physics", arXiv:0901.0512.

[97] ATLAS Collaboration, G. Aad, et. al, "Muon Performance in Minimum Bias pp Collision Data at $\sqrt{s} = 7\,\mathrm{TeV}$ with ATLAS", Tech. Rep. ATLAS-CONF-2010-036, CERN, Geneva, Jul, 2010.

[98] S. Catani, Yu.L. Dokshitzer, B.R. Webber, "The k_T-clustering algorithm for jets in deep inelastic scattering and hadron collisions", *Physics Letters B* 285 (1992), no. 3, 291 – 299.

[99] Yu. L. Dokshitzer, G. D. Leder, S. Moretti, B. R. Webber, "Better jet clustering algorithms", *Journal of High Energy Physics* 1997 (1997), no. 08, 001.

[100] ATLAS Collaboration, G. Aad, et. al, "Jet energy scale and its systematic uncertainty in proton-proton collisions at $\sqrt{s} = 7\,\mathrm{TeV}$ in ATLAS 2010 data", Tech. Rep. ATLAS-CONF-2011-032, CERN, Geneva, Mar, 2011.

[101] ATLAS Collaboration, G. Aad, et. al, *Expected performance of the ATLAS experiment: detector, trigger and physics*. CERN, Geneva, 2009.

[102] ATLAS Collaboration, G. Aad, et. al, "Commissioning of the ATLAS high-performance b-tagging algorithms in the 7 TeV collision data", Tech. Rep. ATLAS-CONF-2011-102, CERN, Geneva, Jul, 2011.

[103] G. Piacquadio, C. Weiser, "A new inclusive secondary vertex algorithm for b-jet tagging in ATLAS", *Journal of Physics: Conference Series* 119 (2008), no. 3, 032032.

[104] ATLAS Collaboration, G. Aad, et. al, "Calibrating the b-Tag Efficiency and Mistag Rate in $35 pb^{-1}$ of Data with the ATLAS Detector", Tech. Rep. ATLAS-CONF-2011-089, CERN, Geneva, Jun, 2011.

[105] I. Nugent, K. Rosbach, C. Zhu, "Missing Transverse Energy for Top Analyses in Release 16.6.5.5.1 with the 2011 dataset", Tech. Rep. ATL-COM-PHYS-2011-1565, CERN, Geneva, Nov, 2011.

[106] ATLAS Collaboration, G. Aad, et. al, "Reconstruction and Calibration of Missing Transverse Energy and Performance in Z and W events in ATLAS Proton-Proton Collisions at 7 TeV", Tech. Rep. ATLAS-CONF-2011-080, CERN, Geneva, Jun, 2011.

[107] J. Bauer, Th. Muller, *Prospects for the Observation of Electroweak Top Quark Production with the CMS Experiment.* PhD thesis, Fakultat fur Physik des Karlsruher Institut fur Technologie (KIT), Karlsruher, 2010. oai:cds.cern.ch:1308713.

[108] Ph. Sturm, "Studies for the Measurement of Single-Top-Quark-Events with the CMS-Experiment.", 2008. oai:cds.cern.ch:1311220.

[109] T. Chwalek, "Measurement of the W boson helicity in top-antitop quark events with the CDF II experiment", 2006. FERMILAB-MASTERS-2006-04.

[110] M. A. Dobbs, S. Frixione, E. Laenen et al., "Les Houches guidebook to Monte Carlo generators for hadron collider physics", arXiv:hep-ph/0403045.

[111] G. Altarelli, G. Parisi, "Asymptotic Freedom in Parton Language", *Nucl. Phys.* B126 (1977) 298.

[112] S. Catani, F. Krauss, R. Kuhn, B. R. Webber, "QCD matrix elements + parton showers", *JHEP* 0111 (2001) 063, arXiv:hep-ph/0109231.

[113] S. Hoeche, F. Krauss, N. Lavesson et al., "Matching parton showers and matrix elements", arXiv:hep-ph/0602031.

[114] S. Agostinelli et al., "GEANT4 - A Simulation Toolkit", *Nucl. Instr. and Meth.* A506 (2003) 250.

[115] ATLAS Collaboration, G. Aad et al., "The ATLAS Simulation Infrastructure", *Eur. Phys. J.* C70 (2010) 823–874, arXiv:1005.4568. Submitted to Eur. Phys. J. C.

[116] S Allwood-Spires, et. al., "Monte Carlo samples used for top physics: Top Working Group Note IX", Tech. Rep. ATL-COM-PHYS-2010-836, CERN, Geneva, Oct, 2010.

[117] M. L. Mangano, M. Moretti, F. Piccinini, R. Pittau, A. D. Polosa, "ALPGEN, a generator for hard multiparton processes in hadronic collisions", *JHEP* 0307 (2003) 001, arXiv:hep-ph/0206293.

[118] S. Frixione, B. R. Webber, "Matching NLO QCD computations and parton shower simulations", *JHEP* 0206 (2002) 029, arXiv:hep-ph/0204244.

[119] G. Corcella, I. G. Knowles, G. Marchesini et al., "HERWIG 6.5 release note", arXiv:hep-ph/0210213.

[120] G. Corcella, I. G. Knowles, G. Marchesini et al., "HERWIG 6: An Event generator for hadron emission reactions with interfering gluons (including supersymmetric processes)", *JHEP* 0101 (2001) 010, arXiv:hep-ph/0011363.

[121] S. Frixione, P. Nason, C. Oleari, "Matching NLO QCD computations with Parton Shower simulations: the POWHEG method", *JHEP* 0711 (2007) 070, arXiv:0709.2092.

[122] P. Nason, "A New method for combining NLO QCD with shower Monte Carlo algorithms", *JHEP* 0411 (2004) 040, arXiv:hep-ph/0409146.

[123] B. P. Kersevan, E. Richter-Was, "The Monte Carlo event generator AcerMC version 2.0 with interfaces to PYTHIA 6.2 and HERWIG 6.5", arXiv:hep-ph/0405247.

[124] T. Stelzer, W.F. Long, "Automatic generation of tree level helicity amplitudes", *Comput. Phys. Commun.* 81 (1994) 357–371, arXiv:hep-ph/9401258.

[125] T. Sjostrand, S. Mrenna, P. Z. Skands, "PYTHIA 6.4 Physics and Manual", *JHEP* 0605 (2006) 026, arXiv:hep-ph/0603175.

[126] B. Andersson, G. Gustafson, G. Ingelman, T. Sjöstrand, "Parton fragmentation and string dynamics", *Phys. Rep.* 97 (July, 1983) 31–145.

[127] J. M. Butterworth, J. R. Forshaw, M. H. Seymour, "Multiparton interactions in photoproduction at HERA", *Z. Phys.* C72 (1996) 637–646, arXiv:hep-ph/9601371.

[128] B. P. Kersevan, I. Hinchliffe, "A Consistent prescription for the production involving massive quarks in hadron collisions", *JHEP* 0609 (2006) 033, arXiv:hep-ph/0603068.

[129] J. M. Campbell, R. K. Ellis, "MCFM for the Tevatron and the LHC", *Nucl. Phys. Proc. Suppl.* 205-206 (2010) 10–15, arXiv:1007.3492.

[130] R. Gavin, Y. Li, F. Petriello, S. Quackenbush, "W physics at the LHC with FEWZ 2.1", arXiv:1201.5896.

[131] S. Catani, M. Dittmar, D. E. Soper et al., "QCD", arXiv:hep-ph/0005025.

[132] H. S. Bansil, et. al, "Performance of the Electron and Photon Trigger in p-p Collisions at $\sqrt{s} = 7\,TeV$", Tech. Rep. ATL-COM-DAQ-2011-008, CERN, Geneva, Jan, 2011.

[133] ATLAS Collaboration, G. Aad et al., "Performance of the Electron and Photon Trigger in p-p Collisions at $\sqrt{s} = 7\,TeV$", Tech. Rep. ATLAS-CONF-2011-114, CERN, Geneva, Aug, 2011.

[134] O. Arnaez, et. al, "Electron efficiency measurements using ATLAS 2010 data at $\sqrt{s} = 7\,TeV$: Supporting note for the 2010 egamma paper", Tech. Rep. ATL-COM-PHYS-2011-322, CERN, Geneva, Mar, 2011.

[135] N. Benekos et al., "Lepton trigger and identification for the Winter 2011 top quark analyses", Tech. Rep. ATL-COM-PHYS-2011-123, CERN, Geneva, Feb, 2011. Supporting document for Winter 2011 top physics measurements.

[136] M. Agustoni et al., "Electromagnetic energy scale in-situ calibration and performance: Supporting document for the egamma performance paper", Tech. Rep. ATL-COM-PHYS-2011-263, CERN, Geneva, Mar, 2011.

[137] ATLAS Collaboration, G. Aad et al., "Measurement of the $W \to \ell\nu$ and $Z/\text{gamma}* \to \ell\ell$ production cross sections in proton-proton collisions at $\sqrt{s} = 7\,TeV$ with the ATLAS detector", *JHEP* 1012 (2010) 060, arXiv:1010.2130. 38 pages plus author list (57 pages total), 16 figures, 15 tables.

[138] ATLAS Collaboration, G. Aad et al., "Determination of the muon reconstruction efficiency in ATLAS at the Z resonance in proton-proton collisons at $\sqrt{s} = 7\,TeV$", Tech. Rep. ATLAS-CONF-2011-008, CERN, Geneva, Feb, 2011.

[139] ATLAS Collaboration, G. Aad et al., "Data-Quality Requirements and Event Cleaning for Jets and Missing Transverse Energy Reconstruction with the ATLAS Detector in Proton-Proton Collisions at a Center-of-Mass Energy of $\sqrt{s} = 7\,TeV$", Tech. Rep. ATLAS-CONF-2010-038, CERN, Geneva, Jul, 2010.

[140] B. Abi, et. al, "Mis-identified lepton backgrounds to top quark pair production: Supporting note 5", Tech. Rep. ATL-COM-PHYS-2010-849, CERN, Geneva, Oct, 2010. Supporting note for the top observation paper.

[141] B. Alvarez, et. al, "Measurement of t-Channel Single Top-Quark Production Cross-section with pp Collisions using a Cuts-Based Approach", Tech. Rep. ATL-COM-PHYS-2011-1402, CERN, Geneva, Oct, 2011.

[142] J. M. Campbell, R. K. Ellis, "An Update on vector boson pair production at hadron colliders", *Phys.Rev.* D60 (1999) 113006, arXiv:hep-ph/9905386.

[143] M. Feindt, U. Kerzel, "The NeuroBayes Neural Network Package", *Nucl. Instrum. Meth.* A559 (2006) 190–194.

[144] Michael Feindt, "A Neural Bayesian Estimator for Conditional Probability Densities", arXiv:0402093v1 [physics.data-an].

[145] V. Blobel, E. Lohrmann, *Statistische und numerische Methoden der Datenanalyse*. Teubner Studienbuecher, 1998.

[146] D. J. C. MacKay, "A practical Bayesian framework for backpropagation networks", *Neural Comput.* 4 (May, 1992) 448–472.

[147] F. James, M. Roos, "Minuit - a system for function minimization and analysis of the parameter errors and correlations", *Computer Physics Communications* 10 (Dec., 1975) 343–367.

[148] Th. Junk, "Confidence Level Computation for Combining Searches with Small Statistics", *Nucl. Instrum. Meth.* A434 (1999) 435–443, arXiv:hep-ex/9902006.

[149] CDF Collaboration, T. Aaltonen et al., "Observation of Single Top Quark Production and Measurement of |Vtb| with CDF", *Phys. Rev.* D82 (2010) 112005, arXiv:1004.1181.

[150] J. Neyman, E. S. Pearson, "On the problem of the most efficient tests of statistical hypotheses", *Philosophical Transactions of the Royal Society of London Series A Containing Papers of a Mathematical or Physical Character* 231 (1933), no. 694-706, 289–337.

[151] B. Alvarez et al., "Measurement of t-Channel Single Top-Quark Production in pp Collisions at $\sqrt{s} = 7\,\mathrm{TeV}$ using Neural Networks", Tech. Rep. ATL-COM-PHYS-2011-1404, CERN, Geneva, Oct, 2011.

[152] ATLAS Collaboration, G. Aad et al., "Jet energy measurement with the ATLAS detector in proton-proton collisions at $\sqrt{s} = 7\,\mathrm{TeV}$", arXiv:1112.6426.

[153] ATLAS Collaboration, G. Aad et al., "Jet energy resolution and selection efficiency relative to track jets from in-situ techniques with the ATLAS Detector Using Proton-Proton Collisions at a Center of Mass Energy $\sqrt{s} = 7\,\mathrm{TeV}$", Tech. Rep. ATLAS-CONF-2010-054, CERN, Geneva, Jul, 2010.

[154] F. Demartin, S. Forte, E. Mariani, J. Rojo, A. Vicini, "Impact of parton distribution function and α_s uncertainties on Higgs boson production in gluon fusion at hadron colliders", *Phys. Rev. D* 82 (Jul, 2010) 014002.

[155] P. M. Nadolsky, H.-L. Lai, Q.-H. Cao et al., "Implications of CTEQ global analysis for collider observables", *Phys.Rev.* D78 (2008) 013004, arXiv:0802.0007.

[156] ATLAS Collaboration, G. Aad et al., "Measurement of ttbar production with a veto on additional central jet activity in pp collisions at $\sqrt{s} = 7\,\mathrm{TeV}$ using the ATLAS detector", arXiv:1203.5015.

[157] CMS Collaboration, S. Chatrchyan et al., "First measurement of $B(t \to Wb)/B(t \to Wq)$ in the dilepton channel in pp collisions at $\sqrt{s} = 7\,\mathrm{TeV}$", *CMS-PAS-TOP-11-029* (2012).

[158] B. Alvarez et al., "Measurement on t-channel single-top quark production using boosted decision trees.", Tech. Rep. ATL-COM-PHYS-2011-1405, CERN, Geneva, Oct, 2011.

Danksagung

Ein besonderer Dank gebührt Prof. Dr. Wolfgang Wagner, dafür dass er mich in seine Arbeitsgruppe in Karlsruhe und Wuppertal aufgenommen hat. Besonders hervorzuhebend ist dass er mir während der Promotionszeit einen 2,5 jährigen CERN Aufenthalt ermöglicht hat sowie seine exzellente Betreuung und die gute Zusammenarbeit in dieser Zeit.

I would like to thank Prof. Dr. Julien Donini for his kindness to take over the job as co-referee of my thesis and the time he actively accompanied my work in the ATLAS single-top group.

Ein grosser Dank an Dr. Dominic Hirschbühl, für seine umfassende Betreuung mit Rat und Tat rund um die Uhr und für das Korrekturlesen der gesamten Arbeit. Kathrin Becker sei gedankt für ihre Unterstützung bei der Analysearbeit in stressigen Zeiten und für ihr immer offenes Chat-Fenster. Ein Dankeschön an Dr. Georg Sartisohn für die gute gemeinsame Zeit am CERN und in Wuppertal. Dr. Daniel Wicke danke ich für das Korrekturlesen von einigen Kapiteln der Arbeit. Ein grossen Dank an alle Mitglieder der Wuppertaler Arbeitsgruppe, insbesondere an Dr. Torsten Harenberg, der immer alle Computing Probleme löste und ein offenes Ohr hatte. Clemens Lange und Dr. Anna Henrichs danke ich für die guten Diskussionen über Physik und andere Themen.

Many thanks to my single top-quark t-channel co-analysers, Dr. Jenny Holzbauer and Prof. Dr. Reinhard Schwienhorst for the good collaboration.

Für ihre unermüdliche Unterstützung während der ganzen Promotionszeit danke ich meinen Eltern und meiner Schwester herzlichst. Marta möchte ich für Ihre Geduld und Ihr Verständnis danken.